Sheffield Hallam University

A Sheffield Hallam University thesis

Auxetic foams for sports applications

Oliver Hamish Duncan

A thesis submitted in partial fulfilment of the requirements
of Sheffield Hallam University
for the degree of Doctor of Philosophy, in collaboration with Manchester
Metropolitan University

January 2019

Declaration

I hereby declare that the work described in this thesis was performed by the author, at Sheffield Hallam University between October 2015 and January 2019, and this thesis has not been submitted for higher degree to any other university or institute.

Author: Oliver Hamish Duncan

Director of study: Professor Andrew Alderson

Acknowledgements

Glossary of common terms

Term	Definition
AM	Additive Manufacture/Manufacturing
ATR	Attenuated total reflectance
DSC	Differential Scanning Calorimetry
E	Young's Modulus
Effective Poisson's ratio	Poisson's ratio calculated using strains obtained in non-uniform tests (i.e. under indentation)
ε_m	Volumetric deformation strain (imposed by mould)
ε_p	Volumetric recovery strain (after re-heating)
ε_u	Volumetric unloading strain (after manual relaxation)
FDR	Final Density Ratio (Original/Final)
FTIR	Fourier transform infrared spectral analysis
FVR	Final Volume Ratio (Original/Final)
H	Hardness or Indentation Resistance
G	Shear Modulus
k	Force Constant
K	Bulk Modulus
Micro-ct	Micro computed tomography
NPR	Negative Poisson's ratio
PE	Protective Equipment
PPE	Personal Protective Equipment
PU	Polyurethane
R_f	Measure of shape fixing from shape memory literature
R_r	Measure of heat induced recovery from shape memory literature
SAN	Styrene and acrylonitrile
Strain dependent Poisson's ratio	Poisson's ratio at stated regions of axial strain, e.g. between 0 and 5% or 5 and 10%
Tangent modulus	Similar to Young's modulus, but measured incrementally (not from zero strain)
TBI	Traumatic Brain Injury
TGA	Thermogravimetric analysis
UC	Unconverted
U_c	Energy absorbed during compression
U_i	Energy absorbed during indentation
ν	Poisson's ratio
VCR	Volumetric Compression Ratio (Original/Final)
XRD	X-ray diffraction
Young's modulus	Young's modulus of foam (unless otherwise stated), measured between a strain of zero to a defined compressive or tensile value

Abstract

This thesis assesses whether current auxetic foams can improve the performance of sporting protective equipment, and lays out steps to realise their commercial potential.

A wide range of conversion temperatures (120 °C to 200 °C) and times (20 to 180 minutes) for ~3 x 3 x 9 cm conversions of polyurethane foam with volumetric compression ratios (VCRs) of 2 or 3 changed polymeric bonding, fixed imposed compression, and changed their mechanical properties. Effects of conversion time and temperature were approximately interchangeable, and are summarised as heat exposure. As predominantly hydrogen bonding between urea segments increased with heat exposure, shape fixing (final volume ratio, FVR) also increased. Shape fixing of imposed compression (i.e. to an FVR of ~2 in samples with a VCR of 3) caused anisotropic foams to become re-entrant and isotropic, initially reducing Young's modulus and Poisson's ratio from ~50 kPa to ~30 kPa and ~0.3 to ~-0.2, respectively. Further heating increased hydrogen bonding, did not change isotropy, continuously increased Young's modulus to ~120 kPa and Poisson's ratio increased to an approximate plateau at zero.

The foams described above, and the conventional parent foam, were indented by two cylinders (10 and 50 mm diameters) and a stud (12 mm diameter). A value (x) connecting elastic properties to indentation resistance in Hertzian indentation theory was calculated for each indenter. Integrating force vs displacement, giving energy absorption, mitigated non-linearity. During cylindrical indentations, x was higher (0.6 to 0.8) than the expected 0.33. During studded indentations x was 0.91, close to its expected value of 1 after outlying unconverted samples were excluded. Digital image correlation showed densification was significantly higher for auxetic samples ($\alpha > 0.95$), which deformed with a flatter surface for the 10 mm cylinder and stud ($\alpha > 0.95$). Densification and flatter deformation could have increased x during cylindrical indentations and caused unconverted samples to be outliers in studded indentations.

To utilise improvements in often large area PPE, sheets (30 x 30 x 2 cm) of auxetic foam were produced with internal compression controlled and varied using through thickness rods. The sheets fabricated with graded compression levels displayed clearly defined quadrants of differing cell structure and mechanical properties, shown through analytical modelling to be fully consistent with expectations from honeycomb theory. Isotropic sheets and quadrants had a maximum magnitude of NPR of ~-0.1, and Young's modulus of ~50 kPa. Anisotropic quadrants had direction dependant Poisson's ratios as low as ~-0.4 and yet Young's moduli similar to open cell foam (~30 kPa in tension and up to ~5% compression, ~0 kPa beyond ~10% compression).

Finally, steam processing produced closed cell foams with a Poisson's ratio of ~-0.1 and Young's modulus (~1 MPa) similar to closed cell foam in sporting PPE.

Table of Contents

Chapter 1: Introduction

1.1. Introduction

Injuries in sport are common and place a significant burden upon participants and national economies [1,2], estimated at $525 (~£380) million per year in The Netherlands [3] for example. The main methods of intervention are elimination, modification (a reduction in severity or likelihood of injury) and reaction (i.e., medical) [2]. Preventative measures such as protective equipment (PE) and Personal Protective Equipment (PPE), and/or rule changes, are more cost effective than reactive procedures [2] and successful products can increase a manufacturer's share of the sporting goods market (~$90/£66 billion in the USA in 2017 [4]). Sporting PE is intended to reduce risks and is typically either an addition to the playing field or environment (e.g., crash mats or barriers, referred to herein as PE) or worn by sports participants (e.g. helmets, back protectors or shin/knee pads, referred to herein as PPE). Both equipment types provide; (i) protection against impact, dissipating and absorbing energy while reducing peak forces/accelerations, pressures and in some cases such as helmets, impulses [1,2,5–7] and (ii) protection from penetration, abrasions and lacerations [5,6,8,9]. Sporting PPE can also provide support to joints, muscles and the skeleton [2,5,6,8,10].

Sporting PPE (Figure 1.1) often contains a shell—typically a stiff material or Shear thickening fluid layer—to spread forces and reduce pressures [5,6,9,11]. Impacts are typically attenuated by elastic [2,11], viscoelastic and/or permanent deformation (e.g. crushable foam in cycling helmets) of a cushioning material with a lower stiffness than the shell [5,6,9,11]. Visco-elastic and permanent deformation reduce impulses, improving the level of protection [2].

Sporting PPE must sometimes cover large areas and should ideally be low in mass and bulk to reduce restriction of movement, fatigue and heat build-up. Closed cell foam or shear thickening material is typically used for the cushioning layer in PPE, and with limited thickness to compress and decelerate impacting bodies, material selection is crucial. In contrast, PE such as crash mats (where bulk, mass and ergonomics are less critical) are often large and thick, allowing more gradual deceleration over a greater distance through compression of compliant foam [11]. For both sporting PE and PPE, deceleration (or force) ideally reaches a maximum yet safe value at low strains, before plateauing and deforming with no additional load to safely maximise energy absorption (the integral of decelerating force with respect to deformation) before foam densification (at high strains) causes high deceleration (or force) [12]. Crash mats are used in different scenarios and conditions; from protecting skiers, snowboarders and mountain bikers (who can travel at high speeds) from hazards on a mountain (i.e., lift poles or

trees), often in extreme and variable climates, to providing padding to gymnasts on flat surfaces at room temperature.
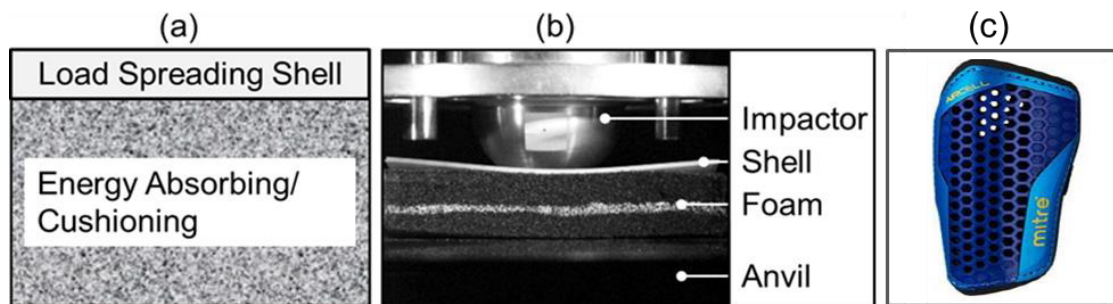
Figure 1.1: (a) Schematic of a typical piece of Personal Protective Equipment containing pressure dissipating material (hard outer shell) and energy absorbing/cushioning material (deformable foam); **(b)** Impact image adapted from British Standard 6183-3:2000; **(c)** Mitre Aircell football shin pad featuring a hard shell with a compliant foam backing.

Sports equipment is a rapid uptake market. Manufacturers search for new technology to remain competitive, achieve the highest possible levels of certification and improve safety. As an example of material development in sporting PPE, trends over the past twenty years have favoured lightweight, ergonomic equipment which does not sacrifice performance in certification tests [7]. Shear thickening fluids with high energy absorption were developed and can act as a shell and cushion [13,14], offering comfort and flexibility under normal use and increased stiffness under impact. Further product and material improvements are still required to continue reducing sports injuries and the burdens they cause [2,15].

Auxetic materials have a negative Poisson's ratio (NPR) [16], meaning they expand laterally in one or more perpendicular direction/s when they are extended axially. Poisson's ratio (ν) is the negative of the ratio of lateral to axial strain (Figure 1.2). The potential application of foams, textiles and additively manufactured (AM) auxetic materials to sporting PE, PPE and other forms of protective equipment [17] has been discussed in articles with a focus on materials (e.g. [18–20]) and sport (e.g. [21–24]). Multi-axial expansion could also be useful in filtration applications [25–28], while gradient structures with discretely or continuously varying Poisson's ratio and/or Young's modulus can dramatically enhance bending stiffness [29,30]. The variety of available processing and fabrication methods could provide sports equipment manufacturers options to reduce the mass of skis, without sacrificing stiffness, impact force attenuation of protective equipment as well as comfort and fit of garments and apparel (to name a few).
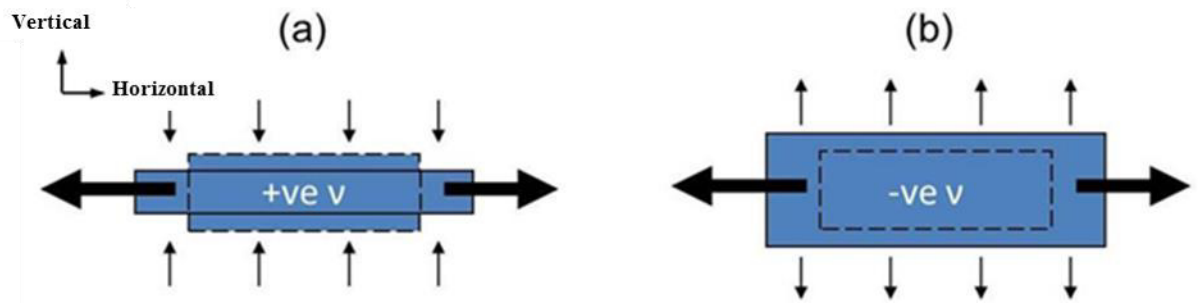
Figure 1.2: Lateral (vertical) deformation due to Poisson's ratio during tensile axial (horizontal) loading for **(a)** a conventional material and **(b)** an auxetic material. Thick and thin arrows correspond to deformation due to loading and Poisson's ratio respectively.

There are numerous reviews into auxetic materials and/or structures [31–38], but at the start of this project there had not yet been one focussing on their application to sporting goods. Auxetic foam was the first man made auxetic material [25]. It makes up a significant proportion of the scientific literature and has been regularly proposed for sporting protective applications [20–24]. Deficiencies in standards used to certify sporting PE and PPE (or a lack of a standard in some instances) and the equipment they certify [8,39] are often highlighted [40,41], and indicate changes in equipment testing and design are likely. Inspection of PPE (impact shorts, knee guards, elbow guards and back protectors etc.) marketed for adventure sports including mountain biking, kayaking and snow sports shows that EN1621 [42] & EN 14120:2003 [43] (for motor-biking) are repeatedly used in place of a dedicated certification. EN1621 [42] & EN 14120:2003 [43] do not measure impact force attenuation while pads are wet, important for kayaking, or at cold temperatures possible during snow sports, which can increase peak forces during impacts by two to three times [44]. Combining cross-disciplinary work on auxetic foams to develop novel and improved materials could help meet new requirements, and findings are likely to relate to general (rather than only sporting) PE and PPE.

NPR can increase indentation resistance [45,46], lending auxetic materials well to impact force or acceleration attenuating scenarios, demonstrated by impacting auxetic foams [18,22,47]. Auxetics' multi-axial expansion [48,49] and double curvature [24,25,50] could improve comfort, fit and durability in sporting garments and PPE. Foam studies typically use established, thermo-mechanical fabrication methods for auxetic polyurethane (PU) foams, with tests based upon those outlined in standards used to certify sporting PE and PPE (i.e., British Standards Institution - BSI, International Organization for Standardization - ISO, International Organization for Standardization - ASTM), comparing auxetic foam to its unconverted parent foam.

The thermo-mechanical fabrication process for auxetic foam [25] first applies tri-axial compression to buckle the ribs of thermoplastic open cell foam, using a mould to apply a

predetermined volumetric compression ratio (VCR, initial volume/final volume). Isotropic compression is usually applied with VCR between two and five [34,51]. Buckled ribs are fixed in position by heating and cooling [25,34], but re-expansion following heat or solvent exposure has been reported [52–54]. Recent developments in the fabrication of auxetic PU foam have deepened understanding of the mechanisms that can fix imposed cellular structures, and provided options to fabricate foams with greater control over final structures. Developments include rapid fabrications [55] and the ability to tailor elastic modulus and Poisson's ratios of anisotropic and gradient foam samples [56]. A recent method using steam penetration [57] may allow fabrication of auxetic closed cell foam with a Young's Modulus close to or above 1 MPa , as often seen in sporting PPE [1,5–7,11].

1.2.   Aims and Objectives

The following requirements have been identified to collect evidence supporting the application of auxetic foam for protective sports equipment:

i) Small scale (and therefore also large scale) thermo-mechanical fabrications have rarely measured changes to the polymer following fabrication [58]. The effects of conversion parameters (fabrication heat and time) on foam polymer bonding are unclear, and so there is poor understanding of how to maximise NPR or create isotropic, iso-density samples with a re-entrant structure and linear stress vs strain relationships for comparative testing (i.e. as in [45]). A lack of clarification of dimensional and structural stability/blocked shape memory over time and following heat/solvent exposure [52–54] could shorten product life-span, put off potential manufacturers and even cause changes between foam fabrication and characterisation or further testing, such as indentation or impact testing.

ii) Because of unknowns in small and large scale fabrications, such as whether foams subject to increased heat exposure with a Poisson's ratio close to zero are isotropic [45], the findings of indentation tests are unclear [45]. Due to stark differences in stress vs strain relationships and densities between auxetic and comparative unconverted samples, large reductions to impact force attenuation [18,22,47,59] and in some cases the enhanced indentation resistance [60,61] of auxetic foams are exaggerated. Unambiguous and unexaggerated clarification of the effect of Poisson's ratio (and NPR) on indentation resistance and impact force attenuation are required.

iii) Density variations within large auxetic foam samples or sheets have not been measured or controlled [51,59,62]. A method to control and predict compression within large foam sheets would facilitate commercial production to produce consistent materials large enough for use in sports equipment, and to reduce fabrication costs. Such foams could already be used as

compliant layers in protective equipment, such as helmet liners that increase linear and/or rotational acceleration during impacts [63]; a high impact area with calls for improvement from the scientific community [15].

iv) Applying the steam processing routes for closed cell foam [57] could allow fabrication of auxetic foams with a Young's modulus close to that of foam found in currently sports equipment [1,5–7,11].

The following aims and objectives form a programme of experimentation addressing areas i) to iv):

Aim 1: To understand the effects of thermo-mechanical fabrication parameters for auxetic polyurethane foam (time, temperature and volumetric compression ratio) on foam's elastic properties (Poisson's ratio and Young's modulus), then observe and explain any correlations between fabrication parameters, elastic properties, dimensional stability and polymeric bonding.

Objective 1.1: To thermo-mechanically convert and mechanically characterise (for Poisson's ratio and Young's Modulus) PU foam samples at a wide range of times, temperatures and multiple VCRs

Objective 1.2: To perform polymeric analysis on the unconverted samples (TGA, DSC, XRD, XRF and FTIR) on both unconverted, and a range of converted samples, to observe the effects of different fabrication conditions

Objective 1.3: To test converted foams' dimensional stability over time and after re-heating.

Objective 1.4: To select conditions to create isotropic, iso-density samples with a range of Poisson's ratios and linear stress vs strain and axial strain vs transverse strain relationships for indentation testing

Aim 2: To understand how Poisson's ratio affects the indentation resistance of auxetic and conventional PU foam over large strain ranges possible in materials for impact protection.

Objective 2.1: To fabricate samples as per objective 1.4, and re-assess their isotropy, density, Poisson's ratio and the linearity of their stress vs strain and transverse vs axial strain relationships

Objective 2.2: To compare changes in the indentation resistance of auxetic/non-auxetic foam caused by Poisson's ratio

Objective 2.3: To study material flow with DIC, and give reasons for differences in indentation resistance (objective 2.2)

Aim 3: To investigate methods to control and alter the internal structure of large sheets of uniform and gradient auxetic foam.

Objective 3.1: To fabricate sheets with internally controlled and varied structures

Objective 3.2: To compare the internal structures and mechanical characteristics (density, Poisson's ratio and Young's modulus) of converted sheets

Objective 3.3: To theoretically validate changes to internal structures through creation of a numerical model and comparison to cell structure and mechanical characterisation

Aim 4: To clarify whether recent methods to convert auxetic closed cell foam can be applied to foam similar to or foam found in sporting protective equipment.

Objective 4.1: To carry out steam treatment on a range of closed cell foams

Objective 4.2: To test dimensional stability over time, Young's modulus and Poisson's ratio of steam treated foams

1.3. Thesis Structure

This thesis will first assess current sporting PE and PPE and auxetic foam in a critical literature review (Chapter 2), adapted from an extensive review including Finite Element Analysis (FEA) and auxetic textiles published as part of this course of study [64]. Each of the aims 1 to 4 will be addressed within the following Chapters 3 to 6. Chapters 3 and 5 are based around publications completed and submitted within this course of study on small [65] and large [66] scale auxetic foam fabrications. Chapter 6 is a shorter feasibility study demonstrating a recent fabrication method for auxetic closed cell foam [57], a possible replacement for closed cell foams often used in PE and PPE. Chapters 2 to 5 are embellished with further findings and connections made between findings following publication. A preceding publication written in the early months of the course of study using data collected at MSc level [59] helped to justify the programme of investigation. Each chapter was completed following pilot or alternative testing, many of which have also been published [60,67–70]. Findings in Chapter 3 are comparable to similar tests using different PU foam [67]. A range of publications completed through this programme of study investigate the fabrication of large sheets of auxetic foam [60,68,69] and will be referenced to validate findings in Chapter 5.

The experimentation to address the aforementioned aims and objectives (Chapters 3 to 6) was carried out at Sheffield Hallam University (under the supervision of Professor Andrew Alderson), based in the Materials and Engineering Research Institute, giving access to a range of polymer characterisation devices, ovens and facilities to make and adapt compression moulds, quasi-static test devices, microscopic analyses and software and equipment for Digital Image Correlation. A bespoke drop rig and high speed cameras were made available by the Centre for Sports Engineering Research through supervision from Dr Leon Foster. Extensive collaboration was made with Manchester Metropolitan University through Dr Tom Allen's supervision and some collaboration on open cell foam fabrications was made with Dr Ruben Gatt and Professor Joseph N. Grima at The University of Malta.

1.4. References

1. Hrysomallis C, Morrison W, He J. Assessing the shock absorption of thigh pads. J Sci Med …. 1999.
2. Payne T, Mitchell S, Halkon B, Bibb R. A systematic approach to the characterisation of human impact injury scenarios in sport. BMJ Open Sport Exerc Med. 2016.2(1). e000017.
3. Schmikli SL, Backx FJG, Kemler HJ, Van Mechelen W. National survey on sports injuries in the netherlands: target populations for sports injury prevention programs. Clin J Sport Med. 2009.19(2). 101–6.
4. Statista. Sporting Goods Industry - Statistics & Facts [Internet]. **2018** [cited 2018 May 1]. Available from: https://www.statista.com/topics/961/sporting-goods/
5. Ankrah S, Mills NJ. Performance of football shin guards for direct stud impacts. Sport Eng. 2003.6(4). 207–19.
6. Ankrah S, Mills NJ. Analysis of ankle protection in Association football. Sport Eng. 2004.7(1). 41–

52.

7.   Hrysomallis C. Surrogate thigh model for assessing impact force attenuation of protective pads. J Sci Med Sport. 2009.12(1). 35–41.

8.   Schmitt KU, Liechti B, Michel FI, Stämpfli R, Brühwiler PA. Are current back protectors suitable to prevent spinal injury in recreational snowboarders? Br J Sports Med. 2010.44(11). 822–6.

9.   Michel FI, Schmitt KU, Liechti B, Stämpfli R, Brühwiler P. Functionality of back protectors in snow sports concerning safety requirements. Procedia Eng. 2010.2(2). 2869–74.

10. Adams C, James D, Senior T, Allen T, Hamilton N. Development of a Method for Measuring Quasi-static Stiffness of Snowboard Wrist Protectors. In: Procedia Engineering. **2016**. p. 378–83.

11. Mills NJ. The biomechanics of hip protectors. Proc Inst Mech Eng H. 1996.210(4). 259–66.

12. Jenkins M. Materials in sports equipment. Vol. 2. Subic A, editor. Cambridge: Woodhead Publishing Ltd.; **2007**. 138-139 p.

13. Dura J V., Garcia a. C, Solaz J. Testing shock absorbing materials: the application of viscoelastic linear model. Sport Eng. 2002.5(1). 9–14.

14. Hayes, S. G. & Venkatraman P. Materials and Technology for Sportswear and Performance Apparel. In: Materials and Technology for Sportswear and Performance Apparel. **2016**. p. 314.

15. Bailly N, Laporte JD, Afquir S, Masson C, Donnadieu T, Delay JB, et al. Effect of Helmet Use on Traumatic Brain Injuries and Other Head Injuries in Alpine Sport. Wilderness Environ Med. 2018.29(2). 151–8.

16. Evans KE. Auxetic polymers: a new range of materials. Endeavour. 1991.15(4). 170–4.

17. Scarpa F, Giacomin J, Zhang Y, Pastorino P. Mechanical performance of auxetic polyurethane foam for antivibration glove applications. Cell Polym. 2005.24(5). 253–68.

18. Lisiecki J, Błazejewicz T, Kłysz S, Gmurczyk G, Reymer P, Mikułowski G. Tests of polyurethane foams with negative Poisson's ratio. Phys Status Solidi Basic Res. 2013.250(10). 1988–95.

19. Zhou L, Zeng J, Jiang L, Hu H. Low-velocity impact properties of 3D auxetic textile composite. J Mater Sci. 2017.53(5). 1–16.

20. Lakes RS. Design Considerations for Materials with Negative Poisson's Ratios. J Mech Des. 1993.115(4). 696.

21. Allen T, Martinello N, Zampieri D, Hewage T, Senior T, Foster L, et al. Auxetic foams for sport safety applications. Procedia Eng. 2015.112(0). 104–9.

22. Allen T, Shepherd J, Hewage TAM, Senior T, Foster L, Alderson A. Low-kinetic energy impact response of auxetic and conventional open-cell polyurethane foams. Phys Status Solidi Basic Res. 2015.9. 1–9.

23. Taha Z, Hassan MHA. Parametric Analysis of the Influence of Elastomeric Foam on the Head Response during Soccer Heading Manoeuvre. Procedia Eng. 2016.147. 139–44.

24. Sanami M, Ravirala N, Alderson K, Alderson A. Auxetic materials for sports applications. Procedia Eng. 2014.72. 453–8.

25. Lakes RS. Foam Structures with a Negative Poisson's Ratio. Science (80-). 1987.235(4792). 1038–40.

26. Alderson A, Evans KE, Rasburn J. Separation process and apparatus - Patent WO1999022838A1. 1999.

27. Alderson A, Rasburn J, Evans KE. An Auxetic Filter : A Tuneable Filter Displaying Enhanced Size Selectivity or Defouling Properties. Ind Eng Chem Res. 2000. 654–65.

28. Alderson A, Rasburn J, Evans KE. Mass transport properties of auxetic (negative Poisson's ratio) foams. Phys Status Solidi - Basic Solid State Phys. 2007.244(3). 817–27.

29. Hou Y, Neville R, Scarpa F, Remillat C, Gu B, Ruzzene M. Graded conventional-auxetic Kirigami sandwich structures: Flatwise compression and edgewise loading. Compos Part B Eng. 2014.59. 33–42.

30. Hou Y, Tai YH, Lira C, Scarpa F, Yates JR, Gu B. The bending and failure of sandwich structures with auxetic gradient cellular cores. Compos Part A Appl Sci Manuf. 2013.49. 119–31.

31. Evans KE, Alderson A. Auxetic materials: Functional materials and structures from lateral thinking! Adv Mater. 2000.12(9). 617–28.

32. Yang W, Li ZM, Shi W, Xie BH, Yang MB. On auxetic materials. J Mater Sci. 2004.39(10). 3269–79.

33. Greaves GN, Greer AL, Lakes RS, Rouxel T. Poisson's ratio and modern materials. Nat Mater. 2011.10. 823–37.

34. Critchley R, Corni I, Wharton JA, Walsh FC, Wood RJK, Stokes KR. A review of the manufacture, mechanical properties and potential applications of auxetic foams. Phys Status Solidi Basic Res. 2013.250(10). 1963–82.

35.   Prawoto Y. Seeing auxetic materials from the mechanics point of view: A structural review on the negative Poisson's ratio. Comput Mater Sci. 2012.58. 140–53.

36.   Kolken HMA, Zadpoor AA. Auxetic mechanical metamaterials. RSC Adv. 2017.7. 5111–29.

37.   Lakes RS. Negative-Poisson's-Ratio Materials: Auxetic Solids. Annu Rev Mater Res. 2017.47. 63–81.

38.   Ren X, Das R, Tran P, Ngo TD, Xie YM. Auxetic metamaterials and structures: a review. Smart Mater Struct. 2018.27. 023001.

39.   Mcintosh AS. Biomechanical considerations in the design of equipment to prevent sports injury. Proc IMechE Part P J Sport Eng Technol. 2011.226. 193–9.

40.   Schmitt K-U, Liechti B, Michel FI, Stämpfli R, Brühwiler PA. Are current back protectors suitable to prevent spinal injury in recreational snowboarders? Br J Sports Med. 2010.44(11). 822–6.

41.   Michel FI, Schmitt KU, Greenwald RM, Russell K, Simpson FI, Schulz D, et al. White Paper: Functionality and efficacy of wrist protectors in snowboarding-towards a harmonized international standard. Sport Eng. 2013.16(4). 197–210.

42.   Standardization EC for. EN 1621-2 2003 Motorradfahrer Schutzkleidung Teil 2 Rückenprotektoren. **2003**.

43.   European Committee for Standardization. EN 14120:2003 Protective clothing — Wrist , palm , knee and elbow protectors for users of roller sports equipment — Requirements and test methods. 2003.3.

44.   Signetti S, Nicotra M, Colonna M, Pugno NM. Modeling and simulation of the impact behavior of soft polymeric-foam-based back protectors for winter sports. J Sci Med Sport. 2019.

45.   Chan N, Evans KE. Indentation resilience of conventional and auxetic foams. J Cell Plast. 1998.34. 231–60.

46.   Alderson KL, Pickles AP, Neale PJ, Evans KE. Auxetic polyethylene: The effect of a negative Poisson's ratio on hardness. Acta Metall Mater. 1994.42(7). 2261–6.

47.   Ge C. A comparative study between felted and triaxial compressed polymer foams on cushion performance. J Cell Plast. 2013.49(6). 521–33.

48.   Cross TM, Hoffer KW, Jones DP, Kirschner PB, Meschter JC. Auxetic Structures And Footwear With Soles Having Auxetic Structures (US 2015/0075034 A1). Vol. 1. 2015.

49.   Martin PG. Filtering face-piece respirator having an auxetic mesh in the mask body (US 2011/0155137 A1). Vol. 1. 2011.

50.   Wang Z, Hu H. 3D auxetic warp-knitted spacer fabrics. Phys Status Solidi Basic Res. 2014.251(2). 281–8.

51.   Chan N, Evans KE. Fabrication methods for auxetic foams. J Mater Sci. 1997.32. 5945–53.

52.   Grima JN, Attard D, Gatt R. A novel process for the manufacture of auxetic foams and for the conversion of auxetic foam to conventional form (WO 2010049511 A2). 2010. 1–5.

53.   Boba K, Bianchi M, McCombe G, Gatt R, Griffin AC, Richardson RM, et al. Blocked shape memory effect in negative Poisson's ratio polymer metamaterials. ACS Appl Mater Interfaces. 2016. acsami.6b02809.

54.   Bianchi M, Scarpa F, Smith CW. Shape memory behaviour in auxetic foams: Mechanical properties. Acta Mater. 2010.58(3). 858–65.

55.   Li Y, Zeng C. Room-Temperature, Near-Instantaneous Fabrication of Auxetic Materials with Constant Poisson's Ratio over Large Deformation. Adv Mater. 2016.28(14). 2822–6.

56.   Sanami M, Alderson A, Alderson KL, McDonald S a., Mottershead B, Withers PJ. The production and characterization of topologically and mechanically gradient open-cell thermoplastic foams. Smart Mater Struct. 2014.23(5). 055016.

57.   Fan D, Li M, Qiu J, Xing H, Jiang Z, Tang T. A Novel Method for Preparing Auxetic Foam from Closed-cell Polymer Foam Based on Steam Penetration and Condensation (SPC) Process. ACS Appl Mater Interfaces. 2018.

58.   Li Y, Zeng C. On the successful fabrication of auxetic polyurethane foams: Materials requirement, processing strategy and conversion mechanism. Polym (United Kingdom). 2016.87. 98–107.

59.   Duncan O, Foster L, Senior T, Alderson A, Allen T. Quasi-static characterisation and impact testing of auxetic foam for sports safety applications. Smart Mater Struct. 2016.25(5). 054014.

60.   Allen T, Duncan O, Foster L, Senior T, Zampieri D, Edeh V, et al. Auxetic foam for snow-sport safety devices. Snow Sport Trauma Saf Proc Int Soc Ski Saf. 2016.21.

61.   Lakes RS, Elms K. Indentability of conventional and negative Poisson's ratio foams. J Compos Mater. 1993.27(12). 1193–202.

62.   Lowe A, Lakes RS. Negative Poisson's ratio foam as seat cushion material. Cell Polym. 2000.19(3).

157–67.

63. Vanden Bosche K, Mosleh Y, Depreitere B, Vander Sloten J, Verpoest I, Ivens J. Anisotropic polyethersulfone foam for bicycle helmet liners to reduce rotational acceleration during oblique impact. Proc Inst Mech Eng Part H J Eng Med [Internet]. 2017.231(9). 1–11. Available from: http://journals.sagepub.com/doi/10.1177/0954411917711201

64. Duncan O, Shepherd T, Moroney C, Foster L, Venkatraman PD, Winwood K, et al. Review of auxetic materials for sports applications: Expanding options in comfort and protection. Appl Sci. 2018.8(6). 941.

65. Duncan O, Clegg F, Essa A, Bell AMT, Foster L, Allen T, et al. Effects of Heat Exposure and Volumetric Compression on Poisson's Ratios, Young's Moduli, and Polymeric Composition During Thermo-Mechanical Conversion of Auxetic Open Cell Polyurethane Foam. Phys Status Solidi. 2018.1800393.

66. Duncan O, Allen T, Foster L, Senior T, Alderson A. Fabrication, characterisation and modelling of uniform and gradient auxetic foam sheets. Acta Mater. 2017.126. 426–37.

67. Duncan O, Allen T, Foster L, Gatt R, Grima JN, Alderson A. Controlling Density and Modulus in Auxetic Foam Fabrications—Implications for Impact and Indentation Testing. Proceedings. 2018.2(6). 250.

68. Allen T, Hewage T, Newton-Mann C, Wang W, Duncan O, Alderson A. Fabrication of Auxetic Foam Sheets for Sports Applications. Phys Status Solidi Basic Res. 2017.254(12).

69. Duncan O, Foster L, Senior T, Allen T, Alderson A. A Comparison of Novel and Conventional Fabrication Methods for Auxetic Foams for Sports Safety Applications. Procedia Eng. 2016.147(0). 384–9.

70. Foster L, Peketi P, Allen T, Senior T, Duncan O, Alderson A. Application of Auxetic Foam in Sports Helmets. Appl Sci. 2018.8(3). 354.

Chapter 2: Literature Review

2.1. Introduction

The following literature review has been adapted from a publication assessing the state of the art of auxetic materials for sports applications [1]. Sections focussing on Finite Element Modelling (FEM) and auxetic textiles have been reduced, and additional information on auxetic foam fabrication, characterisation and indentation testing has been included. Publications written within this programme of study have been omitted, other than one written in the first months using data collected for a preceding MSc Dissertation [2]. Conclusions have been amended and distilled into a series of identified areas for experimentation (Chapter 1, Pages 5).

2.2. Current Sporting Protective Equipment

As previously described (Chapter 1), sport safety equipment including PE and PPE provide protection against impact; by dissipating and absorbing energy to reduce peak forces/accelerations, pressures and in some cases such as helmets, impulses [3–7]. Both types of equipment can also reduce the likelihood abrasions and lacerations [5,6,8,9]. Some forms of sporting PPE (i.e. wrist protectors and neck braces) can provide support to joints, muscles and the skeleton [4–6,8,10].

PE includes crash mats used in gyms and climbing centres and protection from trees and structures (e.g. lift poles) around ski fields and mountain bike centres [11]. It is acceptable for PE to have higher volume and mass than PPE, as it is not worn by the sports participants. Pads utilise compliant materials such as open cell polymer foams to gradually decelerate sports participants [11], protecting them from rapid deceleration and injury upon collision with a surface (i.e. the ground, lift poles, trees etc). Depending on the application, resisting indentation by concentraed loads can improve safety; protecting participants from tree stumps or rocks (to name a few risks) and preventing injury to protruding limbs [11]. Seating and cushioning can also bennefit from high indentation resistance, distributing pressures and improving comfort [12,13].

PPE is more variable than PE, designed for specific sports that require a range of different movements and have different types of falls. Simple PPE such as football shin pads and cricket thigh pads consist of load spreading shells in combination with compliant foam layer(s) (Figure 1.1, Page 2), or shear thickening materials in issolation, to disipate loads and gradually decelerate impacting bodies [5,6,9,14]. Helmets protect the head by reducing high impulses that could cause brain injuries [12,15,16]. Helmets often feature crushable expanded polystyrene foam to permenantly deform and minimise impules aswell as similar combinations (shell and

foam layers) to simple PPE [12,15,16] and compliant, open cell foam to increase comfort (Figure 2.1a) [17]. Back protectors feature a hard, segmented plastic shell (Figure 2.1b) or shear thickening materials in combination with a cushioning material [9,18] to allow the spine to bend while protecting the wearer by dispitating loads and absorbing energy [9,18]. Wrist protectors include a splint to support the wrist and prevent fracture due to hyper extension (Figure 2.1c, [19,20]).
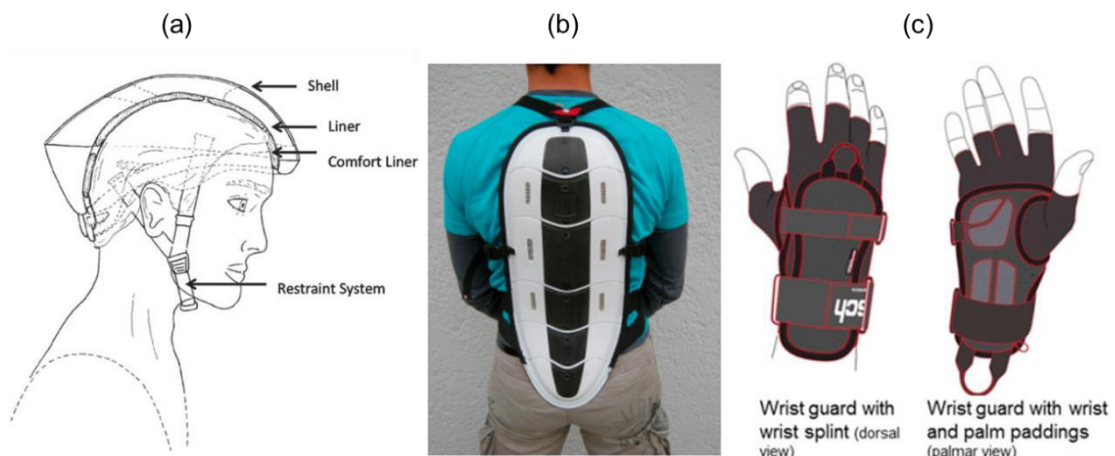
Figure 2.1: (a) Schematic showing a typical bicycle helmet [15]; (b) Picture of a snow-sports back protector with a rigid, segmented shell [9] and (c) a snowboarding wrist-guard [20]

Sport safety equipment is often certified and tested according to tests specified in standards and regulations (e.g., [21–25]), which typically specify a maximum allowable peak force/acceleration under impact. To perform well in certification tests, a product should absorb or dissipate as much energy as possible to prevent force/acceleration from passing its allowable limit [11]. The scientific literature covering sporting PE and PPE focusses on three main areas; replication of certification tests [2,5,11,26], replicating infield falls and collisions to improve certification tests or protective equipment [7,17,19,27–29] and analysing the effects of PPE on injury trends [30–32].

To reduce certification costs and increase repeatability, certification tests typically feature fixed rigid anvils rather than biofidelic (human like) surrogates, meaning they are not always representative of the scenarios where the equipment may be required to perform [4]. Replicating certification tests gives repeatable findings that can be easily interpreted by participants and manufacturers to infer improvements to safety. If a certification test is not realistic, increased chance of injury due to a mismatch in perceived protection offered by equipment is possible [33]. Criteria within certifications (such as impact energies, velocities and masses) are not always well justified [9,10,16,18,33].

In some cases there is no certification, so manufacturers certify products against a certification for another safety device considered to be similar, which can be misleading for consumers. Crash mats are typically certified to BS EN 12503-1:2013 [34] as intended for gymnasium use, but include impact tests for outdoor activities such as pole vaulting. BS EN 12503-1:2013 is not reflective of the sometimes harsh and variable outdoor environment (weather conditions, surfaces, etc.) where these mats can be located, and tested parameters do not reflect realistic impacts [25]. There are other occasions where specific certifications are not available, and so a proxy is used. Two examples from snow sports are wrist protectors, certified to EN 14120:2003 [35] for roller sports [10], and back protectors, which are often certified to EN1621 (motorbike) [36]. Schmitt *et al.* found that snow-sport participants expect back protectors to protect the spine, but EN1621 does not test against scenarios likely to cause spinal injury [8].

Some certifications have received criticism for not providing adequate tests even when applied to their intended field. Reaction to a number of high profile deaths and serious injuries as well as multiple awareness campaigns [32] increased helmet use in snow sports considerably, but head injury rates appear to have remained fairly constant [32,37]. During collisions and falls, helmet wearers are less likely to suffer a minor head injury, but concussions, severe Traumatic Brain Injury (TBI) and skull fractures have remained relatively similar [30]. Scandals in the National Football League (NFL) culminated in high proportions of Chronic Traumatic Encephalopathy (CTE), up to 99% in a biased but large sample set that could have contributed to early death, suicide and dementia in players [38].

In some cases, equipment and regulations intended to protect sports people are clearly unsatisfactory. As an example of equipment not meeting expectations, attenuation of rotational acceleration is thought to be critical in protection from concussion in sports [39,40]. Standards, however, typically assess helmets based upon their attenuation of linear accelerations (e.g., EN1077 & ASTM F2040, & F1446 [21,23,41]) and resistance to penetration (e.g., EN1077 [23]) based upon direct impacts [15,31]. Standards can be updated or replaced, for example BSI 6685-1985 for motorised vehicle helmets (a previous revision of Reference [42]) replaced BS2495:1977 and BS5361:1976 to include oblique impacts. The standard for cricket helmets (BS7928:1998) was amended (BS7928:2013) to include impacts by cricket balls [43] following findings that cricket helmets were not sufficiently attenuating acceleration under high speed impacts [16]. Commuter cycling (where cyclists travel alongside motor vehicles) is becoming increasingly popular due to clear benefits to health, congestion and emission levels, as well as improved facilities such as dedicated lanes. Safety concerns are a major barrier to participation in

commuter cycling [44,45] but helmets are still only certified to protect from linear accelerations [46]. Insufficient protection and high levels of TBI across sports have led to calls for solutions from the scientific community [30]. Reducing barriers to physical activity (that provides numerous benefits to physical [47,48] and mental [49–51] health and well-being) is undoubtedly important.

One approach to solve the problem of rotational acceleration in helmets is a slip plane between the shell and crushable foam [52]. Slip plane technology is included in some commercial helmets, despite a lack of experimental evidence to support a reduction in concussion risk [29,53–55]. The lack of control over the performance of slip plane technology highlights the problem caused by insufficient certification that does not quantify angular acceleration during oblique head impacts. As an example of material development in sporting PPE, trends over the past twenty years have favoured lightweight, ergonomic equipment which does not sacrifice performance in certification tests [7]. Shear thickening materials can act as both a shell and cushion [56,57], offering comfort and flexibility under normal use and increased stiffness under impact. Shear thickening materials in isolation (without a rigid shell) can pass certification tests for sporting PE and PPE [4–6,8,9].

Scientific literature highlights limitations in certifications, which means that associated certified products including helmets [15,53–55], back protectors [8,9] and wrist protectors [10,19,20] are not always designed to offer sufficient protection to wearers. Trends in sporting PPE are moving towards low bulk, flexible devices that will not inhibit movement/performance [3,7,9,18]. Shear thickening materials increase their stiffness dramatically at specific shear strain rates, and can remove the need for rigid shells that can inhibit movement [4–6,8,9]. Shear strain rates in standard tests depend upon unrepresentative impactors traveling at low velocities and striking overly rigid anvils [4,8,33,58], increasing the likelihood of penetration by compliant or large mass impacting bodies that impart a low shear strain rate. Current standards and the protective products they certify create a clear mismatch between equipment certification, user expectation and infield performance. Such mismatches between user expectations and infield performance are known to be dangerous [33]. Recent trends look to include the use of more representative surrogates rather than rigid anvils [19,27,59], more representative impactors [58] and tests designed for specific sports [9,10] to replace proxy standards (e.g., [35]). As certifications are updated (i.e., as per BSI 6685-1985 [42] and BS7928:2013 [43]) to meet requested calls for improvement from the scientific community, solutions including novel materials are needed to maintain certification and trends of improving ergonomics.

2.3. Auxetic Foam and other Auxetic Materials

Auxetic research began in earnest with open cell foam [60], the first example of a man made NPR material. Subsequently, auxetic materials have now been developed or discovered in other nanocrystalline [61] and microporous [62]) polymer, ceramic [63], metallic [64,65] and composite [66] forms, and include natural systems [67]. Auxetic materials such as foams, textiles and AM structures are often classed as mechanical metamaterials with unusual macro-scalar (effective) characteristics caused by their micro/nano-structure [68].

This section will first discuss the modelling of auxetic structures and mechanisms, before considering auxetic foam fabrication, properties and characteristics, followed by some of the other auxetic materials of relevance including textiles and those manufactured by AM.

2.3.1. Auxetic Foam Structures

The most common microstructures of cellular auxetics can be designated into three types; re-entrant cells, with inward pointing ribs (Figure 2.2a) [69], chiral, non-symmetric structures that cannot be superimposed onto their mirror image (Figure 2.2b) [70] and rotating units or shapes connected in such a way that causes in NPR(Figure 2.2c) [71–74]. Auxetic foam cell structure has been described as comprising re-entrant cells [26,69,75,76] (Figure 2.2a & d), a series of connected rotating triangles [77], and the missing rib model, a series of diamond cells with missing connective ribs providing a kinked rib chiral structure [78,79]. Inward folding (in compression) and outward straightening (in tension) of buckled ribs in a re-entrant structure can give NPR [69,77,80–82]. In foams and most honeycombs, the exact mechanism is complex and involves hinging around junctions between ribs, as well as rib flexure and stretching [81,83], as shown using in situ 3D X-ray microtomography and microstructurally faithful finite element modelling [84]. If cell ribs are thicker around joints then some rotation of rigid units (joints) can occur [77]. Rotation of joints is also realised in the aforementioned missing rib model due to straightening of the kinked ribs [78,79]. Missing ribs have only been identified on the surfaces of auxetic samples and not within their bulk [77]. Additionally, the missing rib (auxetic) model has lower density than the intact diamond (conventional) parent model. The increase in density of auxetic foam over the conventional open cell (referred to herein as the parent) foam, imposed through the compression stage of the thermo-mechanical fabrication process, is not then accounted for in the missing rib model. Unlike the missing rib model, both the re-entrant and connected triangles models predict the observed increase in density for auxetic foam.
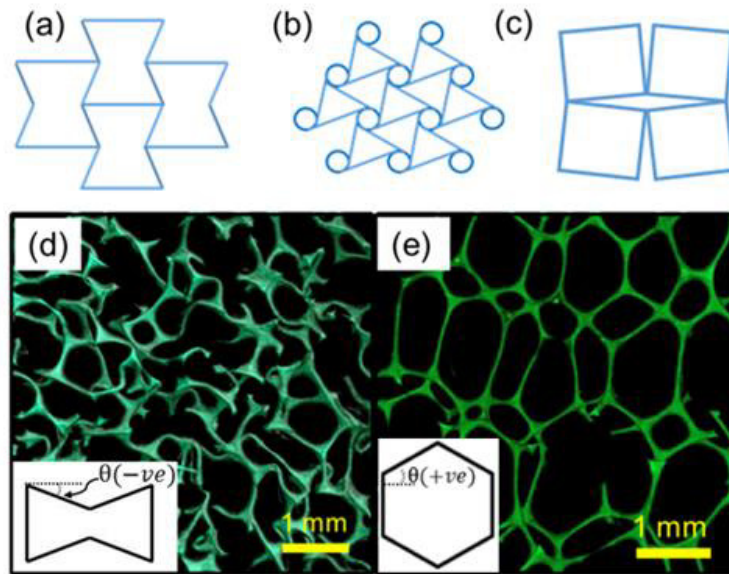
Figure 2.2: (a) Assembled 2D re-entrant structure; (b) 2D Chiral structure; (c) 2D rotating squares structure; (d) Micro Computed Tomography of polyurethane auxetic open cell foam (depth = 1 mm), pop-out showing simplified 2D diagram of a re-entrant cell, θ = re-entrant angle (negative value for angle below horizontal axes); (e) Micro CT scan of conventional open cell PU foam (depth = 1 mm), with pop-out showing simplified 2D diagram of a conventional polyhedral cell, θ = cell rib angle (positive value for angle above horizontal axes).

Re-entrant models have been used to investigate the deformation mechanics of cellular auxetics. Deformation occurs by flexure of the cell ribs (assumed to behave as beams of uniform thickness) [85], as well as rib hinging (change of angle between ribs) and stretching (increase in rib length) [86]. All three deformation modes have been modelled simultaneously both on and off-axis [81,82], confirming that the change of cell parameters (e.g., cell length or rib angle) directly affected Poisson's ratio and Young's modulus. Other than the six sided hexagon, a 14-sided polyhedron has been implemented specifically for open cell foam, with cell rib bending as the main deformation mechanism [87].

FEM [88–91] and micro-computed tomography [84] have confirmed that the angle of re-entrant cell ribs effects Poisson's ratio. Cell dimensions (e.g., rib length and thickness or cell height) can be changed to tune NPR [92,93], and flaws in the cell structure can reduce its magnitude towards zero [94]. The effect of design changes on Young's modulus and Poisson's ratio can be adjusted and improved before manufacture [95]. Full validation of FEM often requires comparison and agreement with experimental testing [96–104], which can potentially lead to models for specific applications. Experimental test data can be input into FEM solvers to validate and develop material models [105]. With a validated model, design changes can be implemented and investigated without numerous iterations of manufacturing and testing,

highlighting the benefit of robust experimental demonstration and explanation of auxetic foam's increased impact force attenuation and indentation resistance [26,106,107].

2.3.2. Fabricating and Characterising Auxetic Foam

Auxetic foam is often fabricated to experimentally show expected enhancements (i.e., to impact force attenuation or vibration damping) due to NPR [26,106,108,109]. Auxetic foam fabrications typically change the cell structure of an open cell parent foam to give it an NPR. Lakes' thermo-mechanical fabrication method [60] first applies a volumetric compression ratio (VCR, normally defined as original/final volume and typically between two and five [110]) to a parent foam in all three orthogonal axes to buckle cell ribs [85]. The applied compression changes the cell shape and causes the re-entrant structure as cell ribs buckle beyond ~5% compression [85]. Buckling the originally straight ribs (Figure 2.2e) gives the polyhedral cells a re-entrant, contorted cell structure [60] (Figure 2.2a & d). Typical sample sizes were initially small, in the order of 20 × 20 × 60 mm (following fabrication), although larger 'scaled up' samples have subsequently been fabricated (e.g., [76,111,112]).

Following volumetric compression, foam is heated to a set temperature to encourage permanent plastic deformation. The temperature is typically applied using an oven set between 130 and 220 °C [113], often close to the polymers softening temperature [76,114]. Samples and moulds are normally heated for between 6 and 60 minutes, but typically less than 30 [113]. Finally, the foam is cooled to fix the imposed structure [60]. Thermal softening and/or heating above any polymer or copolymer transition temperature can cause decreases in hydrogen bond strength [114] and increased polymer chain mobility. Increased mobility allows re-organisation of polymer chains and cell structure when subject to volumetric compression, which is permanently [115] or temporarily [78,116,117] fixed upon subsequent cooling. Degradation in polymer chains typically occurs first in ordered, hard segments, then in soft, amorphous segments [118,119].

Fabrication methods for auxetic foams have developed and diversified since Lakes' initial study [60]. Stretching samples after cooling was introduced to reduce adhesion between cell ribs and residual stresses [120]. More recently, fabrication processes have been split into stages including; multiple heating cycles (with foam removed from the mould and stretched by hand in between to reduce residual stresses, flaws and creases [121]) and the addition of an annealing stage—heating below the softening temperature. Foams are typically annealed at 100 °C for around 20 minutes [76,121,122], but longer heating times have been used for larger samples (converted to 100 x 100 x 100 mm) [26]. Alternatives to annealing include slow cooling in the mould in air [114,116] or cooling outside the mould in air [123]. Rapid cooling of polymers

through their glass transition temperature can prevent recrystallization if amorphous chains become fixed before having a chance to become re-ordered [124]. In an attempt to reduce creases and flaws when inserting foam into the mould, lubricants (olive or vegetable oil) and other oils (WD-40) have been used to lubricate moulds [76,120,125], but the effects lubricants and oils have on creasing and to the base polymer (following heating) have not been assessed systematically and remain unclear. Lubricants, particularly flammable solvents such as WD-40, could increase the likelihood of polymer degradation.

Another line of investigation has attempted to increase the range of Poisson's ratios and Young's moduli achievable following thermo-mechanical fabrications. The heat, time and compression applied during fabrication can be adjusted to give higher magnitude NPR and increased stiffness [126]. Heating for longer or at a higher temperature while using typical compression levels gives a positive or near zero Poisson's ratio re-entrant foam [107]. Positive Poisson's ratio re-entrant samples have comparable density to typical auxetic foams and a linear stress strain curve without the presence of a plateau region, but often have a higher Young's modulus, reported to be around three times higher than typical auxetic foam [107]. Comparing auxetic and re-entrant foam with a positive Poisson's ratio could demonstrate the effect of Poisson's ratio on characteristics such as vibration damping or impact force attenuation.

In depth analysis shows the complexity and diversity of chemical constitution in polymers (including those found in foams) [114]. Polymeric microstructure [114], and microstructural changes caused by heating [115] have only recently been investigated in relation to auxetic foam fabrication. Li & Zeng targeted the thermal glass transition temperature of styrene acrylonitrile copolymer (SAN) particle bonding, which is around 110 °C, to increase polymer chain mobility and fix imposed volumetric compression. Measurement of polymeric bonding changes (using Fourier transform infrared spectral analysis (FTIR)) caused by the thermo-mechanical fabrication have only been undertaken once [115], despite the wealth of studies fabricating auxetic foam.

There is also surprisingly little prior literature comparing the prediction of strain-dependent mechanical properties from structural models with experimental data for auxetic foams. An analytical model for isotropic auxetic foam based on a polyhedron cell gave good agreement with experimental strain dependent Poisson's ratio for auxetic copper foam [110]. Predictions from a 2D analytical model of a hexagonal honeycomb deforming solely by flexure of the ribs were compared with 2D FE model predictions [127]. A multiple-mechanism 3D elongated rhombic dodecahedron analytical model has been developed [128], modified [129] and Poisson's ratio vs. strain comparison have been performed [130]. Auxetic foams are, then,

exemplary systems to further explore processing-structure-properties relationships in cellular solids and offer the potential to produce carefully tailored properties for a range of applications.

Sporting products including football shin pads, cricket thigh pads and crash mats often include foam sections which have a larger planar area than typical auxetic foam samples (~20 × 20 × 60 mm) [60,76,131], and numerous scaled up fabrications have been attempted [111,112,132]. Large fabricated samples often exhibit random and ordered inhomogeneity. Random inhomogeneity is caused by flaws such as surface creasing [76], due to difficulty compressing large samples of foam into the mould [111]. Ordered inhomogeneity was observed in fabricated cubes (150 mm sides), where the centre had the lowest density [2]. Possible explanations include reduced compression towards the centre of the cube during fabrication or a thermal gradient that meant the internal structure was not sufficiently fixed and re-expanded following fabrication. The specific influence of temperature gradients and compression gradients during auxetic foam fabrication is unclear.

Solutions to increase homogeneity when fabricating large samples of foam include; (i) a mould with moveable walls, which can be assembled around the foam and then used to apply compression [111,133]; (ii) a multi-stage compression process with an intermediate VCR to reduce insertion forces [76] and (iii) a vacuum bag to apply compression [112]. Vacuum bags are claimed to reduce external densification and allow fabrication of additional shapes (i.e., curved) [112]. Surface creasing [76,111,133] and densification [112] has not been measured or qualitatively shown in large sample fabrications. Sheets fabricated in vacuum bags were highly anisotropic, suggesting non-uniform triaxial compression, and had a higher than usual VCR (of 7.5) [112]. It is unclear whether vacuum bags can apply controlled planar or through thickness compression. 'Felted foams' are the closest commercially available equivalent to isotropic auxetic foams, fabricated by compressing open cell foam between two heated plates to impart an anisotropic, re-entrant cell structure and direction dependent NPR [108].

Large, homogenous sheets or monoliths of isotropic auxetic foam could facilitate development of prototype sports equipment and ultimately commercial uptake, utilising expected enhancements to indentation resistance caused by isotropic NPR [134–136]. Inserting rods through the bulk of foam during compression and fabrication has been used to apply variable compression and final cell structure in small gradient foam samples [137], but could also provide internal control during uniform VCR. Density measurements have been used to show variable final compression through the bulk of large (150 mm sided) [2] foam cubes and smaller samples [137,138]. Controlling internal compression, then measuring and

estimating the effect of remaining differences in cell structure, compression and surface flaws is a clear extension upon previous work [2,111,112,133].

Alternatives to the thermo-mechanical fabrication process [60] include using a solvent or softening agent instead of, or in combination with, heating. Acetone [131] and pressurised CO_2 [139] can lower the glass transition temperature of some polymers and copolymers (i.e., CO_2 for SAN particles), meaning increased polymer chain mobility and subsequent fixing can be temporarily achieved at low (room) temperatures [114]. Softening methods can be combined, and both acetone [106] and CO_2 [139] have been used in combination with heat. Liquid solvents (such as acetone) will require a drying phase and so some form of gradient is likely in larger samples. Provided there is no significant gradient due to diffusion of gases from the centre of samples during/after fabrication, the CO_2 softening route could reduce the effect of temperature gradients in thermo-mechanical fabrications.

Attempts to apply thermo-mechanical fabrication methods typically used for open cell foam to closed cell foam can rupture the foam's cell walls [76,132]. NPR has still been achieved along one axis in closed cell low density polyethylene (LDPE) foam, by combining thermal softening (at 110° C) and high hydrostatic pressure (662 kPa, applied by a pressure vessel) over 10 h and maintaining the pressure for a further 6 h after cooling [140]. Heating for 1 h at 86° C, then subjecting to vacuum pressure for 5 min prior to sudden restoration of atmospheric pressure also produced uniaxial NPR in the same LDPE closed cell foam [140]. Slow diffusion of gas through cell walls was similar to predicted values, suggesting the cell walls in the auxetic LDPE foam had remained intact. A simpler method, without the need of a pressure vessel, first steams closed cell foam for around six hours at 100°C, until steam enters closed cells [141]. Subsequent cooling to condense the enclosed steam shrinks the cell and imparts a re-entrant structure following compression to around a fifth of the foam's original volume, leaving some water in the cell and increasing foam density by a further 20%. Solid state foaming (sticking together pieces of closed cell foam cut in a re-entrant shape) [142], syntactic foam processes (embedding degradable/collapsible beads with a re-entrant shape into a molten/liquid polymer) [143] and AM [144] have also produced auxetic foam-like structures.

Measuring strain in compliant, often inhomogeneous foam or foam like structures requires non-contact methods. Wide ranging studies, employing a variety of test protocols, have been undertaken to characterise auxetic polymeric foams for structural, mechanical, thermal, filtration and impact properties, for example. Isotropic auxetic foams with Poisson's ratio between 0 and −0.7 have been reported (e.g., [26,75,114,115,120,137,145]). Higher magnitudes of NPR (<−1) have also been reported for anisotropic auxetic foams [112,121]. Standardising

methods for characterising samples would help assess levels of agreement between different studies. Ideally testing should be undertaken in accordance with, or based upon, the appropriate ASTM standard (e.g., ASTM-D412—15a [146]) for quasi-static tensile testing, which requires communication of sample dimensions, strain rate, range and measurement method and joining/contact methods between sample and test rigs.

Off the shelf programmes, bespoke Matlab scripts [2,26] and video-extensometers systems (camera and tracking programme) [92,137] have been used to track markers on/in foam samples. Samples tested with liquid paper makers exhibited strain readings with greater scatter than those with pins [137]. Alternatives include measuring samples frontal area or width to give bulk deformation [92,147], tracking lines rather than points [148], laser measurements of sample area [147] and digital image [145,149] or volume [84,137] correlation (DIC and DVC respectively). DIC and DVC could give a more complete analysis of local strains.

2.3.3. Other auxetic materials

Textiles utilising two-dimensionally auxetic fabrics have been produced [150–152]. 3D auxetic textiles have been developed for composite reinforcement applications [153,154] using warp and weft yarns [155] with stitch yarns [156] and auxetic fibres [157]. A four layer woven 3D auxetic textile structure has been used as composite reinforcement, fabricated using a vacuum-assisted resin transfer moulding process [158]. 3D Auxetic textiles have also been employed to reinforce a foam matrix fabricated by injecting and foaming [159,160].

As alternatives to often inhomogeneous foams or textiles, fabrication of auxetic materials with repeatable structures using various AM techniques has been investigated (e.g., fused deposition modelling [161], selective electron beam melting [162], selective laser sintering [163] and lithography-based ceramic manufacturing [164]). Example materials used for AM in auxetic research include compliant rubbers and plastics. Auxetic 3D chiral lattices have been modelled and produced by AM using TangoBlack®, a rubber-like AM filament [165]. AM has also combined two materials of different stiffness within one re-entrant unit cell [144,166,167] (Figure 2.3).
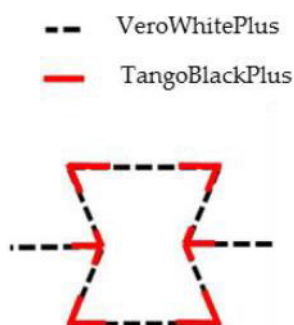
Figure 2.3: Dual material auxetic re-entrant structure

AM structure's Poisson's ratio can be tuned by altering the geometry of a unit cell [168–170], enabling the design and analysis of novel auxetic structures using FEM [171,172] to help validate existing analytical formulae. NinjaFlex®, an elastic and flexible thermoplastic PU, has been used in the AM of auxetic structures [161,173–175], and in impact testing studies [174,175], with FEM used to highlight auxetic structures' desired impact force attenuation. Elsewhere, impact testing on non-auxetic NinjaFlex® honeycombs demonstrated that increasing strain rates (0.01 to 0.1 s^{-1}) resulted in an increased energy absorption (0.01–0.34 J/cm³) [176]. Both strain rate dependency and energy absorption are key considerations for auxetic material applications in sporting PE and PPE.

2.3.4. Gradient Materials

Gradient materials are made from a single material by varying its macro-structure to have different mechanical and structural properties in different regions (e.g., auxetic and conventional regions). Gradients can be discrete [137,177] or continuous [92,137]. Composite sandwich structures employing discretely gradient honeycombs have a higher compressive modulus and are stronger than conventional sandwich structures [178]. The same sandwich structures exhibit a large increase in bending stiffness at the transition between conventional and NPR regions [179]. Opposing synclastic/anticlastic (domed/saddled) curvature associated with negative/positive Poisson's ratio respectively [60] cause increased shear modulus between regions and a localised stiffening effect. A similar stiffening effect can be seen in AM honeycombs with re-entrant inclusions during tensile tests [180]. Stiffening between discrete gradients of conventional and NPR could increase the bending stiffness (of the whole structure or of specific regions) in sports equipment that contains honeycomb or fibre reinforced composites (e.g., skis, snowboards, tennis rackets and hockey sticks to name a few). Auxetic composite sandwich structures have not been tested for sports applications.

Gradient foams have been fabricated, by applying variable compression gradients using rods [137] and/or selecting mismatched uncompressed foam and mould shapes [137,177] (e.g., uniform foam sample compressed in a tapered mould). Gradient structures could be applied to foams or other materials (i.e., fabrics) to allow the development of garments which will fit to the wearer and adapt to their shape as they move.

2.4. Expected Characteristics and Supporting Evidence

Beneficial characteristics of auxetic materials include increased shear modulus, indentation resistance [107,135], dynamic [181,182] and static compressive energy absorption [122] and decreased bulk modulus [107,135]. Increased indentation resistance [107] and compressive

energy absorption [106,108,122,138] have been shown experimentally in comparisons of auxetic and conventional foams. Lateral expansion due to axial tensile loading makes auxetic structures/materials candidates for straps in apparel, increasing area to spread increasing loads and prevent 'digging in' [183]. Many of the characteristics which provide unique enhancements for auxetic materials come from Elasticity theory [135,184].

For isotropic materials experiencing elastic deformation, Young's modulus (*E*) and shear modulus (*G*) are related (Figure 2.4a, Equation 2.1), as are Young's modulus and bulk modulus (*K*, Figure 2.4b, Equation 2.2) [185]:

$$G = \frac{E}{2(1+\upsilon)} \tag{2.1}$$

$$K = \frac{E}{3(1-2\upsilon)} \tag{2.2}$$

Elasticity theory states that Poisson's ratio must be between −1 and 0.5 for 3D isotropic materials [85,186,187], so shear and bulk modulus (Equations 2.1 and 2.2) are both positive (for positive values of Young's modulus). Poisson's ratio is between −1 and +1 for 2D isotropic materials [188]. From Equations 2.1 and 2.2, as Poisson's ratio tends towards −1 both shear (Equation 2.1) and bulk (Equation 2.2) modulus are driven towards extremely high or low values (respectively) in a 3D isotropic material. So, as Poisson's ratio reduces to negative values, a material will retain its shape and undergo greater volumetric deformation in both compression and tension.
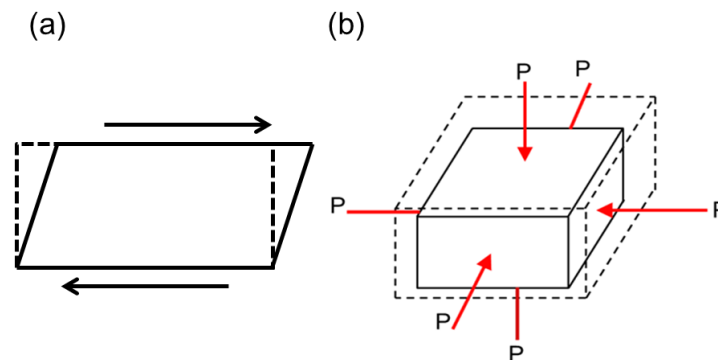
Figure 2.4: Schematic showing (a) shear deformation and (b) bulk/volumetric deformation. Black arrows show shear loading, red arrows show loading due to hydrostatic pressure, dashed lines show original (a) shape and (b) volume.

Indentation resistance is a measure of the load required to indent a material (Figure 2.5a & b). Mathematical consideration of an elastic, isotropic half space relates the force required to indent a shape (whereby contact and incidence are summarised by the value x) to a specific depth, known as indentation resistance or hardness (H) [184]. Considering a point within the half space, resistance to deformation is proportional to Young's modulus, and total (tri-axial) deformation. Expanding over the entire half space due to compression with an indenter,

described by x (1/3 for a cylinder, 2/3 for a sphere and 1 for a flat circle), indentation resistance relates to Poisson's ratio and Young's modulus by [184,189]:

$$H \propto \left(\frac{E}{(1-\upsilon^2)}\right)^x \qquad\qquad (2.3)$$
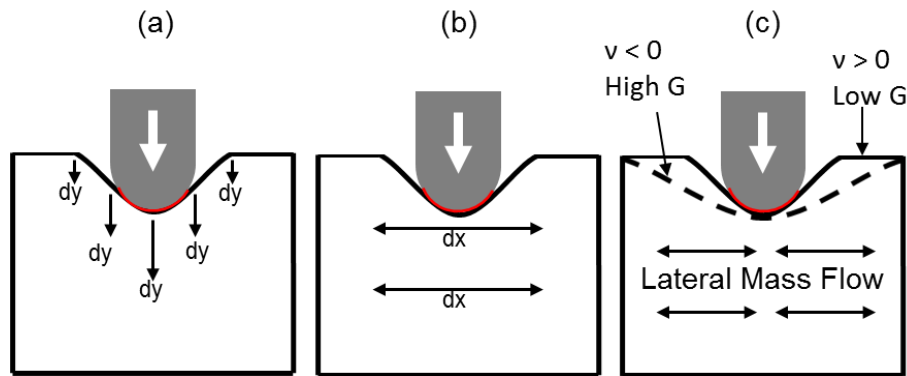
Figure 2.5: Simplified 2D indentation showing (a) Axial deformation; (b) Lateral deformation described in Equation 2.3; (c) Effect of large shear modulus (Equation 2.1) on indentation area (- - -) and lateral mass flow, both un-accounted for in Equation 2.3. The red line shows contact area (a_t, Equation 2.4).

Pads often contain relatively stiff foams, or have rigid shells, to effectively increase their indentation resistance (H in Equation 2.3) and prevent penetration by concentrated loads. A material with a large magnitude of Poisson's ratio could have equally high indentation resistance as one with a high Young's modulus. Such a material could be used to reduce the overall stiffness of a protective pad. A compliant pad with a high indentation resistance would be versatile, reacting to different surfaces to improve its resistance to deformation [13]: e.g. deforming to sufficiently cushion falls onto a flat surface, while resisting penetration by low area objects (e.g. a studs). Assuming a constant Young's modulus, as Poisson's ratio tends towards −1, a material should exhibit infinitely higher resistance to shear deformation (Figure 2.4a, Equation 2.1) and high indentation resistance (Figure 2.5, Equation 2.3), while becoming increasingly easier to deform volumetrically (Figure 2.4b, Equation 2.2). Cell parameters of AM auxetics can be designed to have different (positive and negative) Poisson's ratios [170], and it is likely that Young's modulus could be held constant. Young's modulus often varies between positive, zero and negative Poisson's ratio foams [60,80,126]. Infinite shear modulus and maximum indentation resistance and volumetric compressibility can only be achieved elastically and isotropically with auxetic materials [135], and increased indentation resistance has been shown experimentally [107,189,190].

Equation 2.3 for Hertzian indentation resistance comes from elastic properties and assumes; (i) the surfaces are continuous and have non-conforming profiles; (ii) the area of contact (Figure 2.5) is much smaller than the characteristic dimensions of the contacting bodies;

(iii) the strains are small and purely elastic and (iv) the surfaces are frictionless at the contact interface. These four assumptions for Hertzian indentation are not always held, although Equation 2.3 is often referred to and discussed in the context of non-Hertzian indentations [134,191]. Sporting PPE typically has a low thickness, so does not often meet assumption (ii). A finite thickness model has been developed for soft and thin cushioning materials where Hertzian theory is expected to become invalid, and auxetic cushions have been found to reduce the contact pressure on the buttocks (indenter) [192]. In another approach, Equation 2.3 has been adapted for thin sheets of rubber [193], to include a correctional coefficient (C, Equation 2.4) based on a ratio of contact area (a_t, red line in Figure 2.5) and the sheet's thickness (t) and a constant (A) for sheets of rubber, Equation 2.4, but has not been experimentally validated for NPR materials. The contact area can be calculated based upon indenter shape and material characteristics [193]. As thickness decreases towards zero, contact area/thickness increases and the correction tends towards unity. The force required to indent rubber to a specific depth increases as thickness decreases. The assumption of zero friction has been shown through FEM and continuum mechanics to be invalid [134,136,194,195]. In these simulations, friction was found to enhance NPR's contribution to indentation resistance.

$$C = 1 - \exp^{-A\frac{t}{a_t}} \qquad\qquad (2.4)$$

Equations 2.3 and 2.4 are for instantaneous, linear values. They do not, therefore, account for the different amounts of densification and possible hardening caused by lateral deformation due to Poisson's ratio (Figure 2.5c). Auxetic foam (with a relatively high shear modulus, Equation 2.1) should resist shear deformation more than its conventional counterpart. Auxetic foam's upper surface would, therefore, compress as a larger, flatter area (represented by the dashed line, Figure 2.5c) as shown in cylindrical indentations [107] and using FEM [196]. FEM and analytical models also report a reduction in contact area for simulations with NPR materials [197], suggesting that deformation occurred over a larger radius, rather than the foam wrapping around the indenter. The opposite effect (auxetic foam wrapping around the indenter) has been predicted in FEM simulations of low strain indentation of 2D linear-elastic isotropic blocks [109] and also observed during impacts with a hemispherical dropper onto samples covered with 1 to 2 mm thick polypropylene sheets [26]. In the FEM study, a lower Young's modulus over two times lower than that of the conventional foam was employed for the auxetic foam, providing a shear modulus almost a factor of two lower than the conventional foam (Equation 2.1), despite the NPR, which possibly explains the discrepancy. In the experimental study, the added complexity when considering multi-material systems (e.g.,

featuring a stiff shell and compliant foam), hemispherical or studded indenters (rather than cylindrical) and impacting at high strain rates could explain the observed differences. The relationship between the shell and foam's elastic moduli (as discussed in relation to coatings [198,199]), the foam's Poisson's ratio [197,199] and synclastic/anti-synclastic (domed or saddled) bending in the upper surface may affect indentation resistance.

Hertzian indentation requires corrections for high strain indentations, impacts of non-linear materials or multi-material systems typical in sporting PPE [5,6] and, therefore, testing of auxetic foams for sports applications [134,136]. As noted above, friction (assumption iv) can amplify increases in indentation resistance caused by NPR [134,136], and a correction factor has been applied [136]. Comparative tests between thermo-mechanically converted auxetic foam and conventional foam have shown large increases in indentation resistance [107,181,200]. Only a single study has indented auxetic and non auxetic foams of the same density and comparable (quasi-linear) stress vs. strain relationships, with the conventional comparative sample fabricated by extending the thermo-mechanical fabrication time from 20 minutes to an hour [107]. Isotropy was not shown in the iso-density comparative sample, and direct validation of or comparison to indentation theory (Equation 2.3) was not provided. Further significant modelling and experimental research examining NPR's effect on indentation responses of conforming, non-linear and anisotropic material subject to a range of indenter sizes and shapes is therefore required.

One of the difficulties in testing NPR's effect on the expected benefits (i.e., impact force attenuation or indentation resistance) when using foam is changes to Young's modulus and stress-strain relationships following fabrication [60,80]. Studies report auxetic foams with lower initial Young's modulus than their conventional counterparts [80,120,181]. Reduced Young's modulus has been attributed to the presence of buckled ribs in the auxetic foam being easier to deform than the straighter ribs of the conventional foam [80]. Elasticity theory (Equation 2.1, Figure 2.4a) also supports a reduction in Young's modulus as Poisson's ratio decreases if shear modulus remains constant. Auxetic foams typically have a higher density than their open cell parent foam, so the reduction in Young's modulus is contrary to the usual expectation of an increase in Young's modulus with increased density [85]. Note, though, that Gibson and Ashby refer to a density increase caused by thicker ribs, whereas in the auxetic foam fabrications density increases due to changes in rib orientation. Gibson and Ashby's cellular solid theory actually indicates that Young's modulus can either increase or decrease when moving from a hexagonal to a re-entrant cell geometry, characteristic of auxetic foams [85]. The increased Young's modulus is allowed by elasticity theory—materials with the same bulk modulus

(Equation 2.2, Figure 2.4b) will have increased Young's modulus as Poisson's ratio decreases. Increases [106,121,133,138] as well as the aforementioned decreases in Young's modulus [60,80,181] have been reported in auxetic foam fabrications.

The re-entrant structures typical in auxetic foams usually give an initially quasi-linear compressive stress-strain curve, with hardening as pores close at higher compression levels (>~50%) [13,60,76,109,182]. Conventional open cell foams exhibit a low-stiffness plateau region due to buckling of cell ribs between ~5% and 80% strain (Figure 2.6a) [85]. A plateau is beneficial for impact force attenuation, as energy absorption is maximised while peak force remains below a threshold value (Figure 2.6b). Both of these cases have been explained numerically and validated experimentally [85]. It should be noted that only specific forms of cellular materials that have a hexagonal honeycomb like structure before conversion then adopt a re-entrant structure, such as open cell PU foam and open cell auxetic PU foam [60], exhibit the plateauing and relatively linear stress-strain relationships. Exceptions have been recently presented; re-entrant auxetic PU foams with a plateau region which could be applied to impact protection [115].
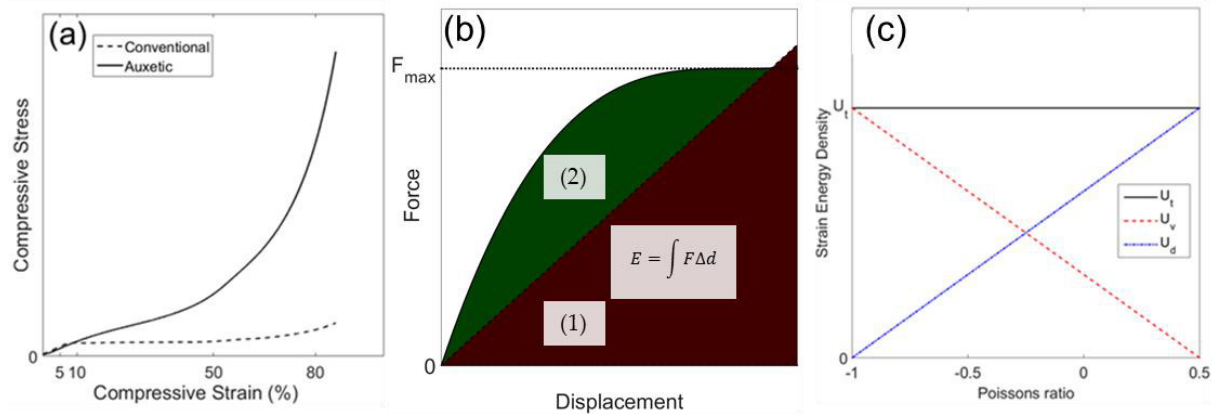
Figure 2.6: (a) Typical compressive stress vs. strain response of auxetic and conventional open cell foam (note cellular collapse between 5 to 10% then hardening beyond 80% strain via densification in open cell foam); (b) Linear (1) vs. Plateauing (1+2) energy absorption (shaded in red/green respectively) before a maximum allowable force; (c) Strain energy density (Volumetric (Uv, Equation 2.5), Distortion (Ud, Equation 2.6) & Ut, Total) vs. Poisson's ratio for a linear elastic isotropic material subject to a uniaxial stress. Uniaxial stress and Young's modulus set to 1 kPa.

For a linear elastic isotropic material subject to a uniaxial stress (σ), the total strain energy density (U_t) is the sum of the volumetric strain energy density (U_v) and the distortional strain energy density (U_d), which are related to the Young's modulus and Poisson's ratio (i.e., [185]):

$$U_v = \frac{(1-2\upsilon)\sigma^2}{6E} \tag{2.5}$$

$$U_d = \frac{(1+\upsilon)\sigma^2}{3E} \tag{2.6}$$

In Figure 2.6c, an applied compressive uniaxial stress and Young's modulus are arbitrarily equated to 1 kPa for simplicity. Plotting these values in Equations 2.5 and 2.6 between elastic limits of −1 and 0.5 for Poisson's ratio (Figure 2.6c) shows an increase in volumetric strain energy density and a reduction in distortional strain energy density as Poisson's ratio tends towards −1. Auxetics material's tendency to volumetric (rather than distortional deformation) could effectively increase indentation resistance (Figure 2.5c, Equations 2.3 and 2.4). As Poisson's ratio decreases, the stress concentration at a crack's tip is also thought to reduce, and auxetic inclusions have reduced crack propagation [201,202]. Von Mises and maximum shear stress theory both define failure when distortional strain energy exceeds a maximum value. The reduction in distortional strain energy (to zero, Figure 2.6c) as Poisson's ratio reduces to −1 [186] is, then, expected to lead to an increase in toughness. A natural example of where this may be exploited may be found in the nacre layer of certain seashells. Nacre has a reported tensile NPR of the order of ~−0.1 [67] and ~−0.4 [203] which is thought to increase volumetric strain energy density by ~11 times while more than halving distortional strain energy density, allowing the system to absorb more energy before failure [203]. A direct link between NPR, reduced distortion close to a crack tip or within a bulk material and increased toughness has not been shown within the scientific literature, either experimentally or by modelling.

Increased energy absorption has been shown experimentally for auxetic foam; under flat plate [108] and studded impacts [181], quasi-statically with flat compression plates [122] and within aluminium tubes [204]. When compressed cyclically at high strain rates (0.036 to 0.36 s^{-1} [205] and 0.033 s^{-1} [106,181]) auxetic foams absorbed up to sixteen times more energy than open cell foams of a different polymeric composition and equivalent density, therefore appearing more useful in cushioning layers of sporting (and general) PPE. The differences in energy absorption do not account for changes in stress/strain relationship or strain rate dependency between conventional and auxetic samples. As strain rates increased, Young's modulus and the magnitude of NPR increased marginally in samples of auxetic PU foam [206]. In some cases the increased linear elastic range of the auxetic foam compared to the parent foam with a plateau region in the stress-strain relationship could have contributed to higher energy absorption [106,108].

Energy absorption, strain rate dependency and (often) indentation resistance combine to influence performance under impact. Theoretically beneficial for impact protection [13], auxetic foam samples have been shown to exhibit between ~3 and ~8 times lower peak force under 2 to 15 J impacts adapted from BS 6183-3:2000 for cricket thigh pads [2,22,26]. During a comparison of high strain rate compression (20 to 40 J impacts) to a conventional commercial foam of

similar density, auxetic samples exhibited (1.2 to 1.8 times) higher peak acceleration, but also exhibited higher compressive elastic modulus [106]. Inward material flow has been shown under impact by rudimental visual inspection of high-speed camera stills, and the samples with the greatest magnitude of NPR exhibited higher lateral contraction, lower through thickness deformation and a similar peak force to other samples [108]. Peak forces can also be decreased (1.2 to 1.5 times) during 5 J impacts by impregnating auxetic foam with shear thickening fluid [207].

Honeycomb sandwich panels with 100 mm thick auxetic aluminium cores were found to resist ~ 17 kJ, ~ 8 m/s impacts (representative of ballistic kinetic energies but at lower strain rates) with a 150 mm hemispherical drop mass better than regular or rectangular aluminium cores with the same size and areal density [208]. Re-entrant cores also absorb more impact energy when the re-entrant cell structure was non-uniform [209]. Laminated composites containing warp knit auxetic Kevlar® fabric reinforcement, fabricated with imparting re-entrant rather than hexagonal repeating units [210], showed similar energy absorption to laminates containing conventional woven Kevlar® reinforcement during 167 m/s impact with a 14.9 g bullet (~200 J) [211,212]. The auxetic Kevlar® laminates, however, displayed enhancements in fracture toughness (225%) and fracture initiation toughness (577%), and a reduction in front and rear face damage area [211,212]. Auxetic composite laminates displayed reduced back face damage during 7–18 J impacts by a stud [213–215]. Auxetic composite laminates could, therefore, improve the durability of protective shells in PPE and other sports equipment (i.e., bicycle frames, skis/snowboards or boat hulls).

Related to energy absorption, auxetic foams have been tested for vibration damping (to ISO 13753 for vibration protecting gloves [216]). At low frequencies (<10 Hz), auxetic foam exhibited lower transmissibility than iso-volume open cell samples made from the parent foam and iso-density uni-axially compressed samples [125]. Auxetic foam had a lower cut off frequency than its parent foam [217]. The transmissibility of auxetic samples was greater than 1 between 10 and 31.5 Hz, but less than 1 over 31.5 Hz [109], equivalent to commercial anti-vibration gloves. Auxetic foams also fatigued uniquely, with higher permanent compression than their parent foam and a general increase (as opposed to the conventional foam's decrease) in measured hardness after 80,000 cycles up to ~120 N (150 mm sided cubic samples) [218].

Curvature of a beam or plate subject to an out-of-plane moment is related to Poisson's ratio [60,219]. Sheets with a positive Poisson's ratio will adopt a saddled shape (anticlastic curvature, Figure 2.7a) and those with NPR will dome (synclastic curvature, Figure 2.7b). Doming is caused by axial (due to loading) and lateral (due to Poisson's ratio) extension on the upper

surface combined with equivalent contractions on the lower surface. Conventional materials will contract laterally on the upper surface and expand laterally on the lower surface.

Synclastic curvature has been observed in auxetic foam [60], analysed in detail in sandwich structures with an auxetic honeycomb core and auxetic laminate skins [219] and demonstrated by FEM [122,220] and experimentally using a simple paper model [122]. Auxetic fabric can conform around a spherical surface (Figure 2.7b) [221]. Bespoke complex curvatures are achievable for gradient honeycombs displaying conventional and NPR regions when subject to an out-of-plane moment [222].
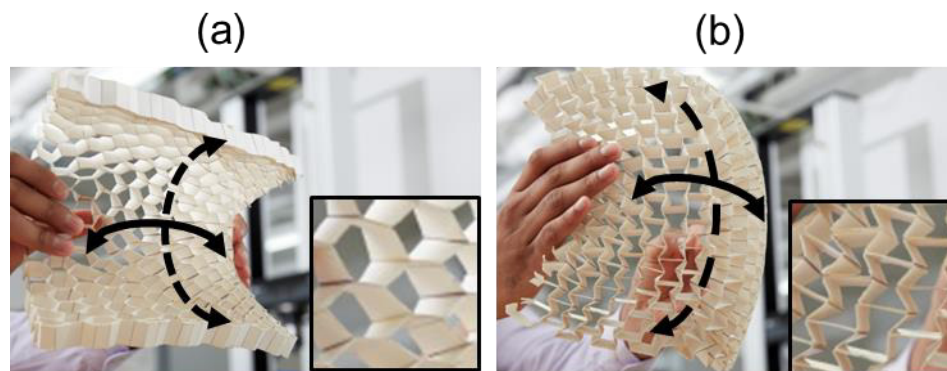
Figure 2.7: (a) Conventional honeycomb showing saddled curvature; (b) Re-entrant auxetic honeycomb showing domed curvature. Solid arrows show applied bending and dashed arrows show bending due to Poisson's ratio. Enlarged pop outs show cell structure.

Shape memory polymers return to one of their previous shapes when triggered [223]. Typical shape memory steps are: 1) Deformation (at elevated stress and temperature); 2) Cooling/fixing (at elevated stress); 3) Unloading (removal of stress at the lower temperature); and 4) Recovery (reheating to elevated temperature under zero stress) [223]. Some auxetic PU foam samples have been shown to exhibit shape memory, meaning they return to their original dimensions when heated [117] or exposed to solvents [131]. Thermo-mechanical conversions map the shape memory cycle; 1) Deforming and heating in a compression mould, 2) Cooling in their moulds, 3) Unloading by removing samples for their moulds and applying gentle hand stretching. Shape memory can then be tested by step 4) Recovery; reheating or solvent exposure without a mould. When heated in an oven, auxetic foams samples returned rapidly towards their original dimensions when the temperature reached 90 °C, reaching their original size when the temperature reached the fabrication temperature of 135 °C.

Marginally re-entrant structures with NPR which exhibit partially blocked shape memory have been fabricated [115]. The fabrication process included numerous cycles of thermo-mechanical fabrication followed by reheating to return samples towards their original state. Auxetic behaviour was found in 'returned' samples from the third returned stage onwards, and

has been attributed to the presence of kinked or corrugated ribs. Clearly shape memory could be detrimental in terms of sport safety equipment, in that pads could be changed irreparably when exposed to heat or solvents (i.e., when machine washed or dried). Blocked shape memory auxetic foams, defined as foams which whilst (nominally) recovering dimensions (step 4, [223]) retain NPR [115], or other solutions to prevent a return to original dimensions (such as constraining auxetic foam in an outer textile/shell layer) could improve a product's lifecycle.

Several characteristics change in the auxetic foam fabrication process, including Poisson's ratio, stress/strain relationships and density [26,75,76,121,224]. So, during comparative impact tests between auxetic and parent foam [2,26,106,138,224], the specific contribution of individual characteristics, including Poisson's ratio, can be difficult to determine, and unambiguous experimental verification of theoretical enhancements due to the NPR requires further work. The same can be said for other studies into auxetic foam, including those into vibration damping [109,125], resilience/strength [148] and energy absorption [122].

Comparing results from scientific literature suggests that the compressive Young's modulus (30 to 50 kPa) of auxetic open-cell PU foams [2,26,76,85,224] is typically more than twenty times lower than that of the closed cell foams often found in sporting PPE (~1 MPa) [3,5–7,14]. Such a large reduction in stiffness suggests that the two materials are not comparable and stiffer auxetic foam is required for sporting PPE. The enhancements provided by NPR (e.g., indentation resistance) might allow for some reduction in stiffness, but to absorb an equivalent amount of energy to current sporting PPE, current auxetic foam would need a contribution from having NPR that would increase energy absorption by ~20 times. The largest reported increase in energy absorption for auxetic vs. conventional foam is 16 times during dynamic cyclic tests [205], but increases of ~3 times are more common in single impacts/compressions [108,138]. Crash mats are typically softer than PPE (~50 kPa [11]), as are compliant comfort layers in helmets [17] and other PPE, and (due to their extensive variety of possible applications and impact scenarios) could benefit from the increased energy absorption and indentation resistance associated with auxetic foams [107,122]. The author is not aware of any publications specifically comparing impacts or indentations of auxetic foam to foam typically found in sports PE and PPE.

2.5. The Potential for Auxetic Materials in Sports Products

The sporting goods sector is characterised by early uptake of new technologies and rapid product development, launch and replace cycles. Consequently, this sector is amongst the first to see commercial products based on auxetic materials, with two commercial sports shoe ranges that utilise auxetic structures. The Under Armour Architech sports shoe range [225]

incorporates either an AM or moulded auxetic (re-entrant or arrowhead [226]) latticed upper (Figure 2.2a) which is claimed to aid conformability, fit and comfort. The added manufacturing benefit of being formable as a one-piece upper, rather than several pieces each individually cut to shape and stitched together is also claimed. The Nike Free RN Flyknit sports shoe [227], on the other hand, employs an architectured closed cell foam outsole with an auxetic rotating triangles structure (shown in Figure 2.8, first proposed in [71–73]). The outsole is claimed to exhibit bi-axial growth as the wearer accelerates or changes direction, for improved traction and impact energy absorption [228]. Nike do not provide any information showing the design works as intended, however, rotating triangles are a well understood method for imparting NPR [71–73] and multi-axial expansion. Underarmour have a patent [225] demonstrating the benefits of the auxetic upper. Like Nike's shoe, the utilised structures have been extensively studied and the stated benefits of bi-axial stretch and double curvature (Figure 2.7b) are well understood.
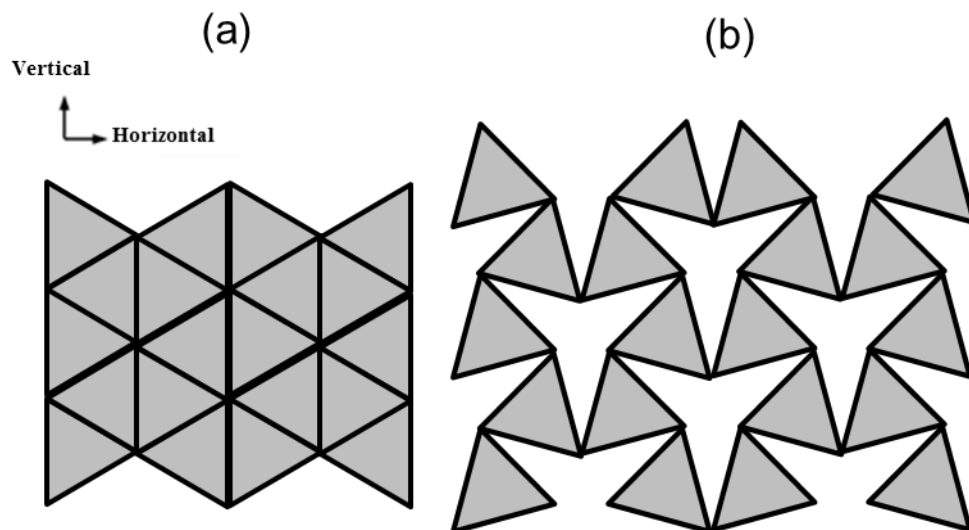
Figure 2.8: Schematic showing (a) rotating triangles (un-deformed); (b) rotating triangles' multi axial expansions (rotation = 15°), tensile load applied either vertically or horizontally.

Multi-axis expansion (due to NPR) has potential benefits in cleaning/shedding of dirt [229]. Multi-axis expansion could be implemented in a conformable facemask [230] to protect against extreme weather during outdoor/adventure sports, or commuter cycling—expanding bi-axially when the mouth is opened to increase breathability [60,229,231,232]. Other benefits of multi-axis expansion include large volume change, allowing design of small size, easily stored garments which can expand when worn (e.g., for spare layers in outdoor/adventure sports), or expand with a growing child [233].

D3O market the Trust Helmet Pad System [234] incorporating pads with a re-entrant auxetic geometry that are claimed to provide increased fit to the head. Although double curvature (Figure 2.7b) is a clear benefit in auxetics, the utilised re-entrant cells are large and it is unclear whether double curvature will be realised in a continuum, rather than a discontinuous, manner. More products are likely to emerge if the increased level of comfort and protection offered by auxetic materials can be further demonstrated, justifying investment in the development of stiffer, more appropriate auxetic materials (such as closed cell [140] or shear thickening fluid impregnated [207] auxetic foams, or novel impact hardening auxetic polymers [235]). The emergence of sports products including auxetic materials could be assisted by the development of a commercially-viable (low cost, large scale) auxetic foam production process [111,132]. 'Felted' foams, fabricated by uniaxial compression, are already commercially produced and exhibit auxetic behaviour in one loading direction [108]). Alternatively AM is becoming a commercially viable option [225] to provide fine control over cell structure for auxetic foam-like structures.

The ability to change the shear modulus of a material through Poisson's ratio [85,236] could provide a useful tool in designing head protection that can reduce rotational acceleration [237]. Helmets and helmet certification standards have been criticised for focussing solely on direct rather than both direct and oblique impacts [15]. Controlling shear modulus by changing Poisson's ratio (to negative or positive values) of any layer within the helmet could contribute to solutions to reduce rotational acceleration (i.e., in combination with or instead of slip plane technology [52]). The benefit of using Poisson's ratio to change shear modulus is that stress vs. strain relationships would change less significantly, limiting the effect on linear acceleration and therefore perceived performance according to current certification standards [39,40].

2.6. Conclusions

In a competitive, rapid uptake market such as sports equipment, it is important to keep searching for new and improved designs and materials. With frequent, catastrophic high-profile injuries, and scandals, particularly involving head injury of sports participants wearing helmets at the time of injury (such as Michael Schumacher's skiing accident and an overwhelming number of long term complications to American Football participants) the importance of improvement increases. Shear thickening materials can be flexible in normal use, but rigid to resist penetration under impact. Increasing in rigidity at very specific strain rates, selected to pass non-representative certification tests, PPE incorporating shear thickening materials may not offer adequate protection under impact. The chance to increase market revenue, while

reducing costs to health services, national economies and burdens on injured individuals, warrants continued research through commercial and state investment.

Auxetics have a wide range of potentially useful characteristics that could increase the protection offered by, and/or comfort of, sporting PPE, PE and other garments. Potential benefits include increased indentation resistance, vibration damping and shear modulus as well as decreased bulk modulus, meaning auxetics show potential to be widely used in place of, or in combination with, shear thickening materials. These have been shown using auxetic foam compared to its parent foam and also iso-density conventional foams. Further experimental comparisons of auxetic and conventional foam's indentation resistance, impact force attenuation and vibration damping are required to determine contributions from other variables, such as stress vs. strain relationships and density, to clearly identify the contribution due to Poisson's ratio (Aim 2, Chapter 1, Page 5).

In 1998, Chan and Evans published work comparing the indentation resistance of re-entrant auxetic foams and foam with a near zero Poisson's ratio, fabricated thermo-mechanically with a longer than normal heating phase, without repeat testing or confirmation of isotropy in the near zero Poisson's ratio samples. Currently, the effect of heating during thermo-mechanical PU foam fabrications is unclear, and polymeric changes have only been observed in one study featuring thermo-mechanical auxetic foam fabrications. Extending upon the fabrication and characterisation methods to ensure isotropy and comparable stress vs. strain relationships (Aim 1, Chapter 1, Page 5) will confirm whether expected increases to indentation resistance remain at high strains and low sample thickness, typical in PE and PPE (Aim 2, Chapter 1, Page 5).

The creation of auxetic foams appropriate and beneficial to sporting goods will require development of fabrication processes, especially for larger samples (Aim 3, Chapter 1, Page 5). Large sample fabrication methods do not control or measure internal compression. Fabricating samples with comparative characteristics (e.g., Young's modulus and density) is also required to show NPR's benefits (e.g., to indentation resistance). The solvent and CO_2 softening routes provide alternative and, in the latter case, faster auxetic foam fabrication. Increasing the stiffness of auxetic foam closer to the closed cell foam (Young's modulus ~1 MPa) found in sporting PPE or ensuring that impact energy absorption is equivalent or higher is an important step for commercialisation (Aim 4, Chapter 1, Page 5). With dynamic energy absorption reported up to sixteen times greater in auxetic foams some reduction in stiffness is likely to be acceptable, but requires confirmation by appropriate testing. A recent steam processing method for closed cell foam can impart a stiff (~60 MPa), re-entrant structure. Fabrication of closed cell

foams with a lower initial Young's modulus should be attempted (Aim 4, Chapter 1, Page 5). Commercially available auxetic foam would improve access, allowing more sport safety equipment manufacturers to design, test and evaluate auxetic prototypes.

The more obvious characteristics of auxetic materials that are backed up with strong supporting evidence (multi axis expansion and domed curvature) have been implemented as auxetic foam and AM materials into sporting footwear and helmet pad products. Commercial success for auxetic sporting PPE requires stronger supporting evidence that responds to trends accurately re-creating infield collisions and falls. Other auxetic materials such as laminates and knitted/woven fabrics that exhibit characteristics including increased fracture toughness and, potentially, tailorable shape change, are currently untested for sports applications within the peer-reviewed scientific literature. Unlike auxetic foam production, the fabrication of auxetic composite laminates and many of the auxetic fabrics is via established commercial processes, requiring little or no modification. With further development and testing auxetic laminates and fabrics could be applied to a range of sporting products, from carbon fibre bicycle frames to swim suits or rugby tops that deform with the movements of the wearer.

2.7. References

1. Duncan O, Shepherd T, Moroney C, Foster L, Venkatraman PD, Winwood K, et al. Review of auxetic materials for sports applications: Expanding options in comfort and protection. Appl Sci. 2018.8(6). 941.
2. Duncan O, Foster L, Senior T, Alderson A, Allen T. Quasi-static characterisation and impact testing of auxetic foam for sports safety applications. Smart Mater Struct. 2016.25(5). 054014.
3. Hrysomallis C, Morrison W, He J. Assessing the shock absorption of thigh pads. J Sci Med …. 1999.
4. Payne T, Mitchell S, Halkon B, Bibb R. A systematic approach to the characterisation of human impact injury scenarios in sport. BMJ Open Sport Exerc Med. 2016.2(1). e000017.
5. Ankrah S, Mills NJ. Performance of football shin guards for direct stud impacts. Sport Eng. 2003.6(4). 207–19.
6. Ankrah S, Mills NJ. Analysis of ankle protection in Association football. Sport Eng. 2004.7(1). 41–52.
7. Hrysomallis C. Surrogate thigh model for assessing impact force attenuation of protective pads. J Sci Med Sport. 2009.12(1). 35–41.
8. Schmitt KU, Liechti B, Michel FI, Stämpfli R, Brühwiler PA. Are current back protectors suitable to prevent spinal injury in recreational snowboarders? Br J Sports Med. 2010.44(11). 822–6.
9. Michel FI, Schmitt KU, Liechti B, Stämpfli R, Brühwiler P. Functionality of back protectors in snow sports concerning safety requirements. Procedia Eng. 2010.2(2). 2869–74.
10. Adams C, James D, Senior T, Allen T, Hamilton N. Development of a Method for Measuring Quasi-static Stiffness of Snowboard Wrist Protectors. In: Procedia Engineering. **2016**. p. 378–83.
11. Lyn G, Mills NJ. Design of foam crash mats for head impact protection. Sport Eng.

2001.4(3). 153–63.

12. Mills NJ, Fitzgerald C, Gilchrist A, Verdejo R. Polymer foams for personal protection: Cushions, shoes and helmets. Compos Sci Technol. 2003.63(16). 2389–400.

13. Lakes RS. Design Considerations for Materials with Negative Poisson's Ratios. J Mech Des. 1993.115(4). 696.

14. Mills NJ. The biomechanics of hip protectors. Proc Inst Mech Eng H. 1996.210(4). 259–66.

15. Mcintosh AS, Andersen TE, Bahr R, Greenwald R, Kleiven S, Turner M, et al. Sports helmets now and in the future. Br J Sports Med. 2011.8. 1258–65.

16. McIntosh AS, Janda D. Evaluation of cricket helmet performance and comparison with baseball and ice hockey helmets. Br J Sports Med. 2003.37(4). 325–30.

17. Vanden Bosche K, Mosleh Y, Depreitere B, Vander Sloten J, Verpoest I, Ivens J. Anisotropic polyethersulfone foam for bicycle helmet liners to reduce rotational acceleration during oblique impact. Proc Inst Mech Eng Part H J Eng Med [Internet]. 2017.231(9). 1–11. Available from: http://journals.sagepub.com/doi/10.1177/0954411917711201

18. Schmitt K-U, Liechti B, Michel FI, Stämpfli R, Brühwiler PA. Are current back protectors suitable to prevent spinal injury in recreational snowboarders? Br J Sports Med. 2010.44(11). 822–6.

19. Adams C, James D, Senior T, Allen T, Hamilton N. Effect of surrogate design on the measured stiffness of snowboarding wrist protectors. Sport Eng. 2018.1. 1–9.

20. Michel FI, Schmitt KU, Greenwald RM, Russell K, Simpson FI, Schulz D, et al. White Paper: Functionality and efficacy of wrist protectors in snowboarding-towards a harmonized international standard. Sport Eng. 2013.16(4). 197–210.

21. (ASTM) AS for T and M. ASTM F 2040-02: Standard Specification for Helmets Used for Recreational Snow Sports. Vol. 15. West Conshohocken; **2002**. p. 1–4.

22. European Committee for Standardization. BS 6183-3:2000-Protective equipment for cricketers. 2000.

23. Institute BS. BS EN 1077:2007 Helmets for alpine skiers and snowboarders. Vol. 3, Bsi. **2007**.

24. European Committee for Standardization. BS EN 13061:2009 Protective clothing — Shin guards for association football players — Requirements and test methods. BS EN: 13061:2009. 2009.

25. Arts FWCM. World Fightsport Martial Arts Council OFFICIAL RULEBOOK. 2010.(May).

26. Allen T, Shepherd J, Hewage TAM, Senior T, Foster L, Alderson A. Low-kinetic energy impact response of auxetic and conventional open-cell polyurethane foams. Phys Status Solidi Basic Res. 2015.9. 1–9.

27. Payne T, Mitchell S, Halkon B, Bibb R, Waters M. Development of a synthetic human thigh impact surrogate for sports personal protective equipment testing. Proc Inst Mech Eng Part P J Sport Eng Technol. 2016.230(1). 5–16.

28. Mills NJ, Gilchrist A. Oblique impact testing of bicycle helmets. Int J Impact Eng. 2008.35(9). 1075–86.

29. Aare M, Kleiven S, Halldin P. Injury tolerances for oblique impact helmet testing. Int J Crashworthiness. 2004.9(1). 15–23.

30. Bailly N, Laporte JD, Afquir S, Masson C, Donnadieu T, Delay JB, et al. Effect of Helmet Use on Traumatic Brain Injuries and Other Head Injuries in Alpine Sport. Wilderness Environ Med. 2018.29(2). 151–8.

31. Casson IR, Viano DC, Powell JW, Pellman EJ. Twelve years of National Football League concussion data. Sports Health. 2010.2(6). 471–83.

32. Dickson TJ, Trathen S, Terwiel FA, Waddington G, Adams R. Head injury trends and helmet use in skiers and snowboarders in Western Canada , 2008 – 2009 to 2012 – 2013 :

an ecological study. 2017. 236–44.

33. Mcintosh AS. Biomechanical considerations in the design of equipment to prevent sports injury. Proc IMechE Part P J Sport Eng Technol. 2011.226. 193–9.

34. The British Standards Institution Bs. Sports mats Part 1 : Gymnastic mats , safety requirements. **2013**.

35. European Committee for Standardization. EN 14120:2003 Protective clothing — Wrist , palm , knee and elbow protectors for users of roller sports equipment — Requirements and test methods. 2003.3.

36. Standardization EC for. EN 1621-2 2003 Motorradfahrer Schutzkleidung Teil 2 Rückenprotektoren. **2003**.

37. Ekeland A, Rødven A, Heir S. Injury Trends in Recreational Skiers and Boarders in the 16-Year Period 1996–2012. In: IS Scher et al (eds), Snow Sports Trauma and Safety. **2017**. p. 3–16.

38. Mez J, Daneshvar DH, Kiernan PT, Abdolmohammadi B, Alvarez VE, Huber BR, et al. Clinicopathological Evaluation of Chronic Traumatic Encephalopathy in Players of American Football. J Am Med Assoc. 2017.02118(4). 360–70.

39. King AI, Yang KH, Zhang L, Hardy W, Viano D. Is head injury caused by linear or angular acceleration? In: In IRCOBI conference. **2003**. p. 1–12.

40. Rowson S, Duma SM. Brain injury prediction: Assessing the combined probability of concussion using linear and rotational head acceleration. Ann Biomed Eng. 2013.41(5). 873–82.

41. (ASTM) AS for T and M. F1446-04 Standard test methods for equipment and procedures used in evaluating the performance charactertistics of protective headgear. Astm. West Conshohocken; **2004**. p. 1–11.

42. BSI. BS 6658:1985. Protective helmets for vehicle users. 2008.

43. The British Standards Institution Bs. BS 7928:2013- Specification for head protectors for cricketers. The British Standards Institution; **2013**.

44. Bekkum JE Van, Williams JM, Morris PG. Cycle commuting and perceptions of barriers : stages of change , gender and occupation. Health Educ. 2011.111(6). 476–97.

45. Heinen E, Maat K, Wee B Van. The role of attitudes toward characteristics of bicycle commuting on the choice to cycle to work over various distances. Transp Res Part D. 2011.16(2). 102–9.

46. Willinger R, Deck C, Halldin P, Otte D. Towards advanced bicycle helmet test methods. Int Cycl Saf Conf. 2014.(November). 1–11.

47. World Health Organization. World Health Organization: Global Recommendations on Physical Activity for Health. Geneva, Switzerland; **2010**.

48. Warburton DER, Nicol CW, Bredin SSD. Health benefits of physical activity : the evidence. Can Medial Assoc J. 2006.174(6). 801–9.

49. Yeh HP, Stone JA, Churchill SM, Wheat JS, Brymer E, Davids K. Physical, Psychological and Emotional Benefits of Green Physical Activity: An Ecological Dynamics Perspective. Sport Med. 2016.46(7). 947–53.

50. Yeh HP, Stone JA, Churchill SM, Brymer E, Davids K. Designing Physical Activity Environments to Enhance Physical and Psychological Effects. Procedia Eng. 2016.147. 793–8.

51. Yeh HP, Stone JA, Churchill SM, Brymer E, Davids K. Physical and emotional benefits of different exercise environments designed for treadmill running. Int J Environ Res Public Health. 2017.14(7).

52. Zuzarte P. Protective helmet (US 6,658,671 B1). Vol. 1. 2003.

53. Kleiven S. Influence of impact direction on the human head in prediction of subdural hematoma. J Neurotrauma. 2003.20(4). 365–79.

54. Kleiven S. Evaluation of head injury criteria using a finite element model validated

against experiments on localized brain motion, intracerebral acceleration, and intracranial pressure. Int J Crashworthines. 2006.11(1). 65–79.

55.   Kleiven S, Hardy WN. Correlation of an FE Model of the Human Head with Local Brain Motion--Consequences for Injury Prediction. Stapp Car Crash J. 2002.46(November). 123–44.

56.   Dura J V., Garcia a. C, Solaz J. Testing shock absorbing materials: the application of viscoelastic linear model. Sport Eng. 2002.5(1). 9–14.

57.   Hayes, S. G. & Venkatraman P. Materials and Technology for Sportswear and Performance Apparel. In: Materials and Technology for Sportswear and Performance Apparel. **2016**. p. 314.

58.   Walker PJ, Rothberg SJ, Holmes CE, Harland AR. Design of a force acquisition system for high-energy short-duration impacts. Proc Inst Mech Eng Part P J Sport Eng Technol. 2010.224(2). 129–39.

59.   Petrone N, Carraro G, Dal Castello S, Broggio L, Koptyug A, Backstrom M. A novel instrumented human head surrogate for the impact evaluation of helmets. Proc 12th Conf Eng Sport ISEA. 2018. 1–7.

60.   Lakes RS. Foam Structures with a Negative Poisson's Ratio. Science (80-). 1987.235(4792). 1038–40.

61.   Nakamura KENI, Wada M, Kuga S, Okano T. Poisson ' s Ratio of Cellulose I ᴺᴸ and Cellulose II. J Polym Sci Part B Polym Phys. 2004.42(August 2003). 1206–11.

62.   Caddock BD, Evans KE. Microporous materials with negative Poisson's ratios. I. Microstructure and mechanical properties. J Phys D Appl Phys. 1989.22(12). 1877–82.

63.   Dominec J, Vase P, Svoboda P, Plechacek V, Laermans C. Elastic Moduli for Three Superconducting Phases of Bi-Sr-Ca-Cu-O. Mod Phys Lett B. 1992.6. 1049.

64.   Baughman RH, Shacklette JM, Zakhidov AA, Stafstro S. Negative Poisson's ratios as a common feature of Cubic Metals. 1998. 362–5.

65.   Li D, Dong L, Lakes RS. The properties of copper foams with negative Poisson's ratio via resonant ultrasound spectroscopy. Phys Status Solidi Basic Res. 2013.250(10). 1983–7.

66.   Clarke JF, Duckett RA, Hine PJ, Hutchinson IJ, Ward IM. Negative Poisson's ratios in angle-ply laminates: theory and experiment. Composites. 1994.25(9). 863–8.

67.   Barthelat F, Tang H, Zavattieri PD, Li CM, Espinosa HD. On the mechanics of mother-of-pearl: A key feature in the material hierarchical structure. J Mech Phys Solids. 2007.55(2). 306–37.

68.   Kolken HMA, Zadpoor AA. Auxetic mechanical metamaterials. RSC Adv. 2017.7. 5111–29.

69.   Gibson LJ, Ashby MF, Schajer GS, Robertson CI. The mechanics of two-dimensional cellular materials. Proc R Soc London A Math Phys Sci. 1982.382. 25–42.

70.   Prall D, Lakes RS. Properties of a chiral honeycomb with a poisson's ratio of - 1. J Mech Sci Vol. 1997.39(3). 305–14.

71.   Grima JN, Evans KE. Auxetic behavior from rotating squares. J Mater Sci Lett. 2000.19(17). 1563–5.

72.   Grima JN, Alderson A, Evans KE. Auxetic behaviour from rotating rigid units. Phys Status Solidi Basic Res. 2005.242(3). 561–575.

73.   Joseph N. Grima, Pierre-Sandre Farrugia, Ruben Gatt VZ. Connected Triangles Exhibiting Negative Poisson's Ratios and Negative Thermal Expansion. J Phys Soc Japan. 2007.76(2).

74.   Attard D, Grima JN. A three-dimensional rotating rigid units network exhibiting negative Poisson's ratios. Phys Status Solidi Basic Res. 2012.249(7). 1330–8.

75.   Lakes RS. Polyhedron cell structure and method of making same (US 4,668,557). 1987. p. 2–6.

76.   Chan N, Evans KE. Fabrication methods for auxetic foams. J Mater Sci. 1997.32. 5945–53.

77. Grima JN, Gatt R, Ravirala N, Alderson A, Evans KE. Negative Poisson's ratios in cellular foam materials. Mater Sci Eng A. 2006.423(1–2). 214–8.

78. Smith CW, Grima JN, Evans KE. Novel mechanism for generating auxetic behaviour in reticulated foams: Missing rib foam model. Acta Mater. 2000.48(17). 4349–56.

79. Gaspar N, Ren XJ, Smith CW, Grima JN, Evans KE. Novel honeycombs with auxetic behaviour. Acta Mater. 2005.53(8). 2439–45.

80. Chan N, Evans KE. The mechanical properties of conventional and auxetic foams. Part I: compression and tension. J Cell Plast. 1999.35(2). 130–65.

81. Masters IG, Evans KE. Models for the elastic deformation of honeycombs. Compos Struct. 1996.35(4). 403–22.

82. Evans KE, Alderson A, Christian FR. Auxetic Two-dimensional Polymer Networks. J Chem Soc Faraday Trans. 1995.91(16). 2671–80.

83. Alderson A, Evans KE. Modelling concurrent deformation mechanisms in auxetic microporous polymers. J Mater Sci. 1997.32(11). 2797–809.

84. McDonald SA, Dedreuil-Monet G, Yao YT, Alderson A, Withers PJ. In situ 3D X-ray microtomography study comparing auxetic and non-auxetic polymeric foams under tension. Phys Status Solidi Basic Res. 2011.248(1). 45–51.

85. Gibson LJ, Ashby MF. Cellular solids. Structure and properties. **1997**. 67, 176-183, 259-264, 286, 498 p.

86. Nkansah MA, Evans KE, I.J. H. Modelling the mechanical properties of an auxetic molecular network. Model Simulations Mater Sci Eng. 1994.2. 337–52.

87. Choi JB, Lakes RS. Analysis of elastic modulus of conventional foams and of re-entrant foam materials with a negative Poisson's ratio. Int J Mech Sci. 1995.37(1). 51–9.

88. Lee J, Choi JB, Choi K. Application of homogenization FEM analysis to regular and re-entrant honeycomb structures. J Mater Sci. 1996.31(15). 4105–10.

89. Scarpa F, Panayiotou P, Tomlinson G. Numerical and experimental uniaxial loading on in-plane auxetic honeycombs Numerical and experimental uniaxial loading on in - plane auxetic honeycombs. 2000.35(5). 383–8.

90. Huang F-Y, Yan B-H, Yang DU. The effects of material constants on the micropolar elastic honeycomb structure with negative Poisson's ratio using the finite element method. Eng Comput. 2002.19(7). 742–63.

91. Yang DU, Lee S, Huang FY. Geometric effects on micropolar elastic honeycomb structure with negative Poisson's ratio using the finite element method. Finite Elem Anal Des. 2003.39(3). 187–205.

92. Alderson A, Alderson KL, McDonald SA, Mottershead B, Nazare S, Withers PJ, et al. Piezomorphic materials. Macromol Mater Eng. 2013.298(3). 318–27.

93. Li H, Luo Z, Gao L, Walker P. Topology optimization for functionally graded cellular composites with metamaterials by level sets. Comput Methods Appl Mech Eng. 2017.328. 340–64.

94. Liu W, Wang N, Huang J, Zhong H. The effect of irregularity, residual convex units and stresses on the effective mechanical properties of 2D auxetic cellular structure. Mater Sci Eng A. 2014.609. 26–33.

95. Alipour MM, Shariyat M. Analytical zigzag formulation with 3D elasticity corrections for bending and stress analysis of circular/annular composite sandwich plates with auxetic cores. Compos Struct. 2015.132. 175–97.

96. Ranga D, Strangwood M. Finite element modelling of the quasi-static and dynamic behaviour of a solid sports ball based on component material properties. Procedia Eng. 2010.2(2). 3287–92.

97. Jiang L, Hu H. Low-velocity impact response of multilayer orthogonal structural composite with auxetic effect. Compos Struct. 2017.169. 62–8.

98. Miller W, Smith CW, Scarpa F, Evans KE. Flatwise buckling optimization of hexachiral

and tetrachiral honeycombs. Compos Sci Technol. 2010.70(7). 1049–56.

99. Novak N, Vesenjak M, Ren Z. Computational Simulation and Optimization of Functionally Graded Auxetic Structures Made From Inverted Tetrapods. Phys Status Solidi Basic Res. 2017.254(12). 1–7.

100. Safikhani Nasim M, Etemadi E. Three dimensional modeling of warp and woof periodic auxetic cellular structure. Int J Mech Sci. 2018.136(September 2017). 475–81.

101. Carta G, Brun M, Baldi A. Design of a porous material with isotropic negative Poisson's ratio. Mech Mater. 2016.97. 67–75.

102. Scarpa F, Blain S, Lew T, Perrott D, Ruzzene M, Yates JR. Elastic buckling of hexagonal chiral cell honeycombs. Compos Part A Appl Sci Manuf. 2007.38(2). 280–9.

103. Wang Z, hu H. A finite element analysis of an auxetic warp-knitted spacer fabric structure. Text Res J. 2015.85(4). 404–15.

104. Gao Q, Wang L, Zhou Z, Ma ZD, Wang C, Wang Y. Theoretical, numerical and experimental analysis of three-dimensional double-V honeycomb. Mater Des. 2018.139. 380–91.

105. Farhan M, Shahid M. Negative Poissons ratio behavior of idealized elastomeric auxetic cellular structures for various carbon black nanoparticles loadings. J Elastomers Plast. 2015.47(6). 479–87.

106. Lisiecki J, Błazejewicz T, Kłysz S, Gmurczyk G, Reymer P, Mikułowski G. Tests of polyurethane foams with negative Poisson's ratio. Phys Status Solidi Basic Res. 2013.250(10). 1988–95.

107. Chan N, Evans KE. Indentation resilience of conventional and auxetic foams. J Cell Plast. 1998.34. 231–60.

108. Ge C. A comparative study between felted and triaxial compressed polymer foams on cushion performance. J Cell Plast. 2013.49(6). 521–33.

109. Scarpa F, Giacomin J, Zhang Y, Pastorino P. Mechanical performance of auxetic polyurethane foam for antivibration glove applications. Cell Polym. 2005.24(5). 253–68.

110. Choi JB, Lakes RS. Nonlinear Analysis of the Poisson's Ratio of Negative Poisson's Ratio Foams. J Compos Mater. 1994.29. 113–28.

111. Loureiro MA, Lakes RS. Scale-up of transformation of negative Poisson's ratio foam: Slabs. Cell Polym. 1997.16(5). 349–63.

112. Bianchi M, Scarpa F, Banse M, Smith CW. Novel generation of auxetic open cell foams for curved and arbitrary shapes. Acta Mater. 2011.59(2). 686–91.

113. Critchley R, Corni I, Wharton JA, Walsh FC, Wood RJK, Stokes KR. A review of the manufacture, mechanical properties and potential applications of auxetic foams. Phys Status Solidi Basic Res. 2013.250(10). 1963–82.

114. Li Y, Zeng C. On the successful fabrication of auxetic polyurethane foams: Materials requirement, processing strategy and conversion mechanism. Polym (United Kingdom). 2016.87. 98–107.

115. Boba K, Bianchi M, McCombe G, Gatt R, Griffin AC, Richardson RM, et al. Blocked shape memory effect in negative Poisson's ratio polymer metamaterials. ACS Appl Mater Interfaces. 2016. acsami.6b02809.

116. Gatt R, Attard D, Manicaro E, Chetcuti E, Grima JN. On the effect of heat and solvent exposure on the microstructure properties of auxetic foams: A preliminary study. Phys Status Solidi Basic Res. 2011.248(1). 39–44.

117. Bianchi M, Scarpa F, Smith CW, Whittell GR. Physical and thermal effects on the shape memory behaviour of auxetic open cell foams. J Mater Sci. 2010.45(2). 341–7.

118. de HASETH JA, Andrews JE, McClusky J V., Priester RD, Harthcock MA, Davis BL. Characterization of Polyurethane Foams by Mid-Infrared Fiber / FT-IR Spectrometry *. Appl Spectrosc. 1993.47(2).

119. Kim BH, Yoon K, Moon DC. Thermal degradation behavior of rigid and soft

polyurethanes based on methylene diphenyl diisocyanate using evolved gas analysis-(gas chromatography)-mass spectrometry. J Anal Appl Pyrolysis. 2012.98. 236–41.

120. Choi JB, Lakes RS. Nonlinear properties of polymer cellular materials with a negative Poisson's ratio. Mater Sci. 1992.27. 4678–84.

121. Alderson A, Davies PJ, Alderson KIML, Smart GM. The Effects of Processing on the Topology and Mechanical Properties of Negative Poisson's Ratio Foams. Proc IMECE2005 2005 ASME Int Mech Eng Congr Expo Proc IMECE200. 2005. 1–8.

122. Sanami M, Ravirala N, Alderson K, Alderson A. Auxetic materials for sports applications. Procedia Eng. 2014.72. 453–8.

123. Bianchi M, Frontoni S, Scarpa F, Smith CW. Density change during the manufacturing process of PU-PE open cell auxetic foams. Phys Status Solidi Basic Res. 2011.248(1). 30–8.

124. Reghunadhan A, Thomas S. Polyurethanes. In: Polyurethane Polymers. Amsterdam, The Netherlands: Elsevier Inc.; **2017**. p. 1–16.

125. Scarpa F, Pastorino P, Garelli A, Patsias S, Ruzzene M. Auxetic compliant flexible PU foams: Static and dynamic properties. Phys Status Solidi Basic Res. 2005.242(3). 681–94.

126. Najarian F, Alipour R, Shokri Rad M, Nejad AF, Razavykia A. Multi-objective optimization of converting process of auxetic foam using three different statistical methods. Meas J Int Meas Confed. 2018.119(August 2017). 108–16.

127. Evans KE, Nkansah MA, Hutchinson IJ. Auxetic foams: modelling negative Poisson's ratios. Acta Metall Mater. 1994.42(4). 1289–94.

128. Chan YNX. The Mechanical Properties of Auxetic Foams. University of Liverpool; **1995**.

129. Attenborough F. The modelling of network polymer (PhD Thesis, University of Liverpool). **1997**.

130. Grima JN, Caruana-Gauci R, Attard D, Gatt R. Three-dimensional cellular structures with negative Poisson's ratio and negative compressibility properties. Proc R Soc A Math Phys Eng Sci. 2012.468(2146). 3121–38.

131. Grima JN, Attard D, Gatt R, Cassar RN. A novel process for the manufacture of auxetic foams and for their re-conversion to conventional form. Adv Eng Mater. 2009.11(7). 533–5.

132. Chan N, Evans KE. Microscopic examination of the microstructure and deformation of conventional and auxetic foams. J Mater Sci. 1997.2. 5725–36.

133. Lowe A, Lakes RS. Negative Poisson's ratio foam as seat cushion material. Cell Polym. 2000.19(3). 157–67.

134. Argatov II, Guinovart-Díaz R, Sabina FJ. On local indentation and impact compliance of isotropic auxetic materials from the continuum mechanics viewpoint. Int J Eng Sci. 2012.54. 42–57.

135. Evans KE, Alderson A. Auxetic materials: Functional materials and structures from lateral thinking! Adv Mater. 2000.12(9). 617–28.

136. Photiou D, Sarris E, Constantinides G. On the conical indentation response of elastic auxetic materials: Effects of Poisson's ratio, contact friction and cone angle. Int J Solids Struct. 2017.110–111. 404.

137. Sanami M, Alderson A, Alderson KL, McDonald S a., Mottershead B, Withers PJ. The production and characterization of topologically and mechanically gradient open-cell thermoplastic foams. Smart Mater Struct. 2014.23(5). 055016.

138. Lisiecki J, Klysz S, Blazejewicz T, Gmurczyk G, Reymer P. Tomographic examination of auxetic polyurethane foam structures. Phys Status Solidi Basic Res. 2013.251(2). 314–20.

139. Li Y, Zeng C. Room-Temperature, Near-Instantaneous Fabrication of Auxetic Materials with Constant Poisson's Ratio over Large Deformation. Adv Mater. 2016.28(14). 2822–6.

140. Martz EO, Lee T, Lakes RS, Goel VK, Park JB. Re-entrant transformation methods in closed cell foams. Cell Polym. 1996.15(4). 229–49.

141. Fan D, Li M, Qiu J, Xing H, Jiang Z, Tang T. A Novel Method for Preparing Auxetic

Foam from Closed-cell Polymer Foam Based on Steam Penetration and Condensation (SPC) Process. ACS Appl Mater Interfaces. 2018.

142. Quadrini F, Bellisario D, Ciampoli L, Costanza G, Santo L. Auxetic epoxy foams produced by solid state foaming. J Cell Plast. 2015. 0021955x15579456-.

143. Xu T, Li G. A shape memory polymer based syntactic foam with negative Poisson ' s ratio. Mater Sci Eng A. 2011.528(22–23). 6804–11.

144. Wang K, Chang YH, Chen Y, Zhang C, Wang B. Designable dual-material auxetic metamaterials using three-dimensional printing. Mater Des. 2015.67. 159–64.

145. McDonald SA, Ravirala N, Withers PJ, Alderson A. In situ three-dimensional X-ray microtomography of an auxetic foam under tension. Scr Mater. 2009.60(4). 232–5.

146. Annual Book of ASTM Standards. Standard Test Methods for Flexible Cellular Materials — Slab , Bonded , and Molded Urethane Foams. Annual Book of ASTM Standards 2008.

147. Wang YC, Lakes R, Butenhoff A. Influence of Cell Size on Re-Entrant Transformation of Negative Poisson's Ratio Reticulated Polyurethane Foams. Cell Polym. 2001.20(4–6). 373–85.

148. Lim TC, Alderson A, Alderson KL. Experimental studies on the impact properties of auxetic materials. Phys Status Solidi. 2014.251(2). 307–13.

149. Chiang FP, Uzer G. Mapping full field deformation of auxetic foams using digital speckle photography. Phys Status Solidi Basic Res. 2008.245(11). 2391–4.

150. Liu Y, Hu H, Lam JKC, Liu S. Negative Poisson's Ratio Weft-knitted Fabrics. Text Res J. 2010.80(9). 856–63.

151. Hu H, Wang Z, Liu S. Development of auxetic fabrics using flat knitting technology. Text Res J. 2011.81(14). 1493–502.

152. Steffens F, Oliveira FR, Mota C, Fangueiro R. High-performance composite with negative Poisson's ratio. J Mater Res. 2017.32(18). 3477–84.

153. Zhou L, Zeng J, Jiang L, Hu H. Low-velocity impact properties of 3D auxetic textile composite. J Mater Sci. 2017.53(5). 1–16.

154. Goto K, Arai M, Matsuda T, Kubo G. Elasto-viscoplastic analysis for negative through-the-thickness Poisson's ratio of woven laminate composites based on homogenization theory. Int J Mech Sci. 2018.000(November). 1–7.

155. ge Z, hu H, Liu Y. Numerical analysis of deformation behavior of a 3D textile structure with negative Poisson's ratio under compression. Text Res J. 2015.85(5). 548–57.

156. Ge Z, Hu H. A theoretical analysis of deformation behavior of an innovative 3D auxetic textile structure. J Text Inst. 2015.106(1). 101–9.

157. Nava-Gómez GG, Camacho-Montes H, Sabina FJ, Rodríguez-Ramos R, Fuentes L, Guinovart-Díaz R. Elastic properties of an orthotropic binary fiber-reinforced composite with auxetic and conventional constituents. Mech Mater. 2012.48. 1–25.

158. Liaqat M, Samad HA, Hamdani STA, Nawab Y. The development of novel auxetic woven structure for impact applications. J Text Inst. 2017.108(7). 1264–70.

159. Zhou L, Jiang L, Hu H. Auxetic composites made of 3D textile structure and polyurethane foam. Phys Status Solidi Basic Res. 2016.253(7). 1331–41.

160. Jiang L, Gu B, Hu H. Auxetic composite made with multilayer orthogonal structural reinforcement. Compos Struct. 2016.135. 23–9.

161. Yang C, Vora HD, Chang YB. Application of auxetic polymeric structures for body protection. Proc ASME 2016 Conf Smart Mater Adapt Struct Intell Syst. 2016. 1–5.

162. Yang, S., Qi C, Guo DM, Wang D. Energy absorption of an re-entrant honeycombs with negative Poisson's ratio. Appl Mech Mater. 2012.148. 992–5.

163. Yuan S, Shen F, Bai J, Chua CK, Wei J, Zhou K. 3D soft auxetic lattice structures fabricated by selective laser sintering: TPU powder evaluation and process optimization. Mater Des. 2017.120. 317–27.

164. Lantada AD, De Blas Romero A, Schwentenwein M, Jellinek C, Homa J. Lithography-

based ceramic manufacture (LCM) of auxetic structures: Present capabilities and challenges. Smart Mater Struct. 2016.25(5).

165. Huang HH, Wong BL, Chou YC. Design and properties of 3D-printed chiral auxetic metamaterials by reconfigurable connections. Phys Status Solidi Basic Res. 2016.253(8). 1557–64.

166. Saxena KK, Calius EP, Das R. Tailoring Cellular Auxetics For Wearable Applications With Multimaterial 3d Printing. ASME 2016 Int Mech Eng Congr Expo Am Soc Mech Eng. 2018. 1–7.

167. Saxena KK, Das R, Calius EP. 3D printable multimaterial cellular auxetics with tunable stiffness. arXiv Prepr arXiv170704486. 2017. 1–18.

168. Li X, Lu Z, Yang Z, Yang C. Directions dependence of the elastic properties of a 3D augmented re-entrant cellular structure. Mater Des. 2017.134. 151–62.

169. Zhang X, Yang D. Mechanical properties of auxetic cellular material consisting of re-entrant hexagonal honeycombs. Materials (Basel). 2016.9(11).

170. Li D, Dong L, Lakes RS. A unit cell structure with tunable Poisson's ratio from positive to negative. Mater Lett. 2016.164. 456–9.

171. Ebrahimi H, Mousanezhad D, Nayeb-Hashemi H, Norato J, Vaziri A. 3D cellular metamaterials with planar anti-chiral topology. Mater Des. 2018.145. 226–31.

172. Fu M, Liu F, Hu L. A novel category of 3D chiral material with negative Poisson's ratio. Compos Sci Technol. 2018.160. 111–8.

173. Hanifpour M, Petersen CF, Alava MJ, Zapperi S. Mechanics of disordered auxetic metamaterials. 2017. 1–13. Available from: http://arxiv.org/abs/1704.00943

174. Yang C, Vora HD, Chang YB. Evaluation of auxetic polymeric structures for use in protective pads. Proc ASME 2016 Int Mech Eng Congr Expo IMECE2016. 2016. 2–8.

175. Yang C, Vora H, Chang Y. Behavior Of Auxetic Structures Under Compression And Impact Forces. Smart Mater Struct. 2017.

176. Bates SRG, Farrow IR, Trask RS. 3D printed polyurethane honeycombs for repeated tailored energy absorption. Mater Des. 2016.112. 172–83.

177. Alderson A, Alderson KL, Davies PJ, Smart MG. Process for the preparation of auxetic foams (US 2010/0029796 A1). Vol. 1. 2010. p. 11.

178. Hou Y, Neville R, Scarpa F, Remillat C, Gu B, Ruzzene M. Graded conventional-auxetic Kirigami sandwich structures: Flatwise compression and edgewise loading. Compos Part B Eng. 2014.59. 33–42.

179. Hou Y, Tai YH, Lira C, Scarpa F, Yates JR, Gu B. The bending and failure of sandwich structures with auxetic gradient cellular cores. Compos Part A Appl Sci Manuf. 2013.49. 119–31.

180. Zorzetto L, Ruffoni D. Re-entrant inclusions in cellular solids: From defects to reinforcements. Compos Struct. 2017.176. 195–204.

181. Lakes RS, Elms K. Indentability of conventional and negative Poisson's ratio foams. J Compos Mater. 1993.27(12). 1193–202.

182. Scarpa F, Yates JR, Ciffo LG, Patsias S. Dynamic crushing of auxetic open-cell polyurethane foam. Proc Inst Mech Eng Part C J Mech Eng Sci. 2002.216(12). 1153–6.

183. Bocquet C. Bra with variable-volume straps - WO2006045935A. 2006.

184. Timoshenko SP, Goodier JN. Theory of Elasticity. 3rd ed. New York: McGraw-Hill, USA; **1970**.

185. Budynas RG. Advanced strength and applied stress analysis. WCB/McGraw-Hill; **1999**. 21, 80 p.

186. Roark RJ, Young WC. Formulas for stress and strain. McGraw-Hill, USA; **2012**. 20-22, 48-50 p.

187. Lempriere BM. Poisson's ratio in orthotropic materials. AIAA Journal. 1968.6(11). 2226–7.

188. Wojciechowski KW. Remarks on "Poisson ratio beyond the limits of the elasticity theory." J Phys Soc Japan. 2003.72(7). 1819–20.
189. Alderson KL, Pickles AP, Neale PJ, Evans KE. Auxetic polyethylene: The effect of a negative Poisson's ratio on hardness. Acta Metall Mater. 1994.42(7). 2261–6.
190. Alderson KL, Fitzgerald A, Evans KE. The strain dependent indentation resilience of auxetic microporous polyethylene. J Mater Sci. 2000.35(16). 4039–47.
191. Lin DC, Shreiber DI, Dimitriadis EK, Horkay F. Spherical indentation of soft matter beyond the Hertzian regime: Numerical and experimental validation of hyperelastic models. Biomech Model Mechanobiol. 2009.8(5). 345–58.
192. Wang YC, Lakes R. Analytical parametric analysis of the contact problem of human buttocks and negative Poisson's ratio foam cushions. Int J Solids Struct. 2002.39(18). 4825–38.
193. Waters NE. The indentation of thin rubberer sheets by cylindrical indetors. Br J Appl Phys. 1965.16(2). 1387–92.
194. Photiou D⊚, Sarris E⊚, Constantinides G⊚. Erratum to "On the conical indentation response of elastic auxetic materials: Effects of Poisson's ratio, contact friction and cone angle" [Int. J. Solids Struct. 81 (2016) 33–42]. Int J Solids Struct. 2017.81(33–42).
195. Guo X, Jin F, Gao H. Mechanics of non-slipping adhesive contact on a power-law graded elastic half-space. Int J Solids Struct. 2011.48(18). 2565–75.
196. Li S, Al-Badani K, Gu Y, Lake M, Li L, Rothwell G, et al. The Effects of Poisson's Ratio on the Indentation Behavior of Materials With Embedded System in an Elastic Matrix. Phys Status Solidi Basic Res. 2017.254(12). 1–8.
197. Aw J, Zhao H, Norbury A, Li L, Rothwell G, Ren J. Effects of Poisson's ratio on the deformation of thin membrane structures under indentation. Phys Status Solidi Basic Res. 2015.252(7). 1526–32.
198. Morris DJ, Cook RF. Indentation fracture mechanics model. 2008.23(9). 2429–42.
199. Argatov II, Sabina FJ. Small-scale indentation of an elastic coated half-space: The effect of compliant substrate. Int J Eng Sci. 2016.104. 87–96.
200. AUXETIC MATERIALS FOR BIOMEDICAL APPLICATIONS Mohammad Sanami. 2015.(September).
201. Adam MM, Berger JR, Martin PA. Singularities in auxetic elastic bimaterials. Mech Res Commun. 2013.47. 102–5.
202. Kwon K, Phan A V. Symmetric-Galerkin boundary element analysis of the dynamic T-stress for the interaction of a crack with an auxetic inclusion. Mech Res Commun. 2015.69. 91–6.
203. Song F, Zhou J, Xu X, Xu Y, Bai Y. Effect of a negative poisson ratio in the tension of ceramics. Phys Rev Lett. 2008.100(24). 1–4.
204. Mohsenizadeh S, Alipour R, Shokri Rad M, Farokhi Nejad A, Ahmad Z. Crashworthiness assessment of auxetic foam-filled tube under quasi-static axial loading. Mater Des. 2015.88. 258–68.
205. Bezazi A, Scarpa F. Mechanical behaviour of conventional and negative Poisson's ratio thermoplastic polyurethane foams under compressive cyclic loading. Int J Fatigue. 2007.29(5). 922–30.
206. Pastorino P, Scarpa F, Patsias S, Yates JR, Haake SJ, Ruzzene M. Strain rate dependence of stiffness and Poisson's ratio of auxetic open cell PU foams. Phys Status Solidi Basic Res. 2007.244(3). 955–65.
207. Nakonieczna P, Wierzbicki Ł, Śladowska B, Leonowicz M, Lisiecki J. Composites with impact absorption ability based on shear thickening fluids and auxetic foams. Compos Theory Pract. 2017.2(17). 67–72.
208. Qi C, Yang S, Wang D, Yang LJ. Ballistic resistance of honeycomb sandwich panels under in-plane high-velocity impact. Sci World J. 2013.2013.

209. Liu W, Wang N, Luo T, Lin Z. In-plane dynamic crushing of re-entrant auxetic cellular structure. Mater Des. 2016.100. 84–91.

210. Ugbolue SC, Kim YK, Warner SB, Fan Q, Yang CL, Kyzymchuk O, et al. The formation and performance of auxetic textiles. Part II: Geometry and structural properties. J Text Inst. 2011.102(5). 424–33.

211. Yang S, Chalivendra VB, Kim YK. Impact behaviour of auxetic Kevlar®/ epoxy composites. IOP Conf Ser Mater Sci Eng. 2017.254(4). 0–7.

212. Yang S, Chalivendra VB, Kim YK. Fracture and impact characterization of novel auxetic Kevlar®/Epoxy laminated composites. Compos Struct. 2017.168. 120–9.

213. Alderson KL, Simkins VR, Coenen VL, Davies PJ, Alderson A, Evans KE. How to make auxetic fibre reinforced composites. Phys Status Solidi Basic Res. 2005.242(3). 509–18.

214. Alderson KL, Coenen VL. The low velocity impact response of auxetic carbon fibre laminates. Phys Status Solidi. 2008.496(3). 489–96.

215. Coenen VL, Alderson KL. Mechanisms of failure in the static indentation resistance of auxetic carbon fibre laminates. Phys Status Solidi Basic Res. 2011.248(1). 66–72.

216. Standardisation IO for. ISO 13753:1999 Mechanical vibration and shock – Hand-arm vibration – Method for measuring the vibration transmissibility of resilient materials when loaded by the hand-arm system. Geneva; 1999.

217. Chen CP, Lakes RS. Dynamic wave dispersion and loss properties of conventional and negative Poisson's ratio polymeric cellular materials. Cell Polym. 1989.8. 343–69.

218. Lisiecki J, Nowakowski D, Reymer P. Fatigue Properties of Polyurethane Foams, With Special Emphasis on Auxetic Foams, Used for Helicopter Pilot Seat Cushion Inserts. Fatigue Aircr Struct. 2014.1. 72–8.

219. Evans KE. The design of doubly curved sandwich panels with honeycomb cores. Compos Struct. 1991.17(2). 95–111.

220. Alderson A, Alderson KL, Chirima G, Ravirala N, Zied KM. The in-plane linear elastic constants and out-of-plane bending of 3-coordinated ligament and cylinder-ligament honeycombs. Compos Sci Technol. 2010.70(7). 1034–41.

221. Wang Z, Hu H. 3D auxetic warp-knitted spacer fabrics. Phys Status Solidi Basic Res. 2014.251(2). 281–8.

222. Mehta R. A nose for auxetics. MATERIALS WORLD; **2010**. p. 9–12.

223. Mather PT, Luo X, Rousseau IA. Shape Memory Polymer Research. Annu Rev Mater Res. 2009.39(1). 445–71.

224. Allen T, Martinello N, Zampieri D, Hewage T, Senior T, Foster L, et al. Auxetic foams for sport safety applications. Procedia Eng. 2015.112(0). 104–9.

225. Toronjo A. Articles of apparel including auxetic materials (US 20140059734 A1). Vol. 1. 2014.

226. Qiao JX, Chen CQ. Impact resistance of uniform and functionally graded auxetic double arrowhead honeycombs. Int J Impact Eng. 2015.83. 47–58.

227. Cross TM, Hoffer KW, Jones DP, Kirschner PB, Meschter JC. Auxetic Structures And Footwear With Soles Having Auxetic Structures (US 2015/0075034 A1). Vol. 1. 2015.

228. Nike. The New Dimensions of Nike Free [Internet]. **2016**. Available from: The New Dimensions of Nike Free

229. Alderson A, Rasburn J, Evans KE. An Auxetic Filter : A Tuneable Filter Displaying Enhanced Size Selectivity or Defouling Properties. Ind Eng Chem Res. 2000. 654–65.

230. Martin PG. Filtering face-piece respirator having an auxetic mesh in the mask body (US 2011/0155137 A1). Vol. 1. 2011.

231. Alderson A, Evans KE, Rasburn J. Separation process and apparatus - Patent WO1999022838A1. 1999.

232. Alderson A, Rasburn J, Evans KE. Mass transport properties of auxetic (negative Poisson's ratio) foams. Phys Status Solidi - Basic Solid State Phys. 2007.244(3). 817–27.

233. Yasin RM. Petit Pli: Clothes that Grow. Utop Stud. 2018.28(3). 576–84.

234. D3O. Trust Helmet Pad System [Internet]. Web Page. **2018** [cited 2018 Jan 25]. Available from: https://www.d3o.com/products/trust-helmet-pad-system/

235. Xu K, Tan Y, Xin JH, Liu Y, Lu C, Deng Y, et al. A novel impact hardening polymer with negative Poisson's ratio for impact protection. Mater Today Commun. 2015.5. 50–9.

236. Doyoyo M, Wan Hu J. Plastic failure analysis of an auxetic foam or inverted strut lattice under longitudinal and shear loads. J Mech Phys Solids. 2006.54(7). 1479–92.

237. Taha Z, Hassan MHA. Parametric Analysis of the Influence of Elastomeric Foam on the Head Response during Soccer Heading Manoeuvre. Procedia Eng. 2016.147. 139–44.

Chapter 3: Thermal effects during thermo-mechanical conversions of small (~2 x 2 x 6 cm) samples of open cell polyurethane foam

3.1. Introduction

This chapter will address Aim 1 (Chapter 1, Page 5), and has been adapted from an article published in PSSB [1]:

Reported values of NPR in isotropic polymeric foams (including PU) are difficult to compare due to differences in the applied strain, strain rates and measurement methods. NPR values ranging from 0 to as low as -0.7 have been reported [2–22]. The heat applied during thermo-mechanical conversions affects the uptake of imposed compression [19,23] and polymeric composition [8], potentially changing the relationship between rib flexure, stretching and hinging around junctions [24–26]. As highlighted in the introduction (Chapter 1, Page 5), changes to the polymeric composition during thermo-mechanical fabrications are not typically measured. Therefore, the physical mechanisms giving rise to the high magnitude NPRs (-0.5 to -1, [2,4,5,19–22]), and the precise processing conditions to achieve them, remain unclear.

Auxetic foams are often shape memory polymers, returning substantially to their original cellular structure and dimensions, accompanied by a return to positive Poisson's ratio, when exposed to an external trigger such as sufficient heat or certain solvents (without the constraint of a mould, [12,13,17,27]). Auxetic foams with 'blocked shape memory' which partially recover their original dimensions/structure but retain NPR after re-exposure to heat have been fabricated with multiple cycles of thermo-mechanical compression and thermal re-expansion [8]. The hydrogen bonds which can fix an imposed re-entrant structure have a lower glass transition temperature (T_g) than other bonds, which can produce shape memory upon weakening by reheating or with solvents [12,13,17]. Dimensional recovery over time can occur following thermo-mechanical auxetic foam conversions [3,8,12,28]. Final density ratio (FDR) has been used to describe the amount of regrowth following conversion [8,12,28], but since foam mass can also change due to degradation and/or solvent loss during heating, final volume ratio (FVR, initial/final volume) will be used.

As highlighted in the introduction and Aims 1 & 2 (Chapter 1, Page 5), attempts have been made to create positive Poisson's ratio foam that is more comparable to auxetic foam than typical open cell foam to use in comparative tests, including anisotropic, marginally NPR uniaxially compressed 'iso-density' (equal density) foams [9,29]. Heating foam under isotropic compression for an extended period or at too high a temperature produces re-entrant foam with a positive Poisson's ratio and increased Young's modulus [3,30]. Suggested reasons why

excessive heat produces a contorted, re-entrant structure without an NPR include adhesion between cell ribs inhibiting transverse deformation [3,21] and decomposition of the polyurethane (PU) [3]. Spectral changes have been identified in one previous study using Fourier transform infrared spectral analysis (FTIR) following PU thermo-mechanical foam conversions [8]. Adhesion of cell ribs does not appear to have been empirically confirmed in samples subject to excessive heat [3,21]. Residual stresses caused by rapid cooling are considered possible and detrimental following conversions, with attempts (annealing and hand stretching) made to remove them [3,31].

The approach during typical thermo-mechanical conversions has been to adjust cell shape while minimising the likelihood of detrimental changes to polymeric structure, residual stresses and adhesion between cell ribs [3,31,32]. The effects of applied compression [2,3,30,32], oven temperature [3,14,30,32], heating time [3,14,22] and cooling method [28] on final density [32,33], cell structure [19,32,33], NPR [3,14,30], and Young's modulus [3,22,33] have been studied, but not together and not with the inclusion of polymeric changes.

Thermo-plastic PU consists of hard (ordered) and soft (amorphous) segments.[34] Copolymers and cross-linkers can affect PU characteristics [14,16,34,35]. Softening temperature (or point) has been used to describe a temperature that will produce auxetic foam under typical volumetric compression ratios (VCR, Initial/final volume, typically two to five). Thermocouples inserted into the foam have been used to accurately monitor heating and cooling [3,11], but leave a hole in samples. Other studies have quoted oven temperatures and conversion times instead [2,8,14]. Softening; decreasing the strength of hydrogen bonds [14] and/or transitioning through any polymer or copolymer glass transition region can lead to permanent [8] or temporary [13,17,23] re-organisation of the polymeric structure, fixing changes imposed (by volumetric compression) on the cell structure. Degradation in polymer chains typically occurs first in hard segments, then in soft segments [36,37]. Assessing dimensional stability, Poisson's ratio, Young's modulus, changes to cell structure and changes to polymeric bonding in samples fabricated with a broad range of thermal and mechanical processing conditions will improve understanding of the whole thermo-mechanical fabrication process. Findings can then be used to determine the conditions to give high magnitude NPR, or to fabricate non-auxetic, iso-density comparative samples with similar stress-strain relationships to high magnitude NPR samples.

3.2. Methods

3.2.1. Foam Conversions

Cuboids of flame retardant PU foam with 30 pores per inch (PUR30FR, Custom-foams, supplied cut to 32 x 32 x 96 mm, Figure 3.1) were thermo-mechanically converted with isotropic compression in aluminium box section moulds (2 mm wall thickness) with a VCR of three. Samples were heat treated in a conventional oven (MCP Tooling Technologies LC/CD) between 120 and 200°C (10°C increments) for either 20, 60 or 180 minutes. Pilot tests found samples took approximately fifteen minutes to reach the oven temperature, which was comparable to other work using similar foam and moulds [3]. Six samples were fabricated for each time and temperature combination and cooled to close to room temperature in their moulds, as in previous work [2,3,14], taking 30 to 60 minutes. Unless a transition temperature is passed through, heating and cooling rate are not expected to have any notable effect (i.e. to polymer crystallisation [34]) beyond changing the amount of heat exposure. Open cell foam's elongated cell rise direction [26] was as received from the supplier, identified visually as being perpendicular to the longest dimension of every sample (Figure 3.1 & Figure 3.3a). From each set of six samples, three were tested for dimensional stability and the remaining three samples were tested for Poisson's ratio, Young's modulus and polymeric bonding using FTIR. Samples that were tested for dimensional stability were first stretched once, by hand, to approximately 30% of their imposed length after removal from the mould to remove residual stresses. Samples fabricated at 140 and 160 °C for 180 minutes were also mechanically characterised following re-heating to test their dimensional stability. Following completion of the initial (VCR = 3) study, additional samples were fabricated (VCR = 2) at combinations of heat and time that gave consistent negative and near zero Poisson's ratios for samples with a VCR of three (140°C and 200°C for 60 minutes respectively).

Figure 3.1: Foam and mould (annotations show cell rise and dimensions. L_1 (x) = 76.5 or 66.5 mm and L_2 (y and z) = 25.5 or 22 mm for VCR = 2 or 3, respectively

3.2.2. Dimensional stability testing

Dimensional stability was tested a week after fabrication, by measuring sample dimensions (Vernier callipers) both before and one hour after heating in an oven set to 200°C (for 10 minutes) without a compression mould [12,23,38]. All samples were tested in the same air-conditioned environments and stored in spacious, sealed containers with no compression between fabrication and testing. Although relative humidity was not measured during storage, it is unlikely to have varied between samples.

The 4 phases typically employed in the shape memory polymer cycle are: (i) Deformation (at elevated stress and temperature); (ii) Cooling/fixing (at elevated stress); (iii) Unloading (removal of stress at the lower temperature); and (iv) Recovery (re-heating to elevated temperature under zero stress [39]). By analogy, the corresponding foam conversion process and dimensional stability testing phases reported here are (i) Heating in a compression mould (Deformation); (ii) Cooling in a compression mould (Cooling/fixing); (iii) Removal from compression mould followed by brief hand stretching and leaving for 1 week (Unloading); and (iv) Unconstrained (out-of-mould) re-heating (Recovery).

The SMP literature [39] defines the following measures of shape fixing, R_f (%), and recovery, R_r (%):

$$R_f(\%) = \frac{\varepsilon_u}{\varepsilon_m} \times 100 \qquad\qquad (3.1)$$

$$R_r(\%) = \frac{(\varepsilon_u - \varepsilon_p)}{(\varepsilon_m - \varepsilon_p)} \times 100 \qquad\qquad (3.2)$$

where ε_m, ε_u and ε_p are the strains after the Deformation, Unloading and heat-induced Recovery phases. In this work we use volumetric strain, and so the strain after the Deformation phase is that imposed by the compression mould:

$$\varepsilon_m = \frac{V - V_0}{V_0} = \frac{V}{V_0} - 1 = \frac{1}{FVR} - 1 \qquad\qquad (3.3)$$

where V and V_0 are the imposed volume and initial volume, respectively. Similarly, ε_u and ε_p are determined by using the volume measured after 1 week and unconstrained heating, respectively, in place of the imposed volume in Equation 3.3.

3.2.3. Mechanical Characterisation

Mechanical testing (Figure 3.2, Figure 3.3) was started one week after fabrication, and took four weeks. After attaching 3 mm thick acrylic end tabs using epoxy resin, cyclic testing

between 0 and 10% tensile strain (strain rate 0.0033 s-1, sample frequency 25 Hz, 5 cycles, Instron 3367, 500 N load cell) allowed controlled sample settling [8], and analysis of the final cycle. Cubes laser cut (Trotec 10000) from the centre of tensile samples (after tensile testing, Figure 3.3b) were compression tested (strain rate 0.0067 s-1) to 10% strain, in all three orthogonal planes. Samples were tested over four weeks in the following order, with a week between tests to allow recovery:

Week 1) Tensile tests measuring E_x and ν_{xz}
Week 2) Tensile tests measuring E_x and ν_{xy}
Week 3) Compression tests measuring E_z and ν_{zx} then E_x and ν_{xz}
Week 4) Compression tests measuring E_x and ν_{xy}

where x, y and z are defined in the caption to Figure 3.1 and Figure 3.3a.
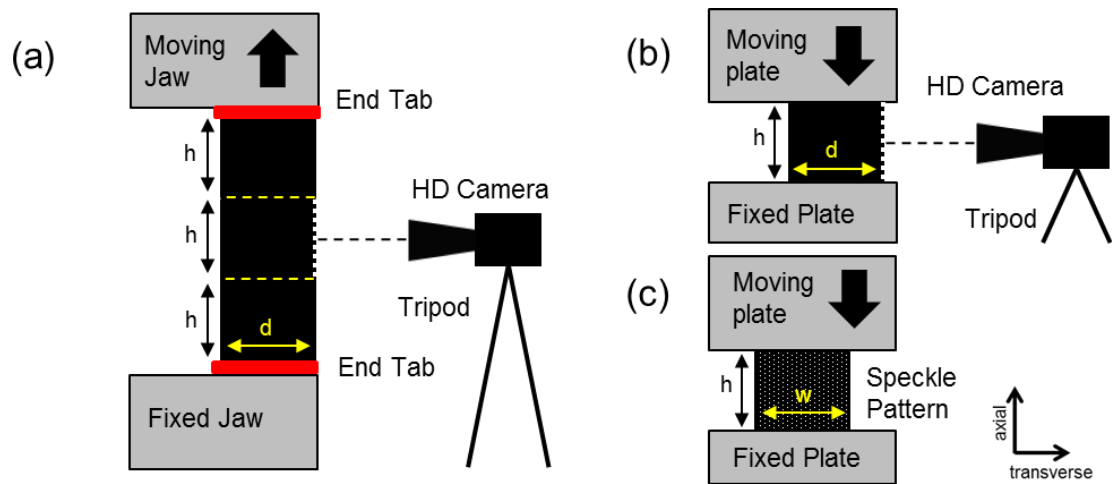
Figure 3.2: Typical a) Tensile (side view), b) Compression (side view) and c) Compression (front view) test setup, using an Instron 3367 with a 500N load cell. Depth (d) $\sim$ width (w) $\sim$ height (h) for area where stress and strain are typically measured. Subfigures (a) and (c) show camera and tripod set up. Figure (c) shows location of speckle pattern, used in compression testing only, and axis labelling (for tensile and compression tests).

Digital Image Correlation (DIC) was used to obtain axial and transverse strains [7,40]. The top and bottom of the square target area in the centre of each sample were marked with ~2 mm diameter pins or liquid paper (Figure 3.3b) (target area sides ~ equal to sample width). Pins were used for samples fabricated at 120, 140, 160, 180 & 200°C and liquid paper for samples fabricated at 130, 150, 170 & 190°C, following concerns that pins caused damage to the cell structure. Powder coating (Figure 3.3c, Laponite RD, BYKAdditives) enhanced the speckle pattern provided by pores in compression. No speckle pattern was used in tension, with sufficient contrast provided by the porous foam surface.
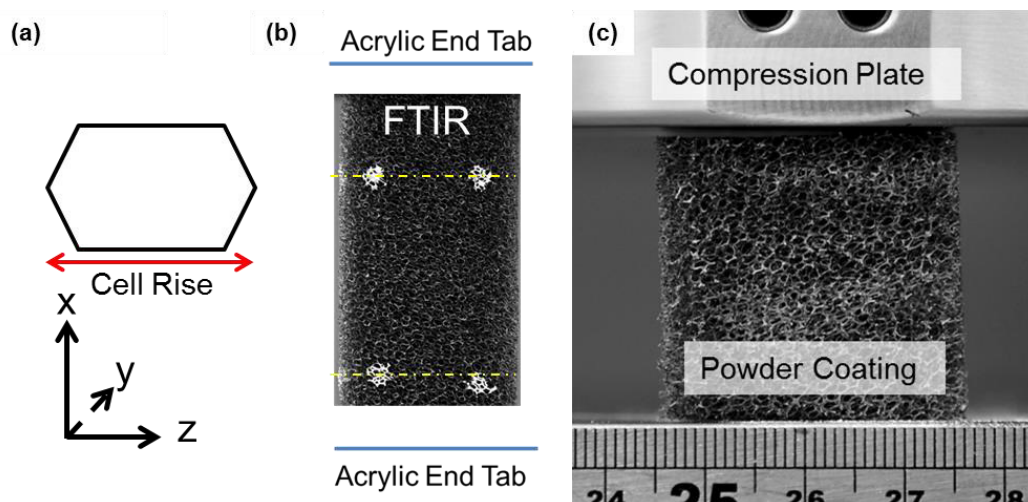
Figure 3.3: a) Sample/cellular orientation, b) Tensile test setup, showing laser cut (yellow dash-dot lines) region, with foam outside this area used for FTIR analysis, c) Compression test setup with powder coating

Tests were filmed (Cannon G16, 28 mm lens or Nikon D810, 28-300 mm lens, both set to 1920x1080p at 25fps), with DIC analysis carried out using commercial software (GOM Correlate, 2016). Cameras were focused prior to each test, and facet sizes were between 25 and 35 pixels (0.04 to 0.06 mm.pixel^{-1}, depending on sample size and camera zoom checked in the centre and edge of images from each camera showing negligible distortion), standard accuracy and matching against definition stage were typically selected. Linear trend lines fitted to plots of transverse strain (ε_t) vs axial strain (ε_a) (mean value across all facets within target area, over the entire 10% strain range) were used to obtain Poisson's ratio, determined from the negative of the gradient of the linear trend line (i.e. ν_{at} = - ε_t / ε_a). Stresses were calculated from cross sectional areas (measured with Vernier Callipers prior to each test) and force data from the Intron's built in software (Bluehill 4.0). Tensile and compressive modulus were calculated from the gradients of linear trend lines fitted (between 0 and 10% axial strain, from DIC) to axial stress (σ_a) vs axial strain (i.e. E_a = σ_a / ε_a).

3.2.4. Polymeric Composition & Cell Structure

Sections cut from tensile samples (Figure 3.3b) of unconverted foam, and foam converted for 20 minutes at 120, 140, 160, 180 and 200°C, and at 200°C for 60 and 180 minutes were analysed in detail. X-ray diffraction (XRD) data were collected using a PANalytical X'Pert Pro diffractometer with Cu Kα X-rays, λ = 1.54050 Å over the range 10-70° 2θ. FTIR were collected on a Nexus FTIR spectrometer over the wavenumber range of 4000 to 600 cm^{-1}, with a resolution of 8 cm^{-1} and taking a mean over 64 scans. The baseline value was taken between 3800 and 4000 cm^{-1}. The higher wavenumber region (2400 to 3700 cm^{-1}) of absorbance spectra were normalised to the non-changing CH$_2$ band (2872 cm^{-1}). The low wavenumber region (1000

to 1900 cm^{-1}) of absorbance spectra were normalised to the non-hydrogen bonded (free) Amide I band of urethane (1727 cm^{-1}), which did not change significantly. The aforementioned spectra were collected using an ATR accessory utilising a diamond crystal. Spectra were also collected using a germanium crystal to assess the presence of styrene and acrylonitrile (SAN) copolymer particles (1700 and 2600 cm^{-1} [14]).

Three heating/cooling cycles during Differential Scanning Calorimetry (DSC, Perkin Elmer DSC 8000, -75 to 120°C, heating and cooling rate 10°Cmin^{-1}) were used to assess T_g following applied heat. Thermogravimetric analysis (TGA, Mettler Toledo TGAIOSC, Stare System, 20 to 300°C, 10°Cmin^{-1}) indicated degradation within (and above) the temperature ranges used for conversion (25 to 300°C). Micro-ct scans (SkyScan1172) of 7 mm diameter, 10 mm long cylinders of unconverted foam and foam converted with VCR of three (190°C, 60 minutes & 200°C, 180 minutes) were collected. Qualitative inspection of a 3 x 3 x 0.5 to 1 mm region (corresponding to 1 pore in depth) compared cell structures through the bulk of the foam. Resolution at the analysis stage was 5 μm/pixel, and a transfer function adapted from bone segment analyses was applied. Samples laser cut to ~1 mm (~1 pore) thick (Trotec, 10000) were qualitatively inspected at rest, then at 10 % tension (applied parallel to the z axis, Figure 3.3a) using a stereoscope over a white background (Leica S6D). A clear, acrylic frame work was used to apply tension.

3.3. Results

3.3.1. Structural Analysis

All samples processed at T ≤ 150°C with a VCR of three underwent some dimensional recovery (FVR < 3) over time, irrespective of heating time (Figure 3.4a). Increasing temperature and time in all conversions decreased the level of re-expansion after a week in ambient conditions (Figure 3.4a) to the point that all samples converted at T ≥ 180°C were dimensionally stable (FVR = 3) over this timescale, irrespective of heating time. Samples converted at low temperatures and short time (T ≤ 140°C for 20 minutes, Figure 3.4a & b) had already returned completely to their original dimensions (FVR = 1) after one week. Unconstrained re-heating to 200°C for 10 minutes accelerated (promoted) dimensional recovery in samples that had undergone partial re-expansion, and some samples that appeared stable, after one week in ambient conditions (150 ≤ T ≤ 190°C for 20 minutes, 120 ≤ T ≤ 170°C for 60 minutes, 120 ≤ T ≤ 150°C for 180 minutes, Figure 3.4b). The accelerated complete or partial re-expansion following re-heating corresponds to shape memory behaviour [8].The remaining samples (T = 200°C for 20 minutes, T ≥ 180°C for 60 minutes, T ≥ 160°C for 180 minutes) exhibited negligible re-expansion, i.e. remained stable, after unconstrained re-heating (Figure 3.4b).
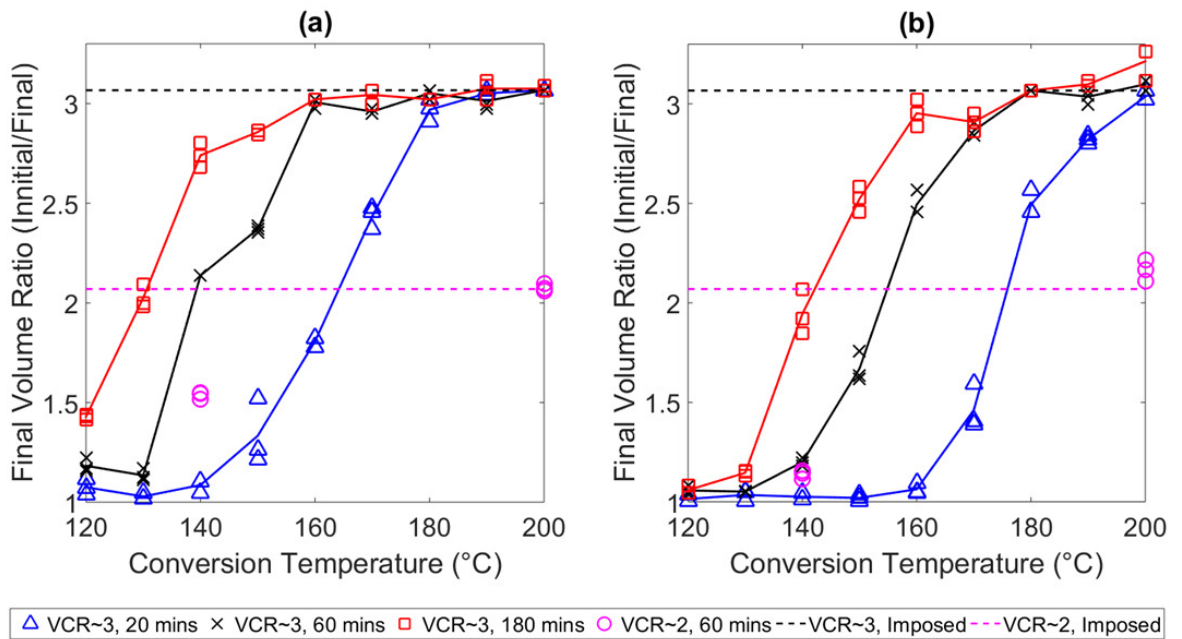
Figure 3.4: a & b) Measured final volume ratio (initial/final volume) after a) 1 week, b) Re-heating to 200°C for 10 minutes. Lines (VCR~3) fitted to VCRs to guide the eye. Legend displayed below figures.

The R_r (%) measure of heat-induced recovery was found to be linearly proportional to the shape fixing measure R_f (%), until R_f (%) approached 100% (Figure 3.5). When R_f (%) was close to 100%, extremely large variation was due to measurement resolution error as ε_m-ε_p (Equation 3.2) approached zero. The data for foams produced at 20, 60 and 180 minutes heating time during conversion were found to overlap the same linear trend in the R_r (%) vs R_f (%) plot (Figure 3.5). The data point at T = 200°C for 180 minutes with an FVR marginally above 3 after unconstrained re-heating agrees within the error (±5%) associated with the volume measurement with VCR = 3.

The change in volume caused by heat induced recovery was close to linear (Figure 3.5b). For the tested foams heat simply accelerates or amplifies re-expansion that had already started following fabrication. For the longer heating times a drop off in heat induced recovery R_r was exhibited close to 95% fixing (Equation 3.2b). It is possible that with the increased shape fixing caused by increased conversion time and temperature, residual stresses that can cause recovery were no longer present. Considering both plots (Figure 3.4 and Figure 3.5) together, only samples converted at or below 160°C for 60 or 180 minutes exhibited re-expansion above ~5% after the unloading phase. Due to the reduced number of samples present, combined with the relatively small measurement increments required for such samples (e.g. 150°C, 180 minutes, whereby FVR decreases from 2.75 or 22.8 mm sides to 2.55 or 23.4 mm sides) the drop off in R_r is most likely caused by measurement error.
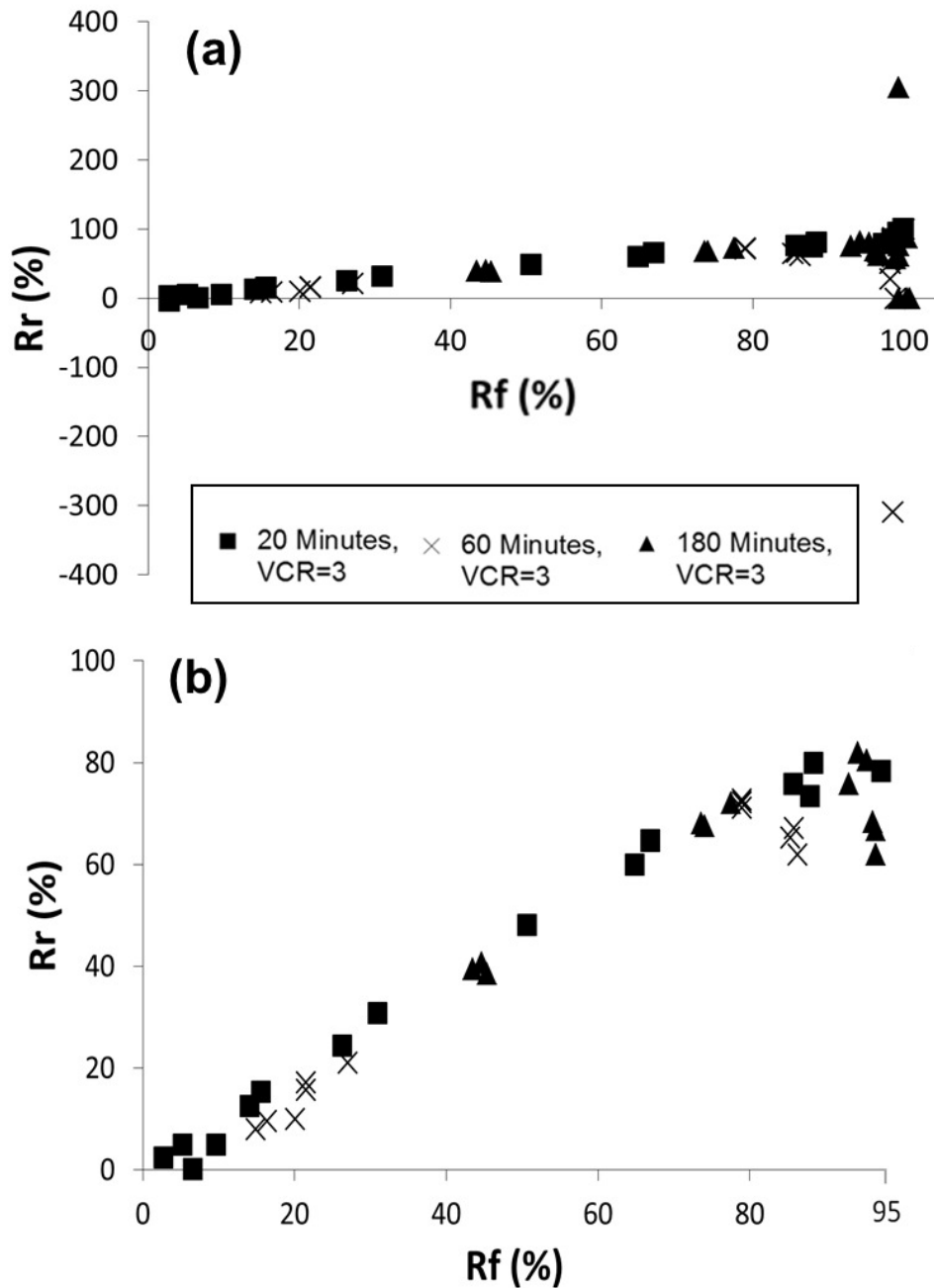
Figure 3.5: Recovery (R_r (%)) vs shape fixing (R_f (%)) measured for all VCR = 3 foam samples produced at 20, 60 and 180 minutes conversion heating times. a) Shows all samples, b) excludes all samples with R_f (%) greater than 95. Legend (a) is the same for both figures

Unconverted, open cell foam showed its classic honeycomb-like, fully reticulated, cell structure (Figure 3.6a & b) and elongated cell rise (Figure 3.6a, [26]). Adhesion between ribs could not be identified in the bulk scans of converted samples (Figure 3.6c to f), neither could any qualitative evidence for the persistence of the original cell rise direction (agreeing with previous work, [2,20]). All apparent missing ribs (Figure 3.6c to f) were checked by adjusting the depth of the target volume and are actually intact but simply passing through its perimeters. Optical microscopy of 1 mm thick slices of unconverted foam (Figure 3.7 a & d) and

foam with an FVR of two and either NPR (Figure 3.7 b & e) or near zero Poisson's ratio (Figure 3.7 c & f) clearly shows re-entrant cells elongating at ~10% tension (Figure 3.7 e & f). The ribs of the foams with an FVR of two remained kinked at 10 % tension (Figure 3.7 e & f). Cell stretching could not be qualitatively identified for the unconverted foam (Figure 3.7d).
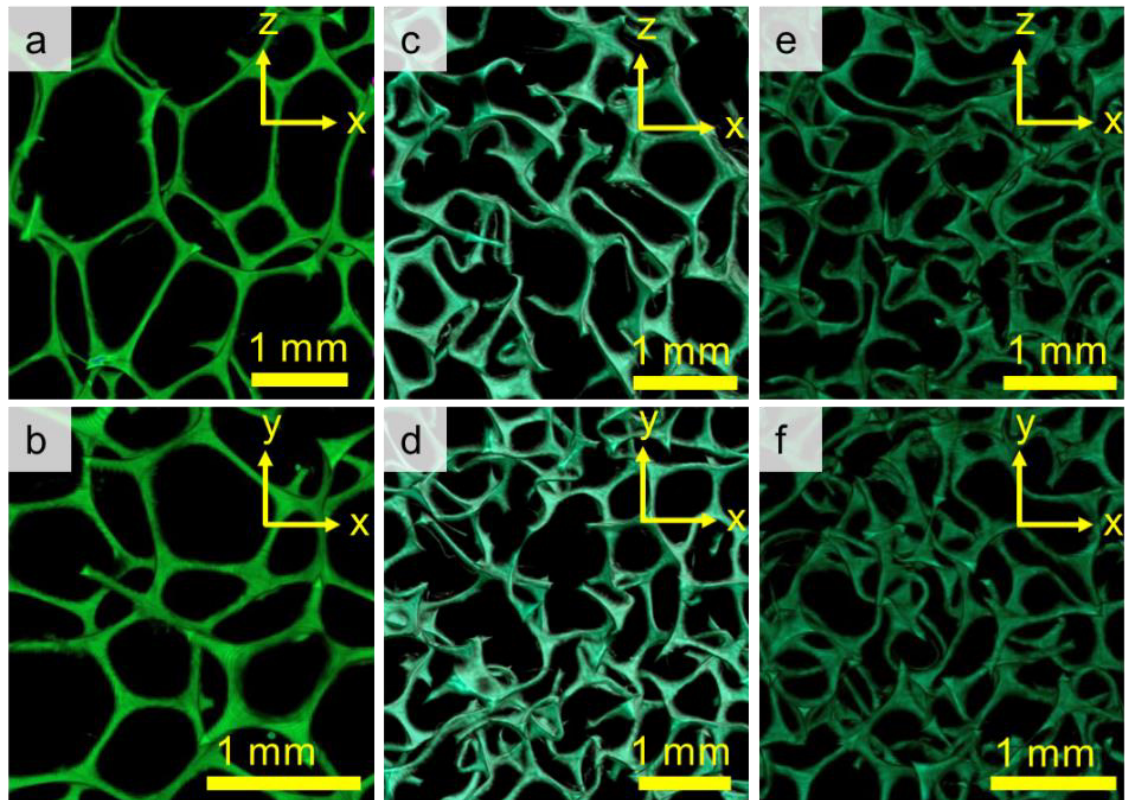

Figure 3.6: Micro-CT scans of: a & b) PUR30 FR (depth = 1 mm), c & d) Foam converted with VCR=3 for 60 minutes at 190°C (depth = 0.5 mm), e & f) Foam converted with VCR=3 for 180 minutes at 200°C (depth = 0.5 mm). Axes show orientation (z = elongated cell rise direction in unconverted foams, or original cell rise direction in converted foams)
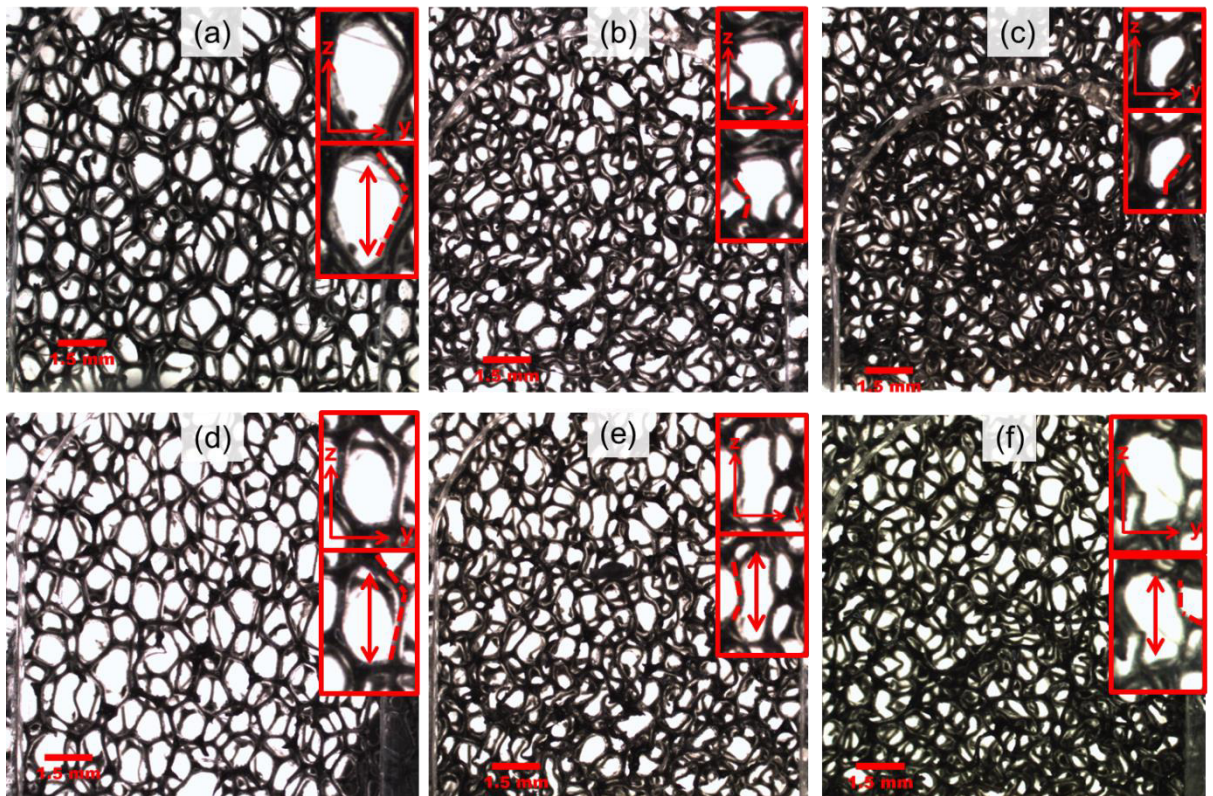
Figure 3.7: Optical stereoscopic images taken of: a) to c) Unstrained a) Unconverted foam, b) auxetic foam, 160°C, 20 minute, VCR=3, FVR=2 foam, c) ~zero Poisson's ratio, 180°C, 60 minute, VCR & FVR =2 foam, d) to f) Foam at 20% tension: d) UC, e) 160-20 & f) 180-60 VCR=2. Pop outs show a single cell enlarged by a factor of two, cell rise/elongation and cell rib angles.

3.3.2. Mechanical Characterisation

Unconverted foam had a positive Poisson's ratio, with little local variation to transverse strain across each sample (Figure 3.8a). Samples with maximum magnitude NPR also had a near-constant NPR with some fluctuation in local strain suggesting some inhomogeneity in the cell structure (Figure 3.8b). Samples heated at the higher temperatures and longer times showed similar local strain fluctuation but spanning positive and negative values (Figure 3.8c). Compressive and tensile transverse strain vs axial strain relationships were quasi-linear for all samples over the tested region (0 to 10% strain, Figure 3.9).
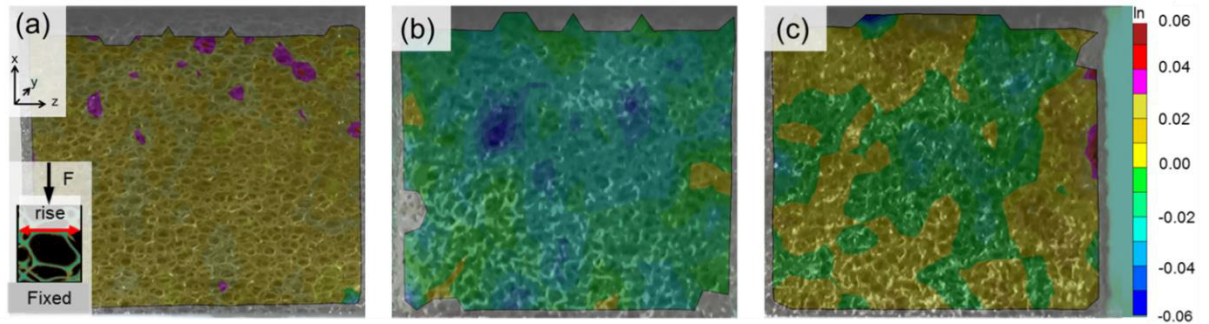
Figure 3.8: Contour plot showing local transverse strain for a) Unconverted PUR30FR, b) Foam with VCR = 3, heated for 180 minutes at 140°C & c) Foam with VCR = 3, heated for 180 minutes at 200°C. Axial loading was parallel to x axis, transverse strain parallel to y axis and shown on scale on right-hand side of figure c
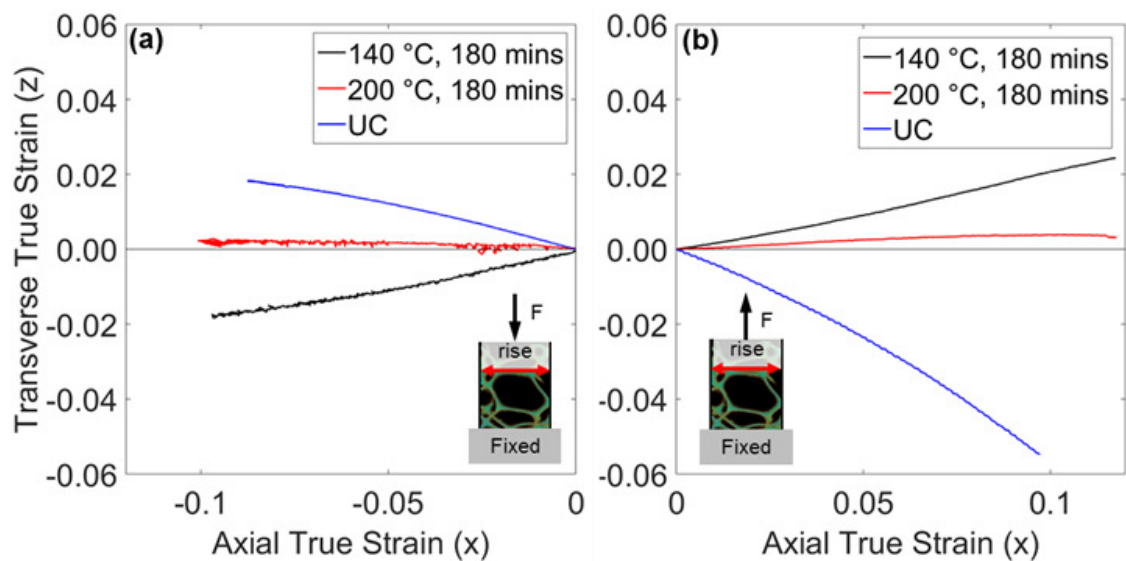

Figure 3.9: Transverse vs Axial (true) strain (mean across all facets) in a) Compression, b) Tension (loading parallel to x axis, transverse deformation parallel to z axis)

Mean anisotropic Poisson's ratios of unconverted samples were ~0.5 in tension and for loading parallel to cell rise in compression, and ~0.25 in compression perpendicular to the rise direction (Figure 3.10). For foams produced with a heating time of 20 minutes, Poisson's ratio was positive, approximately constant and anisotropic (with noticeable differences between orientations) for T ≤ 140°C, then decreased notably in magnitude and anisotropy as temperature increased above 140°C, undergoing a transition to NPR when T = 150°C, and a minimum value at T = 160°C. Further increases in conversion temperature did not change isotropy but gradually (over the next ~30°C of heating) increased Poisson's ratio to marginally positive values in compression (Figure 3.10a) and marginally negative values in tension (Figure 3.10b). Increasing heating time to 60 and 180 minutes gave the same general Poisson's ratio vs conversion temperature trend but systematically moved to lower conversion temperatures (i.e. to the left in Figure 3.10). The maximum magnitude of NPR was the same for all heating times (NPR ~ -0.2),

comparable to other studies thermo-mechanically fabricating and testing isotropic auxetic foam samples over a similar strain range [8,9,18]. Samples tensile tested with pins or liquid paper markers (at odd and even temperatures) showed similar variability (Figure 3.10). Inserting pins for mechanical testing either had negligible effect due to sample damage, or the effect was no greater than scatter due to imperfect liquid paper markers [41].

The foams with an applied VCR of two displayed tensile and compressive Poisson's ratios of ~-0.2 and ~0 for 140°C and 200°C, 60 minute conversions, respectively (Figure 3.11). Samples fabricated at 140°C for 180 minutes with a VCR of 3 retained tensile and compressive NPR following reheating at 200°C for 10 minutes without a mould (Figure 3.11). An increase in NPR magnitude was found for the re-heated samples fabricated at 160°C for 180 minutes, particularly in compression where Poisson's ratio decreased from near zero (Figure 3.10a) to ~-0.1 (Figure 3.11a) following unconstrained re-heating.
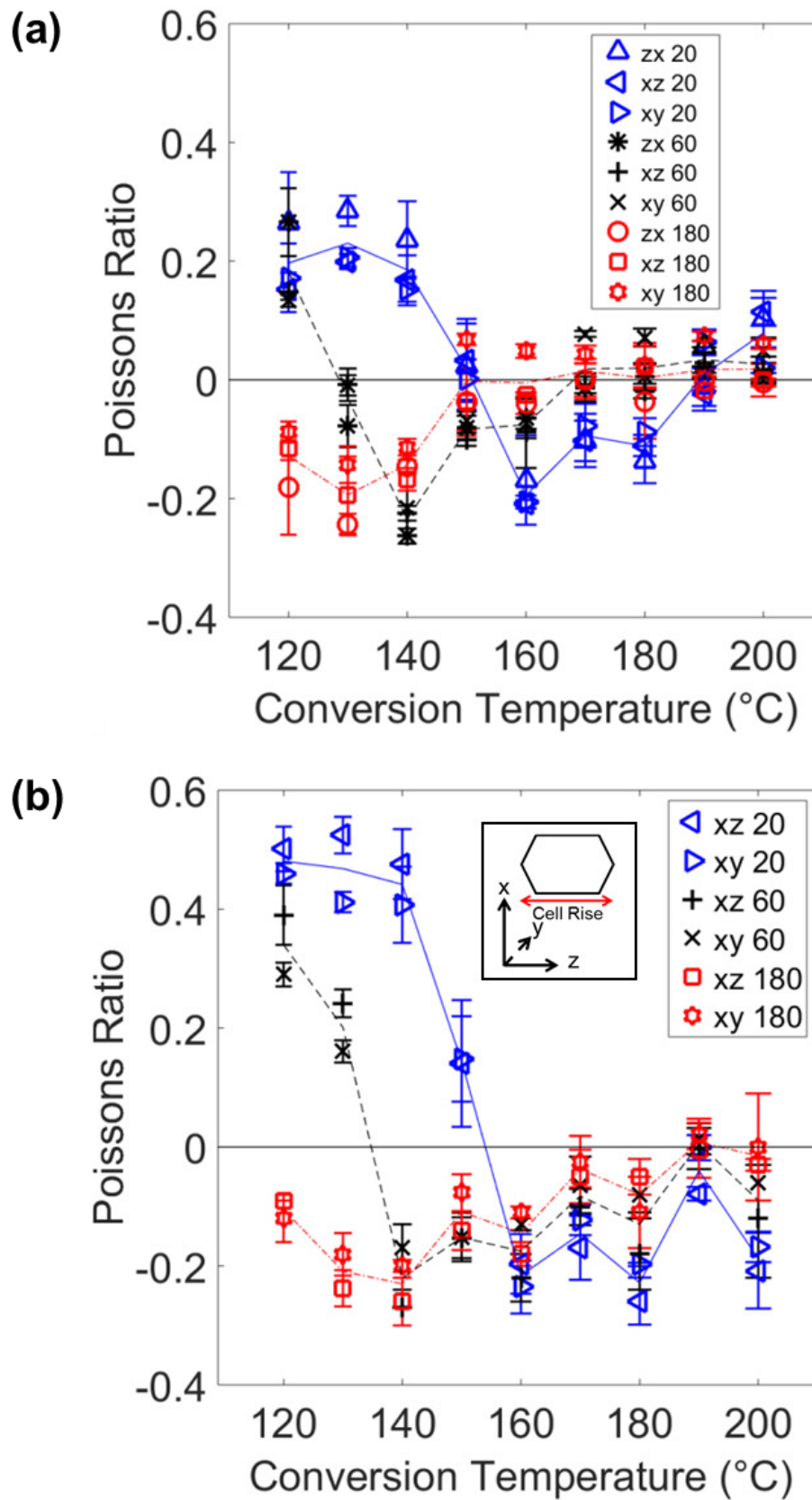
Figure 3.10: Poisson's ratio (0 to 10 % strain) in a) Compression (samples with VCR = 3), b) Tension (samples with VCR = 3). Lines (solid, dash & dash/dot for 20, 60 & 180 minute conversions respectively) connect mean over all orientations tested to guide the eye, error bars = 1 s.d. Y axis in b) same as a)
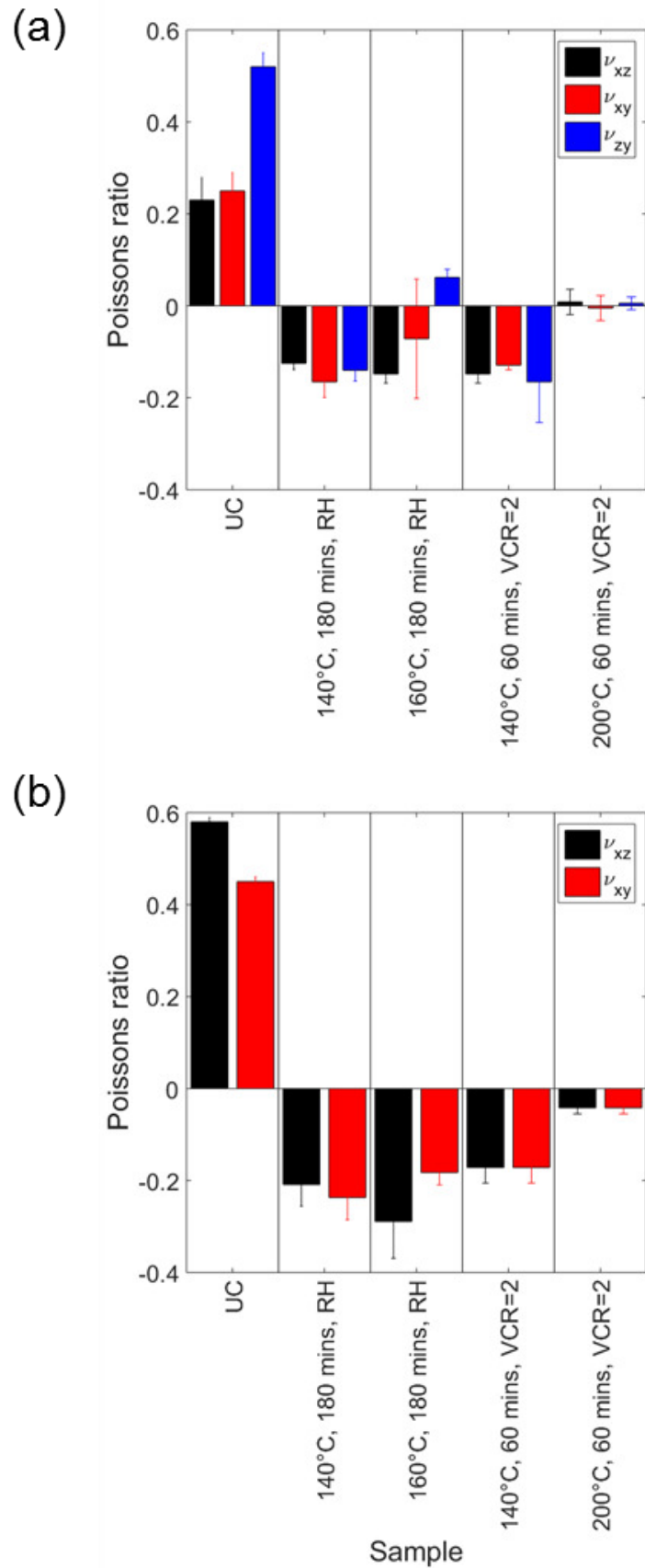
Figure 3.11: a) Compressive and b) Tensile Poisson's ratio (0 to 10 % strain) of additional VCR = 2, those reheated following dimensional stability testing (RH) and unconverted (UC) samples. Error bars = 1 s.d.

The unconverted foam compressive stress vs strain relationship was nonlinear, with a characteristic plateau region beginning between 4 and 6% compression (Figure 3.12a) as previously reported [20,26,32]. Samples with high magnitude NPR exhibited a quasi-linear compressive stress vs strain relationship (140°C, 180 minutes, Figure 3.12a). All stress vs strain relationships were approximately linear in tension (Figure 3.12b). The marginally positive Poisson's ratio sample converted at the higher temperature and time (200°C, 180 minutes) was quasi linear in compression (Figure 3.12a) and required a higher load to reach an equivalent tensile or compressive strain than the maximum magnitude NPR foam (Figure 3.12a & b). Minor variations in linearity were likely caused by changing, strain dependant angles between cell ribs.
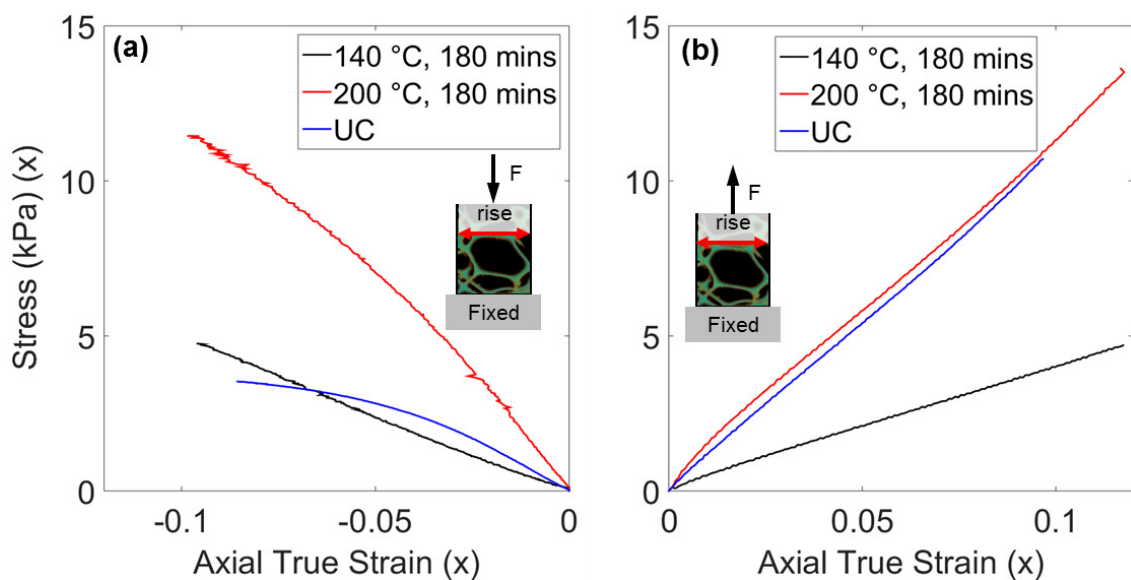

Figure 3.12: Sample stress (from Instron and sample measurements) vs Axial True Strain (from DIC, mean across all facets) in a) Compression, b) Tension (loading parallel to x axis)

The Young's moduli of unconverted samples in tension (E_x = 102 kPa) and compression (E_z = 127 kPa, E_x = 60 kPa) taken up to 10% strain were similar to measurements taken up to 5% compressive strain for the non-linear unconverted foam, E_z = 115 ± 5 kPa, E_x = 74 ± 11 kPa (Figure 3.13). Young's modulus initially decreased with conversion temperature to minimum values of ~30 kPa in tension and ~25 kPa in compression (Figure 3.13a) at the same conditions giving minimum Poisson's ratio (Figure 3.10). Further increasing conversion temperature increased compressive and tensile Young's modulus (Figure 3.13). Increasing heating time moved the Young's moduli vs conversion temperature data to lower temperatures, similar to the Poisson's ratio trends. Samples fabricated with a VCR of two, and those tested for thermal stability, have comparable tensile and compressive Young's modulus (Figure 3.14) to samples fabricated with a VCR of three heated for the same amount of time at the same temperature (Figure 3.13a & b).
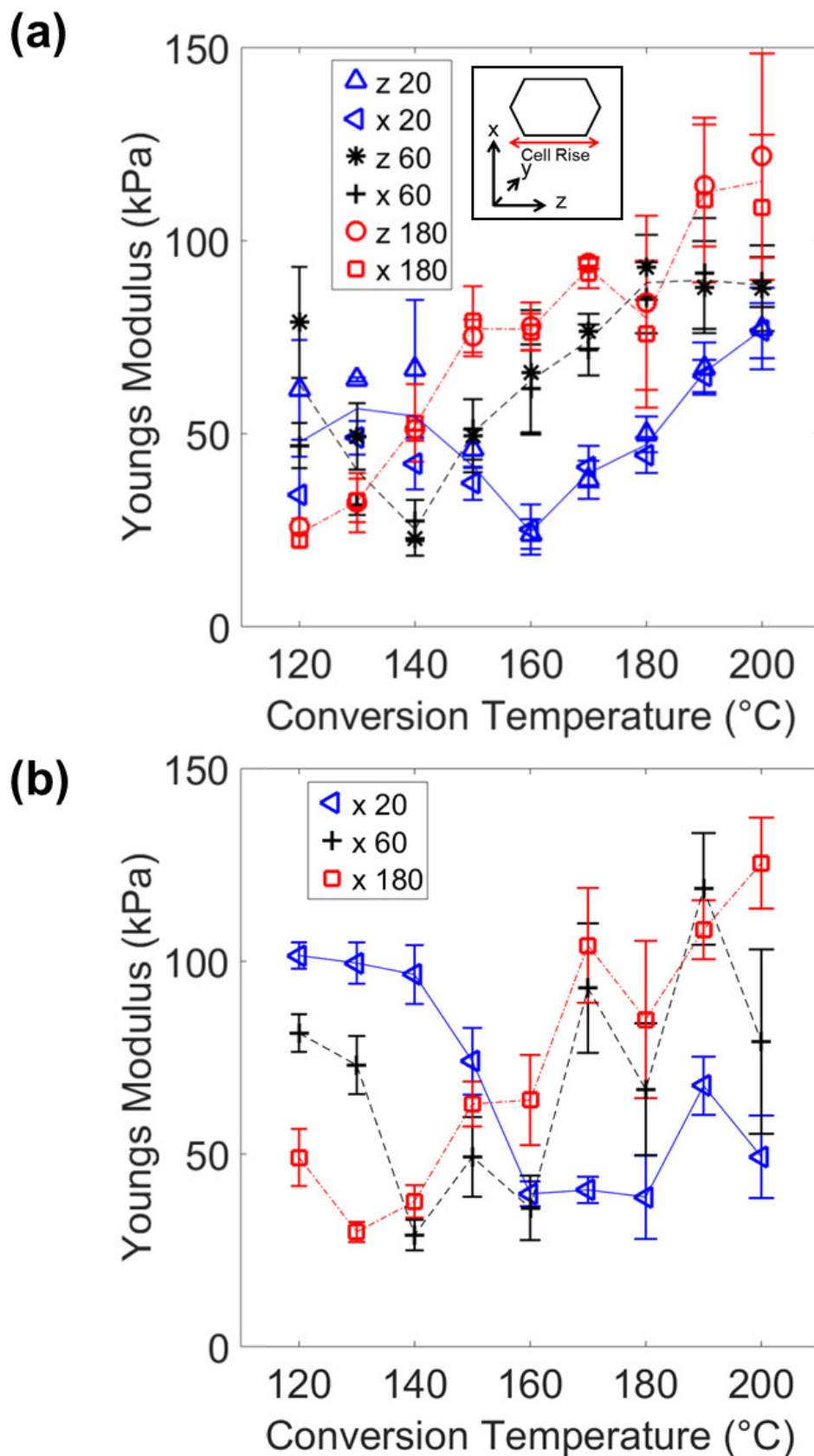
Figure 3.13: Young's Modulus (0 to 10 % strain) in a) Compression (samples with VCR = 3), b) Tension (samples with VCR=3), Lines (solid, dash & dash/dot for 20, 60 & 180 minute conversions respectively) connect mean over all orientations tested to guide the eye, error bars = 1 s.d. Y axis in b) same as a)
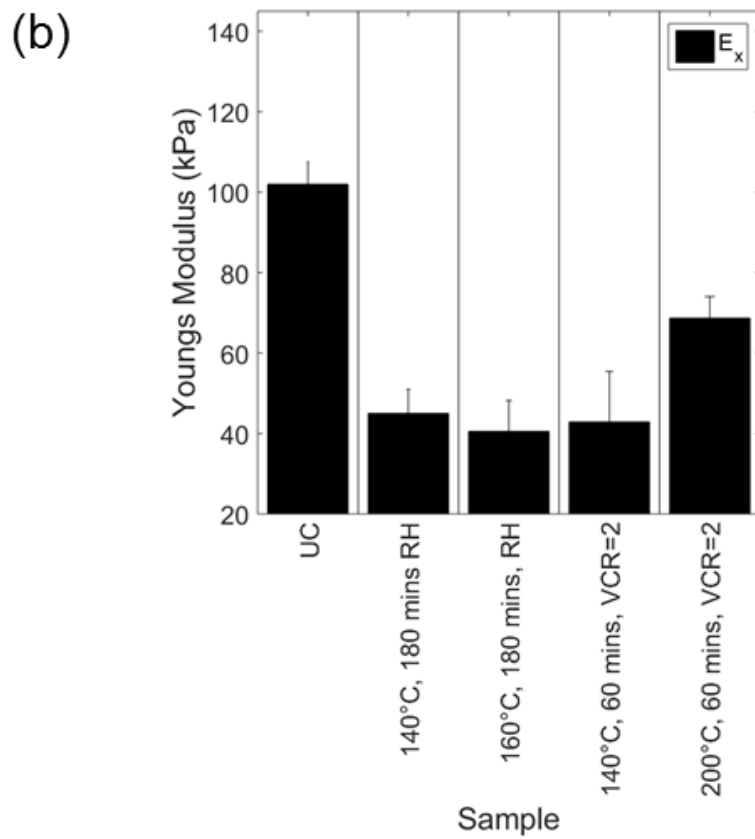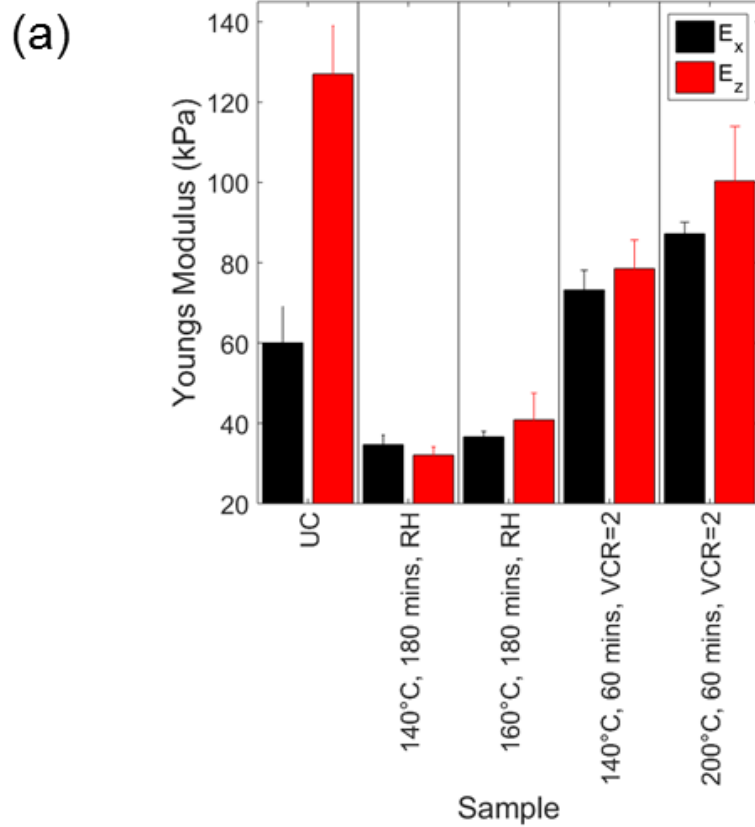
Figure 3.14: a) Compressive and b) Tensile Young's Modulus (0 to 10 % strain) of additional VCR = 2, those reheated following dimensional stability testing (RH) and unconverted (UC) samples. Error bars = 1 s.d.

3.3.3. Polymeric Analysis

Analysis of the XRD data only showed two very broad peaks positioned at 20 and 45° 2θ, characteristic of semi-crystalline polymers with both hard and soft segments (Figure 3.15, [14]).
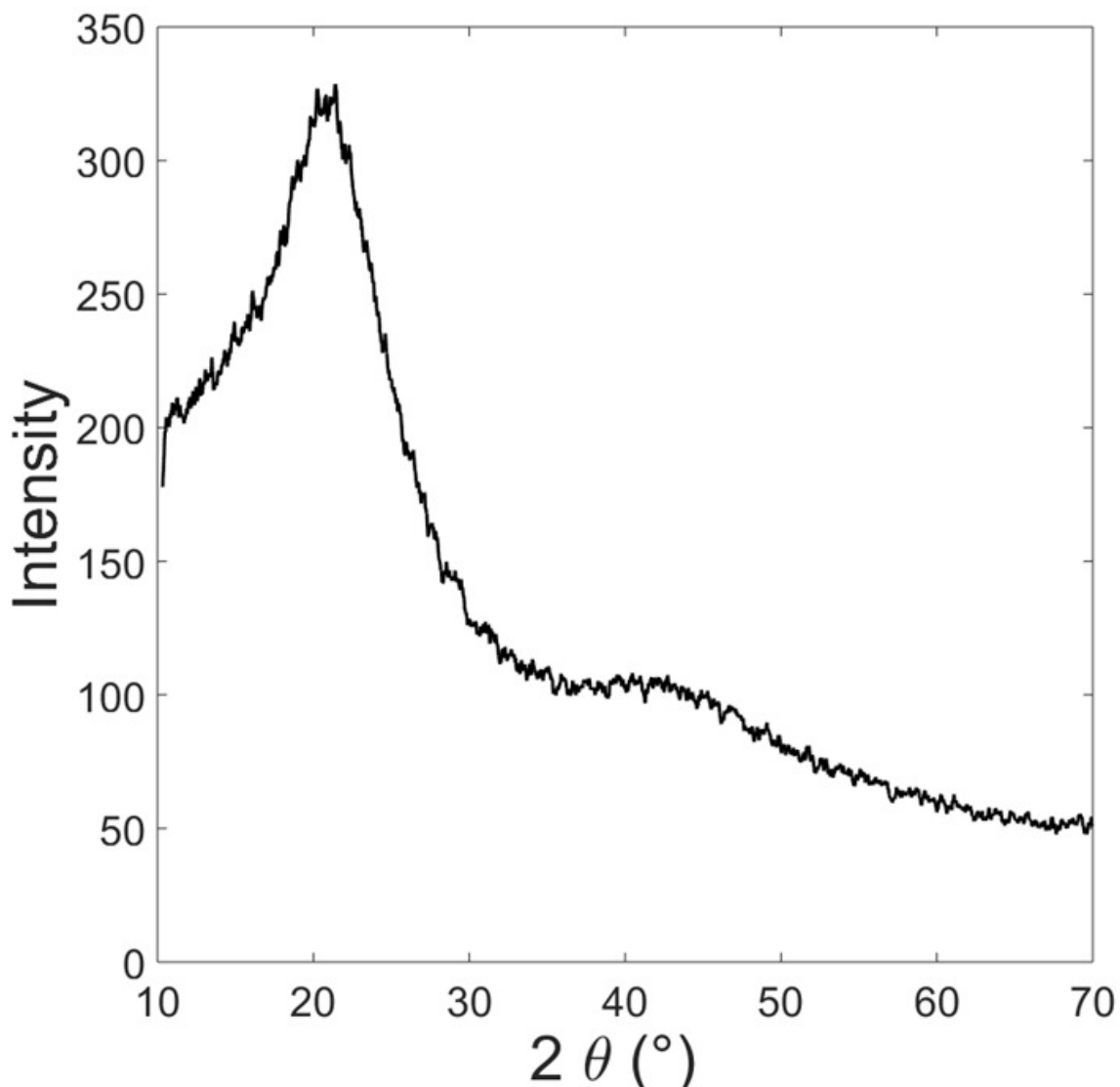

Figure 3.15: XRD of Unconverted PUR30FR

FTIR spectra in the region 2400 to 3700 cm^{-1} (Figure 3.16a) normalised to the symmetric CH$_2$ band at 2872 cm^{-1} showed a small reduction in intensity of the CH$_2$ stretch band at 2912 cm^{-1} for all converted samples, but no significant differences between these until heating increased to 200°C for 180 minutes [35]. The position of the N-H stretch band associated with the unconverted foam (3305 cm^{-1}) [14,35,42] indicates this band is involved in the hydrogen bonding network (free N-H bonds undergoing no hydrogen bonding are typically around 3450 cm^{-1}, [35,43]). As heat exposure increased to 160°C and above this band shifted towards lower wavenumbers (3302 cm^{-1}) and dramatically increased in intensity, indicating an environment

where there is an increase in N-H groups undergoing stronger hydrogen bonding and an increase in their relative population. The full width at half maximum remained (mostly) constant except in the samples heated at 200°C for 180 minutes. A broad underlying increase in intensity was observed between 3600 and 2400 cm^{-1} for the sample heated at 200°C for 180 minutes. FTIR spectra in the region 1000 to 1900 cm^{-1} (Figure 3.16b) normalised to the relatively unchanging Amide I band associated with free urethane (1727 cm^{-1} [14,35]) showed the Amide I band of hydrogen bonded urea groups (predominantly C=O stretching groups, ~1640 cm^{-1} [14,35]) increased dramatically in magnitude when heated to 160°C and above [42]. Minor intensity decreases and broadening of the Amide II band (predominantly C-N stretch & N-H bend, at 1531 cm^{-1}, [36,43]) progressively occurred when heated at 200°C for prolonged periods of time, whilst a large intensity increase and shift to a lower wavenumber for the asymmetric C-O-C stretch of polyol's (1077 cm^{-1}, [36]) was also evident after 180 minutes at 200°C. SAN particles (~2240 cm^{-1} [14]) were not present (Figure 3.17).
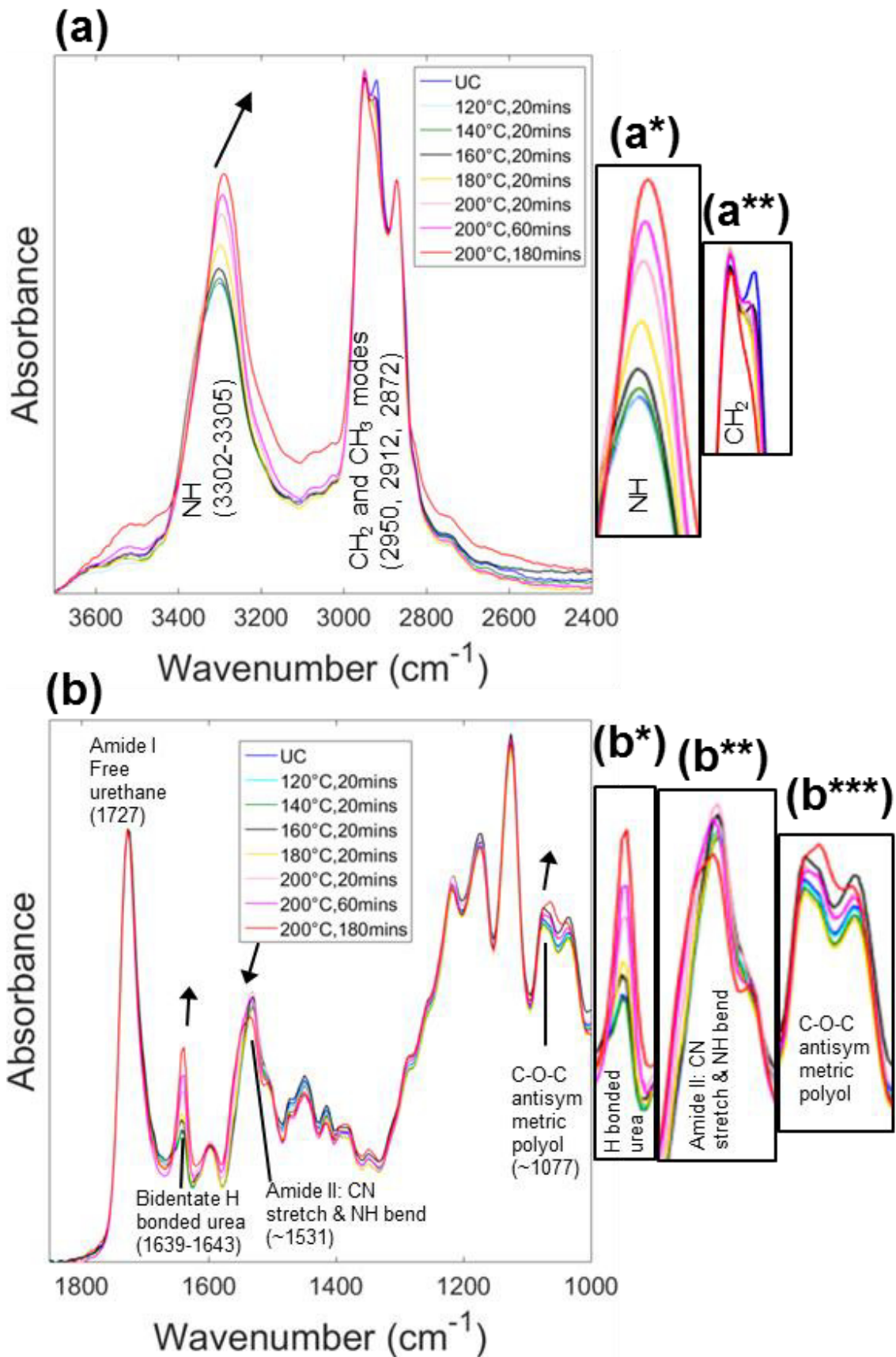
**Figure 3.16:** FTIR of PUR30FR following conversion under the heating conditions defined in the legend, UC = unconverted. a) High wavenumber (enlarged pop-outs a* & a** show NH and CH_2 peaks, respectively) & b) Low wavenumber (enlarged pop-outs b*, b** & b*** show H bonded urea, Amide II and CH_2 peaks, respectively). Arrows highlight approximate trends observed as heat exposure increased.
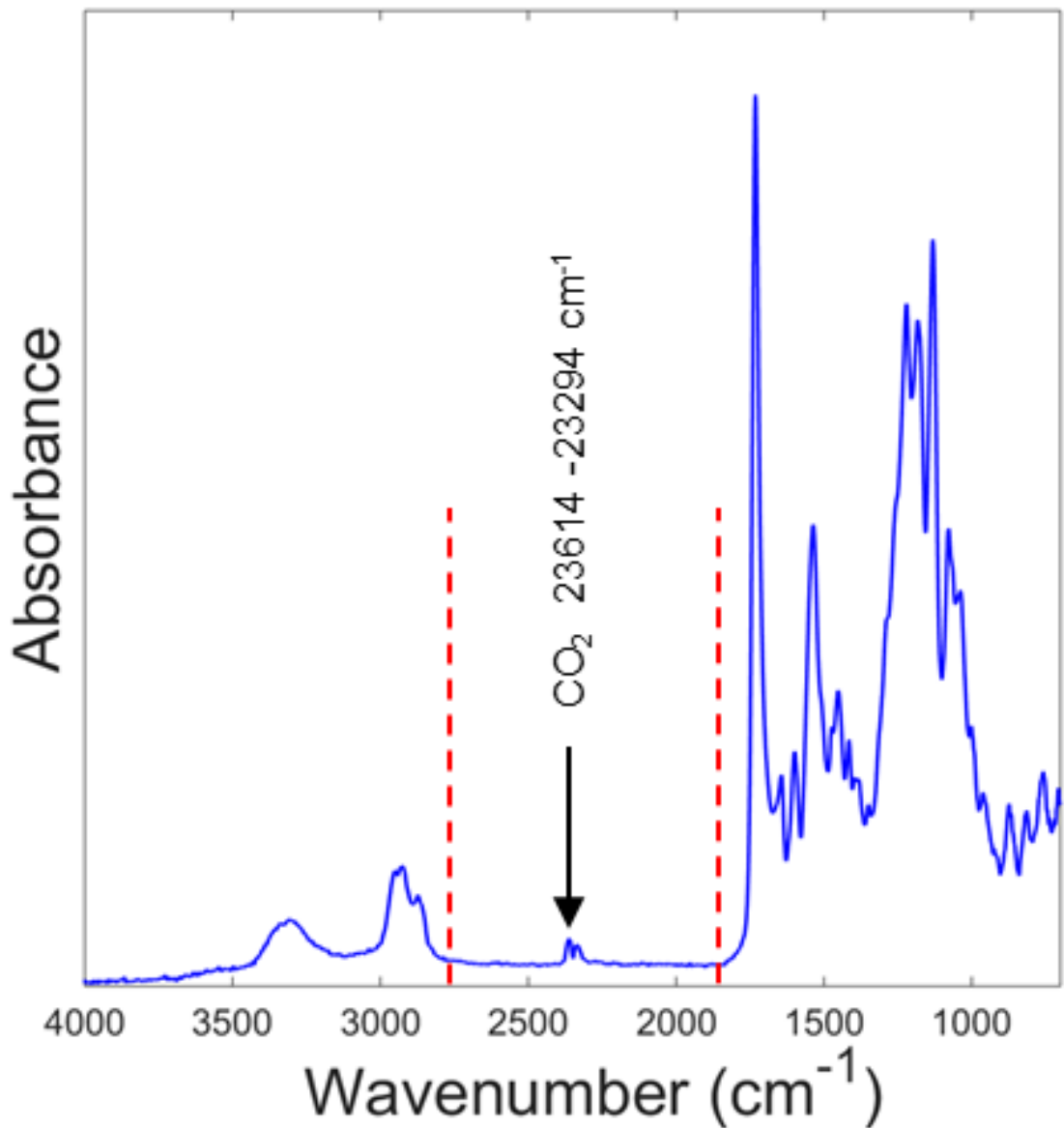
Figure 3.17: FTIR of unconverted foam taken using the Germanium crystal to remove interference between 1700 and 2600cm^{-1} (marked in red dashed lines). Atmospheric CO_2 peak marked [44].

DSC (Figure 3.18) shows T_g was consistent between cycles. The first cycle shows a broad, variable transition between ~20 and ~90°C, which was not present in subsequent cycles (agreeing with previous work [12]). Mass loss, as evidence by TGA, occurred by 1% between 25-90°C and was attributed to the loss of moisture (Figure 3.19). Between 100 and 150°C mass loss was negligible (Figure 3.19) and then increased marginally between 150 and 200°C (typical in thermo-plastics [45]). Significant mass-loss was evident above 200°C (Figure 3.19).
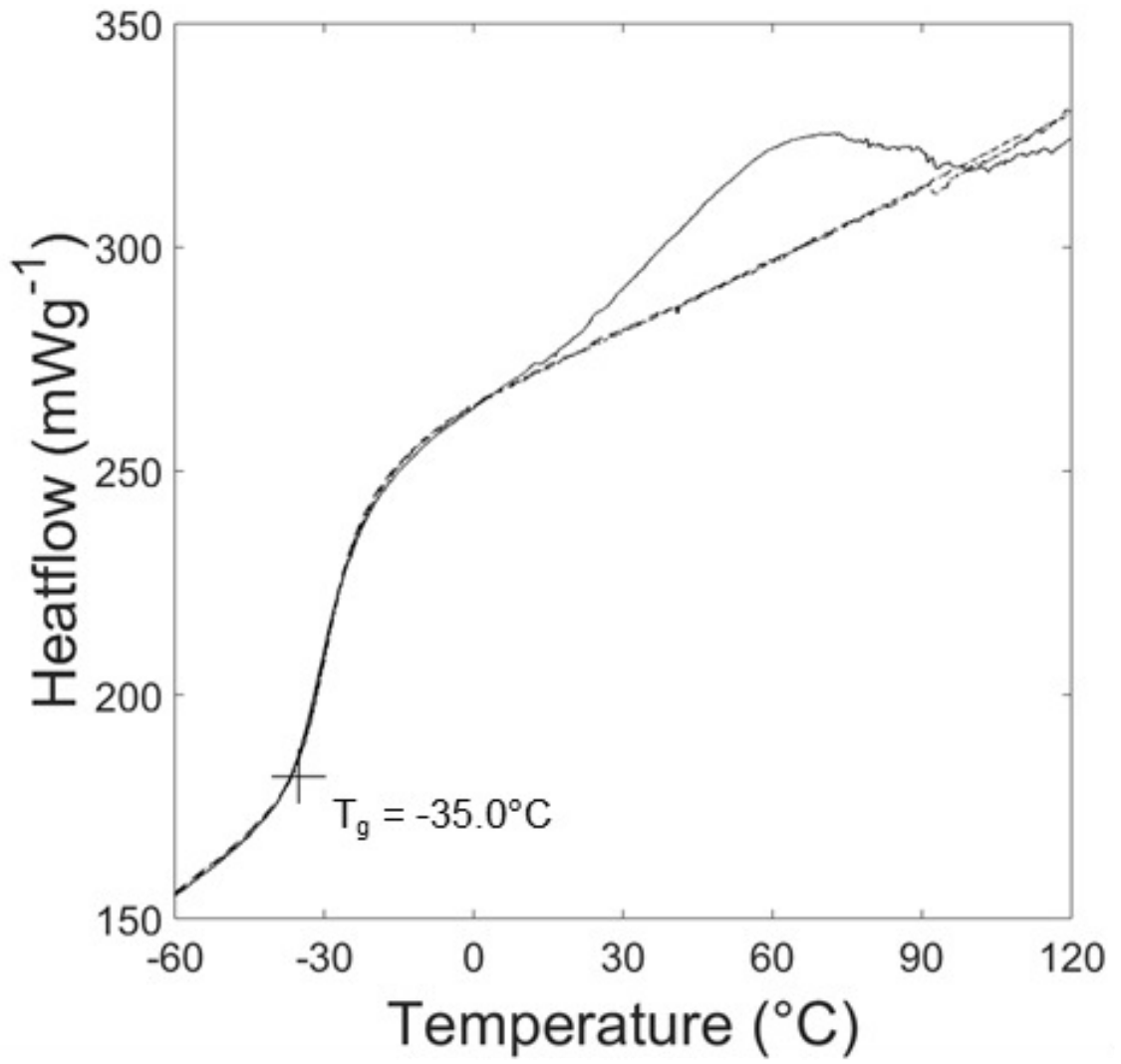
Figure 3.18: DSC (cycles between -75 and 120°C, showing heating following stabilisation only) of PUR30FR samples
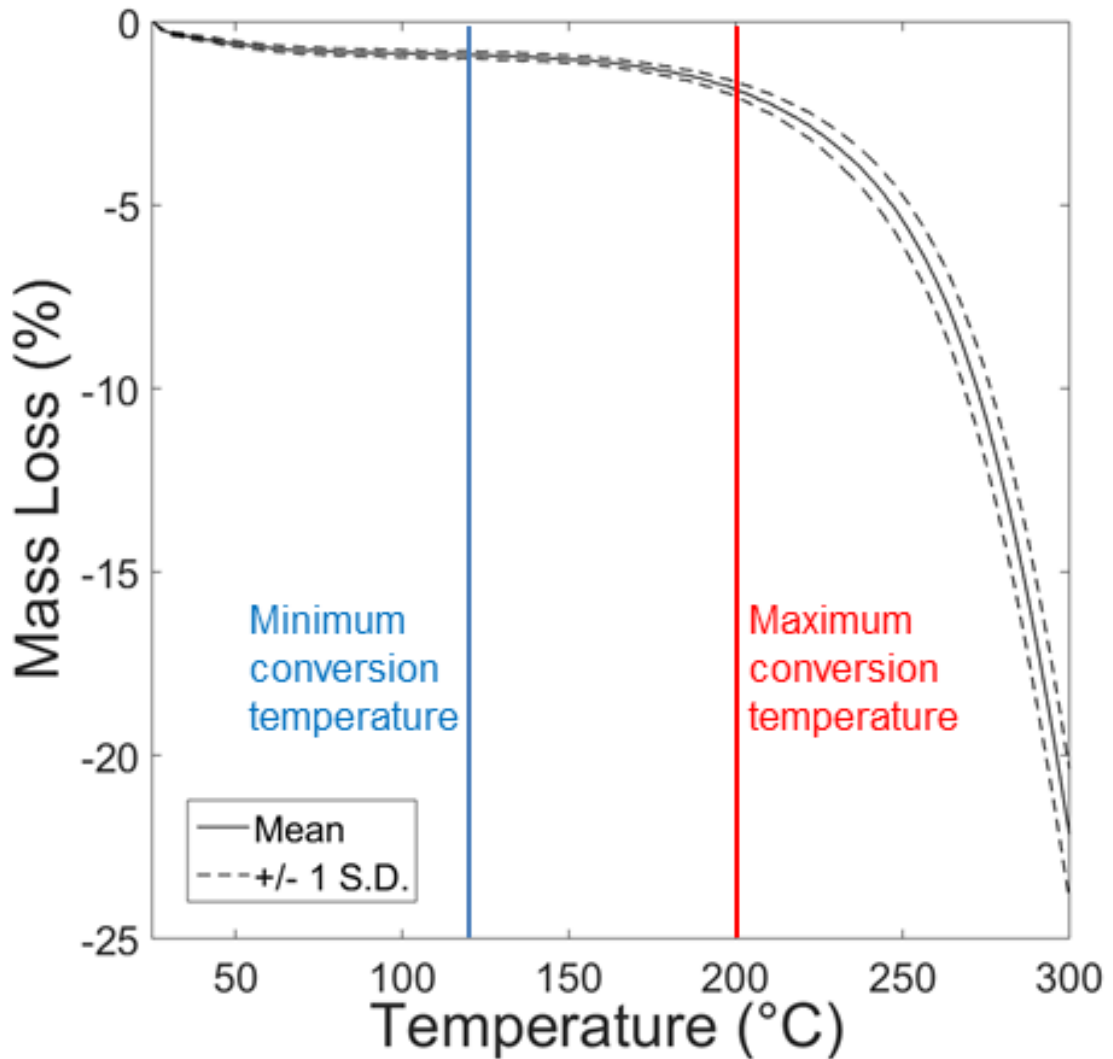
Figure 3.19: TGA of 10-12mg PUR30FR samples

3.4. Analytical model derivation

3.4.1. Developing an isotropic, multi-cellular model

Open cell foam has been described as a 3D dodecahedron with tetragonal symmetry [46], but is often described as a 2D conventional (Figure 3.20) or re-entrant (Figure 3.21) honeycomb, extended in the rise direction [24,26], axis 3. Considering simplified 2D projections of each crystal-like open cell in three orthogonal planes, whereby θ and l are the angle and length of the oblique ribs (equal in each plane), and h is the parallel rib length, the only difference between both vertical planes (parallel to axis 1) and the horizontal planes is the length of the parallel ribs ($h_{13} > h_{12}$). The three-dimensional geometry in Figure 3.20a (or Figure 3.21a) describes both the vertical planes (2-3 and 1-3), and Figure 3.20c (or Figure 3.21c) is the horizontal plane (1-2). The crystal-like assembly of planes 1-2, 1-3 and 2-3 has tetragonal symmetry. The sixth order, four dimensional compliance matrix can be approximated to fourth order, three dimensional terms (note 14, [47]):
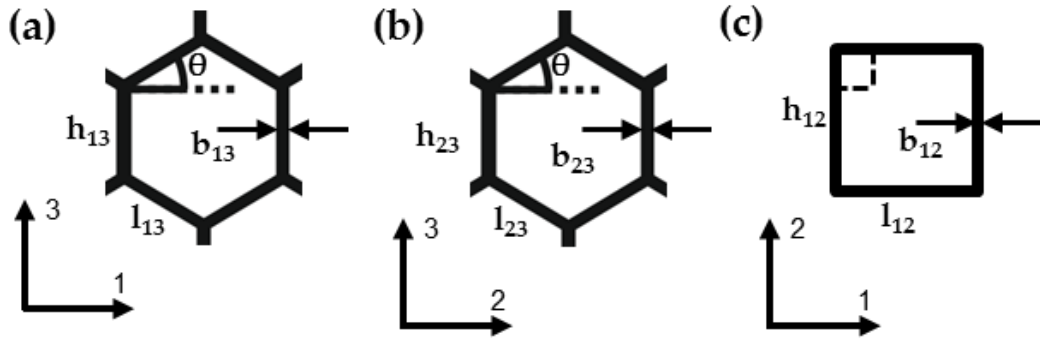
Figure 3.20: Cell geometrical parameters for a typical honeycomb (θ>0) in a) the 1-3 plane (identical to b), the 2-3 plane, 3 parallel to cell rise) and c) the 1-2 plane (θ=0). Parallel rib length is h and l is oblique rib length.
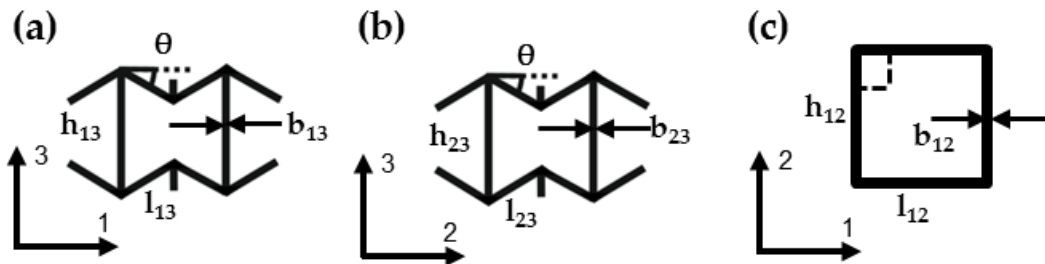
Figure 3.21: Cell geometrical parameters for a re-entrant honeycomb (θ<0) in a) the 1-3 plane (identical to the b), 2-3 plane, 3 parallel to cell rise) and c) the 1-2 plane. Parallel rib length is h and l is oblique rib length.

The cell structure of positive and NPR re-entrant foams was inhomogeneous and non-repeating (Figure 3.6, Figure 3.7), and Young's modulus (Figure 3.13) and Poisson's ratio (Figure 3.10) were isotropic. As in previous work [2,20,48], the effect of open cell foam rise direction was removed following triaxial volumetric compression, likely caused by variable orientation of previously anisotropic cells (Figure 3.6, Figure 3.7). An isotropic model that gives values for elastic constants based upon randomly orientated repeating units (crystals) was previously validated for α-cristobalite [47]. The following section will apply and validate an adapted version of the same isotropic model, assuming the 2D, re-entrant honeycomb models. Reuss (lower) bounds for bulk (K_R) and Shear (G_R) moduli are [49]:

$$K_R = 1/3(S_{11}^* + 2S_{12}^*) \tag{3.4}$$

and:

$$G_R = 5/(4S_{11}^* - 4S_{12}^* + 3S_{44}^*) \tag{3.5}$$

Isotropic aggregate averages for Poisson's ratio (v_v, Equation 3.6) [47] and Young's modulus (E_v, Equation 3.7) [50] are:

$$\nu_R = \frac{(3K_R - 2G_R)}{(6K_R + 2G_R)} \tag{3.6}$$

$$E_R = 2G_R(1 + \nu_R) \tag{3.7}$$

For tetragonal symmetry [49]:

$$S_{11}^* = (2S_{11} + S_{33})/3 \tag{3.8}$$

$$S_{12}^* = (2S_{13} + S_{12})/3 \tag{3.9}$$

$$S_{44}^* = (2S_{44} + S_{66})/3 \tag{3.10}$$

The S_{ij} terms are the coefficients from Hooke's law written in terms of the 3 dimensional stiffness matrix for tetragonal systems (Equation 3.11) [50]:

$$\begin{pmatrix} \varepsilon_1 \\ \varepsilon_2 \\ \varepsilon_3 \\ \gamma_{23} \\ \gamma_{31} \\ \gamma_{12} \end{pmatrix} = \begin{pmatrix} S_{11} & S_{12} & S_{13} & 0 & 0 & 0 \\ S_{21} & S_{11} & S_{13} & 0 & 0 & 0 \\ S_{31} & S_{31} & S_{33} & 0 & 0 & 0 \\ 0 & 0 & 0 & S_{44} & 0 & 0 \\ 0 & 0 & 0 & 0 & S_{44} & 0 \\ 0 & 0 & 0 & 0 & 0 & S_{66} \end{pmatrix} \begin{pmatrix} \sigma_1 \\ \sigma_2 \\ \sigma_3 \\ \tau_{23} \\ \tau_{31} \\ \tau_{12} \end{pmatrix} \tag{3.11}$$

Inputting the terms for the variables in Equation 3.11 ($S_{11} = 1/E_1$, $S_{33} = 1/E_3$, $S_{12} = -\nu_{12}/E_1$, $S_{13} = -\nu_{13}/E_1$, $S_{44} = 1/G_{23}$, $S_{66} = 1/G_{12}$ [50]) into Equations 3.8 - 3.10:

$$S_{11}^* = (2/E_1 + 1/E_3)/3 \tag{3.12}$$
$$S_{12}^* = -(2\nu_{31}/E_3 + \nu_{21}/E_2)/3 \tag{3.13}$$
$$S_{44}^* = (2/G_{31} + 1/G_{12})/3 \tag{3.14}$$

Voigt upper bounds (K_V and G_V) are [49]:

$$K_v = (C_{11}^* + 2C_{12}^*)/3 \tag{3.15}$$

and:

$$G_v = (C_{11}^* - C_{12}^* + 3C_{44}^*)/5 \tag{3.16}$$

Whereby the C_{ij}^* coefficients follow analogous expressions to the S_{ij}^* coefficients (i.e. substituting S for C in Equations 3.8 - 3.10). Similar expressions to those previously applied following Reuss aggregate averaging (Equations 3.6 and 3.7) give Voigt Poisson's ratio and Young's moduli, from Equations 3.15 and 3.16. Voigt-Reuss-Hill bounds (K_H, G_H, E_H and ν_H) are the arithmetic mean of the Reuss and Voigt bounds.

3.4.2. Analytical expressions for the on and off-axis mechanical properties of a hexagonal honeycomb

Values in Equation 3.11 can be calculated through consideration of 2D hexagonal (Figure 3.20) and re-entrant honeycombs (Figure 3.21), and previous analytical expressions [24,26] for Poisson's ratio and Young's modulus due to cell rib stretching, flexure and hinging.

Expressions derived for the 1-3 plane of the hexagonal honeycomb (Figure 3.20a) can be applied for the 2-3 plane (Figure 3.20b) and the equivalent re-entrant honeycomb (Figure 3.21) by changing cell parameters.

Each rib of the 2D honeycombs can be stretched, hinge around a junction and also bend or flex. The force per unit of deformation for each mechanism can be considered as a force constant [24–26], and are described in detail in Chapter 4. Rib stretching is defined by k_s. Noting that the forces responsible for rib hinging and flexure are equal, the respective force constants (k_h and k_f) can be combined as per Equation 3.17 [25]:

$$k_{hf} = \frac{k_h k_f}{k_h + k_f} \tag{3.17}$$

Accordingly, the Poisson's ratio (ν) and Young's modulus (E) expressions for the honeycomb based on the cell geometry (Figure 3.20a, Figure 3.21a) can be adapted from Masters and Evans [24] combining k_h and k_f, Equations 3.18 to 3.21:

$$v_{13} = \frac{sin\theta cos^2\theta \left(\frac{1}{k_{hf}} - \frac{1}{k_s}\right)}{\left(\frac{h_{13}}{l_{13}} + sin\theta\right)\left[\frac{sin^2\theta}{k_{hf}} + \frac{cos^2\theta}{k_s}\right]} \tag{3.18}$$

$$v_{31} = \frac{sin\theta \left(\frac{h_{13}}{l_{13}} + sin\theta\right)\left(\frac{1}{k_{hf}} - \frac{1}{k_s}\right)}{\left[\frac{cos^2\theta}{k_{hf}} + \frac{2\frac{h_{13}}{l_{13}} + sin^2\theta}{k_s}\right]} \tag{3.19}$$

$$E_{1(1-3)} = \frac{cos\theta}{b_{13}\left(\frac{h_{13}}{l_{13}} + sin\theta\right)\left[\frac{sin^2\theta}{k_{hf}} + \frac{cos^2\theta}{k_s}\right]} \tag{3.20}$$

$$E_3 = \frac{\left(\frac{h_{13}}{l_{13}} + sin\theta\right)}{b_{13}cos\theta\left[\frac{cos^2\theta}{k_{hf}} + \frac{2\frac{h_{13}}{l_{13}} + sin^2\theta}{k_s}\right]} \tag{3.21}$$

Where h and l are 'vertical' (aligned along axis 3) and 'oblique' honeycomb rib lengths, respectively, b is the rib thickness, and the subscript '13' applied to the geometrical parameters denotes they are in the 1-3 plane (Figure 3.20). Considering the 1-2 plane, $E_{1(1-2)}$ and $E_{2(1-2)}$ are equal to $E_{1(1-3)}$ (Equation 3.20). The Poisson's ratio ($v_{12} = v_{21}$) are both zero, since flexing and hinging will not occur for on-axis loading and stretching will not incur perpendicular deformation [51,52].

The shear modulus (G_{31}) expression is derived from the shear moduli expressions for each of the individual modes of deformation (Equation 3.22):

$$\frac{1}{G_{31}} = \frac{1}{G_f} + \frac{1}{G_h} + \frac{1}{G_s}$$

(3.22)

Where G_f, G_h and G_s are the rib flexure, hinging and stretching shear moduli, giving Equation 3.23:

$$G_{31} = \left[\frac{b_{13}\left(\frac{h_{13}}{l_{13}}\right)^2\left(1+\frac{2h_{13}}{l_{13}}\right)cos\theta}{k_{hf}\left(\frac{h_{13}}{l_{13}}+sin\theta\right)} + \frac{b_{13}\left(1+\frac{h_{13}}{l_{13}}sin\theta\right)^2}{k_s\left(\frac{h_{13}}{l_{13}}+sin\theta\right)} \right]^{-1}$$

(3.23)

whereby the first term on the right hand side employs the expression for shear modulus due to rib flexure from Gibson and Ashby [26], extended to include rib hinging by acknowledging that the components of applied force causing flexure and hinging, and rib end-to-end displacement directions, are the same for both mechanisms (hence the same individual Poisson's ratio expressions, and Young's moduli expressions which differ only by the respective force constants). The second term on the right hand side of Equation 3.23 is the expression for shear modulus due to rib stretching and is taken from Masters and Evans [24].

Equations for Young's and shear moduli in the 1-2 plane have been previously derived, based on hinging and flexing of cell ribs [52]. Previously equations were for three-dimensional honeycombs rather than the approach used here for the 1-3 and 1-2 planes; separating orthogonal planes. To calculate a similar expression (Equation 3.20) for Young's modulus over small deformations in the 1-2 plane, rib stretching is dominant whereas flexing and hinging are negligible [52]. Therefore;

$$E_{1(1-2)} = \frac{k_s\,l_{12}}{b_{12}h_{12}}$$

(3.24)

The mechanisms which could cause shearing are flexing and/or hinging [52]. For small deformations, the angle between ribs will change (from 90°) by $d\beta$ (Figure 3.22a). Considering hinging which produces shear deformation (of γ) due to a torsional load (τ);

$$G_{12h} = \frac{d\tau_{12}}{d\gamma_{12}} = \frac{dF_1}{l_{12}b_{12}d\beta} = \frac{k_h\,h_{12}}{l_{12}b_{12}}$$

(3.25)

Whereby $dF_1/(h_{12\,x}\,d\beta)$ is the hinging constant k_h. Considering each rib as a beam with a square cross section subject to bending [26], the area of moment (I) is $bt^3/12 = b_{12}{}^4/12$. Beam deflection (δ, Figure 3.22b) is:

$$\delta = \frac{dMh_{12}{}^2}{6E_{s_{12}}I} = \frac{dF_1h_{12}{}^3}{12E_{s_{12}}I}$$

(3.26)

Considering flexing which produces shear deformation (of γ) due to a torsional load (τ);

$$G_{12f} = \frac{d\tau_1}{d\gamma_1} = \frac{dF_1 h_{12}}{l_{12} b_{12} \delta} = \frac{h_{12}}{l_{12} b_{12}} \frac{12 E_{s12} I}{h_{12}} = \frac{k_{f12} h_{12}}{l_{12} b_{12}}$$

(3.27)

Equations 3.25 and 3.27 can be combined using equation 3.22, with force constants (k_h and k_f) combined as per equation 3.17:

$$G_{12} = \frac{h_{12}}{l_{12} b_{12}} k_{hf_{12}}$$

(3.28)
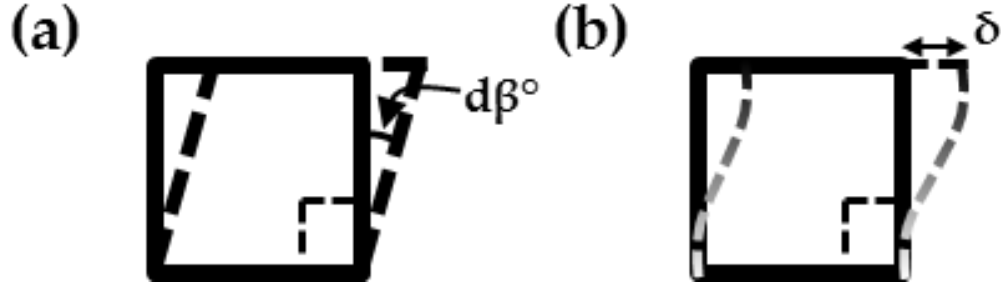
Figure 3.22: Cell rib a) hinging and b) flexing in the 1-2 plane. Dashed ribs show deformed positions

3.4.3. Force constants assuming elastic cell rib material

Expressions relating force constants to material properties and cell rib geometry (Figure 3.20, Figure 3.21) have been developed previously [24]:

$$k_s = \frac{E_s w b}{l}$$

(3.29)

$$k_s^{h_{13}} = \frac{E_s w b}{h} = \frac{E_s w b}{l} \frac{l}{h} = k_s \frac{l}{h}$$

(3.30)

$$k_f = \frac{E_s w b^3}{l^3}$$

(3.31)

$$k_h = \frac{G_s w b}{l} \qquad \text{(Hinging via shearing of junction)}$$

(3.32)

$$k_h = \frac{E_s w b^3}{6 l^2 q} \qquad \text{(Hinging via local bending at junction)}$$

(3.33)

where E_s and G_s are the Young's and shear moduli of the rib material, w is the rib depth, and q is the axial length of the curved hinge.

Dividing Equation 3.17 by 3.29 and substituting Equations 3.31and 3.33, the expression for k_{hf}/k_s when hinging occurs via junction shearing is:

$$\frac{k_{hf}}{k_s} = \frac{1}{\left(\frac{l}{b}\right)^2 + \frac{E_s}{G_s}}$$

(3.34)

Similarly, the expression for k_{hf}/k_s when hinging occurs via junction bending is:

$$\frac{k_{hf}}{k_s} = \frac{b^2}{l^2 + 6 l q}$$

(3.35)

The minimum value of k_{hf}/k_s in Equation 3.35 occurs when $q \to l$:

$$\frac{k_{hf}}{k_s} = \frac{b^2}{7 l^2}$$

(3.36)

Given that $E_{1(1-2)}$ and $E_{1(1-3)}$ are equal, the value for effective Young's modulus of the oblique ribs that can move both in and out of plane can be calculated using Equation 3.29. The hinging mechanism and force constant is not expected to change, but k_f (and therefore k_{hf}) will change as E_s changes to E_{s1-2}, according to Equation 3.31.

3.4.4. Rationale for choice of force constant values used in predictive model

A value of b/l = 0.2 was arbitrarily used, but appears sensible (Figure 3.6, Figure 3.7). The rib material was assumed to be isotropic with a Poisson's ratio ν_s = 0.25, such that E_s/G_s = $2(1 + \nu_s)$ = 2.5. Substituting these values into Equations 3.34 and 3.36, the approximate range for k_{hf}/k_s is between 0.006 and 0.036 – i.e. approximately an order of magnitude difference between the upper and lower limits.

For the purposes of these calculations, $0.006 < k_{hf}/k_s < 0.036$ was employed to show the effect of reasonable changes to the cell rib material. From Equations 3.27 and 3.29, $K_f/K_s = (b/l)^2 = (0.2)^2 = 0.04$ was used. Hence from Equation 3.17, k_f/k_h and k_s/k_h could be calculated for each value of k_{hf}/k_s.

3.5. Analytical model results

As k_{hf}/k_s increases from 0.006 to 0.036, Poisson's ratios (Figure 3.23) and Young's modulus (Figure 3.24) of individual re-entrant honeycomb cells both change. Shear modulus also increases with k_{hf}/k_s (Figure 3.25) in both planes; more dramatically in the 1-2 plane where Shear modulus is dependent upon hinging and flexing only (Equation 3.28).
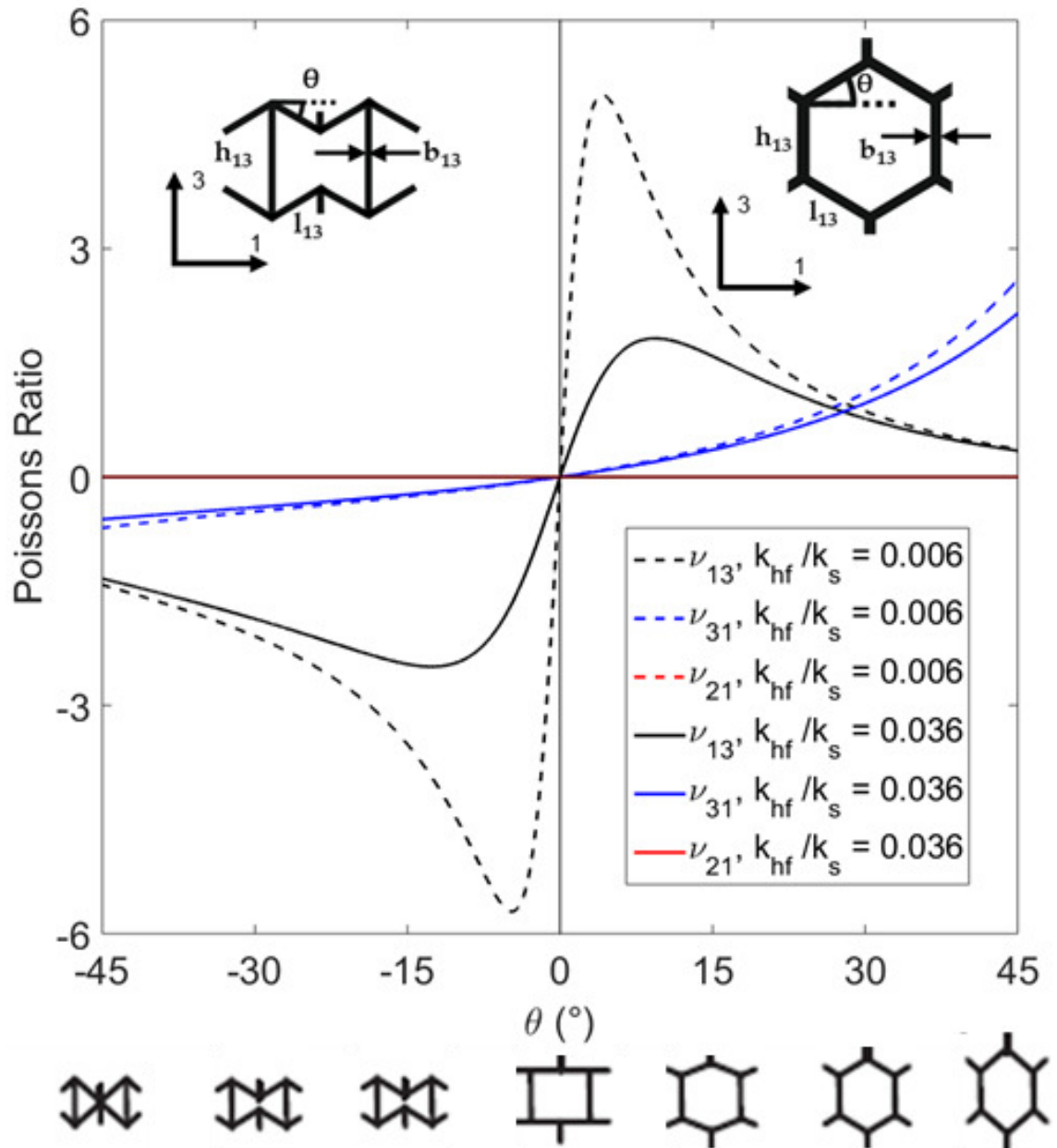
Figure 3.23: Predicted Poisson's ratios ν_{13} (Equation 3.18), ν_{31} (Equation 3.19) and ν_{21} (Equation 3.19) vs cell wall angle (θ_{13}) for maximum (0.036) and minimum (0.006) values of k_{hf}/k_s. Schematic shows cell parameters in the 1-3 plane, approximate cell shapes are shown along x axis for each angle of θ.
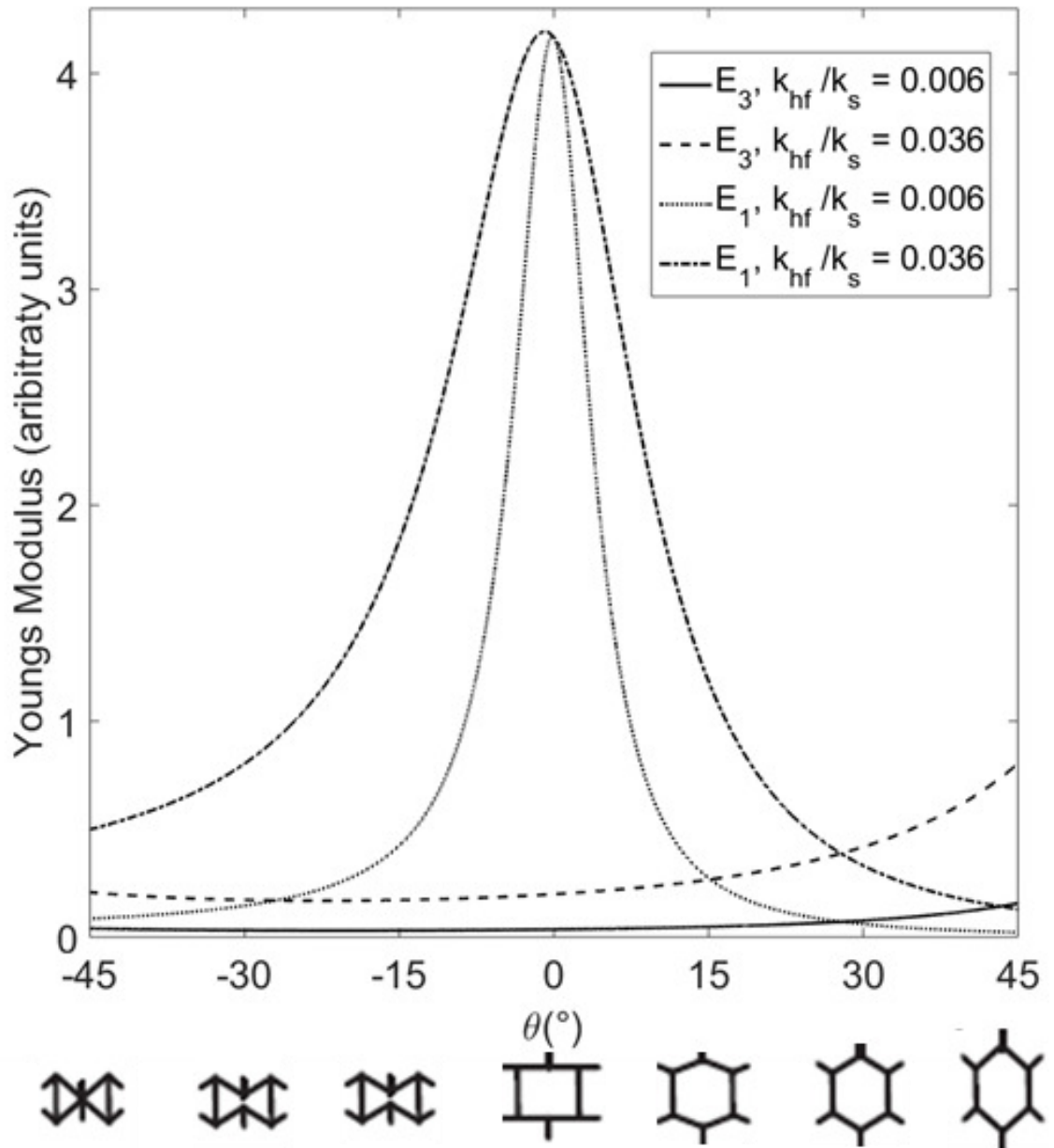
Figure 3.24: Predicted Young's modulus E_1 (Equation 3.20) and E_3 (Equation 3.21) vs cell wall angle (θ_{13}) for maximum (0.036) and minimum (0.006) values of k_{hf}/k_s.
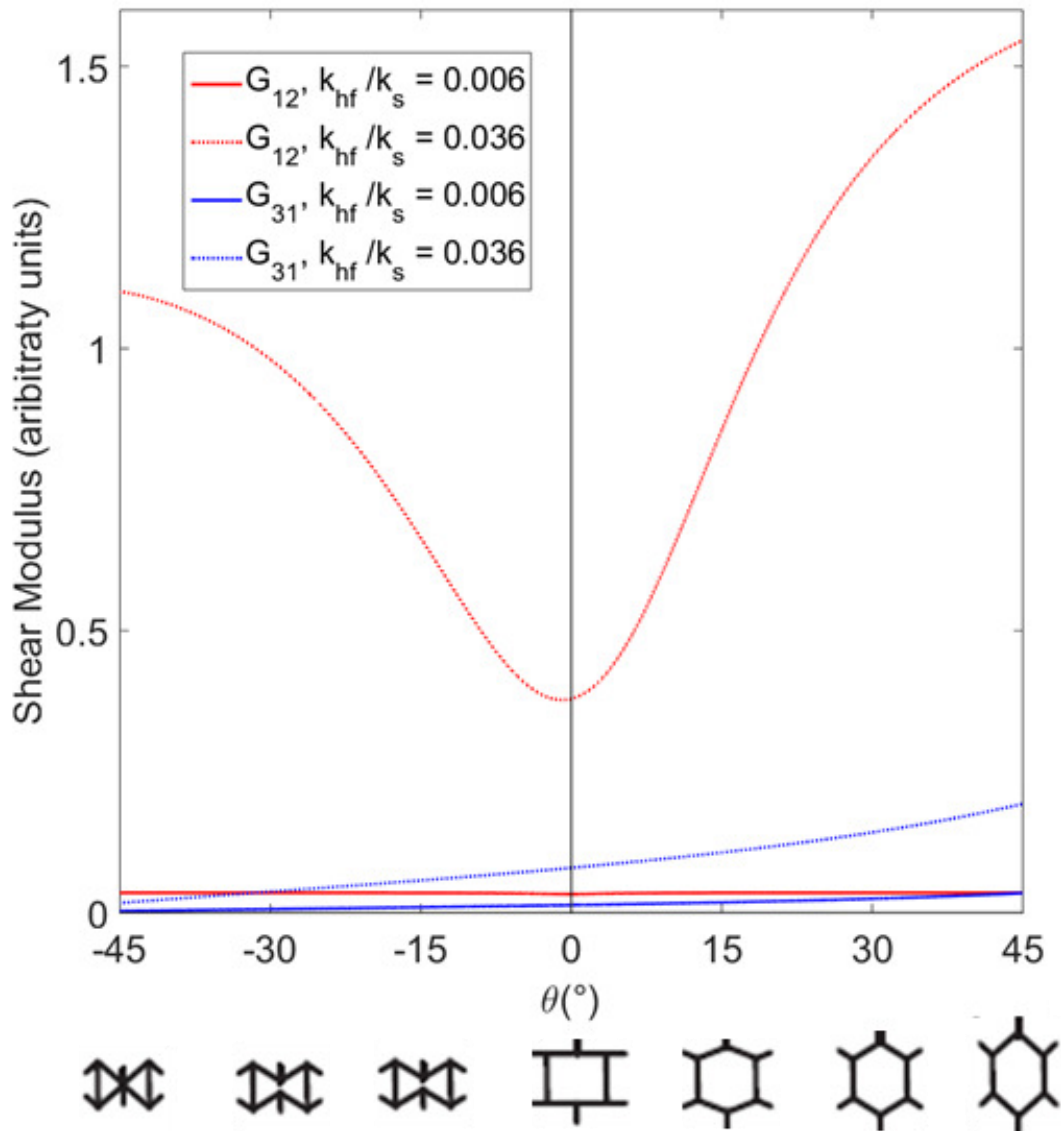
Figure 3.25: Predicted shear moduli G_{31} (Equation 3.23) and G_{12} (Equation 3.28) vs cell wall angle (θ_{13}) for maximum (0.036) and minimum (0.006) values of k_{hf}/k_s.

Plotting the calculated values for isotropic Poisson's ratio (Figure 3.26) and Young's modulus (Figure 3.24) for values within the approximate range $0.006 < k_{hf}/k_s < 0.036$ agrees experimental findings. According to Equation 3.32, unless the PU's Poisson's ratio and the ratio of Shear to Young's modulus change (Equation 2.1, Chapter 2, Page 22), the ratio between force constants would remain constant. As increased heat exposure during conversion increased the fixing of imposed structure, the population and strength of converted foam hydrogen bonding (Figure 3.16b & c) increased. One of two unmeasured possibilities could have changed the ratio of Shear and Young's modulus: i) The PU in the foam could have undergone a marginal amount of crystallisation, reducing the Poisson's ratio of the previously (predominantly) rubbery, amorphous PU (Figure 3.16a). ii) Changes to the PU could have been greater where the largest changes to cell structure occur, around junctions or newly formed kinks. Stiffer hinges and

kinks would be likely to reduce the amount of hinging more than the amount of stretching, effectively increasing k_{hf}/k_s. As rib rigidity increases, Poisson's ratio and Young's modulus also increase (Figure 3.26).
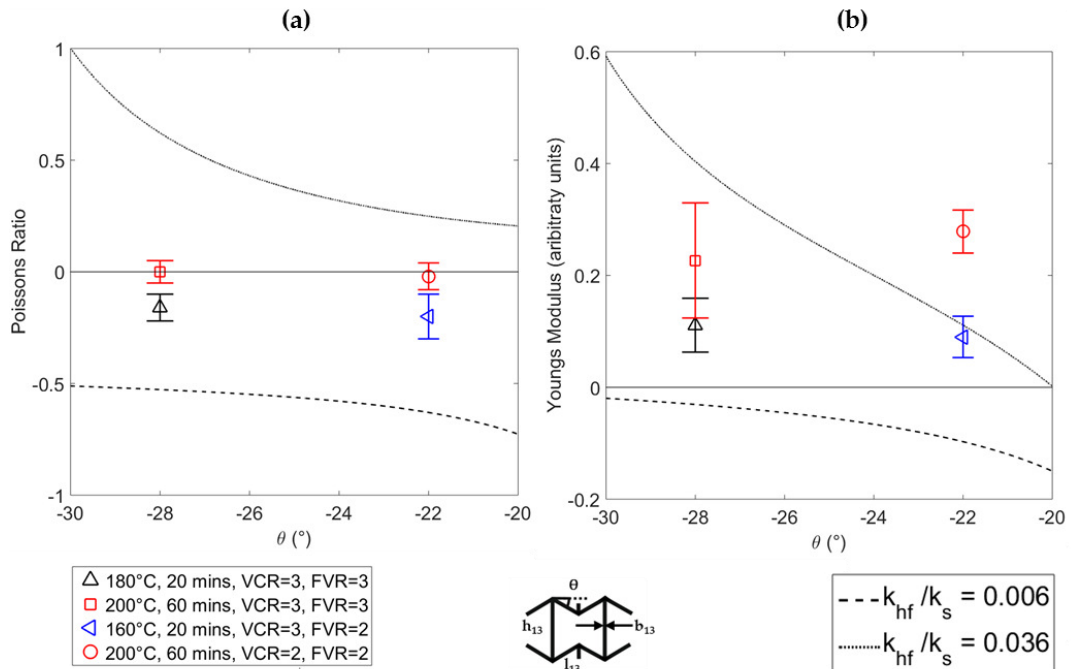

Figure 3.26: Predicted Isotropic a) Poisson's ratio and b) Young's modulus vs re-entrant cell wall angle ($\theta<0$) over the ballpark range of k_{hf}/k_s. Schematic below shows cell parameters. Legends below shows sample conversion conditions and values for k_{hf}/k_s. Sample values (mean across all orientation in tension and compression) are included (Figure 3.10 & Figure 3.11). Young's modulus values (Figure 3.13 & Figure 3.14, mean tensile and compressive values in all orientations) were normalised by dividing a mean value for compressive and tensile modulus by the modulus of the 180 °C, 20 minute sample then multiplying by the calculated value at θ -28°, $k_{hf}/k_s = 0.036$.

The analytical Poisson's ratio and Young's modulus (Figure 3.26) are more extreme than those found experimentally. Young's modulus is also negative for $k_{hf}/k_s = 0.006$, suggesting an unstable/collapsing region. A range of cell rib lengths, thicknesses and angles are evident in both the converted and uncovered foam (Figure 3.6 and Figure 3.7), meaning parameters such as k_{hf}/k_s are likely to change between cells. The combined properties are, therefore, likely to be a combination of the upper and lower analytical values of Poisson's ratio; tending towards the lower line for lesser heated foam and the upper line for foam subject to more heating, as shown by markers representing experimental values in Figure 3.26.

3.6. Discussion

The effects of conversion time and temperature on Young's modulus and Poisson's ratio in thermo-mechanical conversions broadly agree with previous findings [11,20,22]. Samples

converted under conditions which underwent full dimensional recovery (FVR = 1) after one week (T ≤ 140°C for 20 minutes) had similar positive Poisson's ratios (Figure 3.10 & Figure 3.11) and reasonably similar Young's modulus (Figure 3.13 & Figure 3.14) to the unconverted foam.

Measured FVR and NPR values, achieved over time following a single compression-heating process, without any Recovery phase, are very similar to the FDR (final density ratio) and NPR values reported in 'blocked shape memory' foams [8]. The latter foams were produced using a multi-stage repeated cycle process of auxetic conversion (compression-heating) and reconversion (unconstrained heating [8]). The mass loss data in Figure 3.19 indicates the FDR and FVR measures of re-expansion are likely to be similar (i.e. only marginal, ~1%, difference) at these temperatures.

Some foams exhibited shape memory in the (unconstrained re-heating) Recovery phase (150 ≤ T ≤ 190°C for 20 minutes, 120 ≤ T ≤ 170°C for 60 minutes, 120 ≤ T ≤ 140°C for 180 minutes, Figure 3.4b). The foams converted at 140°C for 180 minutes show 'blocked shape memory' as described previously [8], corresponding to nominal dimensional recovery (Figure 3.4b) but retention of NPR (Figure 3.11) following re-heating. The FVR of 1.8 and NPR of ~-0.2 of the blocked shape memory foams produced here in a single shape memory cycle are again very similar to the FDR (~1.5) and NPR (~-0.2) values reported in the blocked shape memory foams, previously produced using three to five cycles of thermo-mechanical conversion and reconversion by unconstrained heating [8].

The foams converted at 160°C for 180 minutes actually increase their magnitude of NPR, particularly in compression (Figure 3.10 & Figure 3.11), with a very small amount of re-expansion/shape memory (FVR = 2.8) following unconstrained re-heating. Therefore unconstrained re-heating can be employed to achieve either blocked shape memory in a single cycle (retaining NPR with nominal heat-induced dimensional recovery) or increased magnitude NPR with (near) dimensional stability.

At high conversion temperatures and/or longer times (T = 200°C for 20 minutes, T ≥ 180°C for 60 minutes, T ≥ 160°C for 180 minutes) the samples exhibited dimensional stability to unconstrained re-heating (Figure 3.4b), and possessed near-zero or positive and low negative Poisson's ratios in compression and tension, respectively (Figure 3.10). Young's moduli increased with further heat exposure (Figure 3.13) but the stress vs strain relationship remained quasi-linear in compression (Figure 3.12a), typical of re-entrant structures (Figure 3.6d & e, [2,53]). The near-zero Poisson's ratios and increased Young's moduli agree with previous work at high conversion temperatures and heating times [3,30].

The applied VCR affected neither time nor heat dependent stability (Figure 3.4), and only produced small changes in Poisson's ratio and Young's modulus. The compressive Poisson's ratio of samples fabricated with a VCR of two was close to zero or marginally negative in compression (Figure 3.11), in agreement with previous work using the same foam [32,33]. Samples fabricated with a VCR of three that partially sprung back after a week to an FVR close to two (130°C, 180 minutes, 140°C, 60 minutes, 160°C, 20minutes, Figure 3.4)) exhibited compressive and tensile NPR (~-0.2, Figure 3.11) but the same compressive and tensile Young's moduli and FVR as samples fabricated with a VCR of two (140°C for 60 minutes, ~40 kPa, Figure 3.14). Extensive heat exposure caused large increases in both Poisson's ratio (Figure 3.10 & Figure 3.11) and Young's modulus (Figure 3.13 & Figure 3.14) whether applied VCR was two or three. Increasing heat-exposure, therefore, provides a route to produce additional combinations of characteristics.

The Poisson's ratios of converted foams span positive and negative values (~-0.2 to 0.5, Figure 3.10), although in foams which retained compression the highest Poisson's ratios are close to zero. Select positive and negative Poisson's ratio re-entrant samples (i.e. VCR 3, 140 or 200°C, 180 minutes) were iso-density (Figure 3.4a), isotropic (Figure 3.10 & Figure 3.13) and had quasi-linear stress vs strain (Figure 3.12) and transverse vs axial strain (Figure 3.9) up to 10% tension or compression, a requirement of Aim 1 and a pre-requisite to Aim 2 (Chapter 1, Page 5). Near zero Poisson's ratio samples fabricated with a VCR of two and heated for 60 minutes at 200°C had the same FVR (of two) as samples with NPR of ~-0.2 fabricated with a VCR of 3 and heated for 20 minutes at 160 °C.

Glass transition temperature did not change following heat cycles up to 120°C (Figure 3.26), but samples went through a broad exothermic transition on their first cycle (only). The broad transition occurred at a lower temperature (between ~30 and 90°C) than increased hydrogen bonding was identified by FTIR (>160°C, Figure 3.16), and the exothermic event did not fix samples' VCR after a week (Figure 3.4a). The transition could be related to a reorganisation of polymer chains after evaporation of water (as evidenced by mass loss in TGA between 35-90°C), through a crystallisation-like process though there is as yet neither other evidence to support this by XRD nor any evidence of an endothermic evaporation process by DSC. A similar change has been shown between cycles of DSC [12], simply attributed to thermal history. Mass loss evident in TGA suggested degradation was present but not below 150°C (Figure 3.19). As samples adopt their VCR (> 150°C, 20 minutes, Figure 3.4a), FTIR identified increases in the strength and population of hydrogen bonding (Figure 3.16) and sample Poisson's ratio reduces towards zero/negative values (Figure 3.7a & b).

FTIR shows the hydrogen bonding nature changes most as heat exposure increases above 160°C for 20 minutes (Figure 3.16). Changes were only evident under FTIR as samples adapt NPR (Figure 3.10) and their imposed VCR (Figure 3.4a), meaning that the onset of changes in mechanical and structural characteristics correlate with changes in polymeric bonding. With increasing heat exposure, the N-H stretch band (3200 to 3300 cm^{-1} Figure 3.16a) shifted to lower wavenumbers and increased in intensity, while the intensity of the band due hydrogen bonded C=O urea groups also increased (Figure 3.16b, ~1640 cm^{-1}, [54]). The unchanging band at 1727 cm^{-1} associated with free urethane groups [14,35] strongly indicates that hydrogen bonding changes are associated with urea rather than urethane groups.

Hydrogen bonded N-H has previously been suggested to fix PU foam's imposed re-entrant structure following similar amounts of heating and compression [8,14], but the only previously measured spectra following thermo-mechanical conversions show different unconverted and converted spectra to the PU used in this study [8]. Figure 3.16 provides evidence of a continually increasing hydrogen bond interaction between N-H and C=O of urea within the hard segments, which correlates with changing mechanical characteristics; increasing Poisson's ratio (Figure 3.10)and Young's modulus (Figure 3.13), and also structural characteristics; increasing shape fixing (Figure 3.4 & Figure 3.5) and reducing recovery (Figure 3.5) following increased heat exposure.

An interaction between the soft segment C-O-C polyol and N-H of either urea or urethane is possible, but changes to the C-O-C stretch band (~1077 cm^{-1}) were only present following conversion at 200°C for 180 minutes and are probably caused by degradation. The minor decreases in the Amide II (1531 cm^{-1}) and CH$_2$ stretch bands (2912 cm^{-1}), the broad underlying intensity increase observed between 3600 to 2400 cm^{-1} (Figure 3.16) in the same sample and significant mass loss at and above ~200°C during TGA (Figure 3.19) support polymer degradation [8,14] during the 200°C, 180 minute conversion.

The findings are summarised in Table 3.1, which describes correlated trends. As hydrogen bonding caused by increased heat exposure during conversion causes greater shape fixing, Poisson's ratio and Young's modulus reduce to minimum values (~-0.2 and ~30 kPa respectively), before Poisson's ratio increases and plateaus around zero, and Young's modulus increases to a maximum of ~120 kPa.

Table 3.1: Summary of correlated findings

Temperature	Peak changes & shifts (Figure 3.16)	FVR, which changes cell structure (Figure 3.4)	Poisson's ratio (Figure 3.10)	Young's modulus (Figure 3.13)
<140°C, 20 minutes 120°C, 60 mins	Negligible change from UC	Negligible change from UC (FVR(a) = 1)	Negligible change from anisotropic UC (Figure 3.11)	Negligible change from anisotropic UC (Figure 3.14)
150°C, 20 mins 130°C, 60 mins	Minor N-H increase	FVR(a) ~ 1 to 1.5 FVR(b) ~ 1	Minor reduction towards 0	Minor reduction to ~30 kPa, become approximately isotropic
160-180°C, 20 mins, 140 -160°C, 60 mins 120-140°C, 180 mins	N-H and H-Bonded urea increase	FVR (a) ~ 1.5 to 3 FVR (b) ~ 1 to 2.5	Minor increase (to ~-0.1) or plateau	Increase to ~ 50 kPa (plateau in tension)
180 -200°C, 20 mins, 160 -180°C, 60 mins 140 -160°C, 180 mins	N-H and H-Bonded urea increase	FVR (a) ~ 2.5 to 3 FVR (b) ~ 2 to 3	Increase toward ~ 0	Increases to ~ 70 kPa
180 - 200°C, 60 mins 160 -180°C, 180 mins	N-H and H-Bonded urea increase	FVR (a) ~ 3 FVR (b) ~ 3	Plateau at ~ 0	Increases to ~ 100 kPa
180 -200°C, 180 mins	CH$_2$ & Amide II decrease & shift COC decrease & shift	FVR (a) ~ 3 FVR (b) ~ 3	Plateau at ~ 0	Increases to ~ 120 kPa

The increase to a positive/near zero Poisson's ratio and increased Young's modulus can be explained by changes in force constants, within reasonable limits for k_{hf}/k_s (Figure 3.26). Increased strength and population of hydrogen bonding (Figure 3.16) around rib junctions and kinks could increase rigidity, and with the increase in rigidity an increase in Poisson's ratio and increased Young's modulus is expected (Figure 3.26). Changing deformation mechanisms have been show previously in a simple 2D material model. The harder junctions actually increased cell rotation and the magnitude of NPR [55], but the structure and original deformation mechanisms were different to the foam tested and modelled in this study. The Poisson's ratio and Young's moduli of samples cover a smaller range than predicted. The model shows upper and lower limits for k_{hf}/k_s, whereas micro-ct and microscopy (Figure 3.6 and Figure 3.7) showed that all tested foams consisted of a range of cell dimensions which are likely to cause k_{hf}/k_s to lie between the upper and lower limits, tending towards the upper limits as heat exposure was increased (Figure 3.26). The model, therefore, predicted more extreme values than experimental data.

3.7. References

1. Duncan O, Clegg F, Essa A, Bell AMT, Foster L, Allen T, et al. Effects of Heat Exposure and Volumetric Compression on Poisson's Ratios, Young's Moduli, and Polymeric Composition During Thermo-Mechanical Conversion of Auxetic Open Cell Polyurethane Foam. Phys Status Solidi. 2018.1800393.

2. Lakes RS. Foam Structures with a Negative Poisson's Ratio. Science (80-). 1987.235(4792). 1038–40.

3. Chan N, Evans KE. Fabrication methods for auxetic foams. J Mater Sci. 1997.32. 5945–53.

4. Friis, E. A., Lakes, R. S., and Park JB. Negative Poisson's ratio polymeric and metallic materials. J Mater Sci. 1988.23. 4406–14.

5. Brandel B, Lakes RS. Negative Poisson's ratio polyethylene foams. J Mater Sci. 2001.36(24). 5885–93.

6. Dai Z, Weng C, Liu L, Hou Y, Zhao X, Kuang J, et al. Multifunctional Polymer-Based Graphene Foams with Buckled Structure and Negative Poisson's Ratio. Sci Rep. 2016.6(August). 1–9.

7. Chiang FP, Uzer G. Mapping full field deformation of auxetic foams using digital speckle photography. Phys Status Solidi Basic Res. 2008.245(11). 2391–4.

8. Boba K, Bianchi M, McCombe G, Gatt R, Griffin AC, Richardson RM, et al. Blocked shape memory effect in negative Poisson's ratio polymer metamaterials. ACS Appl Mater Interfaces. 2016. acsami.6b02809.

9. Scarpa F, Giacomin J, Zhang Y, Pastorino P. Mechanical performance of auxetic polyurethane foam for antivibration glove applications. Cell Polym. 2005.24(5). 253–68.

10. Bianchi M, Scarpa F, Banse M, Smith CW. Novel generation of auxetic open cell foams for curved and arbitrary shapes. Acta Mater. 2011.59(2). 686–91.

11. Bianchi M, Scarpa FL, Smith CW. Stiffness and energy dissipation in polyurethane auxetic foams. J Mater Sci. 2008.43(17). 5851–60.

12. Bianchi M, Scarpa F, Smith CW. Shape memory behaviour in auxetic foams: Mechanical properties. Acta Mater. 2010.58(3). 858–65.

13. Bianchi M, Scarpa F, Smith CW, Whittell GR. Physical and thermal effects on the shape memory behaviour of auxetic open cell foams. J Mater Sci. 2010.45(2). 341–7.

14. Li Y, Zeng C. On the successful fabrication of auxetic polyurethane foams: Materials requirement, processing strategy and conversion mechanism. Polym (United Kingdom). 2016.87. 98–107.

15. Wang YC, Lakes R, Butenhoff A. Influence of Cell Size on Re-Entrant Transformation of Negative Poisson's Ratio Reticulated Polyurethane Foams. Cell Polym. 2001.20(4–6). 373–85.

16. Li Y, Zeng C. Room-Temperature, Near-Instantaneous Fabrication of Auxetic Materials with Constant Poisson's Ratio over Large Deformation. Adv Mater. 2016.28(14). 2822–6.

17. Grima JN, Attard D, Gatt R, Cassar RN. A novel process for the manufacture of auxetic foams and for their re-conversion to conventional form. Adv Eng Mater. 2009.11(7). 533–5.

18. Lisiecki J, Błazejewicz T, Kłysz S, Gmurczyk G, Reymer P, Mikułowski G. Tests of polyurethane foams with negative Poisson's ratio. Phys Status Solidi Basic Res. 2013.250(10). 1988–95.

19. Chan N, Evans KE. Microscopic examination of the microstructure and deformation of conventional and auxetic foams. J Mater Sci. 1997.2. 5725–36.

20. Chan N, Evans KE. The mechanical properties of conventional and auxetic foams. Part I: compression and tension. J Cell Plast. 1999.35(2). 130–65.

21. Choi JB, Lakes RS. Nonlinear properties of polymer cellular materials with a negative Poisson's ratio. Mater Sci. 1992.27. 4678–84.

22. Chan N, Evans KE. Indentation resilience of conventional and auxetic foams. J Cell Plast. 1998.34. 231–60.

23. Gatt R, Attard D, Manicaro E, Chetcuti E, Grima JN. On the effect of heat and solvent exposure on the microstructure properties of auxetic foams: A preliminary study. Phys Status Solidi Basic Res. 2011.248(1). 39–44.

24. Masters IG, Evans KE. Models for the elastic deformation of honeycombs. Compos Struct. 1996.35(4). 403–22.

25. Alderson A, Evans KE. Modelling concurrent deformation mechanisms in auxetic microporous polymers. J Mater Sci. 1997.32(11). 2797–809.

26. Gibson LJ, Ashby MF. Cellular solids. Structure and properties. **1997**. 67, 176-183, 259-264, 286, 498 p.

27. Yao Y, Luo Y, Xu Y, Wang B, Li J, Deng H, et al. Fabrication and characterization of shape memory

polystyrene foams. Compos Part B Eng. 2018.152. 1–7.

28. Bianchi M, Frontoni S, Scarpa F, Smith CW. Density change during the manufacturing process of PU-PE open cell auxetic foams. Phys Status Solidi Basic Res. 2011.248(1). 30–8.

29. Ge C. A comparative study between felted and triaxial compressed polymer foams on cushion performance. J Cell Plast. 2013.49(6). 521–33.

30. Najarian F, Alipour R, Shokri Rad M, Nejad AF, Razavykia A. Multi-objective optimization of converting process of auxetic foam using three different statistical methods. Meas J Int Meas Confed. 2018.119(August 2017). 108–16.

31. Alderson A, Davies PJ, Alderson KIML, Smart GM. The Effects of Processing on the Topology and Mechanical Properties of Negative Poisson's Ratio Foams. Proc IMECE2005 2005 ASME Int Mech Eng Congr Expo Proc IMECE200. 2005. 1–8.

32. Allen T, Shepherd J, Hewage TAM, Senior T, Foster L, Alderson A. Low-kinetic energy impact response of auxetic and conventional open-cell polyurethane foams. Phys Status Solidi Basic Res. 2015.9. 1–9.

33. Duncan O, Foster L, Senior T, Alderson A, Allen T. Quasi-static characterisation and impact testing of auxetic foam for sports safety applications. Smart Mater Struct. 2016.25(5). 054014.

34. Reghunadhan A, Thomas S. Polyurethanes. In: Polyurethane Polymers. Amsterdam, The Netherlands: Elsevier Inc.; **2017**. p. 1–16.

35. Teo L-S, Chen C-Y, Kuo J-F. Fourier Transform Infrared Spectroscopy Study on Effects of Temperature on Hydrogen Bonding in Amine-Containing Polyurethanes and Poly(urethane−urea)s. Macromolecules. 1997.30(6). 1793–9.

36. de HASETH JA, Andrews JE, McClusky J V., Priester RD, Harthcock MA, Davis BL. Characterization of Polyurethane Foams by Mid-Infrared Fiber / FT-IR Spectrometry *. Appl Spectrosc. 1993.47(2).

37. Kim BH, Yoon K, Moon DC. Thermal degradation behavior of rigid and soft polyurethanes based on methylene diphenyl diisocyanate using evolved gas analysis-(gas chromatography)-mass spectrometry. J Anal Appl Pyrolysis. 2012.98. 236–41.

38. Grima JN, Attard D, Gatt R. A novel process for the manufacture of auxetic foams and for the conversion of auxetic foam to conventional form (WO 2010049511 A2). 2010. 1–5.

39. Mather PT, Luo X, Rousseau IA. Shape Memory Polymer Research. Annu Rev Mater Res. 2009.39(1). 445–71.

40. Phillips N, Hassan GM, Dyskin A, Macnish C, Pasternak E. Digital image correlation to analyze nonlinear elastic behavior of materials. Proc - Int Conf Image Process ICIP. 2018.2017–Septe.

41. Sanami M, Alderson A, Alderson KL, McDonald S a., Mottershead B, Withers PJ. The production and characterization of topologically and mechanically gradient open-cell thermoplastic foams. Smart Mater Struct. 2014.23(5). 055016.

42. Lee HS, Wang YK, Hsu SL. Spectroscopic Analysis of Phase Separation Behavior of Model Polyurethanes. Macromolecules. 1987.20(9). 2089–95.

43. Jiao L, Xiao H, Wang Q, Sun J. Thermal degradation characteristics of rigid polyurethane foam and the volatile products analysis with TG-FTIR-MS. Polym Degrad Stab. 2013.98(12). 2687–96.

44. Rege SU, Yang RT. A novel FTIR method for studying mixed gas adsorption at low concentrations: H2O and CO2on NaX zeolite and γ-alumina. Chem Eng Sci. 2001.56(12). 3781–96.

45. Herrera M, Matuschek G, Kettrup A. Thermal degradation of thermoplastic polyurethane elastomers (TPU) based on MDI. Polym Degrad Stab. 2002.78(2). 323–31.

46. Evans KE, Nkansah MA, Hutchinson IJ. Auxetic foams: modelling negative Poisson's ratios. Acta Metall Mater. 1994.42(4). 1289–94.

47. Yeganeh-Haeri A, Weidner DJ, Parise JB. Elasticity of agr-Cristobalite: A Silicon Dioxide with a Negative Poisson's Ratio. Science (80-). 1992.257(5070). 650–2.

48. Smith CW, Grima JN, Evans KE. Novel mechanism for generating auxetic behaviour in reticulated foams: Missing rib foam model. Acta Mater. 2000.48(17). 4349–56.

49. Hill R. The Elastic Behaviour of a Crystalline Aggregate. Proceeding Phys Soc Sect A. 1952. 349–54.

50. Roark RJ, Young WC. Formulas for stress and strain. McGraw-Hill, USA; **2012**. 20-22, 48-50 p.

51. Grima JN, Caruana-Gauci R, Attard D, Gatt R. Three-dimensional cellular structures with negative Poisson's ratio and negative compressibility properties. Proc R Soc A Math Phys Eng Sci. 2012.468(2146). 3121–38.

52. Attenborough F. The modelling of network polymer (PhD Thesis, University of Liverpool). **1997**.

53. Gibson LJ, Ashby MF, Schajer GS, Robertson CI. The mechanics of two-dimensional cellular

materials. Proc R Soc London A Math Phys Sci. 1982.382. 25–42.

54. A. Rudin. The Elements of Polymer Science & Engineering. 2nd ed. Elsevier Inc; **1992**. 379,383.

55. Pozniak AA, Smardzewski J, Wojciechowski KW. Computer simulations of auxetic foams in two dimensions. Smart Mater Struct. 2013.22(8). 084009.

Chapter 4: Indentation resistance of auxetic, iso-density, near zero Poisson's ratio and unconverted open cell PU foam cubes

4.1. Introduction

As previously identified (Chapter 2, Page 21), auxetic materials with a negative Poisson's ratio (NPR) have some enhanced characteristics. For Isotropic materials, Poisson's ratio (v) relates shear modulus (G, Equation 2.1, Page 22, and 4.1) and bulk modulus (K, Equation 2.2, Page 22, and 4.2) to Young's modulus (E) [1]:

$$G = \frac{E}{2(1+v)} \qquad (4.1)$$

$$K = \frac{E}{3(1-2v)} \qquad (4.2)$$

Respective maximum and minimum values for shear and bulk moduli are achieved with NPR (of -1). The force required to indent an elastic half-space with a sphere, radius R, to a specific depth is known as indentation resistance or hardness (H) [2]. Considering a point within the half space, resistance to deformation is proportional to Young's modulus, and total deformation. Considering the entire half space, contact and incidence (summarised by x), contact area (a) and force (F), indentation resistance relates to Poisson's ratio and Young's modulus by Equation 2.3 (Page 23) and 4.3 [2,3]:

$$H = \frac{F}{a} \propto \left(\frac{E}{(1-v^2)}\right)^x \qquad (4.3)$$

Meaning, if Young's modulus is held constant, and E^x is therefore unchanged:

$$H \propto (1-v^2)^{-x} \qquad (4.4)$$

For the case of a sphere, radius R, the radius (r) of the contact area is [3]:

$$r = \left(\frac{3}{4}FR\frac{(1-v^2)}{E}\right)^{1/3} \qquad (4.5)$$

Equations (4.1) and (4.2) have some assumptions:

i) The surfaces are continuous and have non-conforming profiles.
ii) The area of contact is much smaller than the characteristic dimensions of the contacting bodies.
iii) The strains are small and purely elastic.
iv) The surfaces are frictionless at the contact interface.

Maximum indentation resistance is achieved isotropically when Poisson's ratio is -1 (Equations 4.3 & 4.4). An experimentally validated correction factor (C, Equation 2.4, Page 24) for thin sheets of rubber (v = 0.5) is based upon the multiple of a constant A (found

experimentally) and the ratio of t (the sample thickness) to a_t (representing the radius of area of contact) [5]:

$$C = 1 - \exp^{-A\frac{t}{a_t}} \tag{4.6}$$

The definition of 'thin' is not provided, and application of the correction is left to the reader's discretion; presumably when t/a_t becomes influential [5]. The constant A was 0.67 or 0.41 in thin sheets of rubber, with or without lubrication (respectively). The presence of friction between the surfaces can increase the hardening effect caused by NPR below -0.5, as shown using finite element analysis (FEA) and continuum mechanics [6–9]. Whether the same correction factor (Equation 4.6) can be applied to auxetic or conventional foam sheets with different Poisson's ratio to rubber, and whether friction will change NPR's effect on hardness during different scenarios to those previously modelled (i.e. in thin sheets) is unclear.

Samples thicker than they are wide are desirable for compression testing; to minimise friction inhibiting transverse deformation and Poisson's ratio measurements [10]. Foam padding within protective equipment for sports, defence and commercial applications is often relatively thin (1-2 cm) with a larger planar area [11–14] than typical, homogeneous auxetic foam samples (~2 x 6 cm [15–17]). There is no standard test for measuring hardness in foams, but the standard test for measuring hardness in rubber requires an increasing distance from the edge of the sheet to the edge of the point of contact: 13 mm for 25 mm thick samples or 11.5 mm for 15 mm thick samples [18], respectively. Samples cannot be created to meet both standards [10,18], but cubic foam samples (~2 x 2 x 2 cm) have been used for both compression [15,19,20] and indentation [21] testing. As the contact area tends towards cross sectional area of a sample, indentation resistance will become increasingly similar to flat plate compression; reliant upon Young's modulus rather than Poisson's ratio.

The effect of large deformation indentations, causing changes in the shape of the compressed area (Figure 4.1, Figure 2.5, Page 23) requires further experimental and/or computational confirmation. Auxetic foams with a lower initial Young's modulus than their conventional counterpart have been shown to wrap around an indenter in low (1% compression) strain FEA simulations and high strain (~80% compression) impact tests [14,22]. Auxetic materials have also been shown to deform as a flatter unit (Figure 4.1c) than their conventional counterparts, both experimentally (indenting foam) [21] and through FEA (Figure 4.1) [23–26]. Changes in density and Young's modulus from the conventional parent foam have only been accounted for in one indentation test of auxetic foam, but isotropy and linearity were not confirmed [21].

Young's modulus increases with the density of a cellular material, provided that cell shape is unchanged [4]. Transverse contraction or expansion in conventional and auxetic foam has only been quantified under uniformly distributed (flat plate) compression tests, using non-contact strain measurement methods such as marker tracking [27–29] or digital image correlation (DIC [30–33]). Quantifying transverse strain using a full field strain measurement method such as DIC during indentation would begin to identify whether differences in Poisson's ratio can cause a sufficient density difference, due to transverse deformation, to increase stiffness. The relationship between density and Young's modulus would only be applicable in scenarios where cell shape does not substantially change.

Thermomechanical conversion for open cell, thermo-plastic, auxetic foam have been studied in detail (Chapter 3, Page 46) as required by the first Aim of this investigation (Chapter 1, Page 5). A range of conditions are known to give quasi-linear, iso-density, isotropic foams with near zero and NPR. In Chapter 3 methods were presented to mitigate the reduction in tangent modulus (to almost zero) caused by cell buckling between 5% and 80% compression, which is well documented in open cell foams [4,15], and confirmed isotropy in thermo-mechanically fabricated foams. Quasi-linear, iso-density, isotropic foams can now be used to demonstrate and examine the effects of Poisson's ratio on indentation resistance as strains exceed the infinitesimally small values required for direct application of indentation theory, as required by Aim 2.
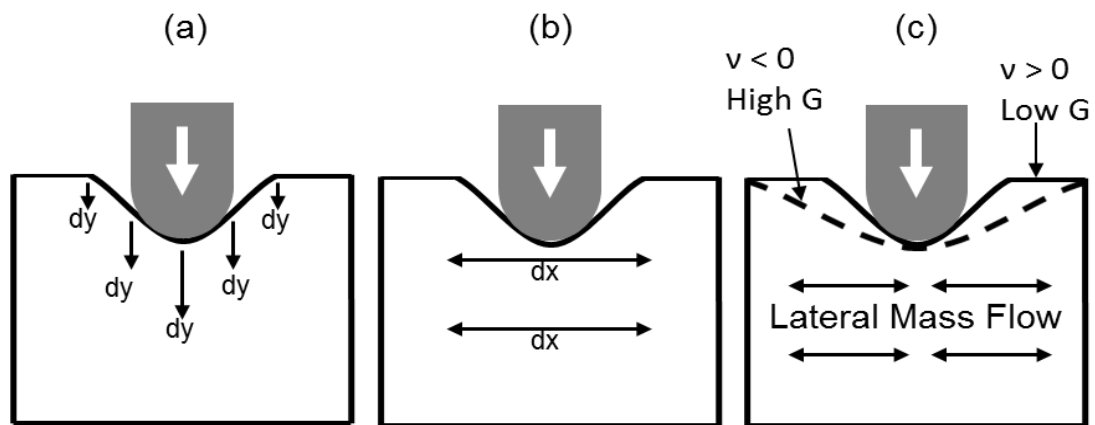

Figure 4.1: Simplified 2D indentation showing a) Axial deformation, b) Transverse deformation described in Equation 4.3 & c) The predicted effect of large shear modulus (and unchanging Young's modulus) on indentation area (- - -) and transverse mass flow, both un-accounted for in Equation 4.3.

4.2. Methods

4.2.1. Foam Conversions

The same samples (PUR30FR, Custom-foams, supplied precisely cut to 32 x 32 x 96 mm) were thermo-mechanically converted with isotropic compression in aluminium box section moulds (2 mm wall thickness) with a triaxial VCR of two or three (Figure 4.2). Samples were

fabricated under the conditions giving comparable density; quasi-linear stress vs strain relationships and a range of negative to marginally positive Poisson's ratios (Chapter 3). Samples with a VCR of three were heated in an oven at 160, 170 & 180°C for 20 minutes and 180°C for 60 minutes. Samples with a VCR of two were heated in an oven at 180°C for 60 minutes. Six samples were fabricated for each time and temperature combination and cooled to close to room temperature in their moulds (30 to 60 minutes).

Following cooling, samples were hand stretched to 10% tensile strain over a scale at approximately five seconds per cycle for five cycles, giving comparable relaxation to previous work (Chapter 3). Samples were laser cut along their length (Trotec 10000) into cubes twenty four hours after fabrication, and the central cube was used for compression and indentation testing. Converted samples had expected Final Volume Ratios (FVR, initial/original volume) of two or three, equating to 25.5 or 22 mm sides (Chapter 3). However, due to re-expansion of samples converted with less heat exposure, not all cubes were the same size. Rather than creating additional cuts, which were not overly precise, a range of sample sizes were used. Comparative unconverted 20 mm sided cubic samples were laser cut (Trotec 10000) from 32 x 32 x 96 mm cuboids, and 32 mm sided cubes were cut to explicitly show the effect of sample size on indentation resistance.
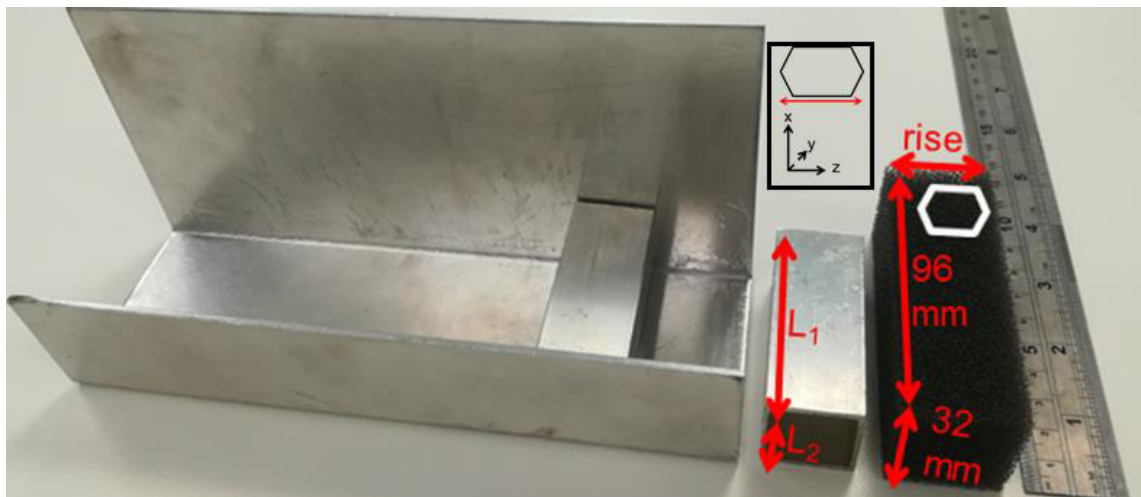

Figure 4.2: Foam and mould (annotations show cell rise, axis orientation and dimensions). L1 (x) = 76.5 or 66.5 mm and L2 (y and z) = 25.5 or 22 mm for VCR = 2 or 3, respectively

4.2.2. Mechanical Testing

Compression (flat plate, Figure 4.3a & b) and indentation (Figure 4.3c) tests began two days after fabrication, and took one week to complete. The first and last round of testing was to 10% compression (Figure 4.3a & b, Instron 3367, 500 N load cell, sample frequency 25 Hz, strain rate 0.0067 s^{-1}). Cell rise (z axis) was aligned transversely: first parallel to the camera (Nikon

D810 1920x1080p, 25fps), then perpendicular (compression parallel to x or y, recorded transverse expansion parallel to y or z respectively, Figure 4.2). Indentations to a depth of 20% of sample thickness (Figure 4.3c) were carried out with three indenters (10 and 50 mm diameter cylinders and a 12 mm diameter aluminium football stud featuring a flat base, almost vertical sides and small (<1 mm) fillet, Figure 4.4). Comparative compression before and after (i.e. pre and post) each round of indentation tests with a different indenter were used to calculate mean Young's modulus and Poisson's ratios for each sample, at the time of indenting. These compression tests were also to 20% compression (Figure 4.3a & b), with cell rise aligned axially (compression parallel to z, recorded transverse expansion parallel to y, Figure 4.2).
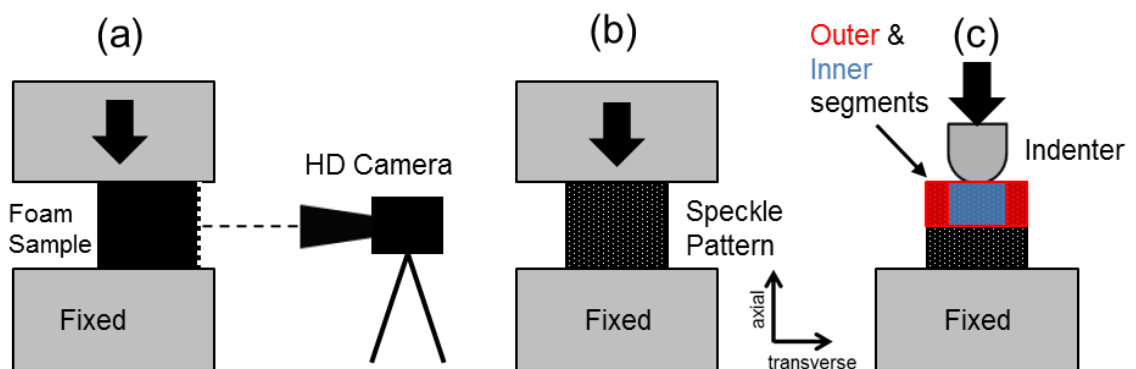

Figure 4.3: a) Flat plate compression set up (side view), b) Flat plate compression and camera set up (front view), showing powder coating speckle pattern c) Indentation test set up (front view), showing powder coating speckle pattern and segments used to obtain indentation shape (outer segments in red, inner in blue). Indentation set up was the same as shown in a). Annotation between b) and c) shows axial and transverse directions in a), b) and c).

Two dimensional Digital Image Correlation (DIC) was used to obtain axial and transverse strains [31,33,34], both during indentation and compression tests. Powder coating applied before each test (Figure 4.2c, Laponite RD, BYKAdditives) enhanced the speckle pattern provided by the porous foam surfaces. DIC analysis was carried out using commercial software (GOM Correlate, 2016). Facet sizes were between 25 and 35 pixels (0.04 to 0.06 mm/pixel), with standard accuracy and matching against the previous stage (due to the large strain range) typically selected. Linear trend lines fitted to plots of transverse vs axial true strain (mean value across all facets within target area, over a 10% strain range) were used to obtain Poisson's ratios in all three orthogonal planes (v_{xz}, v_{yz}, v_{zy}), determined from the negative of the gradient of the linear trend line. All samples were measured (Vernier Callipers) before every compression or indentation test, for calculation of stress (cross sectional area) and strain (axial length) from Instron force and displacement data (Bluehill 4.0) and also FVR. DIC data was manually synchronised by clipping videos to when the Instron trigger was activated ($\pm$ ~40 ms, $\varepsilon \pm 2 \times 10^{-3}$), which was sufficient given the low strain rates. Compressive Young's moduli were calculated

from the gradients of linear trend lines fitted between 0 and 10% compressive axial stress vs strain, and 5% (prior to plateau) for the unconverted foam. Mean values for Poisson's ratio and compressive modulus were taken up to 10% strain. Compression tests compared sample's directional dependency (isotropy).
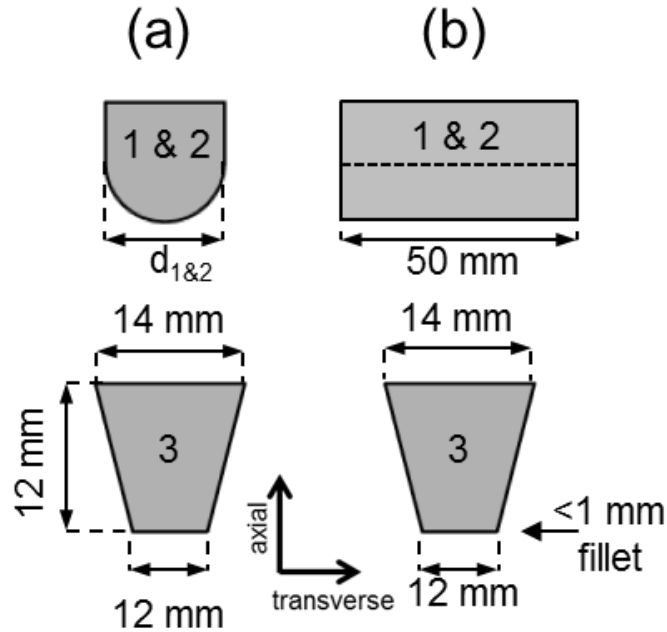

Figure 4.4: a) Front view and b) Side view of cylindrical and studded indenters (top and bottom respectively). Dotted line shows hidden features. The diameters, d1 & d2=50 mm or 10 mm. Annotation between a) and b) shows axial and transverse directions

Mean Young's moduli measured up to 20% strain were used to normalise Hardness (H_{norm} = Force/(a x E)), limiting any differences caused by Young's modulus [21], which is approximately constant up to 10% axial compression in converted samples (Figure 3.12, Chapter 3, Page 61), provided Young's modulus remains constant between 10% and 20% axial strain. Equation 4.3 was applied to quantify Indentation resistance. The stud had a flat surface of diameter 12 mm, so assuming the near vertical walls do not contact the foam, contact area (in mm^2) was:

$$a_{stud} = \pi(6)^2 \tag{4.7}$$

For the 50 mm cylindrical indenter, indentation depths was small relative to the indenter radius, the radius of contact was [3]:

$$r_{cylinder} \approx \sqrt{dh_{mean}} \tag{4.8}$$

Whereby d is cylinder diameter and h_{mean} is the mean indentation depth (which is half of the maximum indentation depth, h, in Figure 4.5, because compression rate set on the test device was constant).

For the 10 mm cylindrical indenter, indentation depth was not small relative to the indenter radius, so the radius of contact was:

$$r_{cylinder} \approx \sqrt{dh_{mean} + h_{mean}{}^2}$$ (4.9)

The length of the cylinder contacting the sample is equal to the sample width (front to back face), and was assumed constant. The area is therefore:

$$a_{cylinder} \approx r_{cylinder} * l_{contact}$$ (4.10)
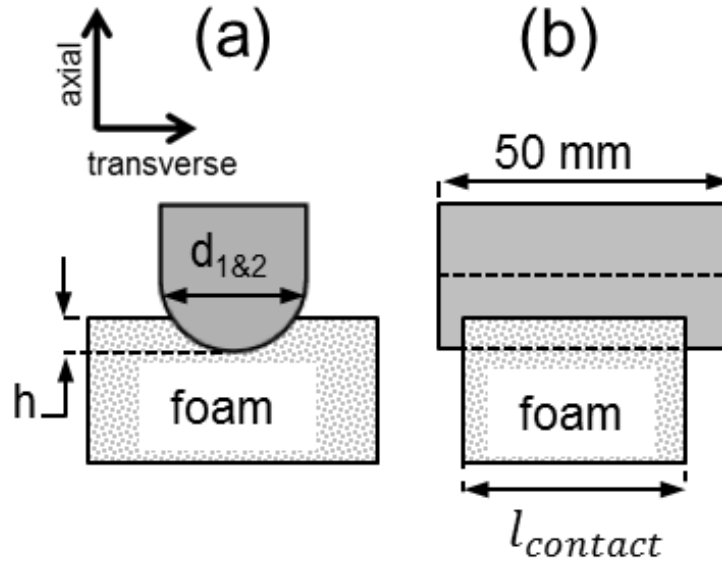
Figure 4.5: a) Front view and b) Side view of the cylindrical indenter indenting foam. Dotted lines show hidden features. The diameters, d1 & d2=50 mm or 10 mm.

Combining Equations 4.5, 4.8 or 4.9 and 4.10 (for the cylinders), or 4.7 (for the stud), and replacing F (Equation 4.3) with k x h$_{max}$, the force constant (the slope of a linear regression of force vs displacement data), gives Equations 4.11 and 4.12 for studded and cylindrical indenters. Equations 4.11 and 4.12 are valid for indentations or impacts where x = 1 (Equation 4.3), and also useful in assessing how a material will behave in impacts with either large/flat bodies or those with concentrated loads:

$$H_{norm\_cylinder} = \frac{k \times h_{max}}{E \times \sqrt{dh} \times L_c}$$ (4.11)

$$H_{norm\_stud} = \frac{k \times h_{max}}{E \times \pi(6)^2}$$ (4.12)

Calculating indentation resistance and normalising hardness to Young's moduli has some assumptions, particularly for the two cylindrical indenters: i) the entire compressed region may not remain in contact with the sample, ii) any non-linearity in stress vs strain relationships will affect the Young's modulus and normalisation, iii) sample thickness was

relatively low compared to indenter shape. The following approaches were also considered:

   i) Normalising to Young's moduli, measured over five or ten % compression

ii) Calculating compressive energy for each indentation test and from compression tests, giving normalised indentation energy as a measure of effective indentation resistance over large strains: Normalised Indentation Energy = Indentation Energy (U_i)/ Mean Compressive Energy (U_c) from pre/post compression tests.

iii) Correcting Normalised indentation energy according to Equation 4.6. The value t is sample thickness and a value of A = 0.67, was used for non-lubricated interfaces [5]. The value a_t is simply the radius of the stud, but was adapted for the two cylinders to be comparable to a spherical indenter:

$$a_{t:\ cylinder} \approx \sqrt{\frac{a_{cylinder}}{\pi}} \qquad\qquad\text{(4.13)}$$

Linear regressions were taken of logarithms of i) the left and right hand side of Equation 4.3 for hardness, and ii) Normalised Indentation Energy or Corrected, Normalised Indentation Energy, and the negative logarithm of the denominator in Equations 4.3 [$-\log(1-v^2)$]. The gradients were compared to expected values for x in Equation 4.3. Expected values for x are 1/3 for a Hertzian hemisphere (from Equation 4.5) [3,21], 1/3 for a cylindrical indenter and 1 for a uniform circular indenter or stud (Equation 4.4) [3].

For samples with an FVR of 2 (Chapter 3), central and edgewise axial compression during indentation tests was obtained by virtually dividing samples into three segments (axial sample centre, inner segment 10 mm width and outer remainder ~7 mm each, Figure 4.3c). The ratio of the mean axial compression for the two outer segments to the axial compression for the inner segment was calculated. A between group's student's T-test was carried out on the ratio of outer to inner axial compression for each group ($p > 0.95$) for each indenter. Shear modulus was calculated from mean compressive Poisson's ratio and compressive modulus up to 10% compression (Equation 4.1). Correlation (Pearson's r^2) between the ratio of outer to inner compression and Poisson's ratio was obtained, as well as an approximation of the effect size of using a linear regression.

Effective Poisson's ratios were calculated under indentation tests of samples with an FVR of 2, found to give the largest range of Poisson's ratios (Chapter 3, Figure 3.10, Page 59), from mean axial and transverse strains (DIC, Figure 4.6) across the entire sample face up to 20% compression. Effective Poisson's ratios were used to compare transverse material flow, related to densification, named 'effective' because they were obtained during indentation and so not true Poisson's ratios. A between group's student's T-test was carried out on the Effective indentation Poisson's ratios for each group ($p > 0.95$) for each indenter. Correlations (Pearson's r^2)

between the ratio of Effective indentation and compressive Poisson's ratios were obtained. Changes to cell shape during indentation were qualitatively compared by manually indenting approximately one millimetre thick slices of unconverted foam and foam laser cut from each group with an FVR of two with a 10 mm diameter cylinder. Indentation was in the same direction as indentation tests (Parallel to z, with transverse expansion parallel to y, Figure 4.2) on a transparent frame work with a white background fixing sample corners to prevent out of plane movement (Figure 4.2c). A stereoscope (Leica S6D) collected images at ~20% indentation.
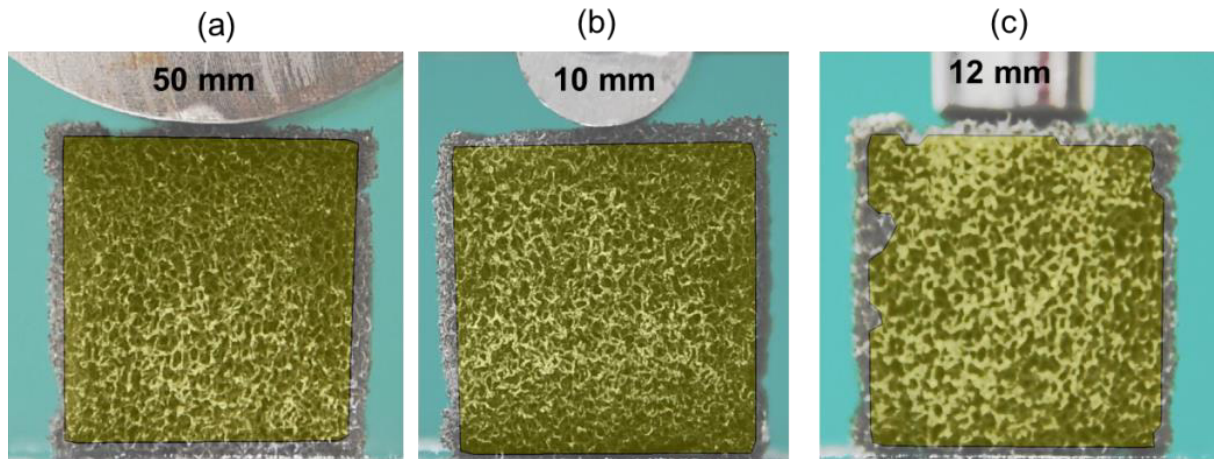

Figure 4.6: Target area (yellow) on surface of NPR sample (~25 mm sides) for a) 50 mm cylindrical, b) 10 mm cylindrical and c) 12 mm studded indenters

4.3. Results

4.3.1. Characterisation

Sample expansion following conversion (Figure 4.7a) was comparable to previous tests (Chapter 3). Mean FVR (through the course of testing) and VCR were close to three for samples fabricated above 170°C, due to low levels of re-expansion following conversion. The 160°C, 20 minute samples converted with a VCR of three (~22 mm sides) expanded to a mean FVR of 2.18 (~25.5 mm sides, Figure 4.7a), meaning they were a similar size and density to samples fabricated with a VCR of ~two (mean FVR of 2.18). The honeycomb-like unconverted open cell foam structure (Figure 4.7b) became re-entrant and contorted following conversion (Figure 4.7c), but there was no noticeable difference to cell structure or shape following prolonged heating (Figure 4.7d). Marginal increases in the density of the cell structures between Figure 4.7c & d were not present in density measurements (Figure 4.7a), and attributed to the increased thickness of sliced samples. Cell rise (Figure 4.7b) could not be qualitatively identified after the re-entrant structure was adopted (Figure 4.7c & d).
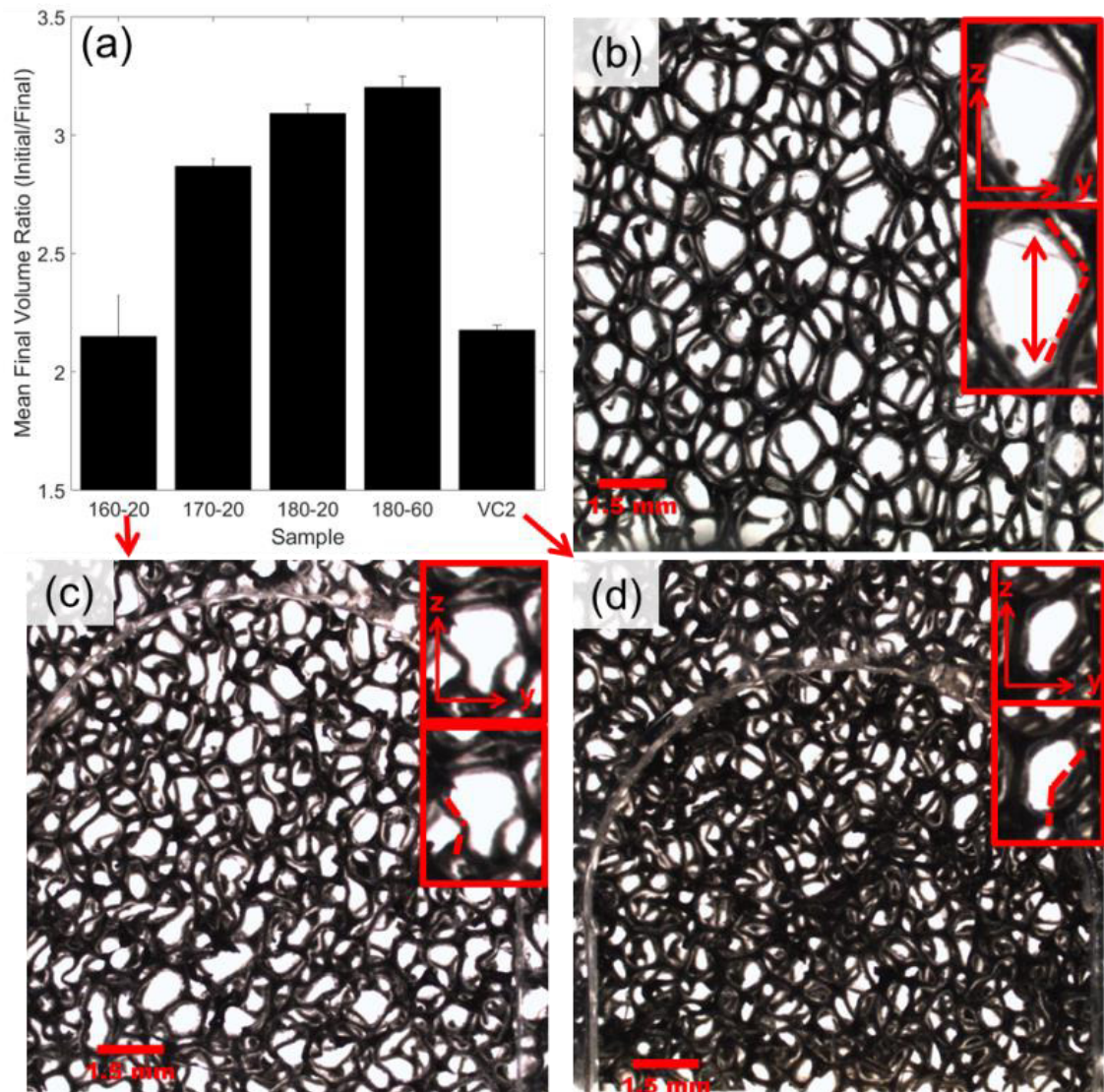
Figure 4.7: a) Mean Final Volume Ratio (all samples within each group). Error bars show 1 standard deviation. X axis naming is conversion temperature (before dash, °C) and time (minutes) for all samples fabricated with VCR=3. VC2 samples had a VCR of 2 and were converted at 180°C for 60 minutes. b) to d) As shown in Chapter 3 (Figures 3.7 a to c), magnified images (Leica S6D) of 1 mm thick slices of b) Unconverted foam sample, c) auxetic foam, 160°C-20minute sample from (a), d) ~zero Poisson's ratio foam, (VC2 in (a)). Annotated pop outs show a single cell enlarged by a factor of two, cell rise in b) and cell rib angles.

Compressive stress vs strain were as expected, with the unconverted sample plateauing at around 5% strain and all re-entrant samples deforming quasi-linearly (Figure 4.8a). Increased heat exposure increased the gradient of stress vs strain relationships, equating to an increase in stiffness. Samples with an expected negative or near zero Poisson's ratio (Chapter 3) exhibited respectively negative or marginal transverse strain in the y direction up to 20% compression parallel to z (Figure 4.8b). All samples axial vs transverse strain relationships were relatively linear, other than the unconverted foam which approximately plateaued beyond ~5% compression (Figure 4.8b). All samples exhibited close to the imposed values of axial

compression, although the unconverted samples did exhibit two to three % lower axial strain than expected (Figure 4.8b).
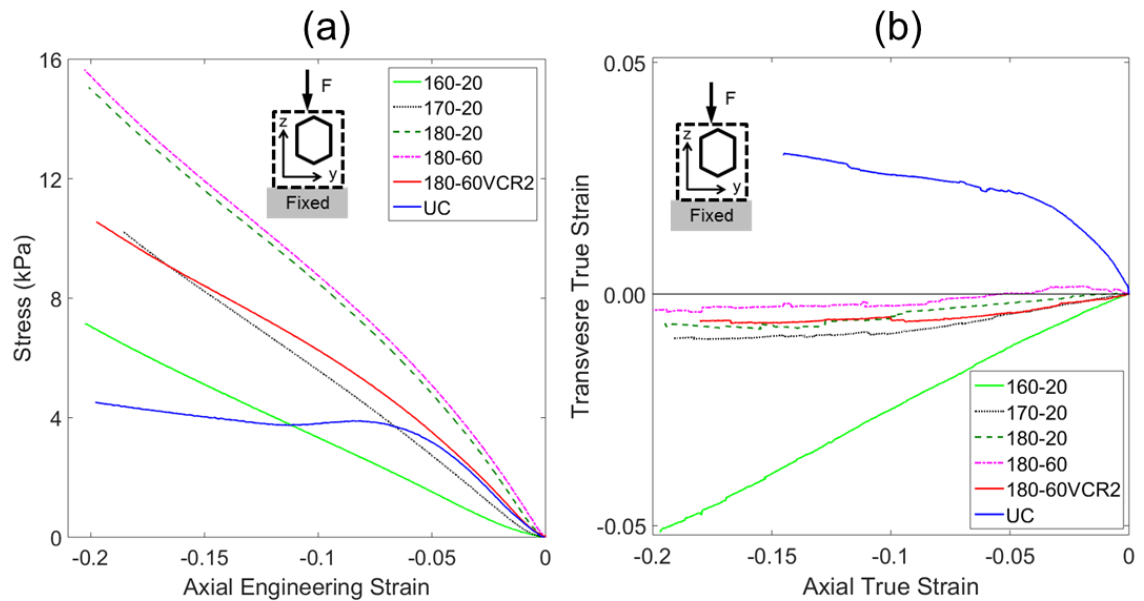

Figure 4.8: Sample a) Stress vs strain Axial Engineering Strain (z) and b) Transverse vs Axial True Strain plots from mean values across the entire samples faces from DIC up to 20% compression for all conversion conditions (UC=unconverted)

Poisson's ratios of each group of samples (taken up to 10%, Figure 4.9a) agree with the previous tests of the same foam (Chapter 3) and Figure 4.8b. Converted samples were relatively isotropic, with Poisson's ratio increasing from ~-0.2 to close to zero as heat exposure increased from 160°C for 20 minutes to 180°C for 60 minutes (Figure 4.9a). The lowest Poisson's ratios were achieved following re-expansion from a VCR of three to an FVR of two (160°C, 20 minutes, Figure 4.7a, Chapter 3). Samples fabricated with increased heat exposure at a VCR of two had Poisson's ratios close to zero (~-0.1 to ~0.1, Figure 4.9a), and were the same FVR, size and density (Figure 4.7a, Figure 4.9a, Chapter 3) as the lowest Poisson's ratio samples (~-0.2, 160°C, 20 minute, Figure 4.9a). The comparison between these two groups of samples would be expected to show any relationship between indentation resistance and Poisson's ratio most clearly. Unconverted samples Poisson's ratios were anisotropic and positive: ~0.25 or ~0.35 when axial strain was perpendicular or parallel to cell rise (z), respectively (Figure 4.9a). Young's modulus of converted samples was isotropic and increased from ~ 25 kPa to ~ 100 kPa with increasing heat exposure (Figure 4.9b). Unconverted samples exhibited a lower Young's modulus up to 10% compression (~30 kPa, Figure 4.9b), but deformation was not linear across the measured range (Figure 4.9a). Unconverted foam's Young's modulus and Poisson's ratio were higher up to 5% than 10% compression (Figure 4.9), and anisotropy was also increased. Symmetric compliance was checked for each group of sample's mean Poisson's ratio and

Young's moduli (Figure 4.10). Data was close to $\nu_{yz}E_z = \nu_{zy}E_y$, suggesting that Young's modulus and Poisson's ratio measurements in the y and z directions were consistent [35].
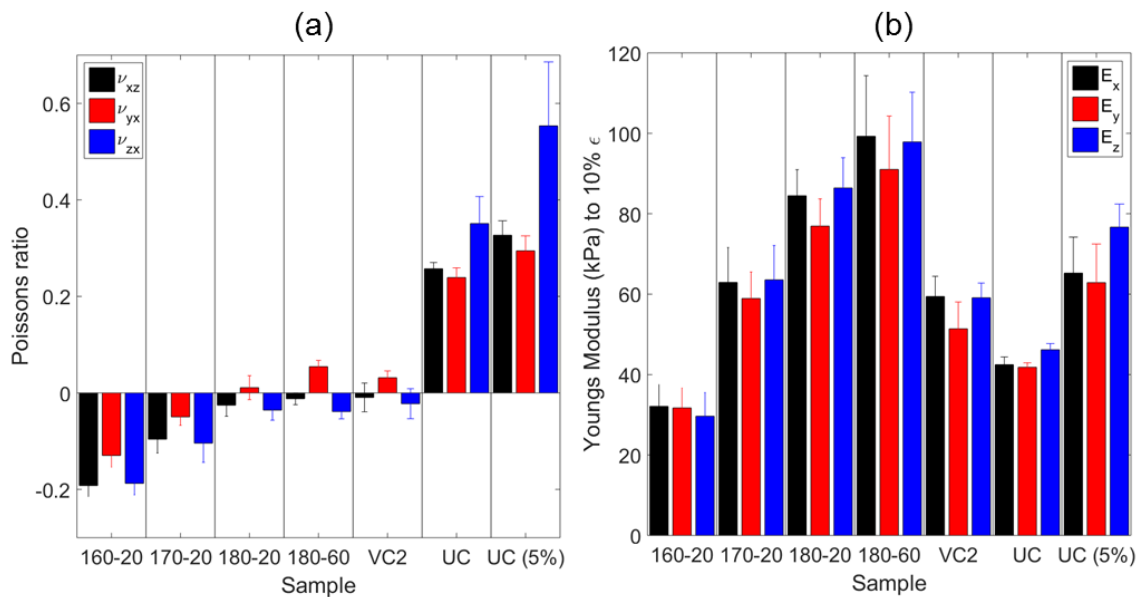

Figure 4.9: Mean directional a) Poisson's ratio and b) Young's Modulus taken up to 10% for all samples, and also 5% for the unconverted samples. X axis naming relates to conversion temperature (before dash, °C) then time (minutes), for all samples fabricated with VCR=3. The 'VC2' samples were heated for 60 minutes at 180°C. UC is unconverted. Error bars are 1 s.d.

Calculated from compressive modulus and Poisson's ratio up to 10% (Figure 4.9), shear and bulk moduli for all converted samples were isotropic (Figure 4.11). Unconverted samples were expected to be anisotropic (Chapter 3), but fitting linear trend lines to non-linear data (Figure 4.8) up to 10% strain meant anisotropy was not noticeable (Figure 4.11). For samples with an FVR of 2, both shear and bulk modulus of the near zero Poisson's ratio samples was larger than the NPR (~-0.2) samples due to the large increases in Young's modulus (Figure 4.9), as expected when heating for a longer time or at a higher temperature (Chapter 3).
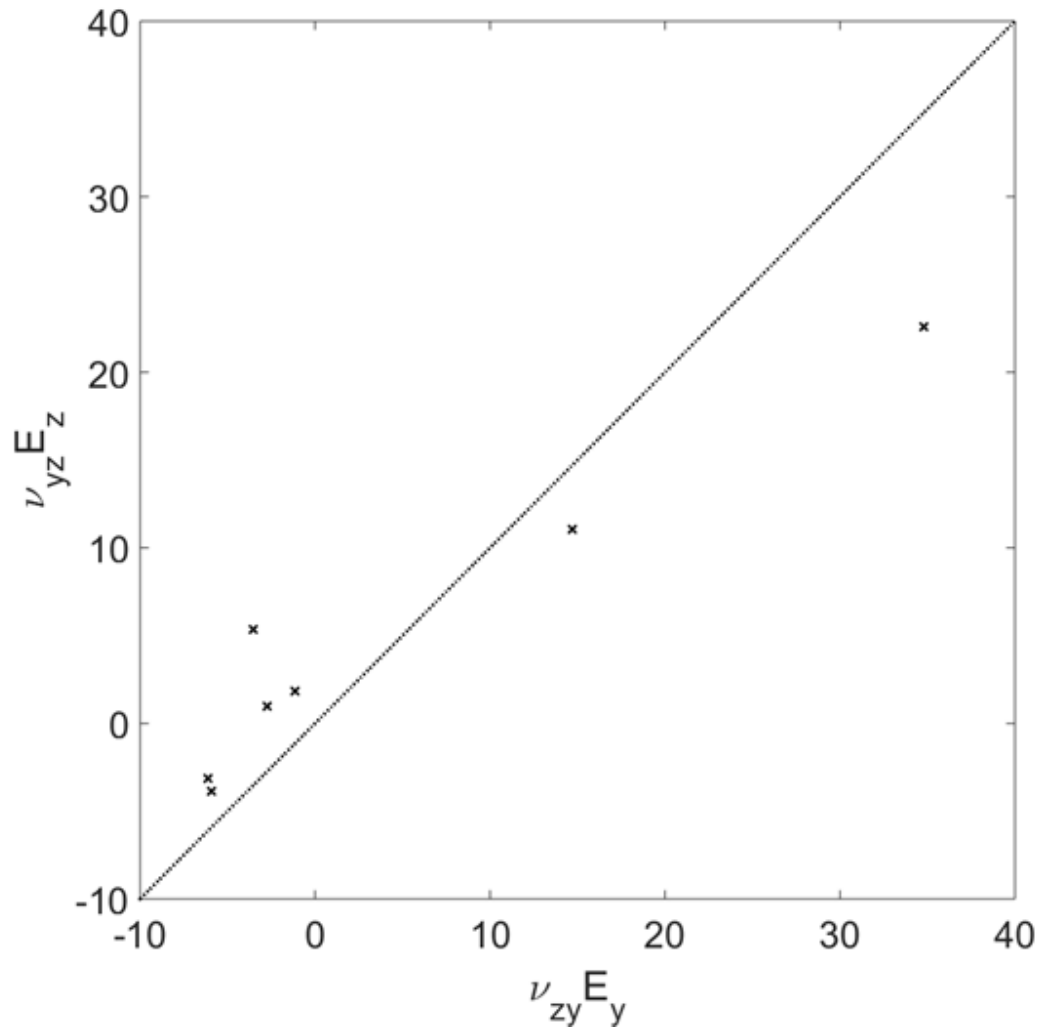
Figure 4.10: Symmetric compliance ($\nu_{yz}E_z$ vs $\nu_{zy}E_y$) for all samples, calculated from mean values for directional Poisson's ratio (ν) and Young's modulus (E). Dotted line shows ideal $\nu_{yz}E_z = \nu_{zy}E_y$
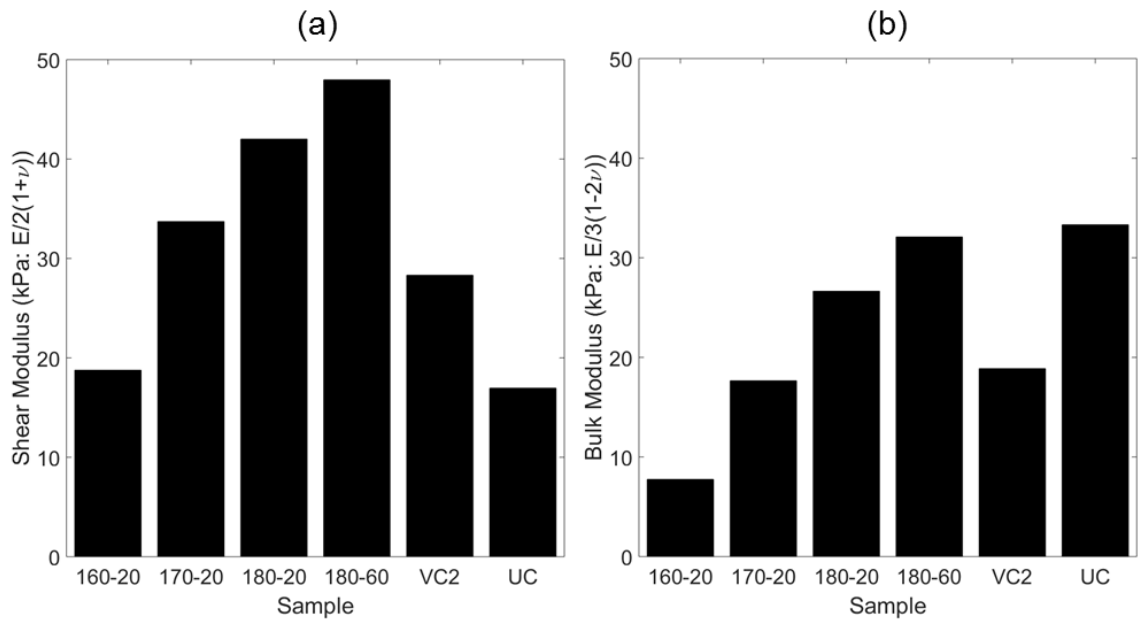
Figure 4.11: Mean a) shear (Equation 4.1) and b) bulk (Equation 4.2) moduli calculated from values up to 10% strain (mean across all three axes). X axis naming relates to conversion temperature (before dash, °C) then time (minutes), for all samples fabricated with VCR=3. The 'VC2' samples were heated for 60 minutes at 180°C. UC stands for unconverted. Error bars are 1 s.d.

4.3.2. Indentation resistance

Iso-volume samples with the same FVR (of two, Figure 4.7a) subject to increased or decreased heat exposure have negative or near zero Poisson's ratio respectively (Chapter 3, Figure 4.9a). NPR and near zero Poisson's ratio samples exhibited either inward (Figure 4.12a) or marginally outward (Figure 4.12b) transverse strain (respectively) when indented with the 10mm diameter cylinder. The positive Poisson's ratio unconverted foam exhibited mostly outward transverse deformation (Figure 4.12c).
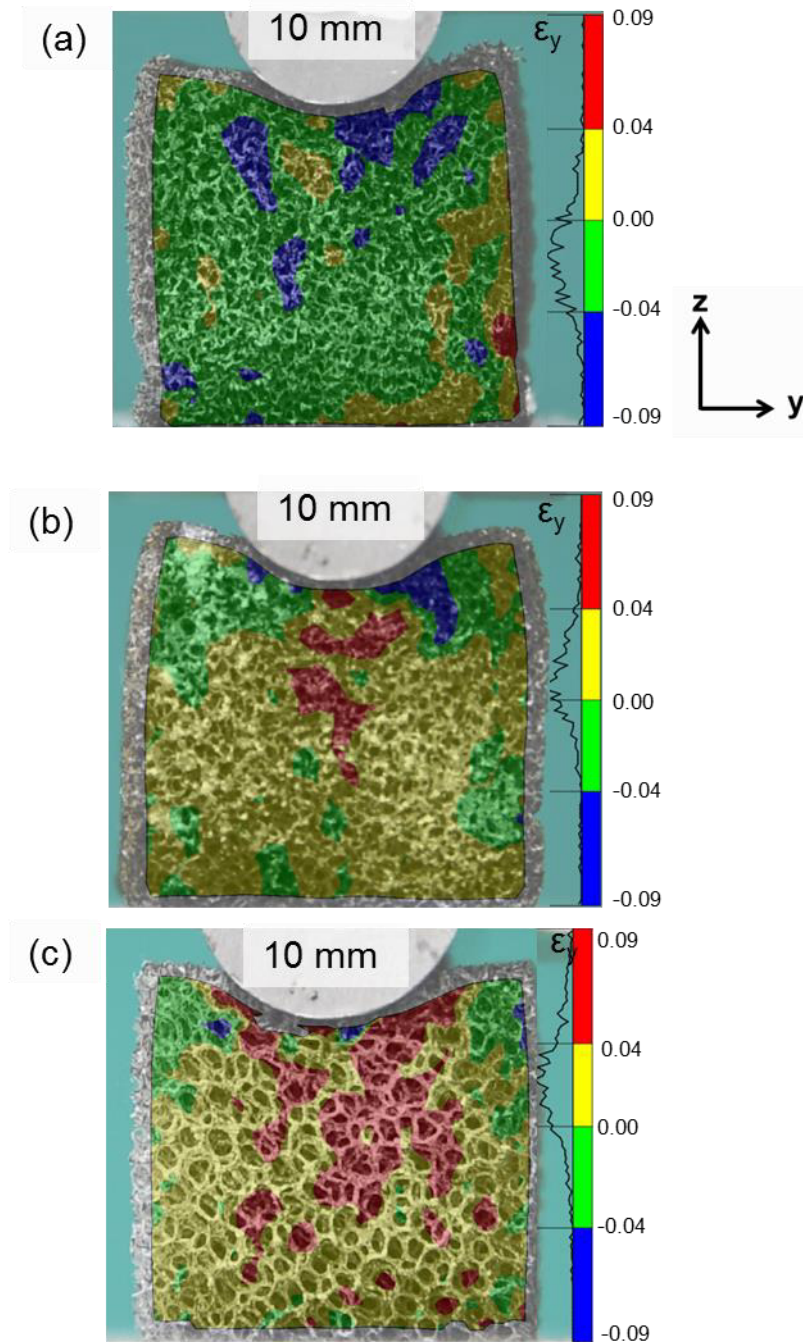
Figure 4.12: Contour plots and histograms of transverse strain at maximum compression with the 10 mm diameter cylindrical indenter for a) auxetic foam with an FVR of 2 (160°C, 20 minutes, VCR=3), b) foam with a Poisson's ratio of ~ zero and an FVR of 2 (180°C, 60 minutes, VCR=2) & c) an unconverted sample.

The NPR and near zero Poisson's ratio iso-volume samples exhibited either relatively constant (Figure 4.13a) or more variable (Figure 4.13b) through thickness compression, respectively. The sample with a Poisson's ratio near zero compressed by a greater amount underneath the indenter than towards its edges (Figure 4.13b). The unconverted sample exhibits a small amount of variation, but was smaller (20 mm) in width than the other two 25 mm samples (Figure 4.13c).
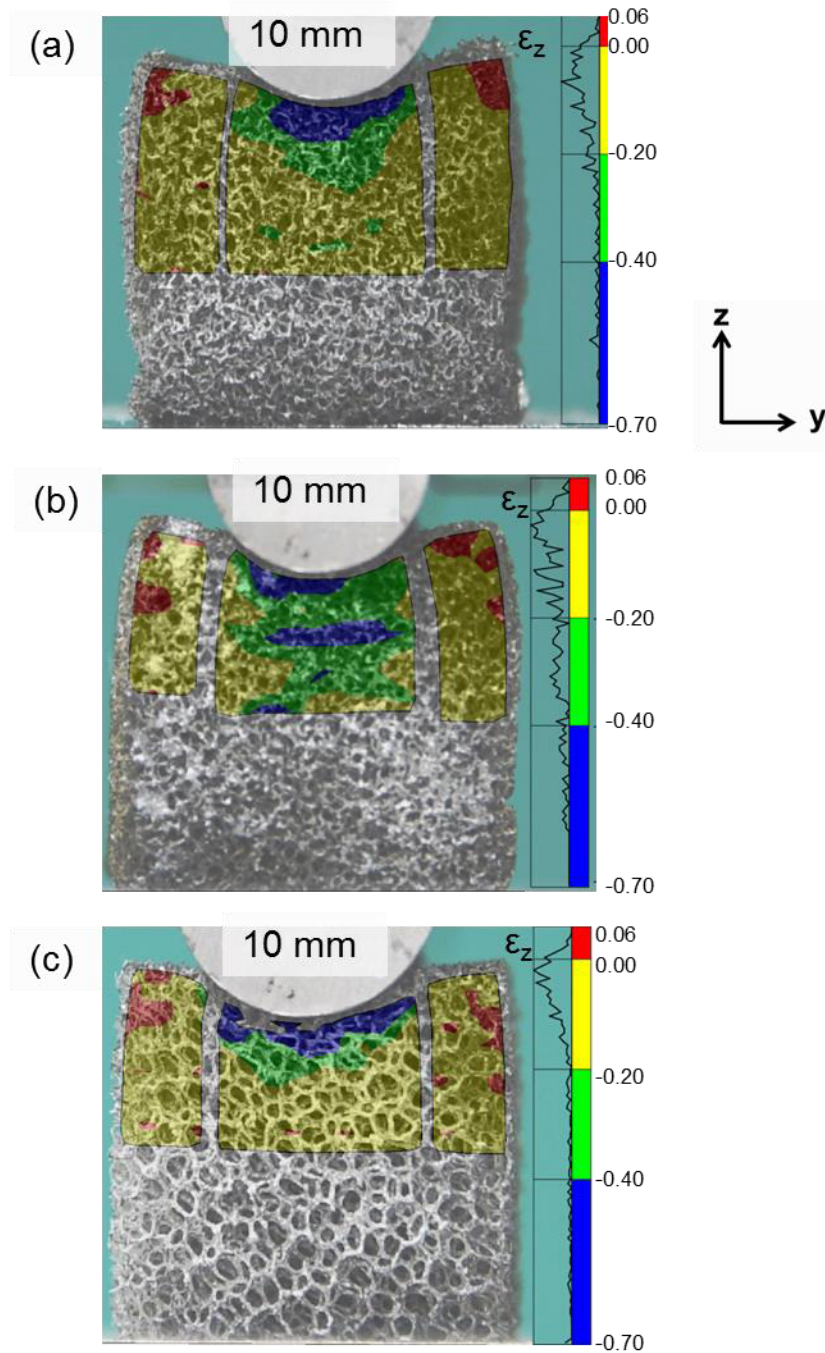
Figure 4.13: Contour plots and histograms of segmented axial compression at maximum compression with the 10 mm diameter cylindrical indenter for a) foam with an FVR of 2 and Poisson's ratio of -0.2 (160°C, 20 minutes, VCR=3), b) foam with a Poisson's ratio of ~ zero and an FVR of 2 (180°C, 60 minutes, VCR=2) & c) an unconverted sample.

During indentation with all three indenters, NPR samples, samples with a near zero Poisson's ratio and unconverted samples with a positive Poisson's ratio (Figure 4.9a) exhibited negative, negligible or positive transverse strain, respectively (Figure 4.14a). As the indenter size decreases, the mean axial compression of all samples decreases (Figure 4.14a). As Poisson's ratio increased from negative to positive values, mean axial compression of the front face under

indentation also reduced (Figure 4.14a). The unconverted foam appears to have wrapped around the studded indenter, causing marginal compression of the frontal face (Figure 4.14b).
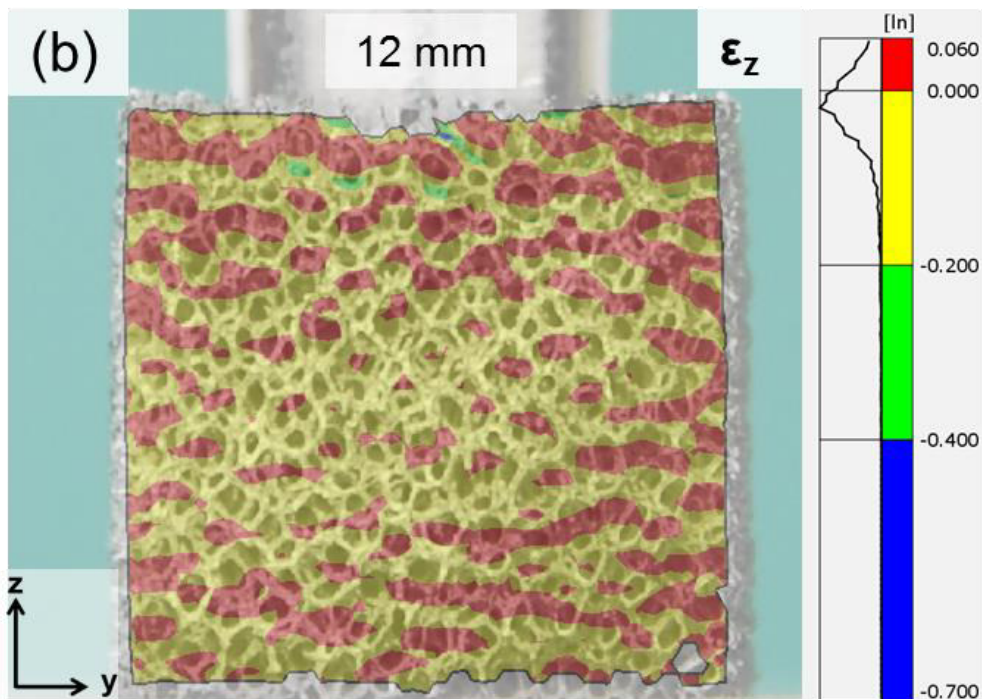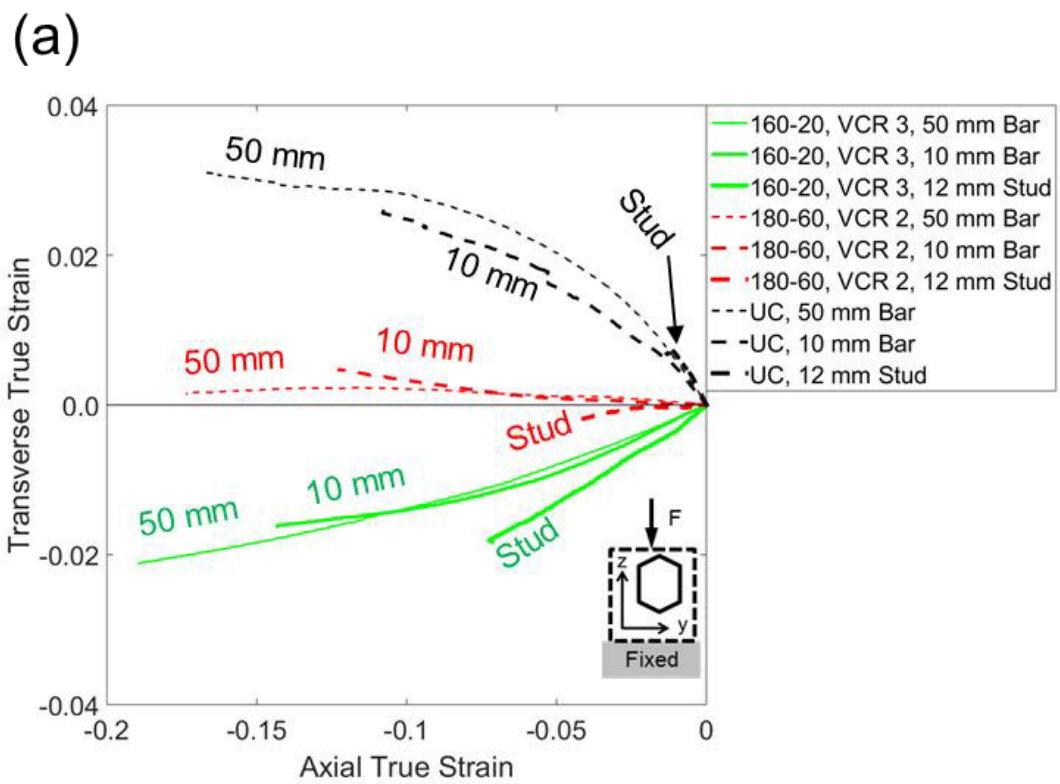
Figure 4.14: a) Mean Transverse vs mean axial True Strains across the full front face of samples for select (NPR-VCR = 3, near zero Poisson's Ratio -VCR = 2 and positive Poisson's Ratio - UC) samples during 50 & 10 mm cylindrical and 12 mm studded indentations, b) Axial compressive strain for an unconverted sample under studded indentation at maximum compression.

Force vs axial displacement relationships of converted samples were similar during compression and studded indentation, when normalised to Young's modulus measured over 20% compression (Figure 4.15a). The unconverted sample had a relatively linearly force vs displacement relationship under indentation (Figure 4.15), suggesting the buckling region was less abrupt than during flat plate compression. The gradient of the unconverted sample's force vs displacement relationship did partially decrease beyond 5% indentation, and it was likely that the foam experiencing the highest amount of compression (i.e. directly underneath the indenter) began to buckle. The lower levels of mean front face compression (i.e. Figure 4.14) during indentation confirm that it was likely that foam from different regions was compressed by different amounts throughout the indentation tests.

Different Regions had compressive strains ranging from higher than the maximum strain imposed by the test device (i.e. 20% at the end of the tests) to zero or tensile values (Figure 4.13). As such, normalising to Young's modulus measured over the entire 20% strain might not be appropriate. Normalising to 10% (Figure 4.15b) and then 5% (Figure 4.15c) compressive strain amplifies the effect of Poisson's ratio. For example, from inspection of Figure 4.14, 5% strain was the most appropriate normalisation for the studded indenters, but axial strain was different both within (Figure 4.13a & b) and between samples (Figure 4.13a & d, Figure 4.14). Calculating mean regions for normalisation is not only overly complex, but also mixes variables: the mean axial compression during indentation changes according to the magnitude of Poisson's ratio [3,5,21]. The following analysis will assess whether the normalisation over the 20% region was appropriate.
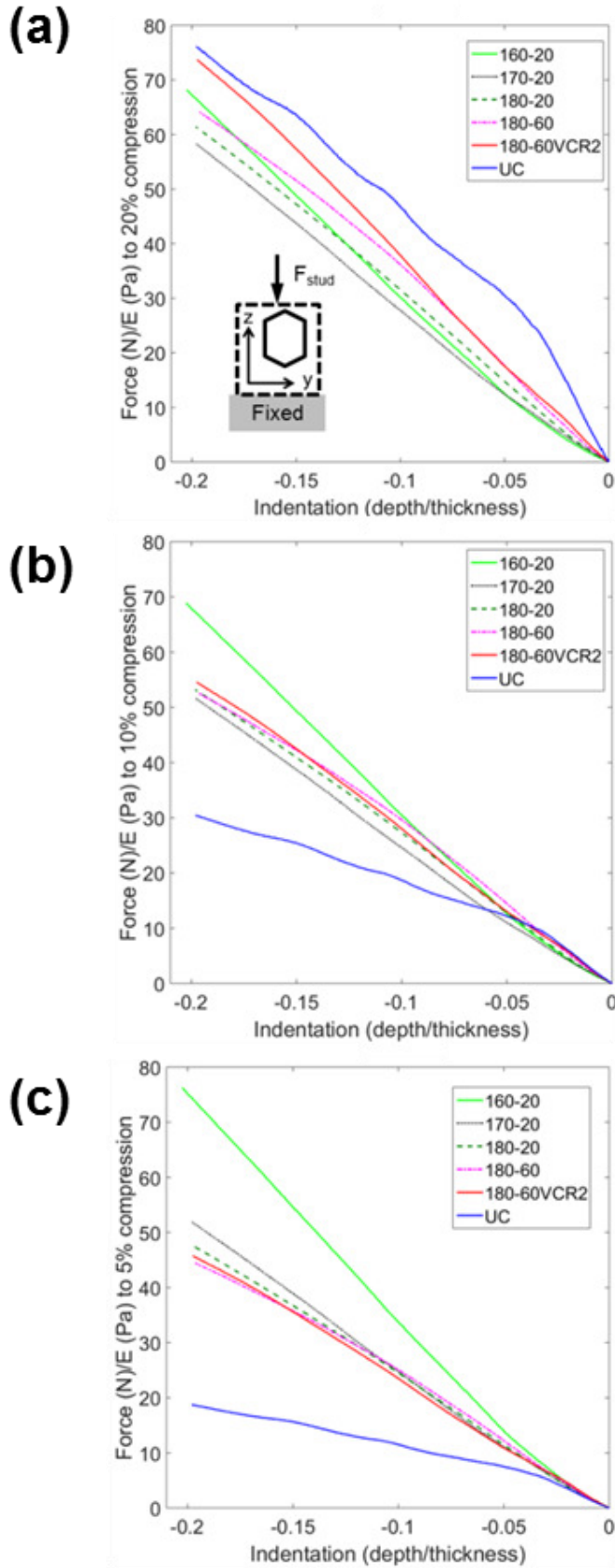
Figure 4.15: Sample Force vs Indentation with the 10 mm cylindrical indenter (as a percentage of original thickness) plots, with Force normalised to mean Young's modulus in Pre/Post indentation over a) 20% strain, b) 10% strain & c) 5% strain regions. UC=unconverted.

Normalised indentation resistance (Equations 4.11 & 4.12) shows reasonable fit with a quadratic curve for each indenter (Figure 4.16). Indentation resistance appears to reduce as Poisson's ratio reduces. In this case, the reduction in indentation resistance was likely caused by normalising the non-linear unconverted samples to a constant value for Young's modulus (Figure 4.15a). Young's modulus for the unconverted foam, calculated up to 20% compression, is lower than Young's modulus calculated up to a lower amount of compression (Chapter 3, Figure 4.9b). Compression under indentation is lower than under flat compression with a flat plate (Figure 4.14), so the normalised indentation resistance was larger than expected for the unconverted foam.
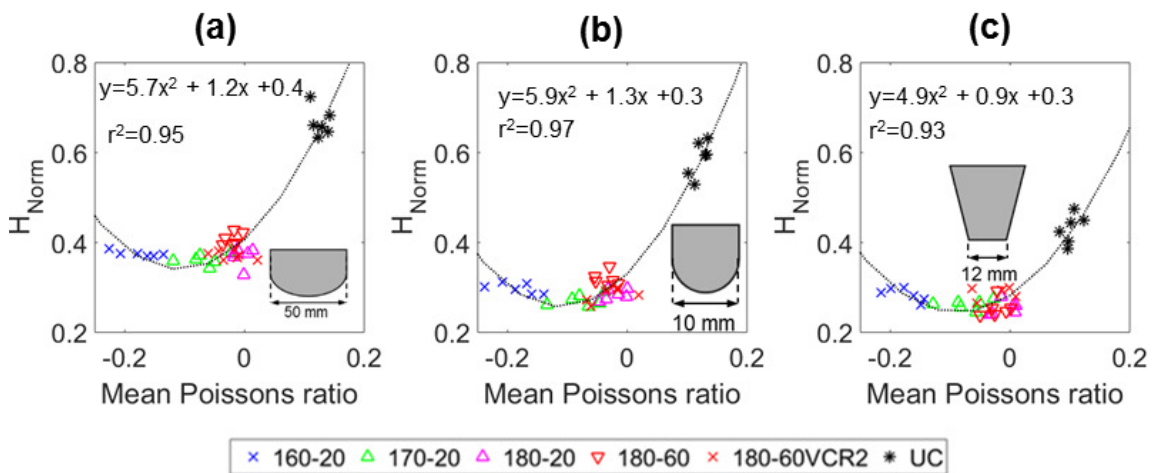
Figure 4.16: Mean Poisson's ratio ν_{zy} (to 20% compression) vs Normalised Indentation Resistance (Equations 4.10 & 4.11) for all sample, measured using the a) 50 mm Cylindrical indenter, b) 10 mm Cylindrical indenter and c) 12mm Studded indenter, up to 20% compression. Legend shows conversion conditions. UC = unconverted.

Removing area differences, which would change the constant in the regression fits taking the form of $y = mx + c$, then plotting natural logarithms (Figure 4.17) of the left and right hand side of Equations 4.3, the effect of the magnitude (m in the regression fit and x in Equation 4.3) of Poisson's ratio is larger than expected. The slope of the logarithmic regression is expected be 1/3 for the cylindrical indenters, and 1 for the stud (Figure 4.17) [3,21], but is ~1 for all cases.
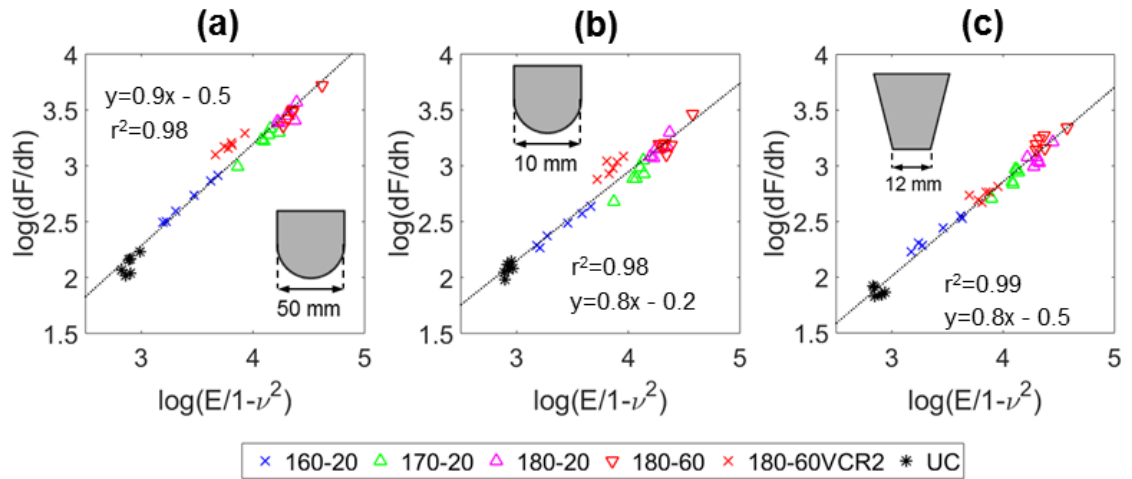
Figure 4.17: The natural logarithm of indentation force/depth vs the natural logarithm of the right hand side of Equation 4.3 & 4.4 for indentation resistance for a) 50 mm Cylindrical indenter, b) 10 mm Cylindrical indenter and c) 12mm Studded indenter, up to 20% compression. Legend shows conversion conditions. UC = unconverted. Formulae show gradients, which should correspond to x (Equation 4.3 & 4.4).

After removing the post-buckling region from unconverted samples' data, however, the values for trends (Figure 4.18) were further from expected. The unconverted foam's H_{norm} decreased substantially due its large, anisotropic Young's moduli (Figure 4.9). When differences in Young's modulus were accounted for in logarithmic plots of the left and right hand side of Equations 4.3 (Figure 4.19), values for x were close to the expected 1/3 for the cylinders, but lower than expected for the stud (0.5 rather than 1) [3,21].
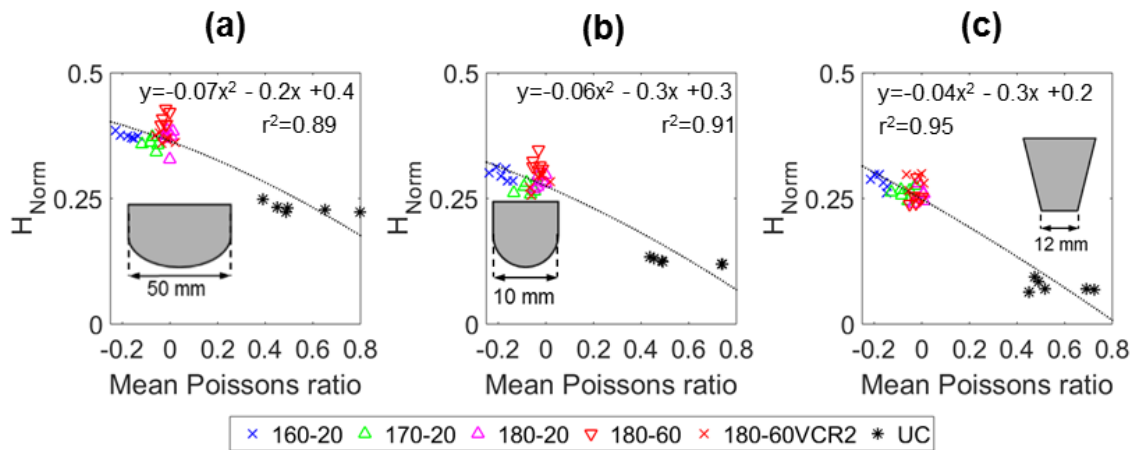

Figure 4.18: Mean Poisson's ratio v_{zy} (to 20% compression) vs Normalised Indentation Resistance (Equations 4.10 & 4.11) for all sample, measured using the a) 50 mm Cylindrical indenter, b) 10 mm Cylindrical indenter and c) 12mm Studded indenter, up to 20% compression. Legend shows conversion conditions. UC = unconverted, with H_{Norm}, and Poisson's ratio calculated in the linear stress/strain regions up to 5% compression, prior to cell rib buckling.
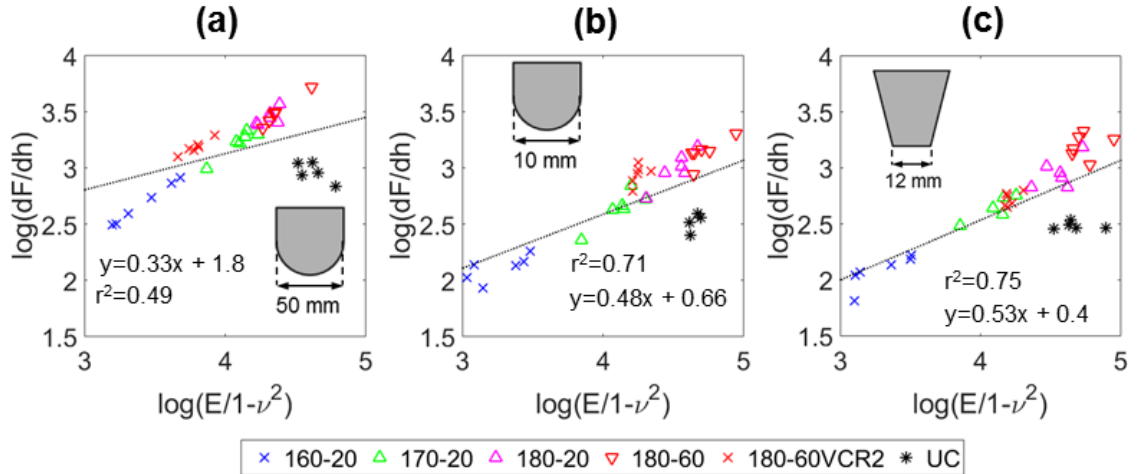
Figure 4.19: The natural logarithm of indentation force/depth vs the natural logarithm of the right hand side of Equations 4.3 & 4.4 for indentation resistance, for a) 50 mm Cylindrical indenter, b) 10 mm Cylindrical indenter and c) 12mm Studded indenter, up to 20% compression. Legend shows conversion conditions. UC = unconverted, data over the linear region to 5 % compression. Formulae show gradients, which should correspond to x (Equation 4.3). Values for x when the correction factor (Equation 4.6) was applied were: 0.46, 0.49, 0.54. Corrected r^2: 0.76, 0.77, 0.79 (for a, b & c respectively).

Removing anisotropic unconverted samples in the logarithmic plots, strong correlations ($r^2 > 0.95$) are obtained for trend lines (Figure 4.20). The gradients of trends lines give values for x (Equation S1) which are larger than expected values for cylindrical indentations (Figure 4.20a & b, expected = 1/3), smaller during studded indentation (Figure 4.20c, expected =1), but less so than in the previous case including the unconverted samples.

Applying the correction factor, the cylinders values for x reduced marginally towards expected values (Figure 4.21) while the correlations remained strong ($r^2 > 0.95$). The value obtained for studded indentation moves marginally away from the expected values. The stud is very different from the sphere for which the correction is intended, since it has a flat surface, and so the correction factor may not be applicable.
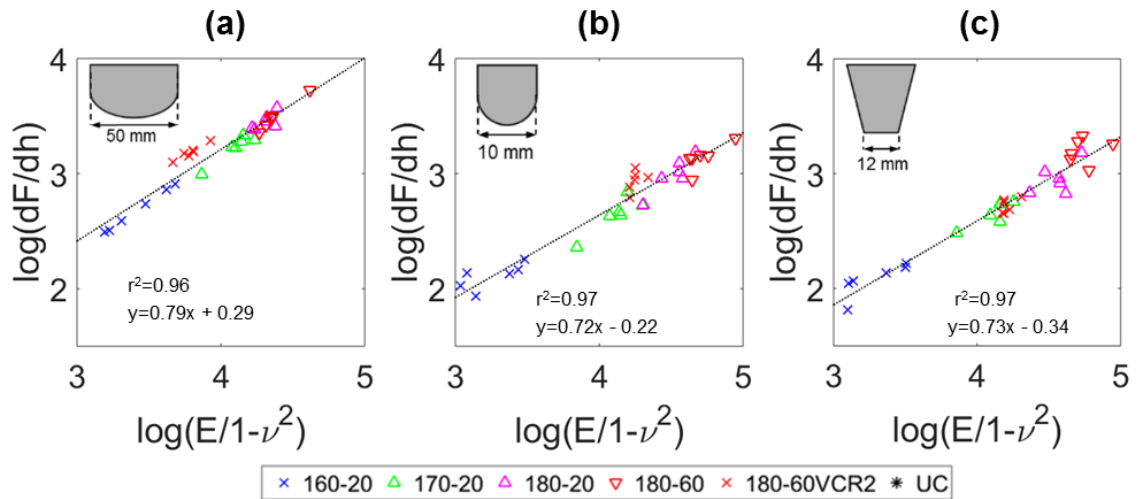
Figure 4.20: the natural logarithm of the gradient of Force (F) vs Indentation depth (h) plots for all samples vs the negative natural logarithm of the denominator in Equation 1 for indentation resistance measured using the a) 50 mm Cylindrical indenter, b) 10 mm cylindrical indenter and c) 12mm studded indenter, up to 20% compression, outlying, anisotropic UC removed. Legend shows conversion conditions. Formulae show gradients, which should correspond to x (Equation 1). Formulae show gradients, which should correspond to x (Equation 4.3).
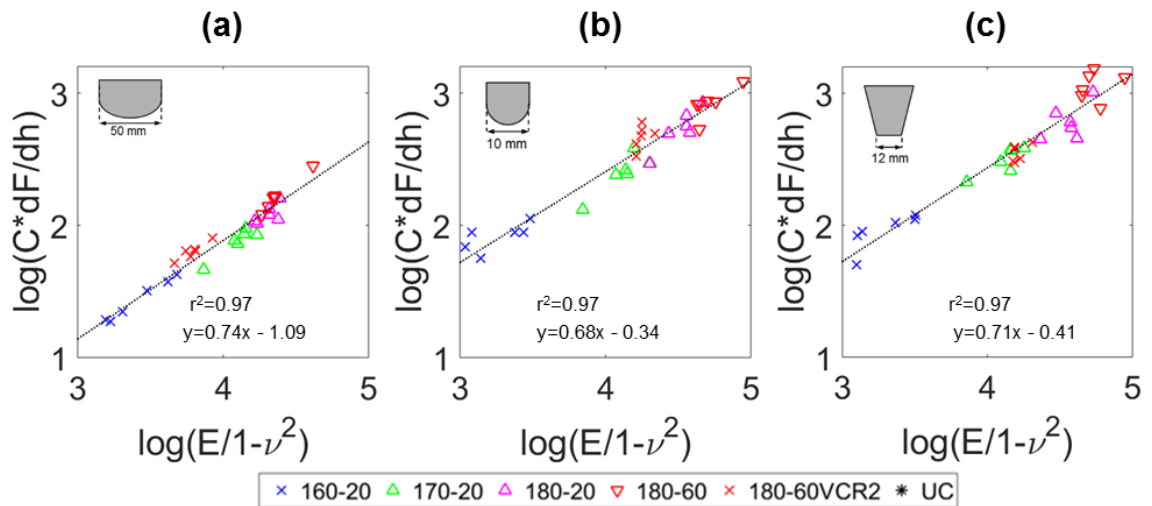
Figure 4.21: the natural logarithm of the gradient of Force (F), with the correction factor applied (Equation 4.6) vs Indentation depth (h) plots for all samples vs the negative natural logarithm of the denominator in Equation 1 for indentation resistance measured using the a) 50 mm Cylindrical indenter, b) 10 mm cylindrical indenter and c) 12mm studded indenter, up to 20% compression, outlying, anisotropic UC removed. Legend shows conversion conditions. Formulae show gradients, which should correspond to x (Equation 4.3). Formulae show gradients, which should correspond to x (Equation 4.3).

4.3.3. Energy absorption

Calculating an appropriate strain range to measure Young's modulus and normalise indentation resistance for each sample requires accurate measurement of mean compressive strain under indentation. Mean compression under indentation varies within each sample (Figure 4.13), between samples and between indenters (Figure 4.14), making it complex and a possible source of error. Energy absorption (Equation 4.14, whereby F and h are force and

indentation depth respectively) gives energy absorbed during either flat plate compression or indentation:

$$U = \int F \, \Delta h \tag{4.14}$$

Equation 4.15, whereby U_i is the energy absorbed during indentation and U_c is the energy absorbed during compression (Equation 4.14), could reduce the effect of non-linearity. In the case of the samples presented here, the effect of anisotropy could also reduce by allowing analysis of the data over a larger strain range (see Figure 4.9 in the thesis). Equation 4.15 would be valid if results of logarithmic plots are comparable to those from Figure 4.20 and Figure 4.21, for Equation 4.3. Figure 4.22 repeats Figure 4.19 but replaces dF/dh with U_i and E with U_c. The fit (r^2) was strong and x was close to one during cylindrical indentations (Figure 4.22a & b), but not during studded indentations (Figure 4.22c) where the unconverted samples were outliers and x was lower than expected.

$$U_i \propto \left(\frac{U_c}{(1-v^2)} \right)^x \tag{4.15}$$
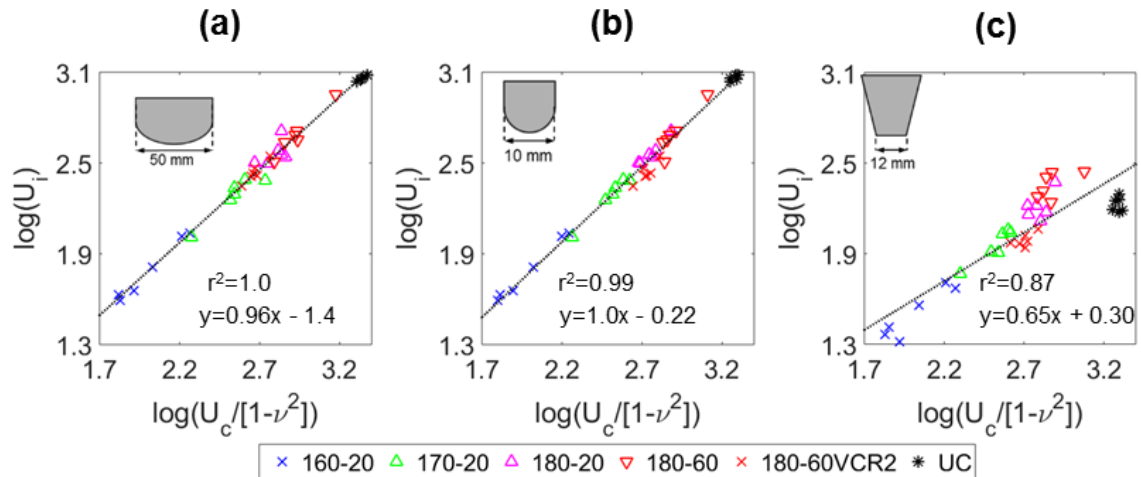
Figure 4.22: the natural logarithm of the gradient of indentation energy (U_i, integral of F w.r.t. h) plots for all samples vs the negative natural logarithm of the denominator in Equation 1 for indentation resistance but with E replaced with U_c measured using the a) 50 mm Cylindrical indenter, b) 10 mm cylindrical indenter and c) 12mm studded indenter, up to 20% compression. Legend shows conversion conditions. UC are unconverted samples. Formulae show gradients, which should correspond to x (Equation 1).

Correcting all measured, normalised indentation energies, the values for x (Figure 4.23) trend towards expected values and also towards those values obtained for corrected dF/dh during cylindrical indentations (Figure 4.21a & b), with strong regression fits. The studded indentation moves further from expected values, with a lower r^2 than in Figure 4.22c.
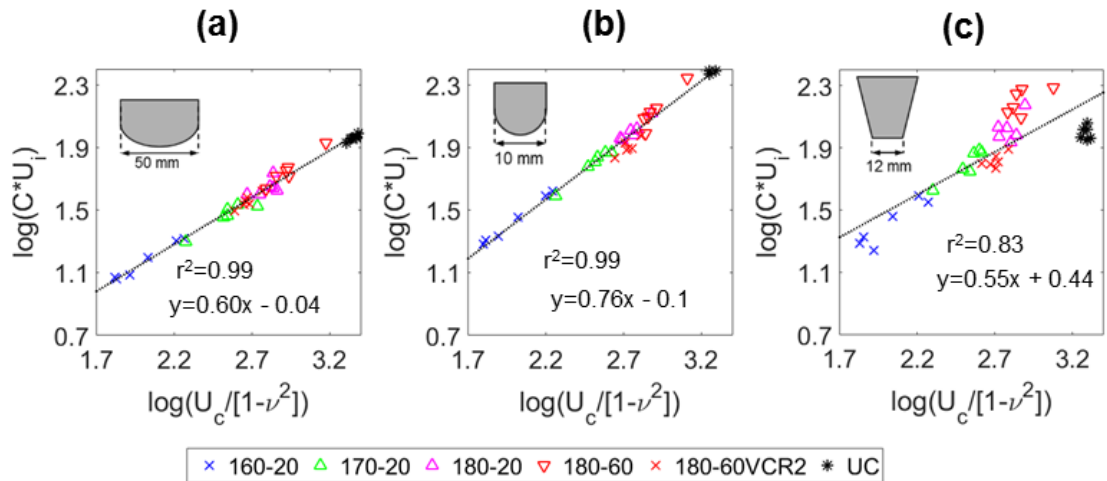
Figure 4.23: the natural logarithm of the gradient of corrected (Equation 3) indentation energy (U_i, integral of F w.r.t. h) plots for all samples vs the negative natural logarithm of the denominator in Equation 1 for indentation resistance but with E replaced with U_c measured using the a) 50 mm Cylindrical indenter, b) 10 mm cylindrical indenter and c) 12mm studded indenter, up to 20% compression. Legend shows conversion conditions. UC are unconverted samples. Formulae show gradients, which should correspond to x (Equation 1).

Figure 4.24 shows the most appropriate analyses method for each case. For the cylindrical indenters, no change was made from Figure 4.23a & b. For the studded indentations, strong correlations were obtained after removing the unconverted samples, which are very different in density, cell structure and size from converted samples, and removing the correction factor, which previously appeared inappropriate, good fit with theoretical values for x (close to 1) and strong correlations are obtained (Figure 4.24c).
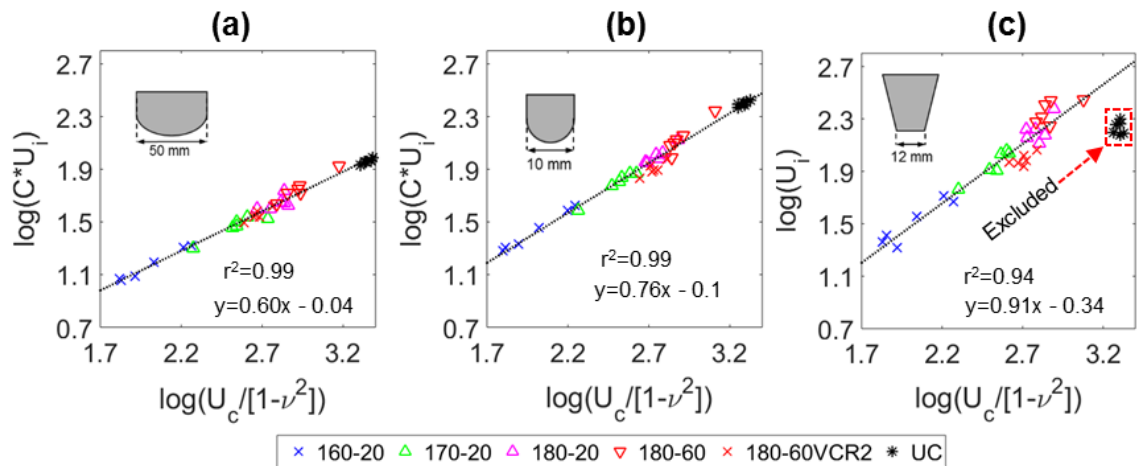
Figure 4.24: the natural logarithm of the gradient of a) & b) corrected (Equation 4.6), and c) uncorrected indentation energy (U_i, Equation 4.15) plots for all samples vs the negative natural logarithm of the denominator in Equation 4.3 for indentation resistance but with E replaced with U_c measured using the a) 50 mm Cylindrical indenter, b) 10 mm cylindrical indenter and c) 12mm studded indenter, outlying UC samples removed, values obtained up to 20% compression. Legend shows conversion conditions. UC are unconverted samples. Formulae show gradients, which should correspond to x (Equation 4.3).

Modest effects of Poisson's ratio on normalised indentation energy were obtained during indentation with either cylindrical indenter (Figure 4.25a & b). The effect was greater for

the lower area, studded indenter (Figure 4.25c). Samples with a negative Poisson's ratio exhibit higher normalised indentation energy than unconverted, positive Poisson's ratio samples (Figure 4.25c). Correlation was only of medium strength ($r^2 \sim 0.4$), due to differences in Young's modulus and also the size of samples. Comparing samples of the same size but different Poisson's ratio, the effect of Poisson's ratio appears to be amplified. The NPR samples were typically larger (~25.5 mm sides) than the near zero (~22 to ~25.5 mm sides) and positive (~20 mm sided) samples (Figure 4.25a to c). Comparing samples of the same Poisson's ratio but different size (Figure 4.25), the smaller samples exhibit higher corrected, normalised indentation energy. Increases to corrected, normalised indentation energy are, therefore, likely to be larger than presented here.

The effect of densification underneath an indenter or impactor could potentially increase stiffness, assuming there is not sufficient change in cell shape [4]. Poisson's ratio was retained during all indentations of iso-volume, iso-density samples with near zero and NPR (Figure 4.26). Therefore auxetic samples (Figure 4.26b - d) exhibited greater densification and could have become stiffer. Indenting 1 mm thick samples of foam and observing structural changes shows that unconverted foam's cells buckle during indentation (Figure 4.27a). The effect of densification is therefore unclear with regards to the unconverted foam. No change was observed with the NPR (Figure 4.27b) and near zero Poisson's ratio (Figure 4.27c) re-entrant foams, and densification due to transverse contraction may affect normalised indentation energy.
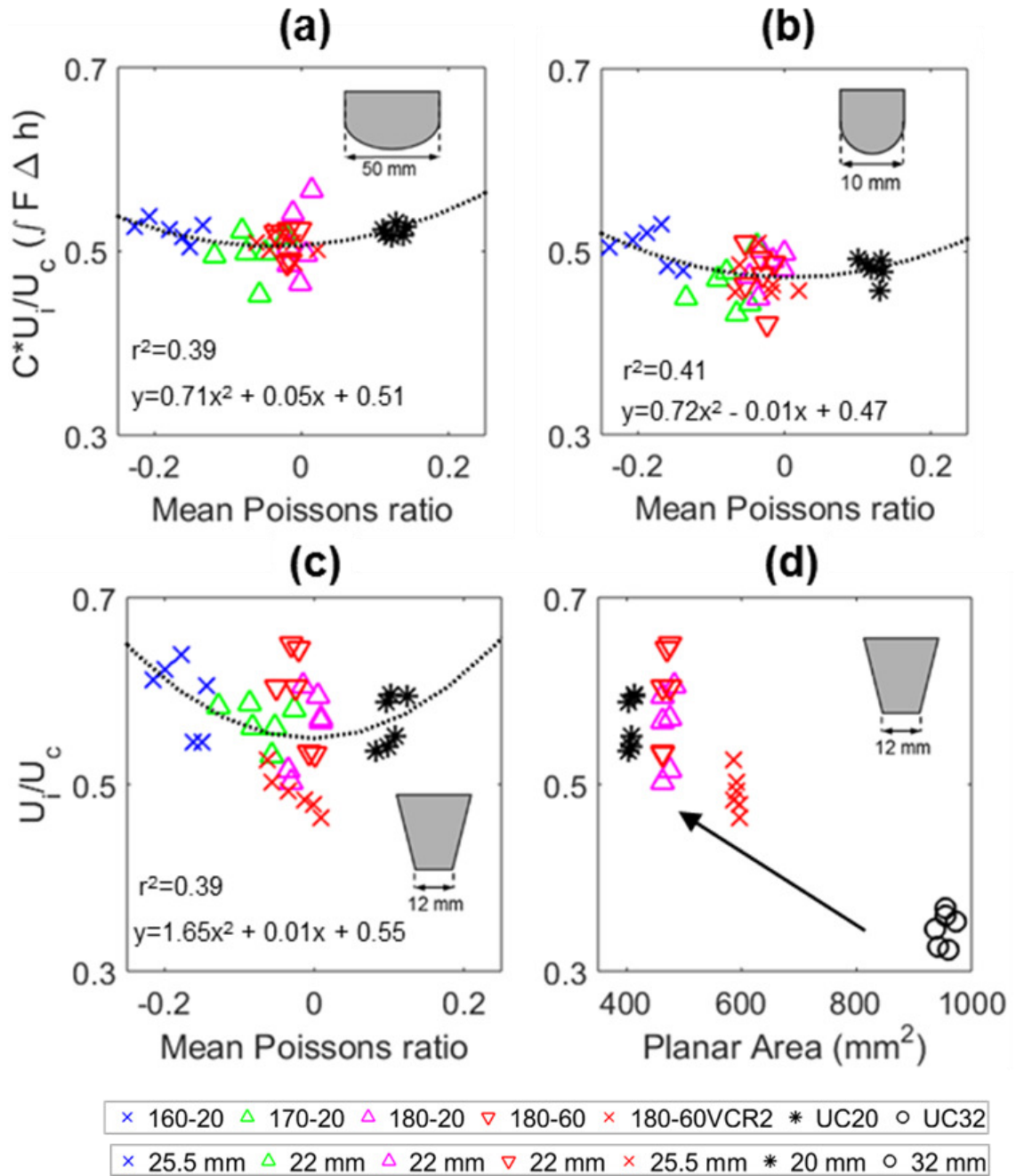
Figure 4.25: a to c) Mean Poisson's ratio v_{zy} (to 20% compression) vs normalised Indentation Resistance (a & b corrected according to Equation 4.6), d) Normalised Indentation Energy vs sample planar area during studded indentations of converted samples with near zero Poisson's ratio and 20mm and 32 mm sided, unconverted samples. Legends show conversion conditions. UC are unconverted samples. Sizes are in mm.
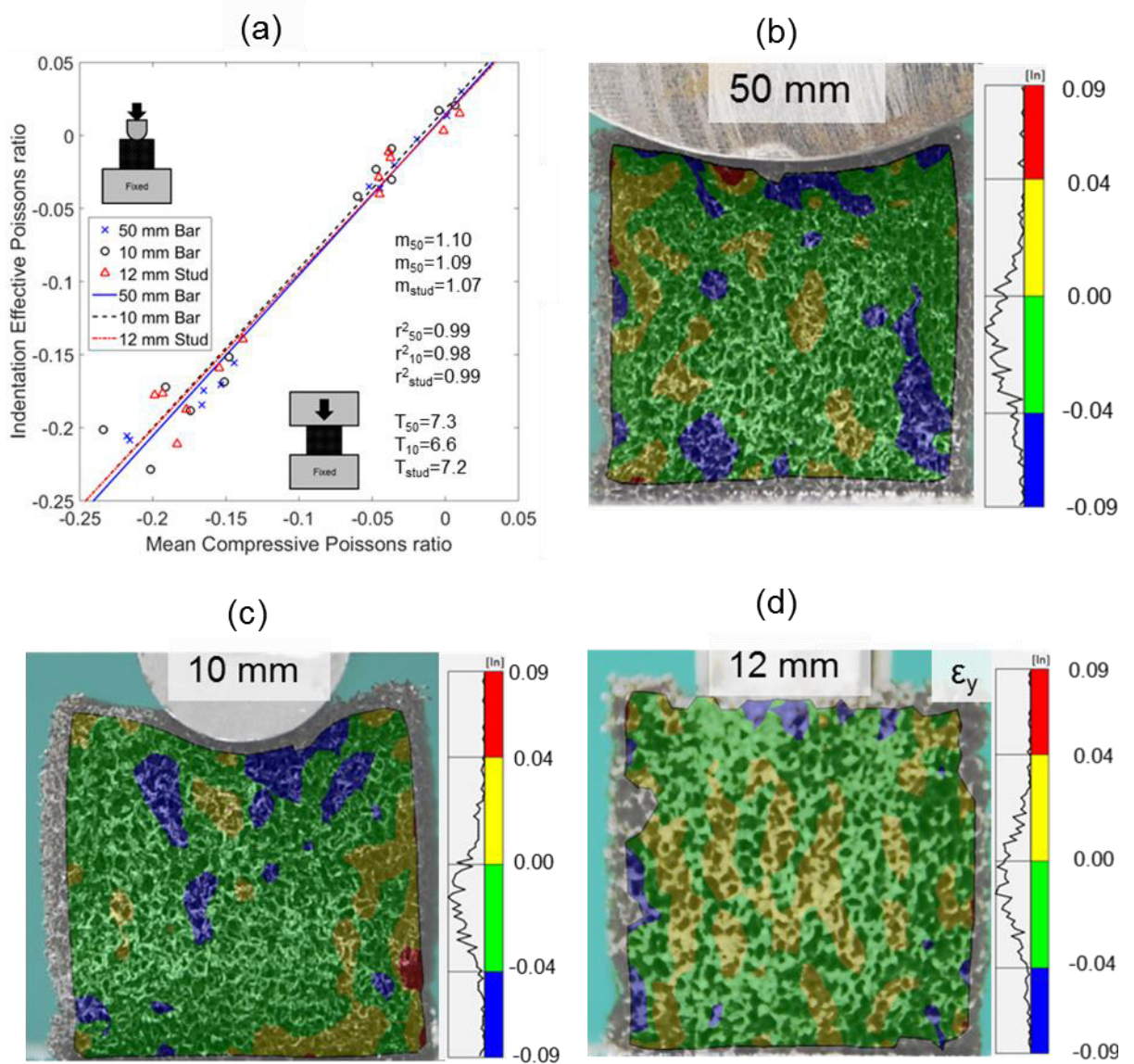
Figure 4.26: a) Indentation Effective Poisson's ratio vs Mean flat plate Poisson's ratio (to 20% compression, Figure 4.12a & b, axial and transverse directions parallel to z & y axes respectively). b) - d) Transverse strain at maximum compression by the b) 50 mm cylindrical, c) 10 mm cylindrical and d) 12 mm studded indenters. Same legend (d) for each.
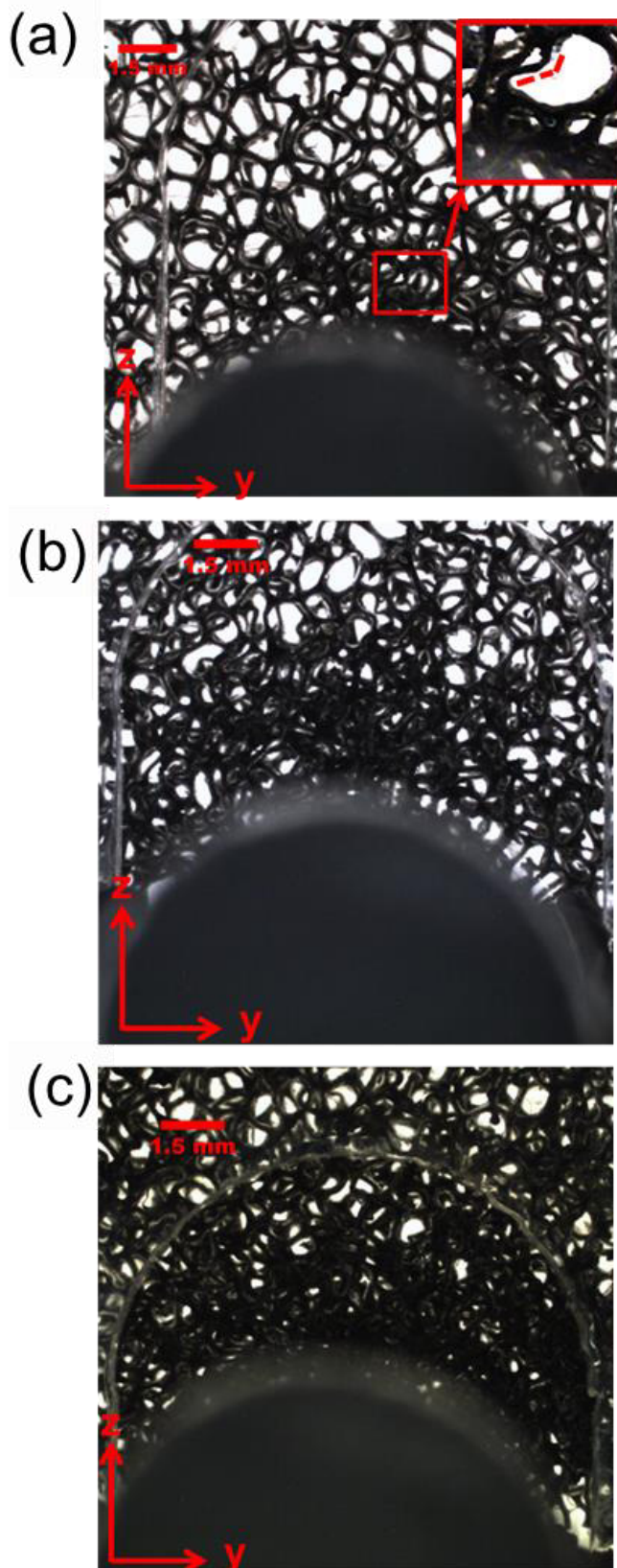
Figure 4.27: Magnified images taken of a) Unconverted foam, b) auxetic foam with an FVR of 2 (160°C, 20 minutes, VCR=3) and c) ~zero Poisson's ratio foam with an FVR of 2 (180°C, 60 minutes, VCR=2) under ~20% indentation with a 10 mm diameter cylinder. Pop-out in a) shows a single cell's shape from location close to the indenter, enlarged by a factor of two with underlying cell ribs removed.

Densification differences were present during indentation with all three indenters (Figure 4.26). For the iso-density, iso-volume samples with near zero and NPR, differences in the shape of the compressed area were not significant during indentation with the 50 mm cylinder (Figure 4.28a). A students T-test found a small but statistically significant difference was present during indentation with the 10 mm cylinder (α=0.05, Figure 4.28b). A large, statistically significant difference was present during the studded indentation (Figure 4.28c). Samples compress by a greater amount close to either cylindrical indenter (Figure 4.26, Figure 4.28d & e). The contact region with the studded indenter was not visible (Figure 4.28f).
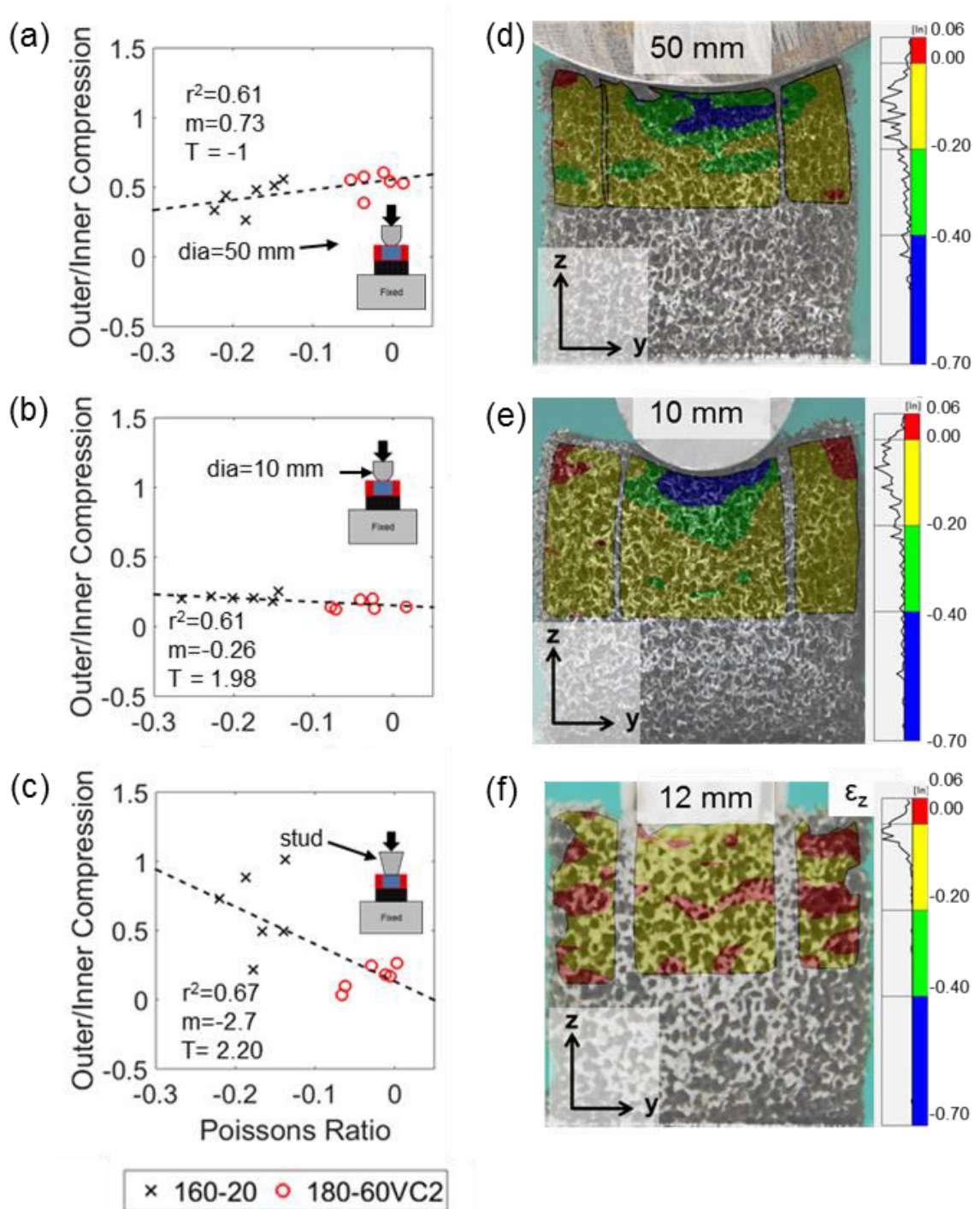
Figure 4.28: a - b) Outer (red in schematic) vs Inner (blue in schematic) axial compression (Figure 4.12c & d) for all samples with an FVR of 2 (160°C, 20 minutes, VCR=3 and 180°C, 60 minutes, VCR=2) during compression with: a) The 50 mm diameter cylinder, b) The 10 mm diameter cylinder, c) The 12 mm diameter stud: d-f) Segmented, axial strain in NPR, FVR = 2 samples (160°C, 20 minutes, VCR=3) at maximum compression. Same legend (f) for each.

4.4. Discussion

Normalising indentation energy to measured compressive energy allowed analysis of non-linear unconverted samples (Figure 4.8), and NPR foams exhibited higher normalised indentation energy than equivalent magnitude positive Poisson's ratio samples (Figure 4.25). The values attained for gradients of the log-log plots were close to expected values when using data from linear stress vs strain and transverse vs axial strain regions, prior to buckling at ~5% compression in the unconverted foam (x, Equation 4.3, Figure 4.19), although only medium/low correlations ($r^2 \sim 0.5$) were obtained. As in previous work ([3,36,37]) some discrepancies, particularly in the value for x during studded indentation (x = 0.53, Figure 4.19), were likely caused by anisotropy (Figure 4.9). All values for x were closer to one after anisotropic foams were removed (Figure 4.20 and Figure 4.21) and correlations were stronger ($r^2 > 0.95$).

When energy absorption, rather than linear quantities were calculated (Equation 4.14) and correction factors were applied (Equation 4.6) to data from the cylindrical indenters (Figure 4.24), but not from the studded indenter, x reduced towards expected values and the unconverted samples were no longer outlying. Excellent agreement was observed between H (Equation 4.3, Figure 4.20c & Figure 4.21a & b) and Ui (Equation 4.15, Figure 4.24). The effect of the ratio of planar dimensions to contact area was not accounted for within corrections. The 50 mm radius indenter was large in comparison to sample planar dimensions (~20 to 26 mm), and contact was across the whole sample (Figure 4.24a), which may have contributed to the increase in the obtained value for x. For the stud, however, the near vertical walls (Figure 4.4) mean additional contact was unlikely. Some minor effect of the filleted edge could have contributed to a reduction in the obtained value for x, tending towards 0.67 (for a hemispherical indenter), but the bevel was very small suggesting additional influencing factors.

One possible reason for the increased indentation resistance of foams with NPR is that effective Poisson's ratio during indentation was still similar to Poisson's ratio measured during flat plate compression (Figure 4.14 and Figure 4.22). Density increase (due to transverse strain) would have increased due to contraction in NPR samples (Figure 4.14 and Figure 4.22). Densification can increase foam stiffness [4] and could therefore effectively increase effective indentation resistance further than predictions by indentation theory, even for modest values (~-0.2) of NPR, comparable in magnitude to the parent foam (Equation 4.3). The ribs of unconverted samples buckled close to the indenter (Figure 4.23). Due to the changing cell shape and clear effect on modulus (Figure 4.8a), Gibson & Ashby's relationship between density and Young's modulus should not be applied to the unconverted samples without further confirmation of its effect, possibly by finite element modelling and micro-computed

tomography showing the fine detail of cell structures [32,38]. There is no evidence to suggest densification would not have increased the stiffness of converted samples, but as images do not show changing cell shapes in detail, they can only be qualitatively inspected and further micro computed tomography or modelling is also required.

Densification would have occurred during indentation with all three indenters (Figure 4.26). It is not clear that increased density can explain why the effect of elastic properties on normalised indentation energy (Equation 4.15) was greater than expected for the studded indenter (Figure 4.24c). NPR samples exhibited higher mean axial compression than samples with a near zero Poisson's ratio under indentation (Figure 4.13, Figure 4.14). Lower variation in mean outer/inner axial compression for the 10 mm cylindrical and 12 mm studded indenters was statistically significant for NPR samples (Figure 4.28b). Samples with a lower Poisson's ratio deformed with a 'flatter' profile, agreeing with previous indentation work [21,23–26], deforming by a greater amount in their extremities and increasing overall axial compression. Along with the previously discussed effects of transverse densification, deforming as a flatter unit would further increase the amount of compressed material and effective indentation resistance, and could explain the increased values obtained for x (Equation 4.3 [3]), particularly during studded indentations.

Since reasons for discrepancies can be explained, it seems that normalised indentation energy is an acceptable measure of resistance to penetrating or concentrated loads. The correction factor for thin sheets of rubber lowered values for x into more elastic regions (Equation 6 [5]), and therefore, appears applicable to auxetic and conventional foams. Poisson's ratios measured up to 10% compression (Figure 4.9a) differ from measurements up to 20% compression (Figure 4.16, Figure 4.24, Figure 4.26) due to sample non-linearity. The amount of axial compression during indentation varies throughout a sample (Figure 4.13, Figure 4.28), and also between samples and indenters (Figure 4.14, Figure 4.28). As with normalising hardness to Young's modulus, finding the correct strain range to calculate Poisson's ratio over would be complex and a possible source of error. Integrating axial vs transverse strain plots to obtain total lateral deformation may be more appropriate than comparing Poisson's ratios.

Rather than measuring Young's modulus and indentation resistance, comparing energy absorption has allowed analysis over a larger strain range than previous work indenting auxetic foam [21]. The lowest NPR auxetic (~25.5 mm sided, FVR ~2, ν~-0.2) foams corrected, normalised indentation energy was: i) comparable to smaller, denser (22 mm sided, FVR ~3) samples with a Poisson's ratio of zero; ii) greater than similar size and density (25.5 mm sided, FVR ~2) samples with a Poisson's ratio of zero, iii) greater than smaller, positive Poisson's ratio

(20 mm sided, ν~0.2) conventional foam samples for both 10 mm cylindrical (Figure 4.25b) indentation and 12 mm studded indentation (Figure 4.25, c & d).

Reducing samples size increased normalised indentation energy (Figure 4.25d). The indenters were a fixed size, so indenting smaller samples meant a greater fraction was compressed by each indenter; which was more similar to compressing them with a flat plate. The findings extend previous work, where the effect of NPR foam samples could have been amplified by sample non-linearity [21,39], density [22,40–42] or anisotropy [14,28]. Auxetic foams with modest NPR (~-0.2) would therefore be expected to reduce penetration in quasi-static indentations (i.e. seating, bedding, climbing/gymnasium mats and packaging) [43,44]. Now that the importance of samples size and amount of expected re-expansion following conversions has been confirmed, in future sample size can be controlled. Samples could be ordered pre-cut to the precise sizes that will give the same final dimensions, using different sized moulds for different conversion conditions.

The findings support the application of auxetic foam to protective equipment: indentation resistance can be increased following single stage thermo-mechanical conversions, even if the magnitude of Poisson's ratio is not increased. Since the normalised indentation energy approach was successful, further work should now confirm whether Poisson's ratios, and increased indentation resistance are retained under impacts at higher maximum strain (~80%) and strain rates [22,28,45], before application to sporting protective equipment. The technique of comparing energy absorption can be applied to force/displacement data following impact tests. Impact energy is typically used to categorise impacts in certification tests [12,46,47], and energy absorption can be used to characterise impact attenuating materials [11,47,48]. Further work using different parent foams, or applying newly proposed CO_2 softening routes could increase the magnitude of NPR and the effect size [49].

Protective sporting equipment often has a larger planar area than the samples presented here [11–13]. The standard test for measuring the indentation resistance of rubber also requires samples with a larger width (11.5 mm to 13 mm outside of the contact area [18]). If indenter size is decreased (rather than sample size increased) the ratio of pore size to contact area may result in non-continuum effects, although the ratio between contact area and indenter size is unknown. As such, larger sheets of auxetic foam are required to facilitate both commercial fabrication and certifiable measurements of indentation resistance. A fabrication method for large, homogenous samples of auxetic foam could also reduce fabrication costs and time. Larger foam fabrications are often difficult, with reported variation and surface creasing [16,43,50,51]. Identifying increased densification, both microscopically (Figure 4.27d - e) and

with DIC (Figure 4.12, Figure 4.26), as well as increased buckling close to the indenter (Figure 4.27d - e), suggests reasons for surface densification in converted samples: previously reported external densification in thermo-mechanical conversion [52]. Distributing surface densification throughout the bulk of the material by controlling and applying internal compression using pins [29] could reduce overall variability, but densification may occur close to pins.

Large homogeneous sheets could be used to quantify the effect of Poisson's ratio on indentation resistance where greater effects would typically be expected than in the small cubes used in this work [5], since reducing sample size appears to reduce the effect of NPR (Figure 4.25d). Using a pressure sensor (e.g. Tekscan) beneath the sample or between the foam and the indenter during indentation tests would be a useful method to cross-validate DIC and quantify pressure concentrations, which can contribute to injury [11,13]. Using multiple cameras could measure front/back displacement of the targeted face and deformation of multiple faces of samples to confirm NPR's affect more precisely.

The effect of thin shells common in current sports equipment [11,13,39] should also be considered in further work. Previous work has suggested larger improvements for an auxetic than a conventional foam, when used in combination with a thin shell [22], but did not account for large differences in density and stress vs strain relationships between auxetic and conventional foams. NPR had the greatest effect when using a smaller indenter (Figure 4.24, Figure 4.25), and so adding a rigid shell appears likely to reduce the benefit of NPR. Testing whether Poisson's ratio still effects indentation resistance, and whether auxetic materials can reduce the need for a thin shell and increase equipment conformability, would show whether auxetic foams can improve protection and ergonomics, meeting current trends and replacing or improving pads featuring shear thickening fluids [11,13]. Increased normalised indentation energy in NPR samples supports: i) a reduction in the rigidity or thickness of a covering shell, or ii) using a combination of auxetic foam and STF to reduce the likelihood of penetration during impacts at strain rates below the stiffening threshold of PPE featuring STFs, as described in Chapter 2, Pages 11-12.

4.5. References

1. Roark RJ, Young WC. Formulas for stress and strain. McGraw-Hill, USA; **2012**. 20-22, 48-50 p.
2. Timoshenko SP, Goodier JN. Theory of Elasticity. 3rd ed. New York: McGraw-Hill, USA; **1970**.
3. Alderson KL, Pickles AP, Neale PJ, Evans KE. Auxetic polyethylene: The effect of a negative Poisson's ratio on hardness. Acta Metall Mater. 1994.42(7). 2261–6.
4. Gibson LJ, Ashby MF. Cellular solids. Structure and properties. **1997**. 67, 176-183, 259-264, 286, 498 p.
5. Waters NE. The indentation of thin rubberer sheets by cylindrical indetors. Br J Appl Phys. 1965.16(2). 1387–92.
6. Argatov II, Guinovart-Díaz R, Sabina FJ. On local indentation and impact compliance of isotropic

auxetic materials from the continuum mechanics viewpoint. Int J Eng Sci. 2012.54. 42–57.

7. Photiou D, Sarris E, Constantinides G. On the conical indentation response of elastic auxetic materials: Effects of Poisson's ratio, contact friction and cone angle. Int J Solids Struct. 2017.110–111. 404.

8. Photiou D⊚, Sarris E⊚, Constantinides G⊚. Erratum to "On the conical indentation response of elastic auxetic materials: Effects of Poisson's ratio, contact friction and cone angle" [Int. J. Solids Struct. 81 (2016) 33–42]. Int J Solids Struct. 2017.81(33–42).

9. Guo X, Jin F, Gao H. Mechanics of non-slipping adhesive contact on a power-law graded elastic half-space. Int J Solids Struct. 2011.48(18). 2565–75.

10. Annual Book of ASTM Standards. Standard Test Methods for Flexible Cellular Materials — Slab , Bonded , and Molded Urethane Foams. Annual Book of ASTM Standards 2008.

11. Ankrah S, Mills NJ. Performance of football shin guards for direct stud impacts. Sport Eng. 2003.6(4). 207–19.

12. European Committee for Standardization. BS 6183-3:2000-Protective equipment for cricketers. 2000.

13. Hrysomallis C. Surrogate thigh model for assessing impact force attenuation of protective pads. J Sci Med Sport. 2009.12(1). 35–41.

14. Scarpa F, Giacomin J, Zhang Y, Pastorino P. Mechanical performance of auxetic polyurethane foam for antivibration glove applications. Cell Polym. 2005.24(5). 253–68.

15. Lakes RS. Foam Structures with a Negative Poisson's Ratio. Science (80-). 1987.235(4792). 1038–40.

16. Chan N, Evans KE. Fabrication methods for auxetic foams. J Mater Sci. 1997.32. 5945–53.

17. Boba K, Bianchi M, McCombe G, Gatt R, Griffin AC, Richardson RM, et al. Blocked shape memory effect in negative Poisson's ratio polymer metamaterials. ACS Appl Mater Interfaces. 2016. acsami.6b02809.

18. The British Standards Institution Bs. BS 903-A26: 1995 ISO 48:1994. Physical Testing of Rubber. **2006**. p. 1–387.

19. Duncan O, Allen T, Foster L, Senior T, Alderson A. Fabrication, characterisation and modelling of uniform and gradient auxetic foam sheets. Acta Mater. 2017.126. 426–37.

20. Chan N, Evans KE. The mechanical properties of conventional and auxetic foams. Part I: compression and tension. J Cell Plast. 1999.35(2). 130–65.

21. Chan N, Evans KE. Indentation resilience of conventional and auxetic foams. J Cell Plast. 1998.34. 231–60.

22. Allen T, Shepherd J, Hewage TAM, Senior T, Foster L, Alderson A. Low-kinetic energy impact response of auxetic and conventional open-cell polyurethane foams. Phys Status Solidi Basic Res. 2015.9. 1–9.

23. Aw J, Zhao H, Norbury A, Li L, Rothwell G, Ren J. Effects of Poisson's ratio on the deformation of thin membrane structures under indentation. Phys Status Solidi Basic Res. 2015.252(7). 1526–32.

24. Argatov II, Sabina FJ. Small-scale indentation of an elastic coated half-space: The effect of compliant substrate. Int J Eng Sci. 2016.104. 87–96.

25. Morris DJ, Cook RF. Indentation fracture mechanics model. 2008.23(9). 2429–42.

26. Li S, Al-Badani K, Gu Y, Lake M, Li L, Rothwell G, et al. The Effects of Poisson's Ratio on the Indentation Behavior of Materials With Embedded System in an Elastic Matrix. Phys Status Solidi Basic Res. 2017.254(12). 1–8.

27. Pierron F, McDonald SA, Hollis D, Fu J, Withers PJ, Alderson A. Comparison of the mechanical behaviour of standard and auxetic foams by x-ray computed tomography and digital volume correlation. Strain. 2013.49(6). 467–82.

28. Ge C. A comparative study between felted and triaxial compressed polymer foams on cushion performance. J Cell Plast. 2013.49(6). 521–33.

29. Sanami M, Alderson A, Alderson KL, McDonald S a., Mottershead B, Withers PJ. The production and characterization of topologically and mechanically gradient open-cell thermoplastic foams. Smart Mater Struct. 2014.23(5). 055016.

30. Duncan O, Allen T, Foster L, Gatt R, Grima JN, Alderson A. Controlling Density and Modulus in Auxetic Foam Fabrications—Implications for Impact and Indentation Testing. Proceedings. 2018.2(6). 250.

31. Phillips N, Hassan GM, Dyskin A, Macnish C, Pasternak E. Digital image correlation to analyze nonlinear elastic behavior of materials. Proc - Int Conf Image Process ICIP. 2018.2017–Septe.

32. McDonald SA, Dedreuil-Monet G, Yao YT, Alderson A, Withers PJ. In situ 3D X-ray

microtomography study comparing auxetic and non-auxetic polymeric foams under tension. Phys Status Solidi Basic Res. 2011.248(1). 45–51.

33. Chiang FP, Uzer G. Mapping full field deformation of auxetic foams using digital speckle photography. Phys Status Solidi Basic Res. 2008.245(11). 2391–4.

34. Allen T, Hewage T, Newton-Mann C, Wang W, Duncan O, Alderson A. Fabrication of Auxetic Foam Sheets for Sports Applications. Phys Status Solidi Basic Res. 2017.1700596. 1–6.

35. Alderson A, Davies PJ, Alderson KIML, Smart GM. The Effects of Processing on the Topology and Mechanical Properties of Negative Poisson's Ratio Foams. Proc IMECE2005 2005 ASME Int Mech Eng Congr Expo Proc IMECE200. 2005. 1–8.

36. Alderson KL, Fitzgerald A, Evans KE. The strain dependent indentation resilience of auxetic microporous polyethylene. J Mater Sci. 2000.35(16). 4039–47.

37. Alderson A, Evans KE. Modelling concurrent deformation mechanisms in auxetic microporous polymers. J Mater Sci. 1997.32(11). 2797–809.

38. McDonald SA, Ravirala N, Withers PJ, Alderson A. In situ three-dimensional X-ray microtomography of an auxetic foam under tension. Scr Mater. 2009.60(4). 232–5.

39. Allen T, Duncan O, Foster L, Senior T, Zampieri D, Edeh V, et al. Auxetic foam for snow-sport safety devices. Snow Sport Trauma Saf Proc Int Soc Ski Saf. 2016.21.

40. Duncan O, Foster L, Senior T, Alderson A, Allen T. Quasi-static characterisation and impact testing of auxetic foam for sports safety applications. Smart Mater Struct. 2016.25(5). 054014.

41. Lakes RS, Elms K. Indentability of Conventional and Negative Poisson's Ratio Foams Rwas. 1993.27(12). 1193–202.

42. Lisiecki J, Klysz S, Blazejewicz T, Gmurczyk G, Reymer P. Tomographic examination of auxetic polyurethane foam structures. Phys Status Solidi Basic Res. 2013.251(2). 314–20.

43. Lowe A, Lakes RS. Negative Poisson's ratio foam as seat cushion material. Cell Polym. 2000.19(3). 157–67.

44. Wang YC, Lakes R. Analytical parametric analysis of the contact problem of human buttocks and negative Poisson's ratio foam cushions. Int J Solids Struct. 2002.39(18). 4825–38.

45. Lisiecki J, Błazejewicz T, Kłysz S, Gmurczyk G, Reymer P, Mikułowski G. Tests of polyurethane foams with negative Poisson's ratio. Phys Status Solidi Basic Res. 2013.250(10). 1988–95.

46. Standardization EC for. EN 1621-2 2003 Motorradfahrer Schutzkleidung Teil 2 Rückenprotektoren. **2003**.

47. Payne T, Mitchell S, Halkon B, Bibb R, Waters M. Development of a synthetic human thigh impact surrogate for sports personal protective equipment testing. Proc Inst Mech Eng Part P J Sport Eng Technol. 2016.230(1). 5–16.

48. Ankrah S, Mills NJ. Analysis of ankle protection in Association football. Sport Eng. 2004.7(1). 41–52.

49. Li Y, Zeng C. Room-Temperature, Near-Instantaneous Fabrication of Auxetic Materials with Constant Poisson's Ratio over Large Deformation. Adv Mater. 2016.28(14). 2822–6.

50. Loureiro MA, Lakes RS. Scale-up of transformation of negative Poisson's ratio foam: Slabs. Cell Polym. 1997.16(5). 349–63.

51. Bianchi M, Scarpa F, Smith CW. Shape memory behaviour in auxetic foams: Mechanical properties. Acta Mater. 2010.58(3). 858–65.

52. Bianchi M, Frontoni S, Scarpa F, Smith CW. Density change during the manufacturing process of PU-PE open cell auxetic foams. Phys Status Solidi Basic Res. 2011.248(1). 30–8.

Chapter 5: Fabrication of large uniform and gradient sheets of auxetic open cell PU foam with internally controlled compression

5.1. Introduction

There are no current methods to control and adapt internal compression during fabrication of large auxetic foam samples, leading to the third aim of this thesis (Chapter 1, Page 5).

Methods to control, adapt and assess the structure of fabricated foam sheets are described in the following method's section. This work was published in Acta Materialia [1], although dimensional stability testing has been included here, to assess the long term behaviour of fabricated foams and assess whether the level of heating was appropriate. In Chapter 3 (Page 46), small samples of the same foam exhibited the highest magnitude of NPR when they exhibited a Final Volume Ratio (FVR, final/initial volume) of ~2, following re-heating without a mould. Descriptions of the analytical model (previously supplementary information [1]) are now included in the text, although reduced due to similarities with the model in Chapter 3 (Page 69).

5.2. Methods

5.2.1. Foam fabrication

A multi-stage thermo-mechanical process [2], adopted from previous studies on the same foam and range of sizes [3–5] was applied to open cell PU R30FR foam (Custom Foams). Foam sheets (508 x 491 x 28.5 mm) were compressed into a metal mould (internal dimensions 355 x 344 x 20 mm), with the rise direction through the thickness. A Linear Compression Ratio (LCR, initial length/final length) of 1.43 was thus applied in all 3 principal directions to two sheets corresponding to a VCR of 2.9. One uniform sheet utilised a square array of 36 steel pins of diameter 3.2 mm inserted through the thickness of the unconverted foam, with a typical spacing of 71.5 mm prior to insertion into the mould and 50 mm after insertion (Figure 5.1). The other sheet was fabricated without pins. A coordinate system was defined whereby z is through the sample thickness (or rise direction in unconverted samples) and x and y are the two planar axes (Figure 5.1a).
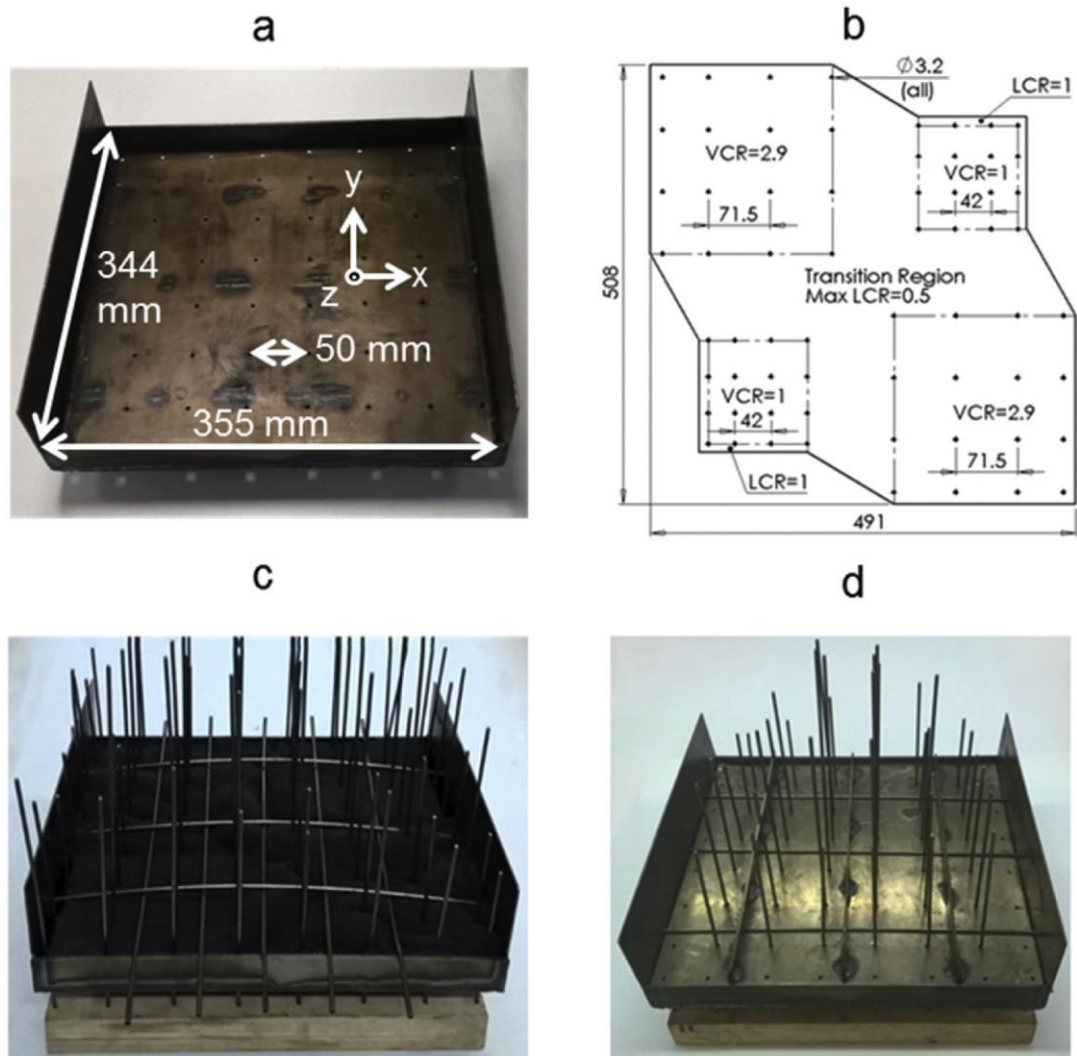
Figure 5.1: Compression mould. a) Mould lower section, b) Design of acrylic template defining overall shape and pin spacing for the non-uniform sheet (dimensions in mm), c) Assembled lower mould section and pins, with horizontal rods to compress bulges, d) Assembled mould and pins, with horizontal lid to apply through thickness compression.

A sheet was also fabricated with non-uniform compression, having quadrants with different VCRs separated by a transition region (Figure 5.1b). The unconverted sample was cut to size with a retractable-blade knife using a laser cut acrylic sheet template. Through-thickness pins applied planar compression or tension to different regions. To impose a VCR of 1, an LCR of 0.84 (i.e. linear extension of 19%) was applied in both planar directions (pin spacing ~ 42 mm prior to insertion, and 50 mm in the mould) in two diagonally opposite quadrants. An LCR of 1.43 was imposed in the remaining quadrants (pin spacing ~ 71.5 mm prior to insertion, and 50 mm in the mould), providing equal compression in each direction with a VCR of 2.9 to match the uniform sheets. In comparison to the uniform sheets, 28 additional pins were used 10 mm from the mould edge to apply tension and control transition regions.

The compression method comprised (only steps 3 & 4 apply without pins):

1) Pins were positioned in the unconverted foam by passing them through holes (maximum clearance = 0.1 mm) in a 5 mm thick laser cut acrylic sheet covering the sample. The acrylic sheet was then removed.

2) The pins were then inserted through holes in the lower box like section of the metal mould (Figure 5.1a) and into corresponding holes in a wooden guide block positioned below (Figure 5.1c & d), working from the centre to the edges of the mould.

3) All corners and edges of the sample were tucked into place around the edge of the mould. Horizontal rods were used to hold the foam in place while creases were removed (Figure 5.1c).

4) The flat lid was put into place (locating the pins in holes in the lid in the case of pinned samples) and the horizontal rods (Figure 5.1c) were removed as compression was applied. The lid was held in place by inserting three 3.2 mm diameter steel rods through holes in the walls of the mould (Figure 5.1d).

The closed mould assembly was subject to two heating stages at 180°C (25 and 15 min respectively) in a conventional oven (MCP Tooling Technologies LC/CD), followed by annealing at 100°C for 20 min in a separate oven (Genlab PWO/600), similar to previous work with this foam [3–5]. After each heating phase the mould was removed from the oven. Uniform sheets were taken out of their mould and gently stretched by hand to avoid adhesion of the cell ribs, with any pins removed after the 1st heating phase and not returned. Pins remained in place, to maintain tension, for both heating phases of the gradient sheet, before removal for annealing. This sheet was agitated between heating phases by compressing and releasing the lid. All samples were gently stretched before annealing.

5.2.2. Testing dimensional stability

Sections (130 x 70 x 20 mm) of the quadrants of the gradient sheet fabricated with a VCR of 1 and a VCR of 2.9 were reheated in an oven without a mould at 190°C for ten minutes (Genlab PWO/600). Dimensions were recording before and after reheating (Vernier Callipers). Final Volume Ratios (FVR, initial/final volume) were calculated for each sample.

5.2.3. Impact testing of the non-uniform sheet

Prior to dissection for structural and mechanical characterisation, the non-uniform sheet was covered un-bonded with a 2 x 350 x 350 mm polypropylene (PP) sheet (Direct Plastics, PPH/PP-DWST-Homopolymer). Impacts were based on the British Standard for cricket pads [6] and previous work [3], with the sample resting on a flat rigid surface rather than a curved anvil. Impacts were performed at 6 J by dropping a 2.095 kg, 72 mm diameter hemispherical hammer from 292 mm. Acceleration was recorded at 50 kHz with a hammer-mounted accelerometer (Analog devices, ADXL001-500 g). The sheet was impacted in the z direction close to the centre of 2 quadrants with different VCRs (Figure 5.2a). Three impacts were performed at each location, alternating between the imposed VCR = 1 and 2.9 quadrants. The interval between impacts was ~7.5 min, equating to ~15 min between repeats in the same location. Three shells were used, 2 impacts per shell, each on opposing corners. Impacted quadrants were not used for further testing.
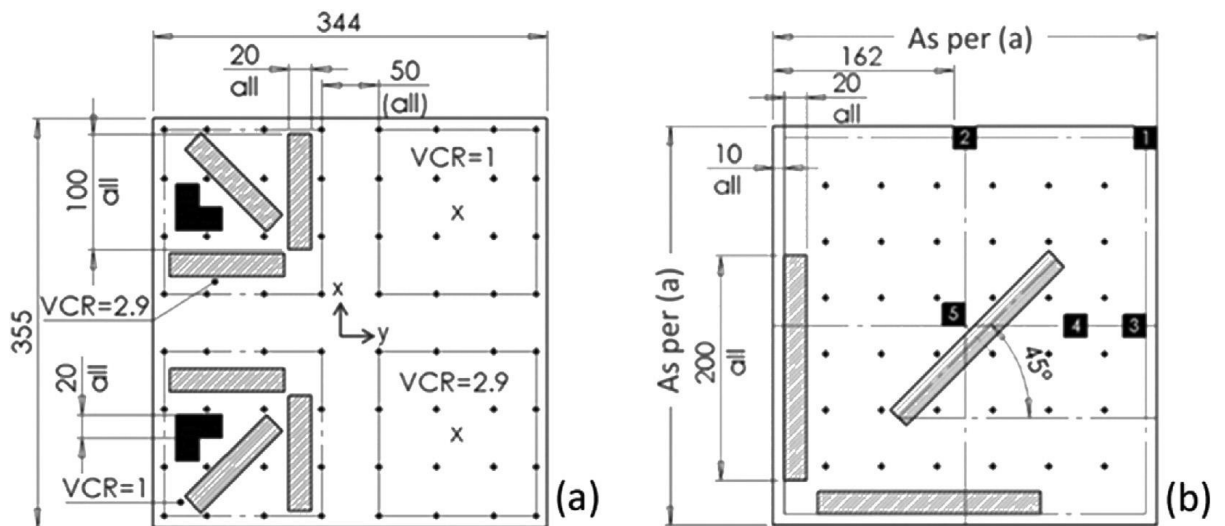
Figure 5.2: Test sample locations. Tensile (hatched rendering) and compression quasi-static test sample locations (black render) for: a) Non-uniform sheet (X marks impact locations, quadrants = 200 x 200 x 20 mm, tensile samples = 100 x 20 x 20 mm, cubes for compression = 20 mm sides), b) Uniform compression conversions [1 = Corner, 2 = edge, 3 = outer ring created by pins, 4 = 2nd ring, 5 = central two rings]. All dimensions in mm, sheets 20 mm thick.

5.2.4. Foam characterisation

Three cubes were cut from each of the distinct quadrants of the non-uniform foam (Figure 5.2a). For the uniform sheet 3 cubes were cut from 5 different regions (15 total), corresponding to: 1) corners, 2) positions along the edge, 3) positions 10 mm from the edge, 4) an intermediate region between 50 mm and 100 mm from the edge and 5) a region within 75 mm of the centre (example positions shown in Figure 2b). Three cuboidal samples were cut

from each of the uniform and distinct quadrants of the non-uniform foams, aligned along each of the in-plane directions, and also along an in-plane diagonal. Additionally, 6 cuboidal samples were cut from a larger block of unconverted foam, with 2 aligned along each axis. Densities of all dissected samples were measured using weighing scales (reliable to 0.001 g) and digital Vernier callipers (with an estimated measurement uncertainty of $\pm$ ~0.5 mm). The final VCR, determined from the ratio of converted to unconverted densities (30 kg/m^3, the centre of the supplier's stated density range of 28 to 32 kg/m^3 and checked using unconverted samples) was compared to the imposed value, to see if the intended amount of compression was achieved.

Mechanical characterisation comprised of tensile tests (strain rate = 0.0042 s^{-1}) on all cuboidal samples, and compression tests (strain rate = 0.0083 s^{-1}) on the cubic samples, to 50% engineering strain in an Instron 3367 machine fitted with a 500 N load cell. The movements of white-headed pins set into the front face of each sample, filmed with a Sony Handycam HFR-CX250, were tracked using an in-house Matlab R2015a (MathWorks) script for strain determination (frame rate of 5 Hz and resolution of 720 by 540 pixels). Poisson's ratio was obtained from linear regression of lateral true strain vs axial true strain. Tangent modulus (the slope of stress vs strain curves at defined intervals of axial strain) was obtained from linear regression of stress vs axial engineering strain from the marker tracking. The cuboidal test specimens were each subject to 4 tensile tests along their length, with the sample being rotated 90° between tests. This allowed tests with the x-y and x-z faces alternately oriented towards the camera, so that an in-plane and a through thickness Poisson's ratio was measured in tests 1 and 2, and also in tests 3 and 4 for each sample. The starting orientation was randomised between samples since it is known that the properties can vary with repeat testing. Hence results are presented for the average directional Poisson's ratios between samples from tests 1 and 2, and from tests 3 and 4. The cubic samples were each tested 3 times in compression: test 1 - loading through the thickness, test 2 - in-plane loading direction with x-z plane facing the camera, and test 3 - in-plane loading with x-y plane facing the camera.

Tested cubic samples were cut into thin (~1 mm) slices using a razor blade and placed on a white background to obtain microscopic images of cellular structure using a Stereoscope (Leica, S6D).

5.3. Analytical model derivation

5.3.1. Analytical expressions for the on and off-axis mechanical properties of a hexagonal honeycomb

The same method as in Chapter 3 was used to derive the on-axis analytical equations. A simplified projection of open cell foam as a 2D hexagonal honeycomb in each orthogonal plane (Figure 5.3) was used to adapt previous analytical expressions [7,8] for Poisson's ratio and Tangent modulus due to cell rib stretching, flexure and hinging. Firstly on axis (parallel to z and x) deformation were considered, before introducing an off-set angle (φ).
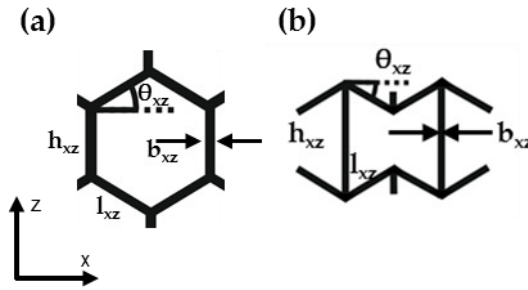
Figure 5.3: Cell geometrical parameters for a) A typical honeycomb (θ_{xz}>0) and b) A re-entrant honeycomb (θ_{xz}<0), same axis for both cells

Force constants (k_h and k_f) are:

$$k_{hf} = \frac{k_h k_f}{k_h + k_f} \tag{5.1}$$

Poisson's ratio (ν) and Young's modulus (E) are [8]:

$$\nu_{xz} = \frac{\sin\theta_{xz}\cos^2\theta_{xz}\left(\frac{1}{k_{hf}}-\frac{1}{k_s}\right)}{\left(\frac{h_{xz}}{l_{xz}}+\sin\theta_{xz}\right)\left[\frac{\sin^2\theta_{xz}}{k_{hf}}+\frac{\cos^2\theta_{xz}}{k_s}\right]} \tag{5.2}$$

$$\nu_{zx} = \frac{\sin\theta_{xz}\left(\frac{h_{xz}}{l_{xz}}+\sin\theta_{xz}\right)\left(\frac{1}{k_{hf}}-\frac{1}{k_s}\right)}{\left[\frac{\cos^2\theta_{xz}}{k_{hf}}+\frac{2\frac{h_{xz}}{l_{xz}}+\sin^2\theta_{xz}}{k_s}\right]} \tag{5.3}$$

$$E_x = \frac{\cos\theta_{xz}}{b_{xz}\left(\frac{h_{xz}}{l_{xz}}+\sin\theta_{xz}\right)\left[\frac{\sin^2\theta_{xz}}{k_{hf}}+\frac{\cos^2\theta_{xz}}{k_s}\right]} \tag{5.4}$$

$$E_z = \frac{\left(\frac{h_{xz}}{l_{xz}}+\sin\theta_{xz}\right)}{b_{xz}\cos\theta_{xz}\left[\frac{\cos^2\theta_{xz}}{k_{hf}}+\frac{2\frac{h_{xz}}{l_{xz}}+\sin^2\theta_{xz}}{k_s}\right]} \tag{5.5}$$

Shear modulus G_{zx} is (Equation 5.6):

$$\frac{1}{G_{zx}} = \frac{1}{G_f} + \frac{1}{G_h} + \frac{1}{G_s} \tag{5.6}$$

giving (Equation 5.7):

$$G_{zx} = \left[\frac{b_{xz}\left(\frac{h_{xz}}{l_{xz}}\right)^2\left(1+\frac{2h_{xz}}{l_{xz}}\right)\cos\theta_{xz}}{\kappa_{hf}\left(\frac{h_{xz}}{l_{xz}}+\sin\theta_{xz}\right)} + \frac{b_{xz}\left(1+\frac{h_{xz}}{l_{xz}}\sin\theta_{xz}\right)^2}{\kappa_s\cos\theta_{xz}\left(\frac{h_{xz}}{l_{xz}}+\sin\theta_{xz}\right)}\right]^{-1} \tag{5.7}$$

The expressions for off-axis Young's modulus (Equation 5.8) and Poisson's ratio (Equation 5.9) can be adapted in a similar manner from Ref [8]:

$$E_x(\phi) = \left[\frac{\cos^4\phi}{E_x} + \cos^2\phi\sin^2\phi\left(\frac{1}{G_{xz}} - \frac{2\nu_{xz}}{E_x}\right) + \frac{\sin^4\phi}{E_z}\right]^{-1} \tag{5.8}$$

$$\nu_{xz}(\phi) = E_x(\phi)\left[\frac{(\cos^4\phi+\sin^4\phi)\nu_{xz}}{E_x} - \cos^2\phi\sin^2\phi\left(\frac{1}{E_x} + \frac{1}{E_z} - \frac{1}{G_{xz}}\right)\right] \tag{5.9}$$

5.3.2. Analytical expressions for the on and off-axis strain of a hexagonal honeycomb

To predict variation of the mechanical properties with loading strain, the generic off-axis strain from the two on-axis components was first determined:

$$\varepsilon_x(\phi) = \varepsilon_x\cos^2\phi + \varepsilon_z\sin^2\phi \tag{5.10}$$

whereby:

$$\varepsilon_x = \ln\left(\frac{X}{X_0}\right) = \ln\left(\frac{l_{xz}\cos\theta_{xz}-\delta_{xz}\sin\theta_{xz}}{l_{xz(0)}\cos\theta_{xz(0)}-\delta_{xz(0)}\sin\theta_{xz(0)}}\right) \tag{5.11}$$

$$\varepsilon_z = \ln\left(\frac{Z}{Z_0}\right) = \ln\left(\frac{h_{xz}+l_{xz}\sin\theta_{xz}+\delta_{xz}\cos\theta_{xz}}{h_{xz(0)}+l_{xz(0)}\sin\theta_{xz(0)}+\delta_{xz(0)}\cos\theta_{xz(0)}}\right) \tag{5.12}$$

and X and Z are the unit-cell lengths along the x and z directions, respectively. δ is the deflection of the beam due to flexing [19], and the subscript '0' denotes the initial (undeformed) value of any geometrical parameter. Substituting Equations 5.11 and 5.12 into 5.10, and assuming $\delta_{xz(0)} = 0$ gives Equation 5.13 for off axis strain, relative to cell parameters (Figure 5.3).

$$\varepsilon_x(\emptyset) = \ln\left(\frac{l_{xz}\cos\theta_{xz}-\delta_{xz}\sin\theta_{xz}}{l_{xz(0)}\cos\theta_{xz(0)}}\right)\cos^2\emptyset + \ln\left(\frac{h_{xz}+l_{xz}\sin\theta_{xz}+\delta_{xz}\cos\theta_{xz}}{h_{xz(0)}+l_{xz(0)}\sin\theta_{xz(0)}}\right)\sin^2\emptyset \tag{5.13}$$

As the cell deforms, each of the values on the right hand side of Equation 5.13 will change (although φ is assumed to remain constant). Consider, firstly, a load applied parallel to the x direction. In this case, there is no component of the applied load to cause axial extension of the ribs of length h_{xz} and so $h_{xz} = h_{xz(0)}$. The variation of oblique rib length l_{xz} with oblique rib angle θ_{xz} under an x-directed load was derived using a similar approach to that used in the

Nodule-Fibril model for microporous polymers [9]. Consider the forces acting on a rib of length l_{xz} subject to loading along the x direction for unit thickness in the y direction, normal to the x-z plane (Figure 5.1). The change in the moment applied to each rib of length l_{xz} is given by:

$$\Delta M = -\frac{\Delta\sigma_x Z l_{xz} \sin\theta_{xz}}{2}$$

(5.14)

whereby $\Delta\sigma_x$ is the change in stress applied along the x axis.
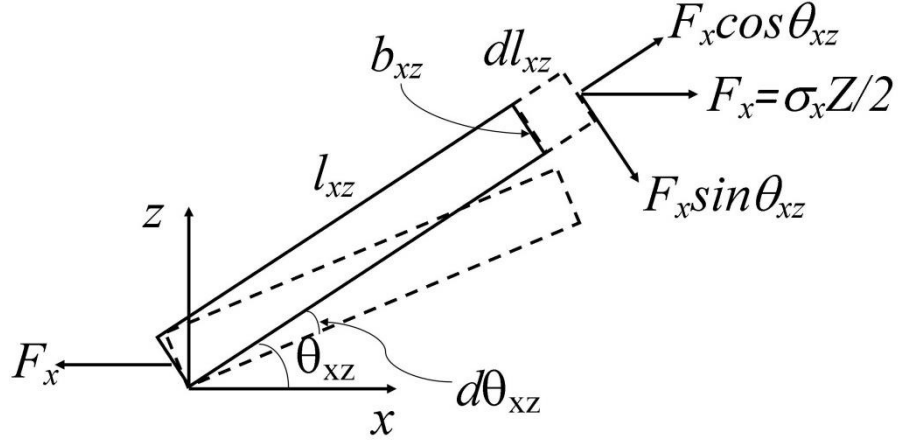
Figure 5.4: Free body diagram of a cell rib (length l_{xz}) subject to loading along the x axis

The hinging force constant is defined by:

$$k_h = \Delta M / \Delta\theta_{xz}$$

(5.15)

where $\Delta\theta_{xz}$ is the change in rib angle due to the change in moment. Substituting Equation 5.14 into 5.15 allows the change in angle (amount of rib hinging) to be related to the change in applied stress:

$$\Delta\theta_{xz} = -\frac{\Delta\sigma_x Z l_{xz} \sin\theta_{xz}}{2k_h}$$

(5.16)

To determine the amount of rib stretching due to the change in applied stress, first consider the change in force applied along the length of the rib:

$$\Delta F = \frac{\Delta\sigma_x Z \cos\theta_{xz}}{2}$$

(5.17)

The stretching force constant relates the change in rib length, Δl_{xz}, to the change in force ΔF along the length of the rib:

$$k_s = \Delta F / \Delta l_{xz}$$

(5.18)

Substituting Equation 5.17 into 5.18 allows the change in rib length to be related to the change in applied stress:

$$\Delta l_{xz} = \frac{\Delta\sigma_x Z cos\theta_{xz}}{2K_S} \qquad (5.19)$$

In the limit of infinitesimal changes in rib angle and length, combining Equations 5.16 and 5.19 gives:

$$\frac{dl_{xz}}{d\theta_{xz}} = -\frac{k_h cot\theta_{xz}}{l_{xz}k_S} \qquad (5.20)$$

Rearranging Equation 5.20 and integrating with the assumption that k_h/k_s remains constant:

$$\int_{l_{xz(0)}}^{l_{xz}} l_{xz} dl_{xz} = -\frac{k_h}{k_S} \int_{\theta_{xz(0)}}^{\theta_{xz}} cot\theta_{xz} d\theta_{xz} \qquad (5.21)$$

Gives:

$$l_{xz}^2 = -\frac{2k_h}{k_S} \ln\left(\frac{sin\theta_{xz}}{sin\theta_{xz(0)}}\right) + l_{xz(0)}^2 \qquad (5.22)$$

The rib flexing constant is:

$$k_f = \Delta F/\Delta\delta_{xz} \qquad (5.23)$$

where $\Delta\delta_{xz}$ is the change in rib deflection due to the change in moment. The change in the force applied perpendicular to the end of each rib of length l_{xz}, causing flexure, in this case is given by

$$\Delta F = -\frac{\Delta\sigma_x Z sin\theta_{xz}}{2} \qquad (5.24)$$

Substituting Equation 5.24 into 5.23 relates the change in deflection (amount of rib flexing) to the change in applied stress:

$$\Delta\delta_{xz} = -\frac{\Delta\sigma_x Z sin\theta_{xz}}{2k_f} \qquad (5.25)$$

In the limit of infinitesimal changes in rib angle and length, Equations 5.15 and 5.25 combine to give:

$$\frac{d\delta_{xz}}{d\theta_{xz}} = \frac{k_h}{l_{xz}k_f} \qquad (5.26)$$

Rearranging Equation 5.24 and integrating with the assumption that k_h/k_f remains constant:

$$\int_{\delta_{xz(0)}}^{\delta_{xz}} d\delta_{xz} = \frac{k_h}{l_{xz}k_f} \int_{\theta_{xz(0)}}^{\theta_{xz}} d\theta_{xz} \qquad (5.27)$$

Gives:

$$\delta_{xz} = \frac{k_h}{k_f}\frac{(\theta_{xz}-\theta_{xz(0)})}{l_{xz}} + \delta_{xz(0)} \qquad (5.28)$$

Now considering loading along the z direction, the change in the moment applied to each rib of length l_{xz} is:

$$\Delta M = \frac{\Delta\sigma_z X l_{xz} \cos\theta_{xz}}{2}$$ (5.29)

where $\Delta\sigma_z$ is the change in stress applied in the z direction.

Substituting Equation 5.19 into 5.15 and rearranging relates the change in angle (amount of rib hinging) to the change in applied stress:

$$\Delta\theta_{xz} = \frac{\Delta\sigma_z X l_{xz} \cos\theta_{xz}}{2K_h}$$ (5.30)

The change in force applied along the length of the rib of length l_{xz} is:

$$\Delta F = \frac{\Delta\sigma_z X \sin\theta_{xz}}{2}$$ (5.31)

Substituting Equation 5.31 into 5.18 allows the change in rib length to be related to the change in applied stress:

$$\Delta l_{xz} = \frac{\Delta\sigma_z X \sin\theta_{xz}}{2k_s}$$ (5.32)

In the limit of infinitesimal changes in rib angle and length, Equations 5.30 and 5.32 combine to give:

$$\frac{dl_{xz}}{d\theta_{xz}} = \frac{k_h \tan\theta_{xz}}{l_{xz}k_s}$$ (5.33)

Rearranging Equation 5.33 and integrating with the assumption that k_h/k_s remains constant:

$$\int_{l_{xz(0)}}^{l_{xz}} l_{xz} dl_{xz} = \frac{k_h}{k_s} \int_{\theta_{xz(0)}}^{\theta_{xz}} \tan\theta_{xz} \, d\theta_{xz}$$ (5.34)

Gives:

$$l_{xz}^2 = \frac{2k_h}{k_s} \ln\left(\frac{\cos\theta_{xz(0)}}{\cos\theta_{xz}}\right) + l_{xz(0)}^2$$ (5.35)

For loading along z it is also necessary to consider stretching of ribs of length h_{xz}. The change in force applied along the length of the rib of length h_{xz}:

$$\Delta F = \Delta\sigma_z X$$ (5.36)

The stretching force constant relating the change in rib length, Δh_{xz}, to the change in force ΔF along the length of the rib:

$$k_s^{h_{xz}} = \frac{\Delta F}{\Delta h_{xz}}$$ (5.37)

Substituting Equation 5.36 into 5.37 allows the change in rib length to be related to the change in applied stress:

$$\Delta h_{xz} = \frac{\Delta\sigma_z X}{k_s^{h_{xz}}} = \frac{\Delta\sigma_z X}{k_s} \frac{h_{xz}}{l_{xz}}$$ (5.38)

Using the relationship between the stretching force constants for both rib types assuming they are both made of the same elastic material gives Equations 5.39 to 5.43 below. In the limit of infinitesimal changes in rib angle and length, Equations 5.30 and 5.38 combine giving:

$$\frac{dh_{xz}}{d\theta_{xz}} = \frac{2h_{xz}k_h}{l_{xz}^2 \cos\theta_{xz}k_s} \qquad (5.39)$$

Rearranging Equation 5.39 and integrating with the assumption that k_h/k_s remains constant:

$$\int_{h_{xz(0)}}^{h_{xz}} \frac{dh_{xz}}{h_{xz}} = \frac{2k_h}{l_{xz}^2 k_s} \int_{\theta_{xz(0)}}^{\theta_{xz}} \sec\theta_{xz}\, d\theta_{xz} \qquad (5.40)$$

Gives:

$$h_{xz} = h_{xz(0)} exp\left[\frac{2k_h}{l_{xz}^2 k_s}\ln\left(\frac{\sec\theta_{xz} + \tan\theta_{xz}}{\sec\theta_{xz(0)} + \tan\theta_{xz(0)}}\right)\right] \qquad (5.41)$$

The change in the force applied perpendicular to the end of each rib of length l_{xz}, causing flexure, for z-directed loading is given by:

$$\Delta F = \frac{\Delta\sigma_z X \cos\theta_{xz}}{2} \qquad (5.42)$$

Substituting Equation 5.42 into 5.23 relates the change in deflection (amount of rib flexing) to the change in applied stress:

$$\Delta\delta_{xz} = \frac{\Delta\sigma_z X \cos\theta_{xz}}{2K_f} \qquad (5.43)$$

In the limit of infinitesimal changes in rib angle and length, Equations 5.30 and 5.43 give Equation 5.27 and so the deflection due to flexing as a function of rib angle change (due to hinging) under z-directed loading is the same as for x-directed loading and is given by Equation 5.28.

5.3.3. Force constants assuming elastic cell rib material.

Expressions relating force constants to material properties and cell rib geometry (Figure 5.3) were introduced in Chapter 3:

$$k_s = \frac{E_s wb}{l} \qquad (5.44)$$

$$k_s^{h_{xz}} = \frac{E_s wb}{h} = \frac{E_s wb}{l}\frac{l}{h} = k_s\frac{l}{h} \qquad (5.45)$$

$$k_f = \frac{E_s w b^3}{l^3} \tag{5.46}$$

$$k_h = \frac{G_s w b}{l} \qquad \text{(hinging via shearing of junction)} \tag{5.47}$$

$$k_h = \frac{E_s w b^3}{6 l^2 q} \qquad \text{(hinging via local bending at junction)} \tag{5.48}$$

$$\frac{k_{hf}}{k_s} = \frac{1}{\left(\frac{l}{b}\right)^2 + \frac{E_s}{G_s}} \tag{5.49}$$

$$\frac{k_{hf}}{k_s} = \frac{b^2}{l^2 + 6 l q} \tag{5.50}$$

The minimum value of k_{hf}/k_s (g) occurs when $q \to l$:

$$\frac{k_{hf}}{k_s} = \frac{b^2}{7 l^2} \tag{5.51}$$

5.3.4. Rationale for choice of force constant values used in predictive model

As per Chapter 3 (Page 69), a value of $b/l = 0.2$ was arbitrarily used, and a ballpark range for k_{hf}/k_s between 0.006 to 0.036 – i.e. an order of magnitude difference between the upper and lower limits, was predicted.

Given the approximations inherent in employing an idealised 2D model of regular cells to real 3D cellular system displaying a distribution of cell sizes and shapes then, for the purposes of these exploratory calculations, $0.004 < k_{hf}/k_s < 0.04$ was employed for the predictions of Poisson's ratio versus cell geometry. For the prediction of the mechanical properties as a function of strain in the x-z plane, the case of $k_{hf}/k_s = 0.004$ and from Equations 5.39 and 5.40, $k_f/k_s = (b/l)^2 = (0.2)^2 = 0.04$ were used. Hence from Equation 5.1, $k_f/k_h = 9$ and $k_s/k_h = 225$.

For the x-y plane predictions as a function of strain, the 'stretching' mode is enhanced over that expected for an elastic 2D material due to the 3D nature and orientation of the ribs in/out of the x-y plane. Accordingly, K_s is reduced in the x-y plane predictions and a value of $k_s/k_h = 3$ was employed ($k_{sy}/k_{hy} = 75 \times k_s/k_h$), larger than in Chapter 3 due to the larger amount of lateral strain expected (and recorded) in the region with a VCR of 1. Retaining $k_f/k_h = 9$ produces a value of $k_{hf}/k_s = 0.3$ in this case.

5.4. Results

5.4.1. Structural Analysis

The mean FVR of the uniform sheet converted with pins was 2.63 ± 0.10 (cuboidal samples) and 2.96 ± 0.42 (cubic samples), which was similar to 2.53 ± 0.04 (cuboidal) and 2.86 ± 0.51 (cubic) for the sheet without pins and the imposed value of 2.9. Cuboidal samples from the

non-uniform sheet had a mean FVR of 2.98 ± 0.33 in the triaxially compressed region and 1.22 ± 0.01 in the region with imposed biaxial planar tension.
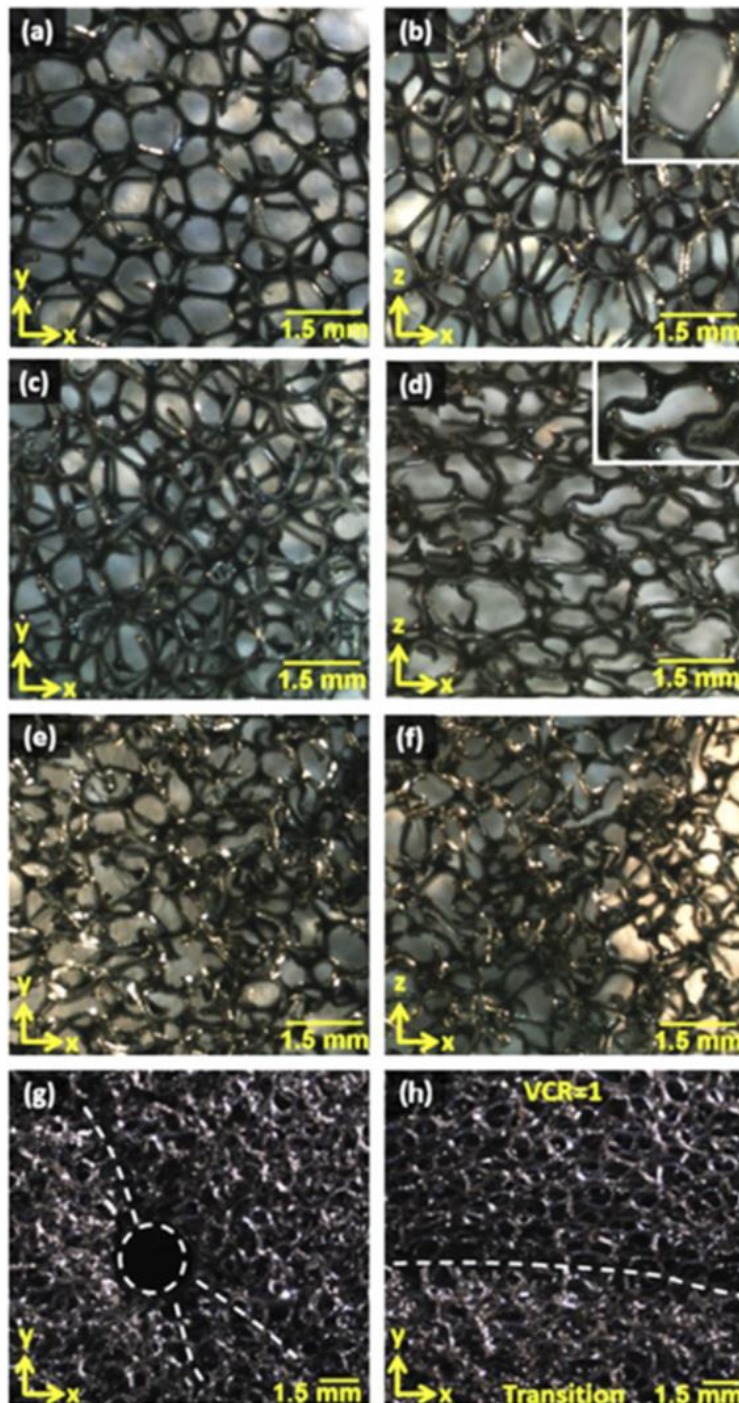
Figure 5.5: Stereoscopic images. Unconverted PUR30FR foam a) x-y plane and b) x-z plane; of the VCR = 1 quadrant of gradient sheet c) x-y plane and d) x-z plane; of the VCR = 2.9 quadrant of gradient sheet e) x-y plane and f) x-z plane; g) Uniform triaxially-compressed auxetic sheet with pin hole and surrounding creases (marked); h) Defined line region between VCR = 1 region (top of image) and higher density transition region (bottom of image) in the gradient sheet (marked). Inserts in b) & d) include detailed images blown up to 1.5 times the main image.

Images of foam cell structure show the regular polyhedral cellular structure of the unconverted foam, with elongation in the rise direction [7] (Figure 5.5a & b). The planar (x-y) structure of the quadrant of the gradient foam converted with biaxial planar tension and through thickness compression (VCR = 1, Figure 5.5c) is similar to the unconverted parent foam planar structure (Figure 5.5a). In the through thickness (x-z) plane, this region of foam has a slightly re-entrant structure consisting of vertically compressed, partially buckled cells (Figure 5.5d). Through-thickness and planar micrographs of the triaxially compressed quadrant (VCR = 2.9) of the gradient foam (Figure 5.5e and f) both show a three dimensional re-entrant cell structure typical of auxetic foam [10] that is denser than unconverted and VCR = 1 foam in Figure 5.5a to d and similar to the uniformly compressed samples (Figure 5.5g and h) as intended. Through-thickness pins left holes in foam sheets (hole diameter $\approx$ pin diameter), surrounded by small creases (~10 mm long sloping down into the holes to a depth of <5 mm) (Figure 5.5g). Random creasing (length <100 mm, depth ~ 5 mm) was evident in the sheet converted without pins. Creases or folds were not present in the region with applied planar tension in the gradient sheet, which exhibited defined boundaries between areas with different VCRs (Figure 5.5h).

FVR of both quadrants of the gradient sheet increased as expected following fabrication. Partial thermal stability was then exhibited following re-heating to 190°C for 10 minutes (Figure 5.6), with a return towards an FVR of 1 (by ~15% the original volume in both quadrants). There was little difference in stability between the two compression regimes.
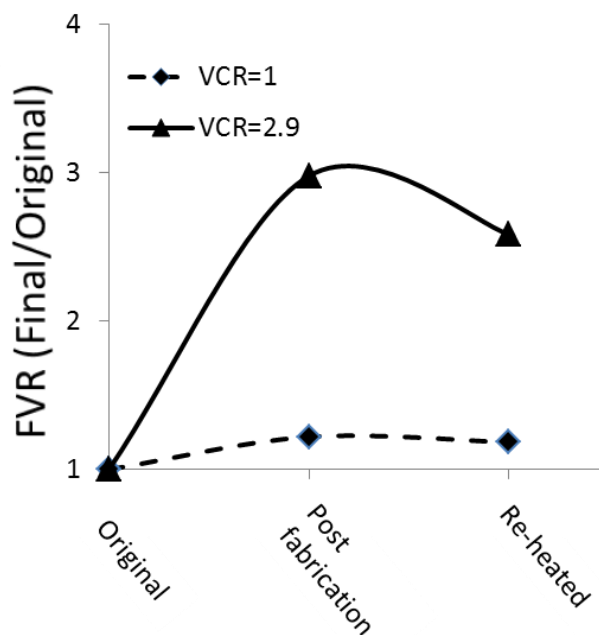

Figure 5.6: Final Volume Ratio of VCR=1 and 2.9 sections of the gradient sheet-before and after fabrication, then proceeding re-heating to 190°C for 10 minutes.

5.4.2. Mechanical Characterisation

There was no clear difference in Poisson's ratios or tangent moduli between samples cut at different orientations from converted sheets (Figure 5.2), so these are displayed and discussed together. The unconverted foam shows the established deformation characteristic of open cell foams, undergoing lateral contraction under axial tension, and lateral expansion under axial compression (Figure 5.7). The strain dependent Poisson's ratios determined from the negative of the slope of the strain-strain data at 5% interval (e.g. 0 to 5 % compression) are, thus, positive for the unconverted foam and attain the highest values at the highest tensile strain and near zero values at the highest compressive strains (Figure 5.8), in agreement with previous work [11,12]. There is evidence for anisotropy in the tensile Poisson's ratio for the unconverted foam, with the systematic trend of $\nu_{zx} > \nu_{xz} > \nu_{xy}$, consistent with the structural anisotropy (rise direction parallel to z axis).
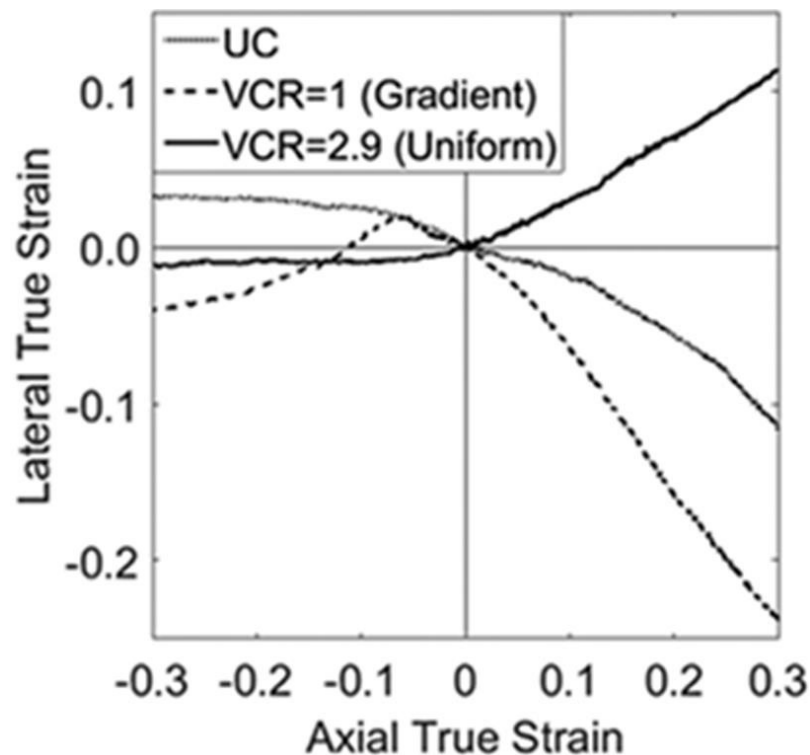
Figure 5.7: Lateral vs axial true strain for a VCR = 2.9 uniform triaxially-compressed sample converted with pins, an unconverted (UC) sample and a VCR = 1 gradient sheet sample

The foam converted with uniform triaxial compression also displays the previously reported response of lateral expansion under axial tension, and lateral contraction under axial compression (Figure 5.7), for foam converted in a similar manner. This corresponds to essentially isotropic negative Poisson's ratio of larger magnitude ($\nu \sim$0.2) in tension than

compression ($v \sim 0$, Figure 5.8). For uniform triaxial compression, samples converted with and without pins exhibited little difference in Poisson's ratio (Figure 5.8).
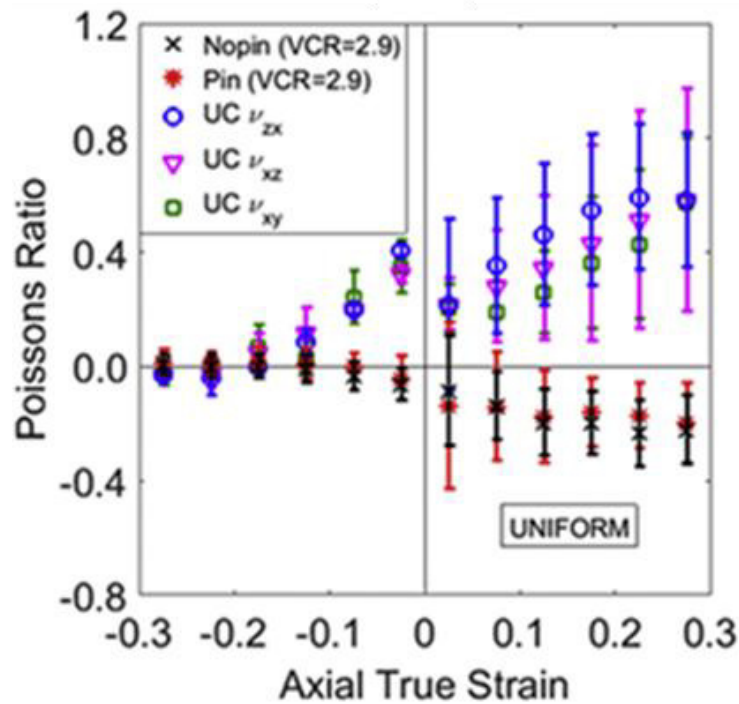
Figure 5.8: Poisson's ratio vs axial true strain for UC and uniform triaxially-compressed samples with a VCR = 2.9. Error bars = 1 S.D.

Turning to the foam converted with non-uniform compression, it is clear from the stark differences in Poisson's ratios between VCR = 1 and VCR = 2.9 quadrants (Figure 5.9a) that a gradient, in terms of mechanical response in addition to foam structure noted above (Figure 5.5c to f), has been produced through the use of pins and foam of a different shape to the mould. The VCR = 2.9 region displays very similar Poisson's ratio vs axial strain (Figure 5.9a) data to the foam sheets converted with uniform triaxial compression (Figure 5.8), as intended. The VCR = 1 region undergoes lateral contraction under axial tension (Figure 5.7), similar to the unconverted foam, although the magnitudes of the positive Poisson's ratios are higher for the VCR = 1 region of the gradient foam (Figure 5.9a). The positive Poisson's ratio is maintained under low (<5%) strain axial compression (Figure 5.7 & Figure 5.9a). However for compressive strains greater than 5%, the VCR = 1 region undergoes lateral contraction under axial compression (Figure 5.7) and, thus, transitions to negative Poisson's ratio (Figure 5.9a). The through-thickness plane shows large anisotropy in this case, with $v_{xz} \sim -0.6$ and $v_{zx} \sim 0$ at compressive loading strains ~10 to 15%. The tensile Poisson's ratio of the VCR = 1 region of the gradient foam was found to be sensitive to repeat testing, decreasing in magnitude with increasing repeat testing (Figure 5.9b).
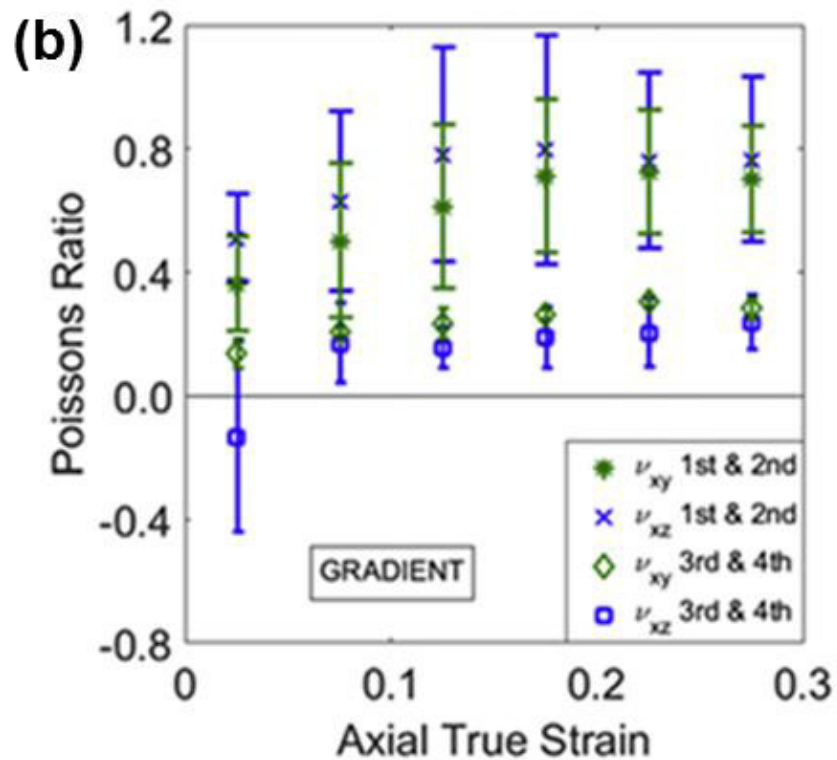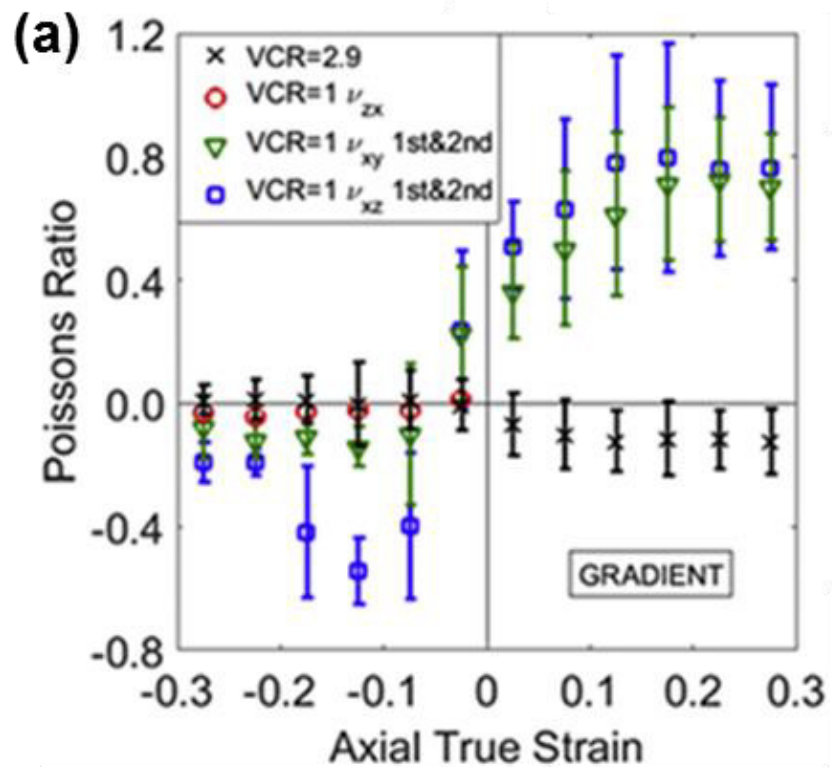
Figure 5.9: a) Poisson's ratio vs axial true strain for gradient sheet samples (VCR = 1 tensile data from 1st and 2nd tests performed on each sample, see text) and b) Poisson's ratio vs axial true strain for all tensile tests on VCR = 1 region (gradient foam), grouped according to tests 1 and 2, and tests 3 and 4 - see text). Error bars = 1 S.D.

The stress vs strain responses of the unconverted foam and the VCR = 1 quadrant of the gradient sheet include the presence of a plateau onset under 5% compression for the unconverted foam (Figure 5.10). The triaxially compressed samples exhibit increased elastic resilience (longer linear stress-strain response) under compression (Figure 5.10). The triaxially compressed foam stress-strain data display lower tensile slope and higher compression slope, corresponding to lower tensile and higher compressive Young's moduli, respectively (Figure 5.11), than the unconverted foam. The elastic anisotropy and isotropy of the unconverted foam and triaxial compression foam, respectively, are again evident in the Young's moduli data. No clear differences were observed in the Young's modulus data for samples converted under uniform triaxial compression with and without pins (Figure 5.11).
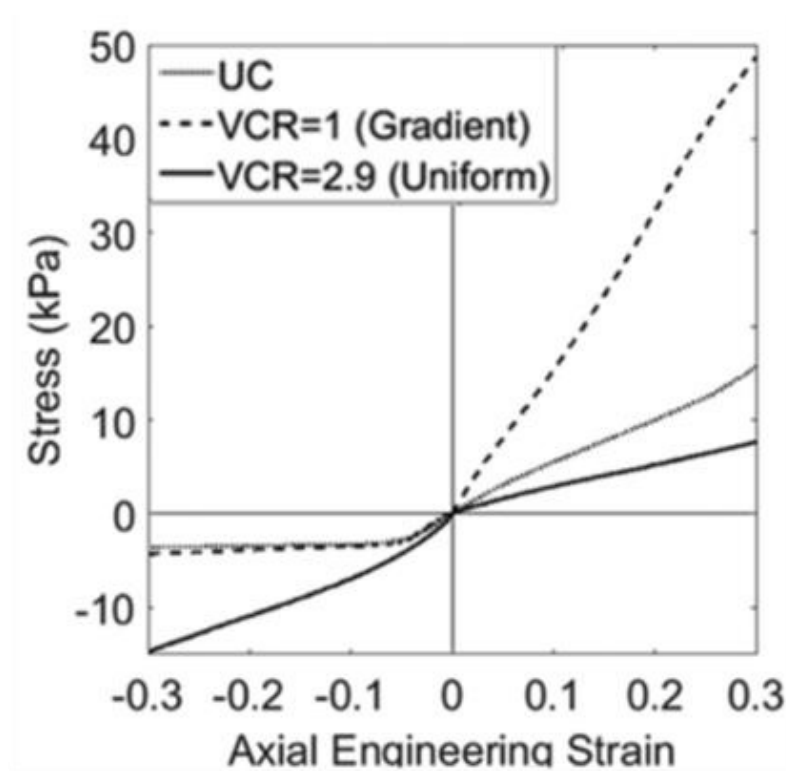
Figure 5.10: Stress vs axial engineering strain for VCR = 2.9 uniform triaxially-compressed sample converted with pins, unconverted (UC) sample and VCR = 1 gradient sheet sample
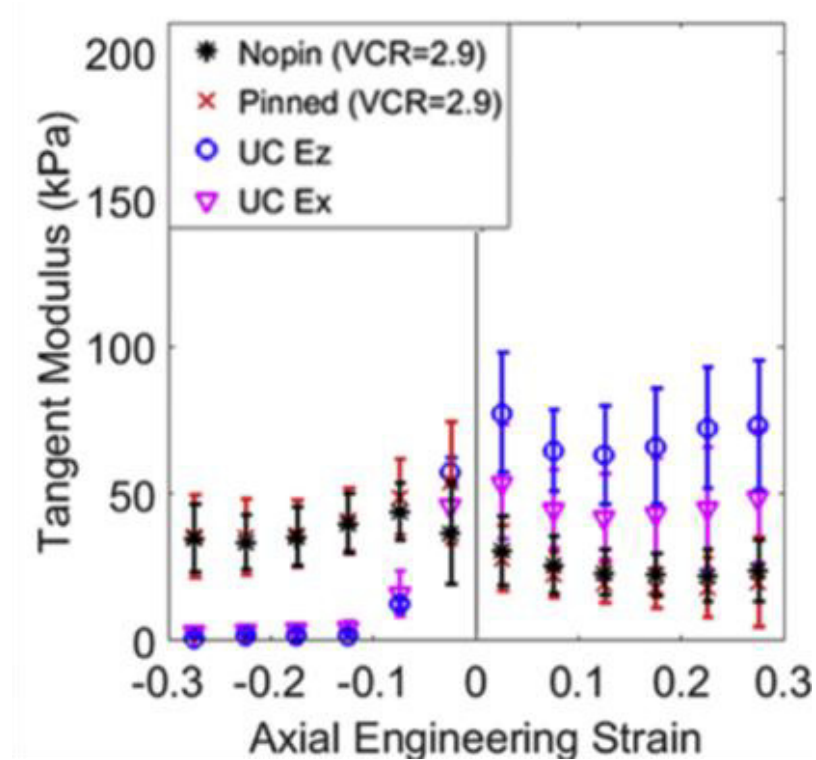
Figure 5.11: Tangent modulus vs axial engineering strain for UC and uniform triaxially compressed, VCR = 2.9 samples

The sheets converted with uniform triaxial compression display the intended similar Young's modulus to the VCR = 2.9 quadrant in the gradient foam (Figure 5.11 and Figure 5.12a, respectively). In the VCR = 1 region, the gradient foam displays similar Young's moduli trends to the unconverted foam. However, the tensile E_x has been increased by a factor of three for the VCR = 1 region of the gradient foam (tensile E_x ~ 150 kPa, Figure 5.12a) compared to the unconverted foam (tensile E_x ~ 50 kPa, Figure 5.11). As with the Poisson's ratio (Figure 5.9b), the Young's modulus of the VCR = 1 region of the gradient foam is susceptible to repeat testing, reducing with the 1st and 2nd tests, before stabilising under the 3rd and 4th tests (Figure 5.12b).
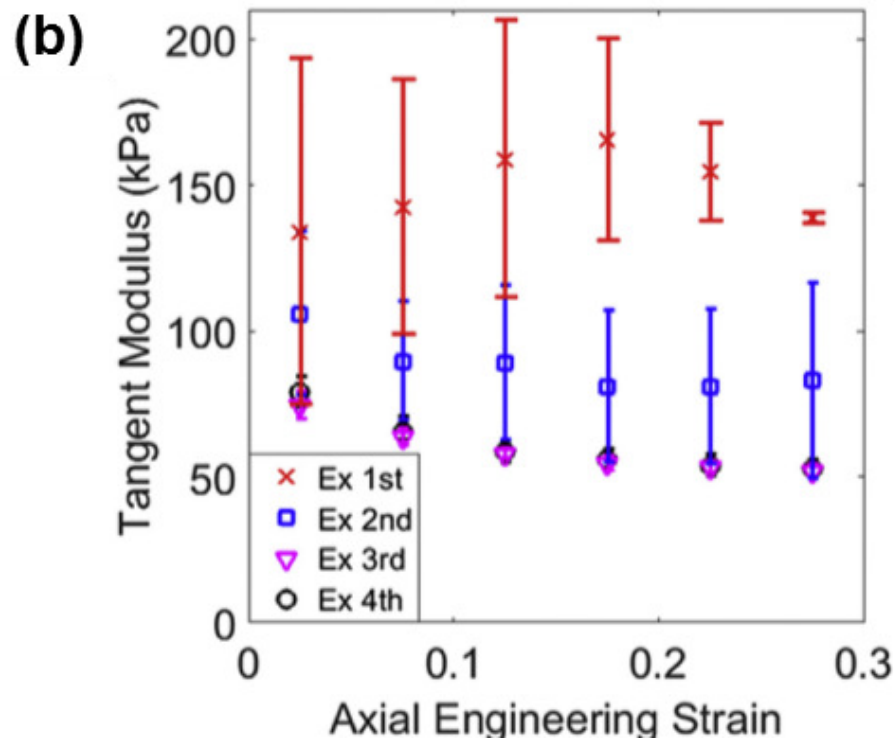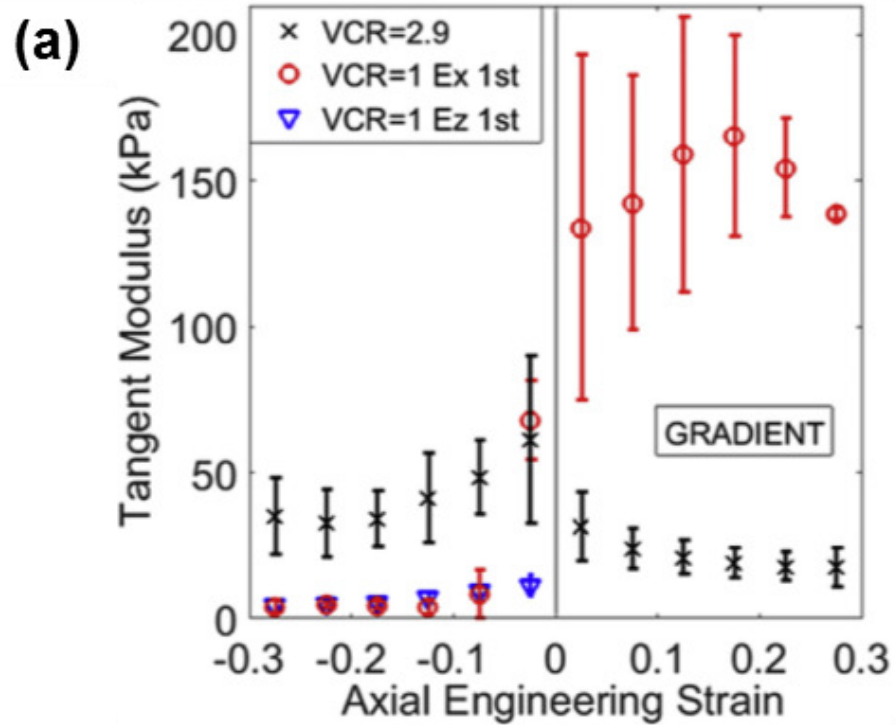
Figure 5.12: a) Stress vs axial engineering strain for VCR = 2.9 uniform triaxially-compressed sample converted with pins, unconverted (UC) sample and VCR = 1 gradient sheet sample, b) Tangent modulus vs axial engineering strain for UC and uniform triaxially compressed samples, c) Tangent modulus vs axial engineering strain for gradient sheet samples (VCR = 1 tensile data from 1st test performed on each sample) and d) Tangent modulus vs axial engineering strain for all tests on VCR = 1 region (gradient foam), separated into test number. Error bars = 1 S.D.

5.4.3. Impact testing

Figure 5.13 shows the median impact acceleration/time trace in each region of the gradient sheet. The VCR = 2.9 quadrant exhibited a mean peak acceleration ~4 times lower than the VCR = 1 region, which appeared to "bottom out" under impact (characterised by a sharp increase in acceleration). Mean peak accelerations were 43 g (s.d. = 0.1 g) and 162 g (s.d. = 47 g) for the VCR = 2.9 and 1 regions, respectively (Figure 5.13).
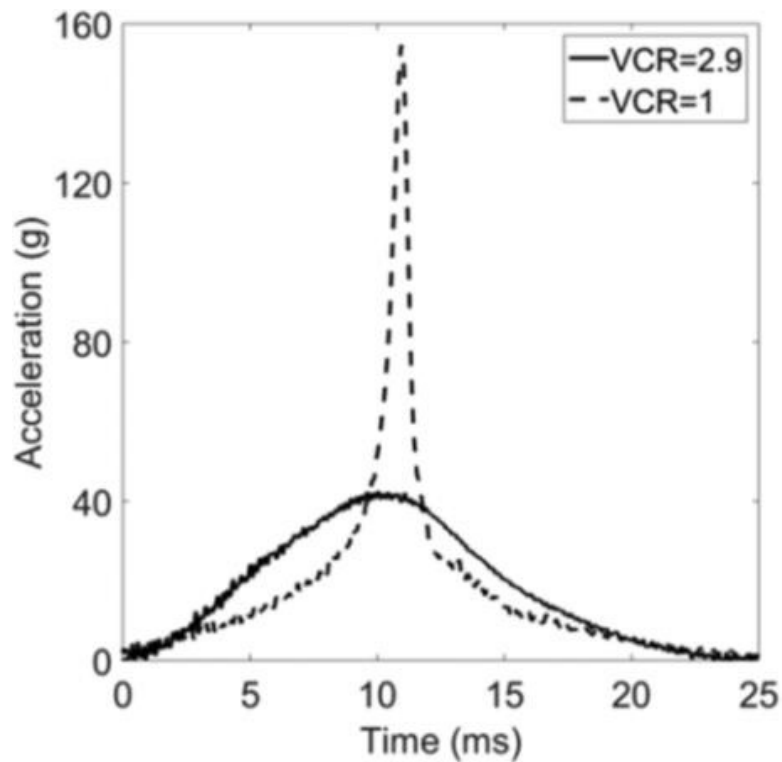
Figure 5.13: Median acceleration-time traces for the 6J impacts to the gradient sheet impacted through thickness (parallel to the z-axis) in regions with VCR = 2.9 and VCR = 1 with the 2 mm PP shell placed on top. Start of impact manually selected at a point when acceleration was greater than 0.

5.4.4. Analytical model
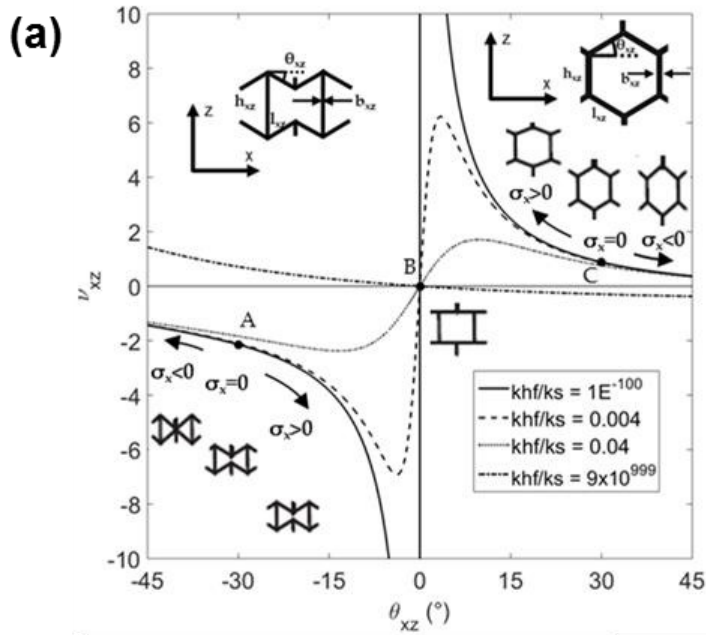
$$v_{xz} = \frac{\sin\theta_{xz}\cos^2\theta_{xz}\left(\frac{1}{k_{hf}}-\frac{1}{k_s}\right)}{\left(\frac{h_{xz}}{l_{xz}}+\sin\theta_{xz}\right)\left[\frac{\sin^2\theta_{xz}}{k_{\sim f}}+\frac{\cos^2\theta_{xz}}{k_s}\right]}$$
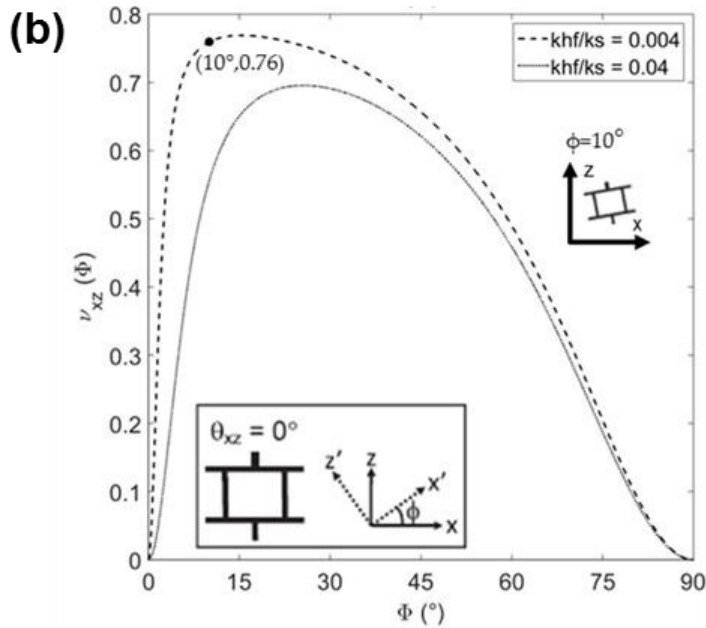
$$v_{xz}(\phi) = E_x(\phi)\left[\frac{(\cos^4\phi+\sin^4\phi)v_{xz}}{E_x}-\cos^2\phi\sin^2\phi\left(\frac{1}{E_x}+\frac{1}{E_z}-\frac{1}{G_{xz}}\right)\right]$$

Figure 5.14: (a) v_{xz} vs θ_{xz} for a honeycomb having $h_{xz} = 1.2$, $l_{xz} = 1$, $b_{xz} = 0.2$ and $k_{hf}/k_s = 0$ (flexing/hinging), 0.004, 0.04 and ∞ (stretching). Cell geometrical parameters are shown (insert top left), and cell size/shape variation vs θ_{xz} is shown schematically below the figure. (b) v_{xz} vs ϕ for the same honeycomb with $\theta_{xz} = 0$ and $k_{hf}/k_s = 0.004$ and 0.04. Cell shape for $\theta_{xz} = 0$ and definition of rotation angle ϕ are shown in schematic insert.

To show the effect of processing induced changes in foam structure on the effective Poisson's ratio, Figure 5.14a shows the ν_{xz} expression and the predicted ν_{xz} vs θ_{xz} trends for k_{hf}/k_s = 0 (flexing/hinging), 0.004, 0.04 and ∞ (stretching), when h_{xz} = 1.2, l_{xz} = 1 and rib thickness b_{xz} = 0.2. These parameters provide a slight elongation of the cell along the rise (z) direction when θ_{xz} = 30° (see cell schematics in Figure 5.14a), and are taken as the simplified 2D representation of the 3D unconverted foam structure in the x-z plane (Figure 5.5b). The curves for finite values of k_{hf}/k_s lie between the stretching and flexing/hinging extremes, with the (lower) k_{hf}/k_s = 0.004 curve closest to the flexing/hinging case. Points A, B and C on the k_{hf}/k_s = 0.004 curve in Figure 5.14a correspond to honeycombs qualitatively approximating the observed cellular structures in the x-z plane, shown in Figure 5.5, for the unconverted foam and VCR = 2.9 and 1 gradient foam quadrants, respectively. Inspecting foam cell structures (Figure 5.5), the arbitrarily selected value for b/l of 0.2 appears reasonable for this representation. Points A and B lie in regions of clear negative and positive predicted values of ν_{xz}, respectively, whereas ν_{xz} varies dramatically (from negative through zero to positive values) for small variation in θ_{xz} around point C.

As an example of predicted off-axis properties, Figure 5.14b shows the variation of ν_{xz} for rotation about the y axis, normal to the x-z plane, by angle φ when θ_{xz} = 0° (see insert to Figure 5.14b) for k_{hf}/k_s = 0.004 and 0.04. This example, then, approximates the VCR = 1 quadrant of the gradient foam. ν_{xz} (φ) = 0 when φ = 0 and 90°, is positive when 0 < φ < 90°, and is symmetric about φ = 0 and 90°. The maximum value of $\nu_{xz}(\varphi)$ increases, and is approached more rapidly, as φ increases from 0 for the lower k_{hf}/k_s value, occurring at φ = 26 and 15° when k_{hf}/k_s = 0.04 and 0.004, respectively. A range of 5 < φ < 15° produces predicted positive ν_{xz} (φ) values for k_{hf}/k_s = 0.04 and 0.004 of similar magnitude to the experimental ν_{xz} value at zero strain (Figure 5.14b and Figure 5.9a, respectively).
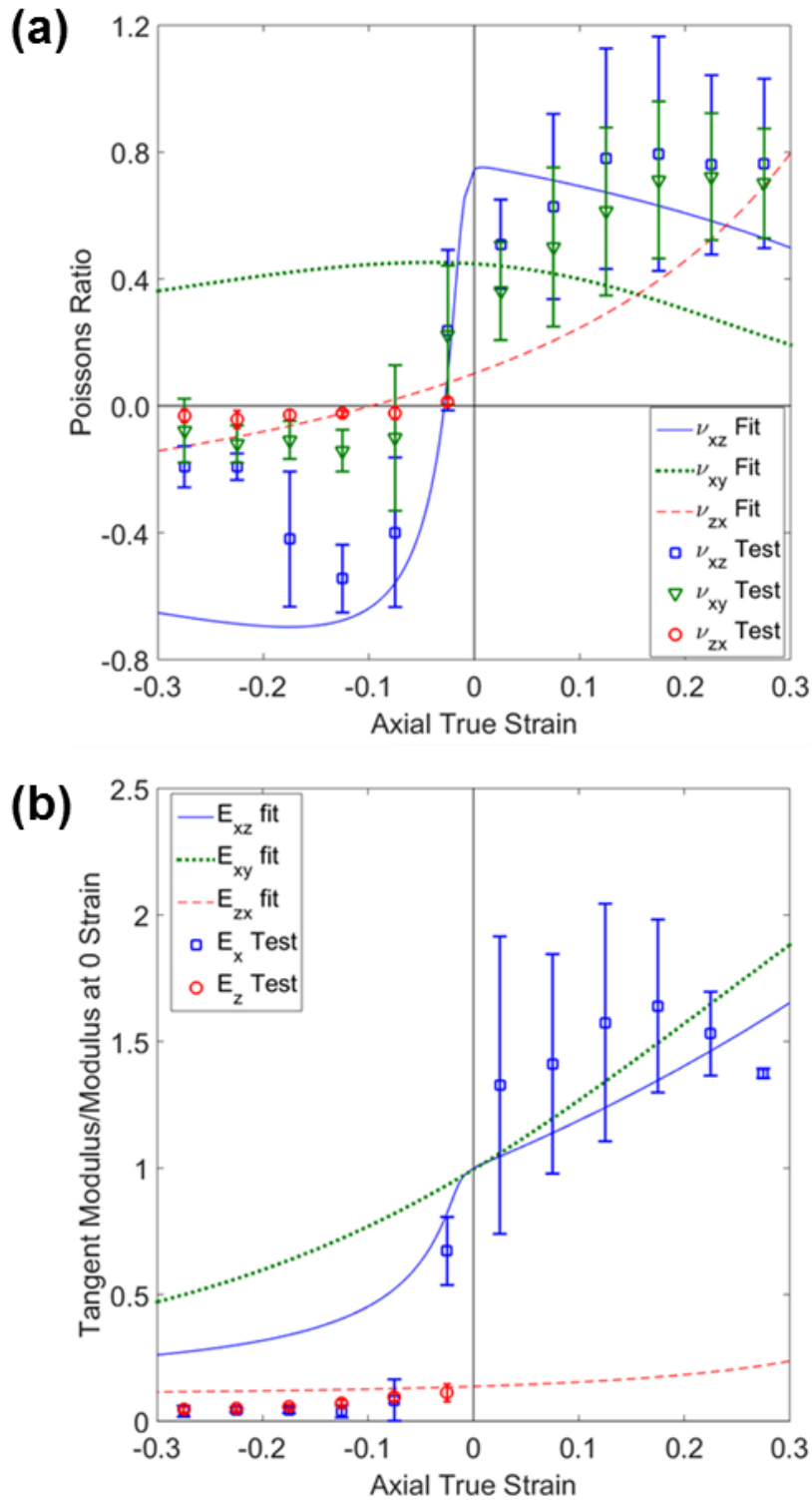
Figure 5.15: (a) Strain (Equation 5.13) dependent, directional Poisson's ratio predictions (fits, Equation 5.8) and experimental VCR = 1 (gradient foam) data (tests) vs loading strain: ν_{xz} and ν_{zx} predictions for $h_{xz}(0)$ = 1.2, $l_{xz(0)}$= 1, b_{xz} = 0.2, $\theta_{xz(0)}$ = -0.1°, φ = 10° and k_{hf}/k_s = 0.004 (k_f/k_h = 9, k_s/k_h = 225); ν_{xy} predictions for $h_{xy(0)}$ = $l_{xy(0)}$ = 1, b_{xy} = 0.2, $\theta_{xy(0)}$ = 30°, φ = 0° and k_{hf}/k_s = 0.3 (k_f/k_h = 9, k_s/k_h = 3); (b) Directional Young's moduli (normalised to undeformed E_x) predictions (fits, Equation 5.9) and experimental data (symbols) vs loading strain: model parameters as for (a). Values for w, b and k are assumed to remain constant.

The x-y plane comparison between ν_{xy} vs ε_x predictions (dotted line) and experimental data (green triangles) is also shown in Figure 5.15a. The x-y plane model predictions employ $h_{xy} = l_{xy} = 1$, $b_{xy} = 0.2$ and $\theta_{xy} = 30°$ since the cell structure in the x-y plane of the VCR = 1 quadrant of the gradient foam is similar to that of the unconverted foam (Figure 5.5a & c) and they replicate the symmetrically equivalent x and y directed mechanical properties. No rotation of axes was considered for the predicted x-y plane properties (i.e. $\varphi = 0°$). The ν_{xy} vs ε_x model predictions follow the experimental trends reasonably well when employing a value of $k_{hf}/k_s = 0.3$ (by reducing k_s/k_h to 3). This is significantly higher than the value used in the x-z plane predictions, and corresponds to a stiffening of the rib flexing and/or hinging mechanisms relative to the rib stretching mechanism in the x-y plane.

The model parameters used in the Poisson's ratio predictions also produce Young's moduli (normalised to the respective zero strain E_x value) vs strain trends in reasonable agreement with experiment (Figure 5.15b). There are E_x model predictions from each of the x-z and x-y plane parameters, with the trends from the x-z plane parameters in particular reproducing an enhanced drop off in E_x in compression.

5.5. Discussion

Through-thickness pins can be used to control local compression levels to fabricate large gradient foam sheets containing regions with dramatically different structures and properties. The controlled production of desired auxetic regions (within pre-defined quadrants with VCR = 2.9) has been shown. The VCR = 1 regions display a transition from positive to negative Poisson's ratios moving from tensile to compressive loading (Figure 5.9a), and possess highly anisotropic cellular structure (Figure 5.5c and d) and mechanical properties (Figure 5.9a and b, Figure 5.12a and b). The use of pins for local control of compression or tension in the thermo-mechanical conversion process can be extended to the alternative solvent [13] and compressed carbon dioxide [14] foam conversion routes.

The observed structures and mechanical properties of the unconverted and uniform triaxial compression-converted foams are consistent with previous reports [15–17]. Uniform samples fabricated with pins exhibited no clear difference in mechanical properties to those without. For the production of homogeneous foams, pins are then expected to be most beneficial when applying compression to thinner sheets than those fabricated here (where folding can prevent uniform planar compression) and thicker monoliths to aid insertion into the mould and minimise density gradients/variation. The conversion of thicker samples may also benefit from the addition of an orthogonal set of pins in a modified mould. Metallic pins, such as those used here, are expected to aid heat conduction through thicker samples. Densification

of the same open cell foam nearby a stiff indenter (i.e. a pin, as shown in Figures 4.26 & 4.27, Chapter 4, Pages 114 & 115, both microscopically and using digital image correlation), could have affected the cell structure. Creases were predominantly contained to areas surrounding pins (Figure 5.5). Further work should assess the effect of pins size and spacing on surrounding cellular structure, or using alternative methods to control internal compression (i.e. thread, yarn or visual markers and surface manipulation).

The uniformly compressed quadrant of the gradient sheet returned to its initial volume by ~15 % upon reheating (Figure 5.6). The amount of re-expansion was comparable to smaller samples of the same foam with a VCR of 3 heated at 140°C for 180 minutes, 160°C for 60 minutes or 180°C for 20 minutes (Chapter 3, Figure 3.4, Page 53). The Poisson's ratios (up to 10 % strain) of the gradient sheet in tension (~-0.2, Chapter 3, Figure 3.10, Page 59, compared to ~0, Figure 5.9a) and compression (~-0.1 to -0.2, Figure 3.10, Page 59, compared to ~0, Figure 5.9a) were lower in magnitude than the smaller conversions with equivalent dimensional stability in Chapter 3. The uniform sheet exhibited equivalent tensile (~-0.2) and marginally lower magnitude compressive (~-0.1 to -0.2, Figure 3.10, Page 59, compared to ~-0.1, Figure 5.8) Poisson's ratios than the smaller samples. Tensile and compressive Young's moduli (up to 10% strain) were ~50 kPa for the uniformly compressed quadrant of the gradient sheet (Figure 5.12a), the uniform sheet (Figure 5.11) and the small samples (Figure 3.13, Page 62). The increased chances of flaws caused by pins and/or uneven compression when pins were not applied (most obvious in the gradient sheet) may explain the marginally lower magnitude NPRs. The balance between time and temperature dimensional stability and magnitude NPR appears reasonable, during comparison to foams in Chapter 3.

The Poisson's ratios and Young's modulus of the VCR = 1 region of the gradient foam both reduced with repeat testing until stabilising around the 4th test (Figure 5.9b and Figure 5.12b). Reduced mechanical properties in both auxetic and conventional open cell PU foams under cyclic loading have been reported previously, with most decrease occurring over the first few loading cycles [18]. Dimensional stability following re-heating (Figure 5.6) was higher than small (~2 x 2 x 7 cm) samples with the largest magnitude of NPR, which exhibited an FVR of ~1 following re-heating (Chapter 3, Figure 3.4, Page 53). Small sample fabricated at 180, 160 & 140 °C for 20, 60 and 180 minutes respectively exhibited comparable FVRs following re-heating (Chapter 3). The small samples with comparable dimensional stability exhibited Poisson's ratios between -0.1 and -0.2 (Chapter 3, Figure 3.10, Page 59). Given the intention to permanently impart very different structures to the gradient sheet (rather than maximise the magnitude of NPR), the heating conditions can be considered appropriate.

When the gradient sheet was impacted in the z direction at 6 J, peak acceleration was ~4 times lower for the VCR = 2.9 region than the VCR = 1 region (Figure 5.13). In both cases the compressive ν_{zx} ~0 (Figure 5.9a) and so Poisson's ratio cannot account for the different impact responses. It is likely due to the compressive tangent modulus (beyond ~5% compressive strain) being close to zero for the VCR = 1 region (Figure 5.12a), resulting in the material offering little resistance to the impactor, so the sample reached 'densification' and the associated increase in stiffness while the impactor still had a large amount of kinetic energy, causing a higher peak acceleration. Nevertheless, the ability to modify impact response in a one-piece foam is demonstrated, leading to potential applications in sport, healthcare and defence apparel requiring localised impact protection (e.g chest and shoulder regions in rugby), for example. The plateau region is often considered beneficial in impact protection, maximising energy absorption (the integral of force and displacement) for a specific peak force or acceleration as discussed in Chapter 2, Page 26. The NPR, VCR=1 quadrant should, therefore, be tested during lower energy impacts, impacts over a larger area or where a larger (thicker) pad is acceptable (i.e. crash mats).

Extending the existing model of a hexagonal honeycomb deforming by multiple mechanisms [8] allows predictions as a function of strain, and provides increased insight into the mechanisms giving rise to the experimental foam mechanical properties. Reasonable agreement between experiment and predicted properties is demonstrated for the VCR = 1 quadrant of the gradient foam (Figure 5.15).

For reasons of brevity, a comparison of model and experimental strain-dependent properties is not reported for the unconverted foam, nor for the foam converted with uniform triaxial compression or the VCR = 2.9 quadrants of the graded foam. Qualitative trends can still be inferred from Figure 5.14a for these cases. Consider, firstly, the structure and properties in the x-z plane of the unconverted foam, indicated by point B at θ_{xz} = 30° and the schematic cell inserts for θ_{xz} > 0° on the ν_{xz} vs θ_{xz} plot of Figure 5.14a. Increasing θ_{xz} beyond 30° leads to a narrowing of the cell along the x direction and thus corresponds to a compressive stress (σ_x < 0) applied in the loading (x) direction. Similarly, decreasing θ_{xz} below 30° corresponds to a tensile stress (σ_x > 0). In this case, the positive value of ν_{xz} at θ_{xz} = 30° decreases under compression, and increases under tension, and is consistent with the experimental ν_{xz} vs ε_x data for the unconverted foam (Figure 5.8).

A similar consideration can be extended to point A (θ_{xz} = -30°) in Figure 5.14a, assumed to approximate the re-entrant cell structures of the triaxially compressed foam and also the VCR = 2.9 region of the gradient foam (Figure 5.5f). The predicted negative value of ν_{xz} at θ_{xz} = -30°

decreases in magnitude under compression ($\theta_{xz} < -30°$), and increases in magnitude under tension ($\theta_{xz} > -30°$), along x. This is also consistent with the experimental ν_{xz} vs ε_x data for the foam converted under triaxial compression, and the VCR = 2.9 region of the gradient foam (Figure 5.8 & Figure 5.9a).

The equivalent honeycomb structure for the x-z projection of the VCR = 1 region of the gradient foam (Figure 5.5d) corresponds to $\theta_{xz} \sim 0°$. In this case, the reconciliation of the experimental and model data trends required a consideration of the off-axis properties [8]. There is a suggestion that buckling of the ribs in the x-z plane of the VCR = 1 region of the gradient foam may be accompanied by some re-orientation of the pores (insert in Figure 5.5d), and perfect alignment of the irregular pore structure with the testing direction would be difficult, if not impossible, to achieve in practice in any event. It might be expected, therefore, that some off-axis loading of cells occurs in practice. The value of $\varphi \sim 10°$ required to reproduce the experimental ν_{xz} value at zero strain (Figure 5.14b and Figure 5.9a, respectively) appears reasonable and consistent with Figure 5.5b.

No rotation of axes was considered (i.e. $\varphi = 0°$) for the x-y plane properties of the VCR = 1 region of the gradient foam, since there is no clear experimental evidence for this from Figure 5.5c, and isotropic properties are predicted by the model for the undeformed honeycomb in this case. Reasonable agreement with experimental ν_{xy} vs ε_x trends was obtained when employing an apparently high value of $k_{hf}/k_s = 0.3$ in the model predictions. Buckling of ribs in the through-thickness (z) direction was observed following conversion (Figure 5.5d), and this is not evident in the projection of the structure in the x-y plane (Figure 5.5c). In which case, hinging may be mediated by (lower stiffness) rib bending in the x-z plane and (higher stiffness, k_{hf} increasing) shearing of junction material in the x-y plane. Additionally, compression along x leads to an increased buckling of the ribs along their length, along with increased rotation out of the x-y plane, both leading to a decrease in their projected length in the x-y plane. This will be a much lower stiffness (k_s decreasing) contribution to the apparent rib stretching mechanism than actual stretching/contraction of the rib material itself. Taken together, these 3D effects lead to the potential for $k_{hf}/k_s \gg 0.04$ (the upper limit for deformation due to stretching and shearing of rib material in the 2D system), consistent with the value of $k_{hf}/k_s = 0.3$ required in the model predictions.

5.6. References

1. Duncan O., Allen T., Foster L., Senior T., Alderson A. Fabrication, characterisation and modelling of uniform and gradient auxetic foam sheets. Acta Mater. **2017**.126. 426–37.
2. Chan N., Evans K.E. Fabrication methods for auxetic foams. J. Mater. Sci. **1997**.32. 5945–53.
3. Duncan O., Foster L., Senior T., Alderson A., Allen T. Quasi-static characterisation and impact

testing of auxetic foam for sports safety applications. Smart Mater. Struct. **2016**.25(5). 054014.

4. Allen T., Martinello N., Zampieri D., Hewage T., Senior T., Foster L., et al. Auxetic foams for sport safety applications. Procedia Eng. **2015**.112(0). 104–9.

5. Allen T., Shepherd J., Hewage T.A.M., Senior T., Foster L., Alderson A. Low-kinetic energy impact response of auxetic and conventional open-cell polyurethane foams. Phys. Status Solidi Basic Res. **2015**.9. 1–9.

6. European Committee for Standardization. BS 6183-3:2000-Protective equipment for cricketers. 2000.

7. Gibson L.J., Ashby M.F. Cellular solids. Structure and properties. **1997**.pp.67, 176-183, 259-264, 286, 498p.

8. Masters I.G., Evans K.E. Models for the elastic deformation of honeycombs. Compos. Struct. **1996**.35(4). 403–22.

9. Alderson A., Evans K.E. Modelling concurrent deformation mechanisms in auxetic microporous polymers. J. Mater. Sci. **1997**.32(11). 2797–809.

10. Lakes R.S. Foam Structures with a Negative Poisson's Ratio. Science (80-.). **1987**.235(4792). 1038–40.

11. Wang Y.C., Lakes R., Butenhoff A. Influence of Cell Size on Re-Entrant Transformation of Negative Poisson's Ratio Reticulated Polyurethane Foams. Cell. Polym. **2001**.20(4–6). 373–85.

12. Choi J.B., Lakes R.S. Nonlinear Analysis of the Poisson's Ratio of Negative Poisson's Ratio Foams. J. Compos. Mater. **1994**.29. 113–28.

13. Grima J.N., Attard D., Gatt R. A novel process for the manufacture of auxetic foams and for the conversion of auxetic foam to conventional form (WO 2010049511 A2). **2010**. 1–5.

14. Li Y., Zeng C. Room-Temperature, Near-Instantaneous Fabrication of Auxetic Materials with Constant Poisson's Ratio over Large Deformation. Adv. Mater. **2016**.28(14). 2822–6.

15. Lisiecki J., Błazejewicz T., Kłysz S., Gmurczyk G., Reymer P., Mikułowski G. Tests of polyurethane foams with negative Poisson's ratio. Phys. Status Solidi Basic Res. **2013**.250(10). 1988–95.

16. Lisiecki J., Klysz S., Blazejewicz T., Gmurczyk G., Reymer P. Tomographic examination of auxetic polyurethane foam structures. Phys. Status Solidi Basic Res. **2013**.251(2). 314–20.

17. Choi J.B., Lakes R.S. Nonlinear properties of polymer cellular materials with a negative Poisson's ratio. Mater. Sci. **1992**.27. 4678–84.

18. Bezazi A., Scarpa F. Tensile fatigue of conventional and negative Poisson's ratio open cell PU foams. Int. J. Fatigue. **2009**.31(3). 488–94.

Chapter 6: Fabrication of closed cell auxetic foams using foam found in sporting PPE

6.1. Introduction

This chapter will address Aim 4 (Chapter 1, Page 5):

Sporting PE and PPE often use closed cell foam with a Young's modulus (~1 MPa) that is ~30 times greater than typical open cell auxetic foam (Chapter 2). Auxetic closed cell foam has been fabricated using conventional thermo-mechanical methods [1], heating foam inside a pressure vessel (100°C, 100kPa) [2] and recently using steam treatment [3]. Typical thermo-mechanical conversions rupture cells [1], heating hydrostatic pressure vessels has safety risks and so an expensive vessel is required. As identified in Aim 4 (Chapter 1, Page 5), the only reported steam treated foams were for relatively rigid closed cell foams [3] with a high Young's modulus both before and after fabrication (~20 MPa then ~60 MPa, Figure 6.1).
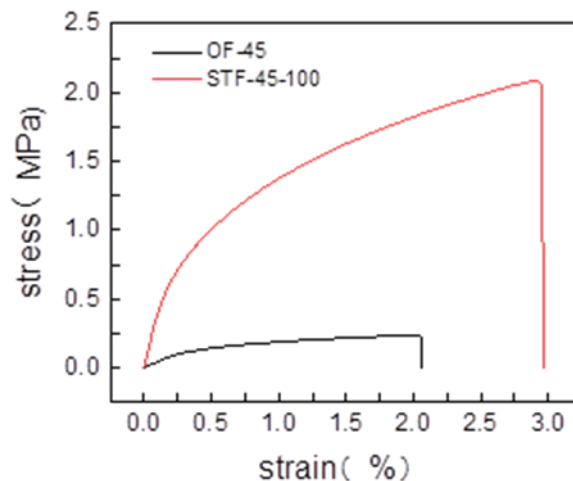
Figure 6.1: Stress vs Strain of steam processed and unprocessed foam (from private communication with the authors of [3])

Steam can permeate closed cells (Figure 6.2, [3]), if heating time is sufficiently long. When cooled (Figure 6.2), the trapped steam reduces in volume, causing cells to contract and imparting a buckled, re-entrant-like structure [3]. In conversions that produced NPR foam, the foam's volume decreased to a final volume ratio of ~5 (FVR = initial/final volume), and mass increased by ~20% due to water trapped in the cells [3]. The closed cell polyethylene foam's glass transition temperature was ~100°C, so the imparted structure was retained [3]. Variables are available to adjust the final cell structure, for example, the conversion time and temperature, and subsequent cooling temperature can all cause different volumetric reductions [3]. The following exploratory work aims to show whether the structure of foams used in sports equipment can be changed using steam processing.
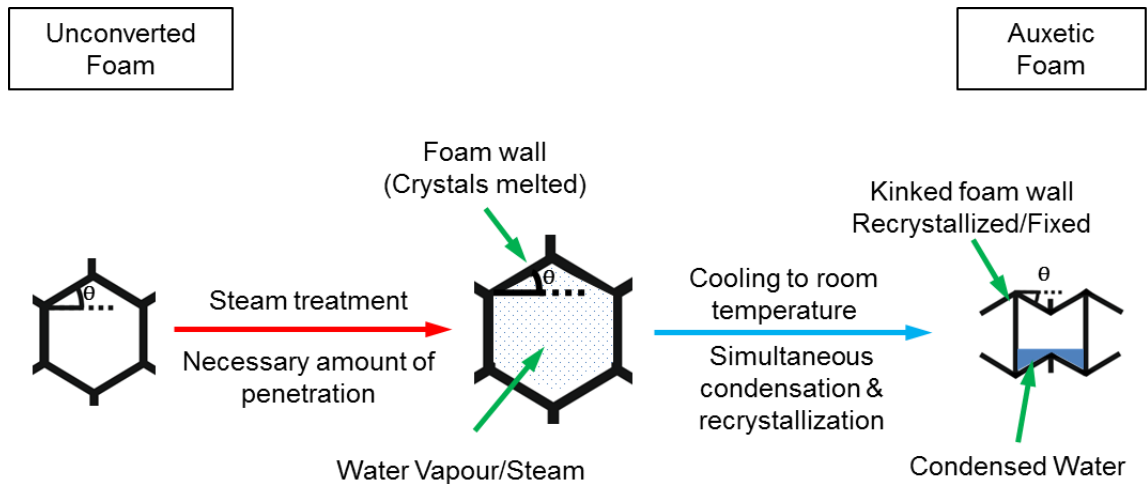
Figure 6.2: Steam permeation and subsequent closed cell shrinkage, leading to kinked cell walls and NPR

6.2. Methods

6.2.1. Foam fabrication

Samples were cut from pre-sourced sheets of foam taken from commercial football shin pads (Mitre Aircell, 50 x 10 x 6 mm and Mitre, IC Tungsten 50 x 10 x 5 mm) and Plastazote LD60 closed cell foam (LDPE-60, 80 x 50 x 10 mm, supplied by Algeos.com, see Appendix A). Samples were placed in a covered container filled to 80% with water in an oven (MCP Tooling Technologies LC/CD) for five or seven hours (mitre of Zotefoams respectively) at 101°C, conditions selected following a pilot test that gave an FVR of ~5 [3]. Immediately after heating all contents of the vessel were poured into an unplugged sink, and foams were cooled in air in the sink.

6.2.2. Characterisation

Fourier transform infrared spectral analysis (FTIR) were collected of the unprocessed foams on a Nexus FTIR spectrometer over the wavenumber range of 4000 to 600 cm^{-1}, using an ATR accessory utilising a diamond crystal. Resolution was 8 cm^{-1} and a mean was taken over 32 scans. Differential Scanning Calorimetry (DSC, Perkin Elmer DSC 8000) while heating 6-7 mg unprocessed foam samples from 25 to 120°C, cooling to 25°C, and then re-heating to 120°C (at a rate of 10°Cmin^{-1}) assessed thermal transition temperatures.

Dimensions and mass were recorded (Vernier Callipers) immediately before and after fabrication, and 16 hours after removal from the oven. Due to low sample thickness (< 5 mm), only tensile characterisation was possible. The LDPE 60 sample was cut (50 x 10 mm) with a Stanley knife. A speckle pattern was applied to all samples (matt Acrylic spray paint, Halfords). Samples were clamped in the test device jaws (Instron 3367, 500N load cell) and tested to 20% strain (0.0033 s^{-1}). Tests were filmed (Nikon, D810, 1920 x 1080 pixels, 25 fps) and videos

analysed using digital image correlation (DIC) in GOM Correlate (as in Chapters 3 and 4). A target area was defined over the central third of samples (Figure 6.3), giving axial and lateral true strains. Force data was taken from the Instron software (Bluehill 4.0, sample frequency 25 Hz). Young's modulus was calculated from linear regressions fitted to stress (Instron & sample measurements) vs axial strain (DIC). Poisson's ratio was the negative of linear regressions fitted to axial vs transverse strain (DIC). An unconverted sample of each foam (80 x 10x 10, 6 or 5 mm for LDPE, Aircell and IC Tungsten respectively) was tensile tested using the same method as described above.
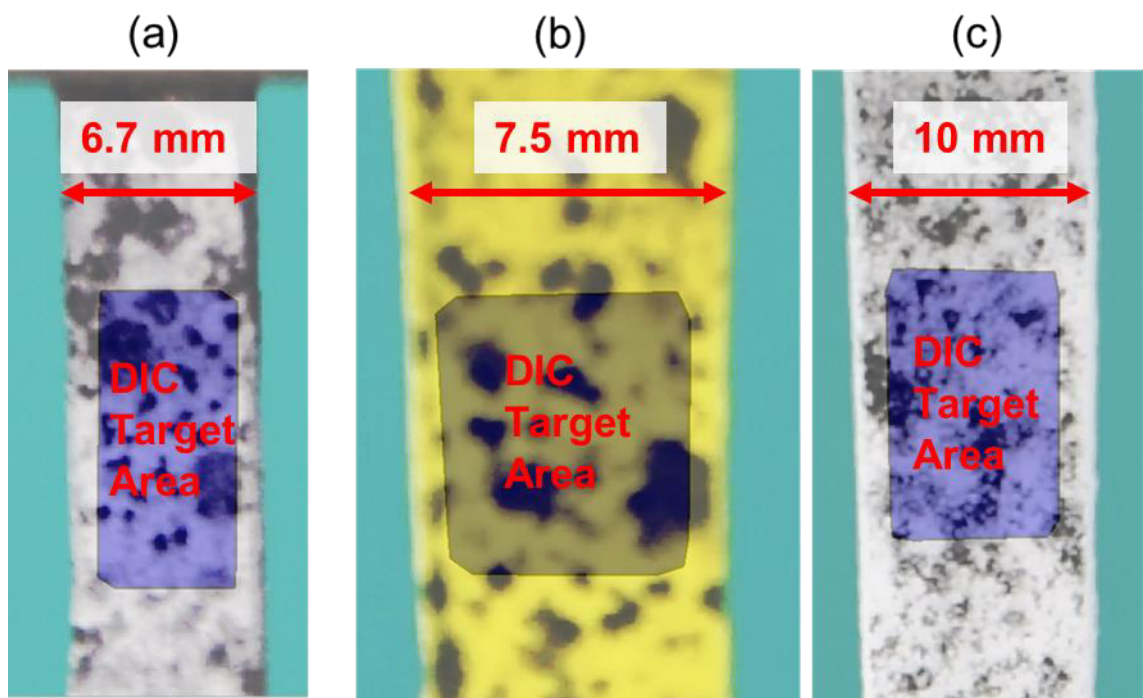
Figure 6.3: Steam treated a) Mitre Aircell foam, b) Mitre IC Tungsten foam and c) Algeos LDPE-60 foam with speckle pattern and target area over central third (Instron jaws above and below image). Dimensions show sample width.

6.3. Results

The mass of all samples was found to have increased, when measured 16 hours after steam processing (Table 6.1). FVR increased for all samples, less for the LDPE foam than the Aircell and Mitre (Table 6.1).

Table 6.1: Mass and FVR 16 hours after fabrication

	Aircell	IC Tungsten	LDPE
Mass (% original)	103	111	117
FVR	5	3.6	2.3

All three unprocessed foams exhibited a thermal transition in both DSC heating cycles, relating to melting, starting at ~100°C; then another relating to recrystallization at ~90°C during

the cooling cycle (Figure 6.4). The converted LDPE and Aircell foams exhibited mostly positive Transverse strain at maximum (~15%) tensile strain, the converted IC Tungsten foam exhibited near zero transverse strain (Figure 6.5). These suggest negative or near zero Poisson's ratios respectively.
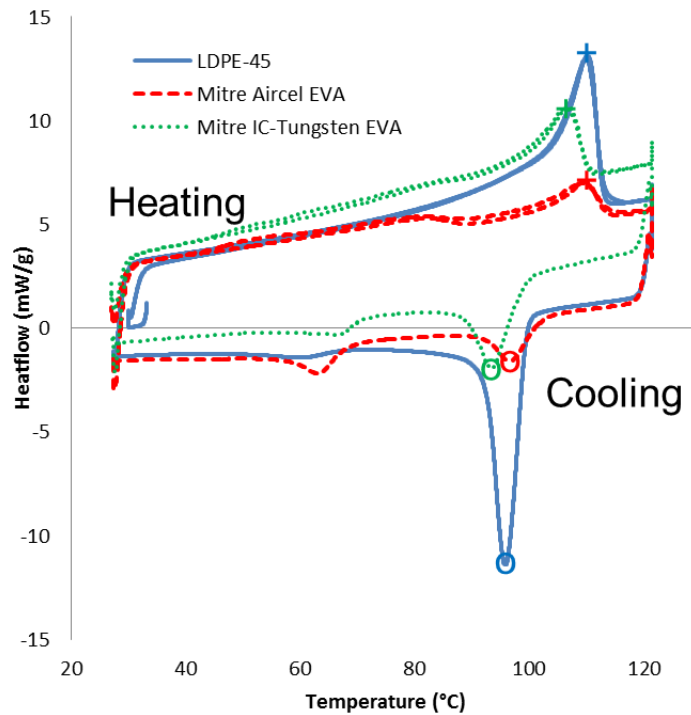
Figure 6.4: DSC cycles between 25 and 120°C for the unprocessed foams. Thermal transitions relating to melt (+) and re-crystallisation (o) are labelled
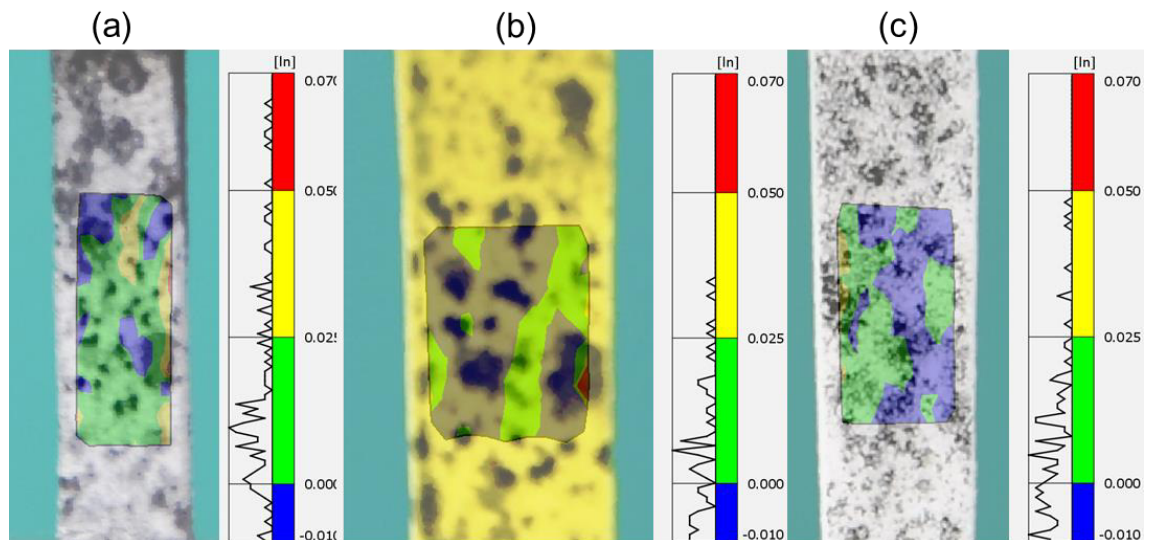
Figure 6.5: Contour plot of transverse strain of steam treated a) Mitre Aircell foam, b) Mitre IC Tungsten foam (blue showing grey due to mixing with yellow) and c) Algeos LDPE-60 foam at maximum (20%) tensile strain

The unconverted Mitre foams were Ethyl Vinyl Acetate (~90% spectral match) [4], Appendix B. The LDPE-60 was a Low Density Polyethylene (~96% spectral match), as expected

[4], Appendix B. All unconverted samples exhibited Poisson's ratios close to 0.5 (Figure 6.6a), and Young's moduli between 1.5 and 2 MPa (Figure 6.6b). The unconverted foams have non-linear stress vs strains relationships (Figure 6.6b), although as an indication of stiffness in this instance the values for Young's modulus seem reasonable.
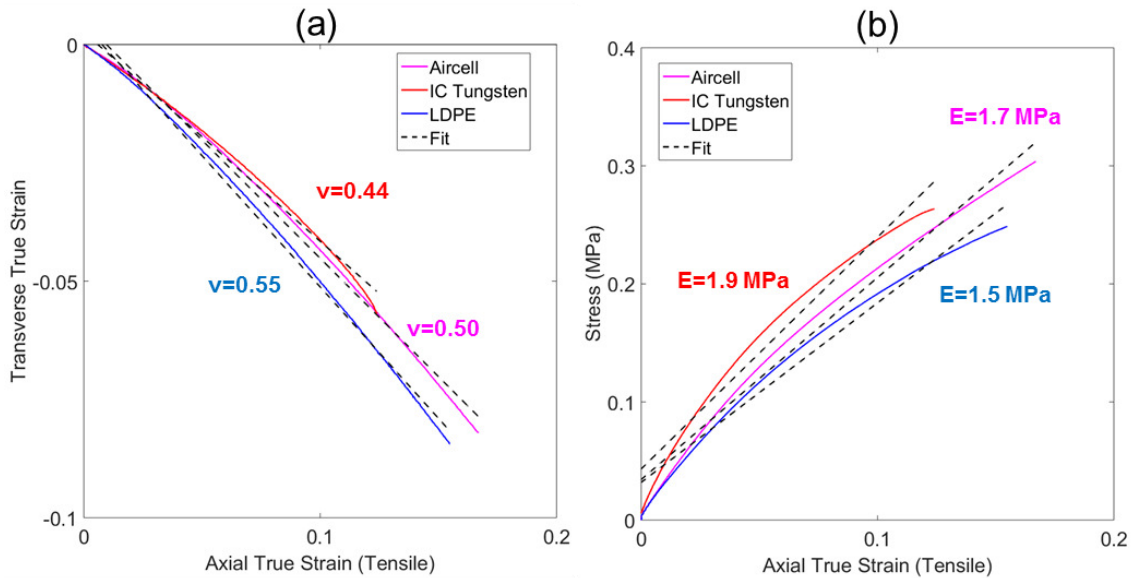
Figure 6.6: Axial tensile strain vs: a) Transverse Strain and b) Stress for all three unconverted foams.

All converted samples exhibited near zero or marginally negative Poisson's ratio up to 10% tensile strain, and near zero or marginally positive Poisson's ratios between beyond 10% tensile strain (Figure 6.7a). Young's moduli were between 1 and 3 MPa over the entire 20% tensile strain (Figure 6.7b). The LDPE foam exhibits a non-linear stress vs strain relationship, although both the Mitre foams are relatively linear (Figure 6.7b).
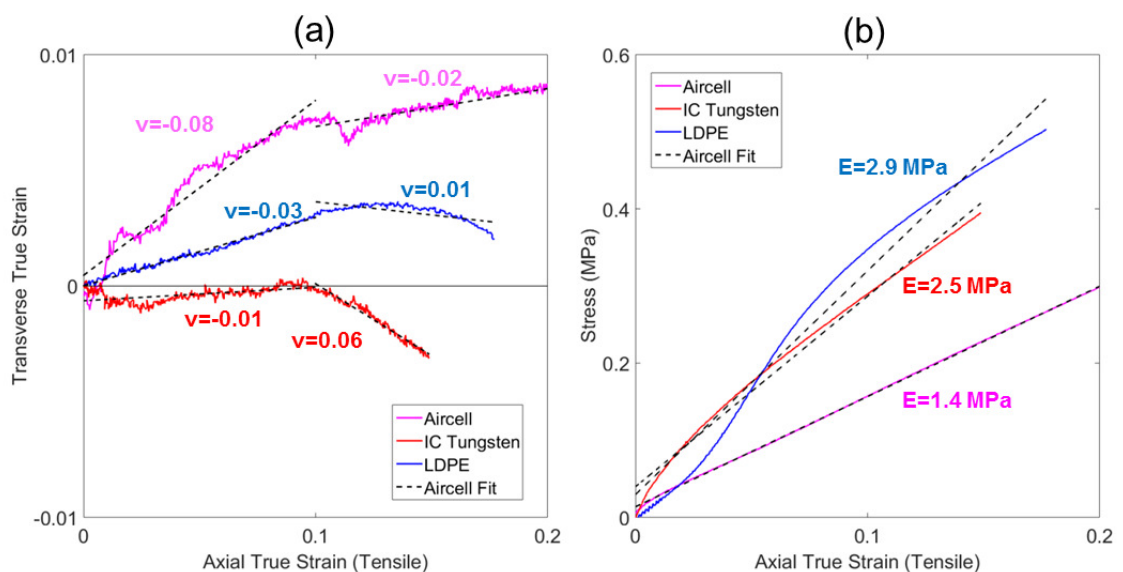
Figure 6.7: Axial tensile strain vs: a) Transverse Strain and b) Stress for all three converted foams (ν and E are Poisson's ratio and Young's modulus respectively).

6.4. Discussion

Recently developed steam treatment methods can be applied to closed cell foams found in two sports shin pads, and readily available closed cell foam with a comparable Young's modulus to foam found in sports equipment (~1 MPa). Steam processing successfully reduced the volume of each sample (FVF between 2.3 and 5), increasing their mass by up to 20% in a similar manner to previous work [3] and imparting marginally negative Poisson's ratios (lowest NPR = -0.08). Tensile Young's moduli increased in two of the three samples, giving a range (1 to 3 MPa) comparable to foams found in sporting PE and PPE (~1 MPa, Chapter 2).

A comprehensive study is required to fabricate samples from a range of foams with different Poisson's ratios, Young's moduli and densities, prior to indentation and impact testing in comparison to materials currently used in sporting PE and PPE. Heating time and temperature, and subsequent heating are options to further change cell structure [3]. DS (Figure 6.4) confirmed that the polymer foams passed through a transition temperature upon heating, increasing then decreasing polymer chain mobility and the likelihood that their FVR was fixed, rather than being held by negative pressure following condensation.

The processing time would affect the amount of steam absorbed by the foam, again changing the FVR upon cooling. Further work could measure Poisson's ratios and Young's moduli in compression, in different orientations and at high strains and strain rates. Fabrication of gradient sheets using steam proof lacquer or a bespoke rig to prevent/allow steam penetration in certain regions could produce tailorable, increasingly ergonomic PE and PPE. With the large volume of work required, such a recent finding cannot be rigorously assessed within this PhD, but leaves exciting opportunities for further work and the increased possibilities for the application of auxetic foam in sports equipment.

6.5. Reference List

1. Chan N, Evans KE. Fabrication methods for auxetic foams. J Mater Sci. 1997.32. 5945–53.
2. Martz EO, Lee T, Lakes RS, Goel VK, Park JB. Re-entrant transformation methods in closed cell foams. Cell Polym. 1996.15(4). 229–49.
3. Fan D, Li M, Qiu J, Xing H, Jiang Z, Tang T. A Novel Method for Preparing Auxetic Foam from Closed-cell Polymer Foam Based on Steam Penetration and Condensation (SPC) Process. ACS Appl Mater Interfaces. 2018.
4. Scientific T. Comprehensive Forensic FT-IR Collection. Altrincham, UK; **2018**.

6.6. Appendices

Property	Test Standard	Units	Typical value
Apparent Density			(nominal)
Skin/Skin	BS EN ISO 7214:2012	kg/m³	60
Cell Size (Cell Diameter)	Internal	mm	0.6
Compression Stress-Strain	BS EN ISO 7214:2012	kPa	
25% compression	25 mm cell-cell		124
50% compression			204
Tensile Strength	BS EN ISO 7214:2012	kPa	615
Tensile Elongation		%	144
Flammability			
Automotive	FMVSS.302 – Burn rate	<100mm/min.	Pass at 6mm
Compression Set	BS EN ISO 7214:2012	% set	
25% comp., 22hr, 23°C	25 mm cell-cell		
½ hr recovery			7
24 hr recovery			3
Tear Strength	BS EN ISO 8067:2008 Method B	N/m	3034
Shore Hardness	BS EN ISO 868:2003		
OO Scale			66
Recommended maximum operating temperature*	Internal	°C	100
Water absorption	ISO 2896:2001 Ed3.	%	<2

Appendix A: Details of Plastazote LD60 available from zotefoams©
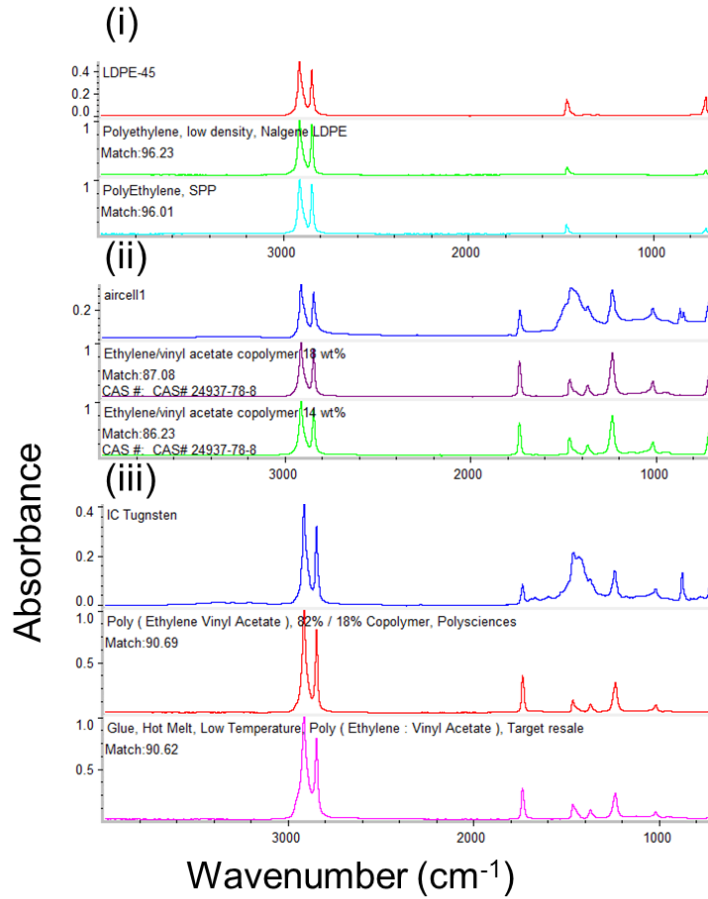
Appendix B: Absorbance spectra and comparisons to database materials for: i) LDPE-60, Algeos, ii) Aircell, Mitre and iii) IC Tungsten, Mitre

Chapter 7: Discussions and Conclusions

7.1. Discussions

Following a review of the relevant scientific literature (Chapter 2, Page 10), aims (Chapter 1, Page 5) were formed, and addressed in Chapters 3 to 6. The work addressing each aim and objective will be discussed, leading to a summary of findings and implications, suggestions for further work then concluding statements.

7.1.1. Discussion of Aim 1

Effects of thermo-mechanical auxetic foam conversion parameters for polyurethane foam: i) applied volumetric compression, ii) conversion temperature and iii) the duration of conversions on elastic properties (Young's modulus & Poisson's ratio) and dimensional stability over time or after heating had not previously been compared to polymeric changes. Fourier transform infrared spectral analysis (FTIR) of samples converted with heat exposure greater than 150°C for 20 minutes suggests continuously increasing hydrogen bond interactions in urea groups (C=O---H-N), and an increase in hydrogen bonding population. Spectral changes inferred soft segment degradation following extensive heat exposure (200°C, 180 minutes), specifically a shift and intensity change in CH_2 and C-O-C polyol bands and a broad baseline increase between 3600 and 2400 cm^{-1}. These changes are linked to: i) resistance to shape memory over time and when re-heated, ii) Poisson's ratio becoming negative, then zero in tension, or marginally positive in compression iii) stiffness reducing then increasing, iv) mass loss (evidenced by Thermogravimetric analysis, increasing from 150°C). The minimum mean values of Poisson's ratio are ~-0.2 (to 10% compression/tension) which is comparable to other studies. All samples that retain compression are isotropic, with near constant elastic moduli and Poisson's ratios between ~-0.2 and 0 (to 10 % compression/tension).

Samples with the largest magnitude of NPR (VCR = 3, 160°C, 20 minutes, 140 °C, 60 minutes and 120°C, 180 minutes) expanded to an FVR of two a week after fabrication. Iso-density samples, fabricated with a VCR of two at 180°C for 60 minutes were isotropic, had near zero Poisson's ratios, and quasi-linear stress vs strain relationships. Iso-density, isotropic, quasi-linear samples with a range of negative and near zero Poisson's ratios can, therefore, be fabricated for comparative tests for the effect of Poisson's ratio on Indentation resistance (and other characteristics such as double curvature [1] and vibration damping [2,3]). Samples heated at 160°C to 180°C for 20 minutes, 140°C to 160°C for 60 minutes and 120°C to 140°C exhibited gradually increasing dimensional stability ($2 \leq FVR \leq 3$), Poisson's ratio ($-0.2 \leq \nu \leq 0$) and Young's modulus (30 kPa $\leq E \leq$ 50 kPa).

A small change in conversion temperature (20°C) had a comparable effect on shape fixing, Poisson's ratio and Young's modulus to a large change of approximately three times in conversion time (Table 3.1, Chapter 3, Page 83). Increasing conversion temperature gradually increased hydrogen bonding, as observed with FTIR. There was no significant change until the samples were held at 200°C for 180 minutes, when the C-O-C polyol peak shifted and reduced. For all other conversions, increasing temperature or time had a comparable effect, and so conversion time and temperature have been grouped together as increased heat exposure.

As in other work [1,4–7], missing ribs were not able to be identified within micro-ct scans or microscopy of converted foams, regardless of heat exposure, meaning that they were unlikely to have been present (Figure 3.6 & 3.7, Chapter 3, Pages 55-56). The presence of kinked and inward folding ribs was clear under micro-ct and optical microscopy at rest and in tension (Figures 3.6 & 3.7, Pages 55-56). With marginal mass loss apparent, the Thermo-Mechanical process appears to have changed the structure of open cell foam, creating quasi-linear stress vs strain relationships and a reduction in Poisson's ratio (from ~0.3 to zero or below to ~-0.2, Figure 3.10, Page 59). 2-D honeycombs models [8,9] and Reuss - Voigt - Hill isotropic averaging [10] were used to approximate the expected effects of polymeric and structural changes to mechanical properties (Figure 3.26, Page 79). The different Poisson's ratios of converted samples can be explained by changes to the cell rib material, with reasonable estimates for the relationship between force constants associated with rib flexure and/or hinging and rib stretching (i.e. increasing rigidity) allowing Poisson's ratios between ~-0.1 and zero. Increasing rib rigidity (due to increased hydrogen bonding interaction and populations, most likely close to rib junctions and kinks) can also explain larger Young's moduli in samples fabricated with more heat exposure which had higher (i.e. near zero) Poisson's ratio. The experimental values for Poisson's ratio (Figure 3.10, Page 59) and Young's modulus (Figure 3.13, Page 62) are likely caused by a mixture of rib stiffness between the lower and upper limits of those included in the analytical model. The foams subject to increased heat exposure during conversion appear to have contained a greater concentration of cells with k_{hf}/k_s ranging towards the maximum value (0.036) than the foams converted with decreased heat exposure (Figure 3.26, Page 79). Additional structural factors such as adhesion between cell ribs and thickening of rib material close to junctions was not identified (Figures 3.6 & 3.7, Pages 55-56) or included in the model, but could explain further differences between the Poisson's ratios of converted foams.

The foams fabricated in Chapter 3, showed a gradual range of complete, partial and blocked shape memory [11,12] (Figures 3.4 & 3.5, Pages 53-54). These levels of dimensional and structural stability were: i) Complete dimensional recovery after the Unloading phase (removal

from their mould and hand stretching) and a return to the parent foam's Young's modulus and Poisson's ratio, ii) Partial dimensional recovery after Unloading, retaining NPR, but complete dimensional recovery during the Recovery (re-heating phase), iii) Partial dimensional recovery in the Recovery phases, retaining NPR (also known as partially blocked shape memory), and iv) Complete dimensional stability during the Recovery phase. Foams with complete dimensional stability exhibited near zero Poisson's ratio in tension and compression, both before and after Recovery, and so have blocked shape memory, but were not auxetic. Foams in group (iii) are auxetic, exhibit blocked shape memory and were fabricated in one heating phase, simplifying previous fabrication methods for blocked shape memory auxetic foams [11].

7.1.2. Discussion of Aim 2

Using a range of foams fabricated based on findings in Chapter 3, Page 46, indentation resistance of auxetic foams has been tested, and for the first time variables other than NPR have been eliminated and accounted for. The quasi-linear stress vs strain relationships were still not sufficiently linear over the large strain ranges tested to calculate normalised indentation resistance [13], showing little agreement to theoretical values. Excluding the anisotropic unconverted foams (Figure 4.20, Page 109) gave values for x between 0.7 and 0.8 for all indenters; a value of 0.33 is expected for cylinders and 1 for the stud [14]. Considering integrated energy absorption rather than typical measures for indentation resistance (Figure 4.24, Page 111), showed better agreement to the theory [14] and allowed inclusion of unconverted samples during studded indentations. Unconverted samples remained outliers during studded indentations, falling below the fitted linear regression line.

The application of a correction factor previously used for sample thickness in thin sheets of rubber [15], currently untested for foam, appeared appropriate for the cylindrical indenters. Following application of the correction factor, values for x reduced from 0.96 and 1 to 0.6 and 0.76 for the 50 and 10 mm diameter cylinders, respectively (Figure 4.22 & 4.23, Chapter 4, Pages 110-111). A value of x = 0.91 was obtained for the stud (Figure 4.24, Chapter 4, Page 111), where the correction factor, designed for spherical indenters, did not appear appropriate and reduced x to 0.55 (Figure 4.23, Chapter 4, Page 111).

Remaining discrepancies, such as increased x in cylindrical samples and the unconverted samples remaining outliers during studded indentations, were likely be caused by: i) different amounts of densification, caused by transverse strain (due to Poisson's ratio, Figure 4.26, Page 114), and ii) differences in the shape of the indented surface, caused by changes in shear modulus/Young's modulus (due to Poisson's ratio, Figure 4.28, Page 117). Both of these would be expected to increase normalised indentation energy in NPR than zero or positive

Poisson's ratio samples. The effect of changes to cell shape vastly changes how density increases affect stiffness, and could mean that any assumed proportionality between density and stiffness becomes invalid [16]. Changes to cell shape were qualitatively assessed via indentation of ~1 mm thick samples (Figure 4.27, Page 115). The unconverted foam's cells buckled and changed considerably, no clear change was able to be identified in the converted samples.

As identified in Chapter 2, page 10-11, materials which react to the size and shape of impacting bodies while remaining ergonomic and flexible during normal operation could help to reduce the current dependence upon Shear thickening materials, which are designed and certified for highly specific conditions and strain rates that don't reflect infield scenarios. Comparing the normalised indentation energy absorption of NPR and conventional materials indicates that PE and PPE incorporating auxetic materials could react to resist penetration during falls or collisions with a variety of shapes of impacting bodies and surfaces. The increases to indentation resistance, unlike previous work [17–21] whereby differences were amplified by density changes and changes in stress vs strain relationships, show the minimum expected increases. Increases to indentation resistance between positive Poisson's ratio and NPR samples were modest during cylindrical indentations, but larger during studded indentations, whereby indentation resistance was affected by Poisson's ratio in both lateral dimensions.

7.1.3. Discussion of Aim 3

The use of pins facilitated the application of uniform and variable, isotropic and anisotropic linear compression ratios in large foam sheets (final dimensions = 350 x 350 x 20 mm). Isotropic sheets (fabricated with and without pins) and quadrants of the gradient sheet with a VCR of 2.9 had similar dimensional stability (Figure 5.6, page 121, ~15% re-expansion upon re-heating), Poisson's ratio (Figure 5.8 to 5.9, Pages 139, ~-0.1 to ~-0.2) and tangent modulus (Figure 5.11, page 142, ~50 kPa) to smaller samples of foam fabricated at 140°C for 180 minutes, 160°C for 60 minutes and 180°C for 20 minutes (Chapter 3, Figures 3.10 & 3.13, Pages 59 & 62). Lower NPR (~-0.2) is possible with less heat exposure (Figures 3.10, Page 59), but dimensional stability (Figure 3.4, Page 53) would be sacrificed.

Anisotropic quadrants (Figure 5.1, Page 125) that were stretched in both planar directions and compressed through thickens to buckle ribs, giving a VCR of 1, exhibited high transverse contraction through thickness when compression tested parallel to either planar direction, corresponding to a uni-axial NPR of ~-0.4. Because the cells ribs did not buckle in the two planar directions (Figure 5.5, Page 136), stress vs strain relationships (Figure 5.8, Page 139) retained the unconverted foam's plateau due to cell rib buckling during compression [1,9]. Experimental data in all three axes fitted reasonably well with an analytical model for off-axis

deformation of cellular structures (Figure 5.15, Page 147), adapted from previous works [8,9,22]. Surprisingly little prior work has included or validated such a model, which can now be used along with presented methods to apply gradient or uniform compression and to design cell structures for specific applications-e.g. with a protective function in one area, but increased conformability or breathability in another.

While controlling compression throughout the bulk of a foam monolith, pins also created holes in the foam. The holes were often surrounded by creases (Figure 5.5, page 136). Chapter 4 (Figures 4.26 & 4.27, Pages 114 & 115) showed that densification occurs close to an indenting cylinder or pin. Holes, creases and densification all created flaws within the converted foam, and so although there was greater control of internal compression the sheets fabricated both with and without pins had similar magnitude of, and similar variability in, Poisson's ratios, tangent moduli and density (agreeing with the preceding pilot study [23]). For thinner sheets, pins were required to apply planar compression [24]. It is likely that pin size and spacing could be adjusted to reduce the size and effect of flaws caused by pins, without sacrificing control over applied compression.

7.1.4. Discussion of Aim 4

The method for fabricating closed cell auxetic foam by steam penetration, discovered towards the end of this PhD by another group [25], shows significant potential to produce auxetic foam with comparable stiffness (1 MPa) to foams currently used in sporting PPE. The initial work produced NPR foam with a Young's modulus of 70 MPa from a 25 MPa parent foam (Figure 6.1, page 133 [25]). The preliminary study presented in this thesis using an LDPE and two EVA closed cell foams shows it is also possible to produce foam with a Young's modulus close to 1 MPa (Figure 6.7, page 157). The Poisson's ratio of steam processed NPR foam was low (~-0.1, Figure 6.7, page 157), but samples retained their imposed compression over-night. Starting from sheets of foam found in sports equipment (5 to 10 mm thick), final thicknesses (3 to 6 mm) were too low for compression testing.

Further work should fabricate larger samples for compression and indentation testing in a variety of orientations. The length of conversion time affects the amount of steam absorbed by the foam, and therefore changes to cell shape [25]. The presented conversion times successfully produced NPR in the tested foams, but have not been optimised. Differential Scanning Calorimetry (DSC) measured polymer transition temperatures (Figure 6.4, page 136), and peaks present at ~100°C suggest polymer fixing upon cooling was likely [25].

7.2.   Findings and implications

Demonstration of a thermo-mechanical fabrication process for isotropic, iso-density, quasi linear open cell foam with Poisson's ratios spanning positive and negative values means that the independent effect of NPR on potentially beneficial characteristics (e.g. vibration damping, indentation resistance, pressure distribution) can now be experimentally tested. Measuring polymeric, structural and mechanical changes concurrently in single cycle thermo-mechanical conversions had not been done before and provided deeper understanding of the conversion process. The correlation between thermal mechanical processing conditions, dimensional stability, Young's modulus, Poisson's ratio and polymeric changes during auxetic foam fabrications will be useful when designing future conversion methods using a variety of compression regimes to increase the range of Young's moduli and Poisson's ratio of open cell foams (Table 3.1, Chapter 3, Page 83). Correlation of changes that can be simply measured, such as dimensional stability, allow simple checks to infer whether appropriate thermal processing conditions have been used during fabrication using different sample sizes, as demonstrated in Chapter 5. Fabricating auxetic foams with blocked shape memory in one heat cycle facilitates low cost commercial production of materials that could withstand washing (i.e. for garments) or high temperature applications.

Comparing energy absorption during indentation tests successfully showed increases to effective indentation resistance of non-linear open cell foam samples and close fit to the theory, with larger than expected effects of elastic properties, NPR in particular. As the magnitude of Poisson's ratio increased, so did normalised indentation energy and effective indentation resistance. Findings demonstrate: i) the benefits of auxetic foams; they resist penetration by concentrated loads which would be useful for seating or PPE more than their conventional counterparts, and ii) the benefits of fabricating foams using methods described in Chapter 3. Novel analysis methods for DIC furthered understanding of indentation of auxetic foam. An increase in effective indentation resistance at large (>20%) strain in NPR samples appears to differ marginally from indentation theory. DIC showed: i) NPR samples with a higher ratio of Shear to Young's modulus deformed as flatter units, causing higher mean axial compression, and ii) NPR samples exhibited transverse contraction, meaning larger increases in density and stiffness than zero or positive Poisson's ratio samples.

Pins successfully controlled and adapted compression, and therefore cell shape, in thermo-mechanical conversions of large (350 x 350 x 20 mm) sheets of open cell auxetic foam.

The connection between cell shape, Young's modulus and Poisson's ratio (up to 50% compressive and tensile strains), was demonstrated experimentally and by an analytical model for off axis deformation of re-entrant cells, of which there are surprisingly few prior examples. Based on comparison of measured Young's modulus, Poisson's ratio and dimensional stability upon re-heating to foam fabricated in Chapter 3, the thermal processing conditions for the large auxetic foam sheets were appropriate. Large magnitude anisotropic NPR (of ~-0.4) was achieved in the VCR = 1 quadrant of the gradient sheet where pins were essential in applying tension.

Fabricating closed cell auxetic foam using steam penetration from foam used in sports equipment produced the first known auxetic foam samples with Young's modulus comparable to foam in sporting PPE (~1 MPa). The fabricated closed cell foam retained its imposed compression over a short period of time (measured after 16 hours, prior to tensile testing).

7.3. Further work

Only one type of open cell foam (PU FR30, Custom Foams) was used throughout this thesis, meaning results from each study are comparable but not conclusive. Studying a range of thermo-mechanical conversion mechanisms by using foam with different original polymeric constitutions (e.g. [26]) could show which conversion mechanisms and foam types give the largest magnitude NPRs. Applying larger VCRs to kink ribs further, before allowing them to re-expand following conversion may also increase the magnitude of NPR [11]. Annealing and cooling methods should also be considered, although will be more critical in foam T_g above or close to room temperature.

Indentation testing open and closed cell auxetic foam using multiple cameras for 3D DIC, and analysis of multiple faces would show volume change and increase experimental rigour. Applying pressure sensors between the sample and indenter and underneath the sample could help validate findings from DIC, and show NPR's effect on pressure concentrations (important for comfort and protection). Compliance with the relevant standards [27], and comparison to sporting PPE, both require indentation testing using samples with larger planar dimensions. Indentation testing to higher strains (>20%), and at high strain rates or under impact is also necessary to show whether NPR and effective indentation resistance are maintained. Micro-structurally faithful Finite Element Modelling should estimate the effect of densification and the shape of the compressed area caused by Poisson's ratio on increased effective indentation resistance over large strains.

The effect of pin size and spacing on homogeneity of cell structure, density, Young's modulus and Poisson's ratio of thermo-mechanically fabricated open cell foam samples should

be considered. Additional options include conversion of gradient and uniform sheets using methods to locate visual markers, without causing damage to fabricated samples. There has not yet been a comparison of all methods for fabricating large samples of open cell auxetic foam; using vacuum bags [28], compression by multiple moulds with gradually increasing VCR [29] and by moulds with movable walls [30,31]. Such a comparison may be useful in designing a commercial fabrication route. Continued improvements to fabrications for large sheets and monoliths of auxetic foam will then require repeated testing for potential applications: for example as crash mats [19], helmet liners [32] and cricket pads [23,33].

Now that small samples of closed cell auxetic foam can be fabricated with Young's modulus close to materials in sporting PPE, future work should look to fabricate larger samples. Larger samples would facilitate compression testing, more applicable to PPE than tensile testing. Testing should also be carried out in multiple orientations, including repeat testing to infer degradation and under indentation and impact, in comparison with current materials in sporting PPE. Fabrication of gradient sheets may also be possible, using steam proof lacquer or a bespoke rig to prevent or allow steam penetration in certain regions. Measuring polymeric changes and changes to cell structure during conversions would facilitate informed selection of processing routes to adjust cell shape and mechanical characteristics (i.e. Young's modulus and Poisson's ratio). Conversion time, temperature and cooling rate could all be adjusted.

7.4. Conclusions

In Chapter 3, thermo-mechanical auxetic conversions for open cell PU foam were analysed in detail. The imposed re-entrant structure required sufficient softening (in this case by heat) to fix it in place. The effect on dimensional stability, Poisson's ratios and Young's moduli of small increases in conversion temperature were comparable to large increases in conversion time. Little change was noted for conversions below 130°C for 60 minutes or 120°C for 20 minutes.

As heat exposure increased above 150°C for 20 minutes, which appeared comparable to 130°C for 60 minutes, several observations were noted:

i) Samples became stiffer and Poisson's ratio generally increased from its minimum value (~-0.2) towards (but not necessarily reaching) zero in tension, or small positive values in compression.

ii) Sample expansion over time and after re-heating gradually reduced.

iii) The hydrogen bonding strength between urea groups (C=O---N-H) increased relatively as did their population which was likely to have led to fixing of applied VCR.

iv) Mass loss became significant at 200°C showing onset of degradation - which was backed up by several spectral changes.

Samples fabricated at higher temperatures and longer times (200°C for 20 minutes, > 190°C for 60 minutes, > 160°C for 180 minutes) exhibited dimensional stability and tensile NPR, but did not have compressive NPR. The correlating trends are as useful as the specific conditions under which minimum NPR was obtained. Tests of shape fixing, for example, can now be quickly applied to converted foams to infer whether appropriate amount of heat exposure has been used, rather than repeatedly carrying out lengthy parametric studies to minimise NPR. A similar approach comparing correlating changes would be useful across a wide range of thermo-mechanically converted foams.

The findings in Chapter 3, in response to Aim 1, were applied to larger conversions (Aim 3) in order to verify heating time and temperature were appropriate. Finding the specific conversion conditions under which minimum and maximum Poisson's ratios were obtained for iso-density, converted samples allowed fabrication of comparative samples for indentation testing (Aim 2). Calculating the indentation energy absorbed by non-linear auxetic and conventional foams allowed comparisons over a greater strain range than calculating indentation resistance did, reducing errors caused by non-linearity. A correction factor for thin sheets of rubber appeared applicable for cylindrical, but not studded, indentations. Following an assessments of errors, unconverted samples were notable outliers during studded indentation tests and also exhibited lower normalised indentation energy than NPR samples. Elastic properties, Young's modulus and Poisson's ratio (x in Equation 4.3, Chapter 4, Page 87), had a greater than expected effect during cylindrical indentations. A combination of increased densification due to transverse contraction in NPR foams and/or changes in the deformation profile (with NPR foam deforming as a flatter unit) could have contributed to discrepancies. The increased indentation energy of NPR foams is useful to manufacturers looking to improve open cell protective equipment and reduce the chances of penetrating through an entire pad or item of PPE. Further work can now apply the methods to indentations at higher strains and strain rates or under impact to show effective indentation resistance of protective equipment during impact scenarios.

The internal cell structure and mechanical properties of open-cell PU foam were altered by changing the compression regime applied while thermo-mechanically fabricating large sheets of auxetic and gradient foam. The Poisson's ratios, thermal stability and Young's moduli suggest the foam was heated by an amount which gave a good balance between structural

stability and the magnitude of NPR, as found previously in Chapter 3. Control of localised compression was achieved by employing pins inserted through the foam, although changing pin size and spacing could further decrease structural variation. Triaxially-compressed sheets fabricated with through thickness pins exhibited similar properties to those fabricated without pins, suggesting effects of densification and creasing surrounding pin holes were comparable to the effects of uncontrolled planar compression. The pins did, however, control compression levels effectively to enable the fabrication of heterogeneous sheets of foam having regions displaying markedly different cellular structure, and mechanical and impact properties. A consideration of projections of the cellular structure in terms of simplified idealised 2D honeycombs deforming via simultaneous flexing, rotation and stretching of the cell ribs can explain the observed mechanical properties reasonably well.

Following fabrication of closed cell auxetic foams from foam found in sporting PPE, and foam with a similar Young's modulus to that of foam in sporting PPE, a new line of research and future product development has become available. Combined with collected evidence suggesting that theoretical benefits of NPR can be maintained under indentation to high strains, auxetics do appear useful in sporting impact protection, particularly crash pads that use open cell foam. Further work is required to develop control during large scale open cell auxetic foam fabrications. A parametric study into the effects of steam processing time to create a series of conditions for different closed cell auxetic foams should be carried out and publicised, allowing commercial manufacturers of sporting and other PPE to consider auxetic closed cell foam during material selection. In the future, the benefits of NPR should be shown using a similar approach to methods in Chapter 4, controlling and explaining the effects of variables other than NPR. Equipment designers would then be able to make informed decisions as to how auxetic foam could improve their products.

7.5. References

1. Lakes R.S. Foam Structures with a Negative Poisson's Ratio. Science (80-.). **1987**.235(4792). 1038–40.
2. Scarpa F., Giacomin J., Zhang Y., Pastorino P. Mechanical performance of auxetic polyurethane foam for antivibration glove applications. Cell. Polym. **2005**.24(5). 253–68.
3. Bezazi A., Scarpa F. Tensile fatigue of conventional and negative Poisson's ratio open cell PU foams. Int. J. Fatigue. **2009**.31(3). 488–94.
4. Chan N., Evans K.E. Microscopic examination of the microstructure and deformation of conventional and auxetic foams. J. Mater. Sci. **1997**.2. 5725–36.
5. Gatt R., Attard D., Manicaro E., Chetcuti E., Grima J.N. On the effect of heat and solvent exposure on the microstructure properties of auxetic foams: A preliminary study. Phys. Status Solidi Basic Res. **2011**.248(1). 39–44.
6. Chan N., Evans K.E. The mechanical properties of conventional and auxetic foams. Part I: compression and tension. J. Cell. Plast. **1999**.35(2). 130–65.
7. Li Y., Zeng C. On the successful fabrication of auxetic polyurethane foams: Materials requirement, processing strategy and conversion mechanism. Polym. (United Kingdom). **2016**.87. 98–107.

8. Masters I.G., Evans K.E. Models for the elastic deformation of honeycombs. Compos. Struct. **1996**.35(4). 403–22.
9. Gibson L.J., Ashby M.F. Cellular solids. Structure and properties. **1997**.pp.67, 176-183, 259-264, 286, 498p.
10. Yeganeh-Haeri A., Weidner D.J., Parise J.B. Elasticity of agr-Cristobalite: A Silicon Dioxide with a Negative Poisson's Ratio. Science (80-.). **1992**.257(5070). 650–2.
11. Boba K., Bianchi M., McCombe G., Gatt R., Griffin A.C., Richardson R.M., et al. Blocked shape memory effect in negative Poisson's ratio polymer metamaterials. ACS Appl. Mater. Interfaces. **2016**. acsami.6b02809.
12. Behl M., Lendlein A. Shape-memory polymers. Mater. Today. **2007**.10(4). 20–8.
13. Chan N., Evans K.E. Indentation resilience of conventional and auxetic foams. J. Cell. Plast. **1998**.34. 231–60.
14. Alderson K.L., Pickles A.P., Neale P.J., Evans K.E. Auxetic polyethylene: The effect of a negative Poisson's ratio on hardness. Acta Metall. Mater. **1994**.42(7). 2261–6.
15. Waters N.E. The indentation of thin rubberer sheets by cylindrical indetors. Br. J. Appl. Phys. **1965**.16(2). 1387–92.
16. Gibson L.J., Ashby M.F., Schajer G.S., Robertson C.I. The mechanics of two-dimensional cellular materials. Proc. R. Soc. London. A. Math. Phys. Sci. **1982**.382. 25–42.
17. Allen T., Shepherd J., Hewage T.A.M., Senior T., Foster L., Alderson A. Low-kinetic energy impact response of auxetic and conventional open-cell polyurethane foams. Phys. Status Solidi Basic Res. **2015**.9. 1–9.
18. Allen T., Duncan O., Foster L., Senior T., Zampieri D., Edeh V., et al. Auxetic foam for snow-sport safety devices. Snow Sport. Trauma Saf. Proc. Int. Soc. Ski. Saf. **2016**.21.
19. Allen T., Martinello N., Zampieri D., Hewage T., Senior T., Foster L., et al. Auxetic foams for sport safety applications. Procedia Eng. **2015**.112(0). 104–9.
20. Lisiecki J., Błazejewicz T., Kłysz S., Gmurczyk G., Reymer P., Mikułowski G. Tests of polyurethane foams with negative Poisson's ratio. Phys. Status Solidi Basic Res. **2013**.250(10). 1988–95.
21. Ge C. A comparative study between felted and triaxial compressed polymer foams on cushion performance. J. Cell. Plast. **2013**.49(6). 521–33.
22. Alderson A., Evans K.E. Modelling concurrent deformation mechanisms in auxetic microporous polymers. J. Mater. Sci. **1997**.32(11). 2797–809.
23. Duncan O., Foster L., Senior T., Allen T., Alderson A. A Comparison of Novel and Conventional Fabrication Methods for Auxetic Foams for Sports Safety Applications. Procedia Eng. **2016**.147(0). 384–9.
24. Allen T., Hewage T., Newton-Mann C., Wang W., Duncan O., Alderson A. Fabrication of Auxetic Foam Sheets for Sports Applications. Phys. Status Solidi Basic Res. **2017**.1700596. 1–6.
25. Fan D., Li M., Qiu J., Xing H., Jiang Z., Tang T. A Novel Method for Preparing Auxetic Foam from Closed-cell Polymer Foam Based on Steam Penetration and Condensation (SPC) Process. ACS Appl. Mater. Interfaces. **2018**.
26. Duncan O., Allen T., Foster L., Gatt R., Grima J.N., Alderson A. Controlling Density and Modulus in Auxetic Foam Fabrications—Implications for Impact and Indentation Testing. Proceedings. **2018**.2(6). 250.
27. The British Standards Institution Bs. BS 903-A26: 1995 ISO 48:1994. Physical Testing of Rubber. **2006**. p. 1–387.
28. Bianchi M., Scarpa F., Banse M., Smith C.W. Novel generation of auxetic open cell foams for curved and arbitrary shapes. Acta Mater. **2011**.59(2). 686–91.
29. Chan N., Evans K.E. Fabrication methods for auxetic foams. J. Mater. Sci. **1997**.32. 5945–53.
30. Loureiro M.A., Lakes R.S. Scale-up of transformation of negative Poisson's ratio foam: Slabs. Cell. Polym. **1997**.16(5). 349–63.
31. Lowe A., Lakes R.S. Negative Poisson's ratio foam as seat cushion material. Cell. Polym. **2000**.19(3). 157–67.
32. Foster L., Peketi P., Allen T., Senior T., Duncan O., Alderson A. Application of Auxetic Foam in Sports Helmets. Appl. Sci. **2018**.8(3). 354.
33. Duncan O., Foster L., Senior T., Alderson A., Allen T. Quasi-static characterisation and impact testing of auxetic foam for sports safety applications. Smart Mater. Struct. **2016**.25(5). 054014.

Appendix 1: List of publications

The following publications, ordered chronologically, were written, submitted and accepted as a part of this PhD, although data was collected for [1] during a previous MSc course. Publications [8], [9] and [4] are the most relevant publications relating to Chapters 1 and 2, Chapter 3 and Chapter 5, respectively and are included for reference.

1. Duncan O, Foster L, Senior T, Alderson A, Allen T. Quasi-static characterisation and impact testing of auxetic foam for sports safety applications. Smart Mater Struct. 2016.25(5). 054014.

2. Duncan O, Foster L, Senior T, Allen T, Alderson A. A Comparison of Novel and Conventional Fabrication Methods for Auxetic Foams for Sports Safety Applications. Procedia Eng. 2016.147(0). 384–9.

3. Allen T, Duncan O, Foster L, Senior T, Zampieri D, Edeh V, et al. Auxetic foam for snow-sport safety devices. Snow Sport Trauma Saf. Proc Int. Soc. Ski. Saf. 2016.21.

4. Duncan O, Allen T, Foster L, Senior T, Alderson A. Fabrication, characterisation and modelling of uniform and gradient auxetic foam sheets. Acta Mater. 2017.126. 426–37.

5. Allen T, Hewage T, Newton-Mann C, Wang W, Duncan O, Alderson A. Fabrication of Auxetic Foam Sheets for Sports Applications. Phys Status Solidi Basic Res. 2017.254(12).

6. Duncan O, Allen T, Foster L, Gatt R, Grima JN, Alderson A. Controlling Density and Modulus in Auxetic Foam Fabrications—Implications for Impact and Indentation Testing. Proceedings. 2018.2(6). 250.

7. Foster L, Peketi P, Allen T, Senior T, Duncan O, Alderson A. Application of Auxetic Foam in Sports Helmets. Appl Sci. 2018.8(3). 354.

8. Duncan O, Shepherd T, Moroney C, Foster L, Venkatraman PD, Winwood K, et al. Review of auxetic materials for sports applications: Expanding options in comfort and protection. Appl Sci. 2018.8(6). 941.

9. Duncan O, Clegg F, Essa A, Bell AMT, Foster L, Allen T, et al. Effects of Heat Exposure and Volumetric Compression on Poisson's Ratios, Young's Moduli, and Polymeric Composition During Thermo-Mechanical Conversion of Auxetic Open Cell Polyurethane Foam. Phys. Status Solidi. 2018.